Topology Optimization of Metamaterials and Applications to RF Component Design

By

Raoul Ouatagom Ouedraogo

A DISSERTATION

Submitted to
Michigan State University
in partial fulfillment of the requirements
for the degree of

DOCTOR OF PHILOSOPHY

Electrical Engineering

2011

ABSTRACT

Topology Optimization of Metamaterials and Applications to RF Component Design

By

Raoul Ouatagom Ouedraogo

Metamaterials are artificially engineered macroscopic composites that are designed to produce a combination of permittivity and permeability properties that are not readily available in nature. The creation of metamaterial media relies on embedding metallic or dielectric inclusions into a host medium, with the most common metallic inclusions being split ring resonators and their derivatives. Unfortunately, these resonant structures have limited flexibility since their design involves very few parameters such as ring radii and slot widths, which do not allow for much tuning of the material properties. Additionally, the performance of these resonant structures is dependent on the orientation of the exciting electric and magnetic fields. When placed next to a device, the effects of mutual coupling usually lead to an undesirable performance of the combined structure, which is coined a "metamaterial-inspired device". Therefore, additional tuning of the resonant structure becomes necessary to achieve the desired performance of the metamaterial-inspired device.

This dissertation introduces a new design methodology that can be used to synthesize new resonant structures for the design of metamaterial media. By using a pixelization approach with a binary optimizer such as a genetic algorithm, it is shown that it is possible to create resonant structures quite different from SRRs and with improved flexibility. This dissertation also introduces an in situ optimization technique as an effective means to naturally compensate for the mutual coupling between the metamaterial elements and the surrounding structure.

Using a combination of the pixelization approach and the in situ optimization technique, it is shown that it is possible to create metamaterial-inspired RF components that outperform existing RF components. Designs and prototypes of various metamaterial-inspired miniaturized patch antennas, loop antennas, folded monopole antennas, ultra-compact broadband waveguide filters, and widely tunable resonant structures that are easy to fabricate and at a low cost are presented.

In loving memory of my mother, Charlotte Ouedraogo

ACKNOWLEDGMENTS

There are many people who deserve acknowledgment for both the work contained in this dissertation, and the countless other activities I was involved in throughout my years at Michigan State University. First and foremost, a special thanks to Dr. E. Rothwell for being a very resourceful and exceptional advisor. You have always made time for me and provided me with lots of help and guidance to be successful both in school and in life. I could not have asked for a better advisor.

My gratitude goes to Dr. A. R. Diaz for the countless insightful discussions, his guidance and his generosity over the past three years. Dr. B. Shanker, Dr. L. Kempel, and Dr. G. Wei provided invaluable input and I am grateful for their generous agreement to serve on my PhD committee. Finally, the members of the Electromagnetics Research Group and Metamaterials Group, in particular K. Fuchi, B. Crowgey, A. Temme, T. Janyun, and K. Akinlabi are deserving of my sincere thanks on both a professional and personal level as they kept me focused, engaged and enthusiastic.

I am indebted to my parents Justin and Charlotte Ouedraogo for their tremendous sacrifice, for their unconditional love and all their support. A special acknowledgment to my in-laws and the Katz family who have loved and supported me as their own throughout my studies. My deepest gratitude is reserved for my wife, Clarice Ouedraogo for her love, support and understanding throughout my studies. My wife's love, help, and support made it all possible. She is my angel and I love her with all my heart.

TABLE OF CONTENTS

LIST OF TABLES

LIST OF FIGURES

Images in this thesis are presented in color

xv

KEY TO SYMBOLS AND ABBREVIATIONS

- SRR: Split Ring Resonator

- BC-SRR: Broadside Coupled Split Ring Resonator

- EC-SRR: Edge Coupled Split Ring Resonator

- MSRR: Multiple Split Ring Resonators

- MNG: Mu Negative

- ENG: Epsilon Negative

- DNG: Double Negative

- LHM: Left Handed Medium

- GA: Genetic Algorithm

- MMA: Method of Moving Asymptotes

- MEMS: Micro Electromechanical systems

- FEM: Finite Element Method

- GUI: Graphical User Interface

- HFSS: High Frequency Structure Simulator

- HIS: High Impedance Surface

- RIS: Reactive Impedance Surface

- AMC: Artificial Magnetic Conductor

- RF: Radio Frequency

- FSS: Frequency Selective Surface

- RFID: Radio Frequency Identification

- PDA: Personal Digital Assistants

KEY TO ACRONYMS

- Double Negative (DNG): $\mu_r < 0$, $\epsilon_r < 0$

- Left Handed medium (LHM): $\mu_r < 0$, $\epsilon_r < 0$

- Epsilon Negative (ENG): $\epsilon_r < 0$

- Mu Negative (MNG) : $\mu_r < 0$

CHAPTER 1

INTRODUCTION

Metamaterials are artificially engineered materials that have received significant attention in the scientific community over the past decade. The interest in these artificial materials arises from the unconventional electromagnetic characteristics they exhibit near resonance. Their peculiar resonance behavior has ignited an intensive study of their phenomena across multiple disciplines including acoustics, electromagnetics, mathematics, microfabrication, and physics. The frequency spectrum over which they are studied is as broad as the disciplines, extending from high frequency (HF) to optical frequencies.

The ability to create artificial materials with desired values of permittivity and permeability, in particular double negative or near zero values, has led to multiple conceptual applications that are impossible to realize with naturally existing materials. Some of the most exciting conceptual applications include cloaking (which requires a medium with slowly varying permittivity and permeability values) and perfect flat lenses (which require a medium with an index of refraction of negative unity). Other proposed applications of metamaterials include absorbers, acoustics, antennas, filters, medical instrumentations, and sensors.

The creation of metamaterial media relies on embedding metallic or dielectric inclusions into a host medium, with the most common metallic inclusions being split ring resonators and their derivatives. Unfortunately, these resonant structures have

very limited functionality and their design involves very few parameters (ring radii, split and slot widths) that do not allow for much tuning of the material properties. Additionally, the performance of these resonant structures is dependent on the orientation of the exciting electric and magnetic fields. When placed next to a device, the effects of mutual coupling usually lead to an undesirable performance of the combined structure, which is coined a "metamaterial device". Therefore, additional tuning of the resonant structure becomes necessary to achieve the desired performance of the metamaterial device.

There are countless books, conferences, and journal publications addressing metamaterials. However, the core definition of metamaterials, the types of designs that can be considered as true metamaterials, and the practical implementation of double negative media continue to be the subjects of fierce debate among scientists and engineers. The goal of the work presented in this dissertation is not to champion any specific definition of metamaterials, nor is it to design metamaterial media. Rather, the aim here is to use the concept of metamaterials to create new device designs and introduce new design methodologies that can be used to improve upon the performance of existing RF components. The focus of this dissertation is the synthesis of alternative resonant structures with improved functionality compared to the typical SRRs, and new design techniques that can be used to create highly miniaturized antennas, filters, and widely tunable metamaterial unit cells.

The material included in this dissertation is organized as follows. Various concepts and suggested applications of metamaterials are reviewed in chapter 2. Chapter 2 starts with a historical review of metamaterials. Such review spans the extensive

works of W. E. Kock on dielectric lenses and the works of S. A. Schelkunoff and H. T. Friis on artificial magnetics in the 1940's, to the works of J. B. Pendry and D. R. Smith on perfect flat lenses and cloaking in the present day. The chapter also provides a literature review of the application of metamaterials to the design of miniaturized antennas and filters as well as tunable devices based on metamaterials.

Chapter 3 presents an approach to synthesize new resonant structures that can be used in the construction of metamaterial media. A pixelization approach is presented as an effective means to create new resonant structures with improved functionally compare to conventional resonant structures such as SRRs. Chapter 3 also discusses the implementation of a Matlab-HFSS interface.

The pixelization approach presented in Chapter 3 is used in Chapter 4 to create waveguide filters. By optimizing a grid of metallic pixels on a dielectric sheet placed longitudinal to the waveguide axis, compact broadband waveguide filters that are easy to fabricate can be produced. Measured and simulated performance of an F-band waveguide filter showing strong rejection in the stopband with a rapid roll off at the band edges, and low insertion loss outside the stopband are presented.

Chapter 5 introduces an in situ optimization technique as a means to create miniaturized metamaterial-inspired antennas suitable for integrated device and on-chip applications. The beauty of the proposed in situ optimization technique is that the resonant structures are optimized in closed proximity to a device to improve upon the performance of the device. Thus the proposed technique naturally compensates for the mutual coupling between the metamaterial element and the surrounding structure. Chapter 5 also discusses the concepts of metamaterial-based and metamaterial-

inspired devices.

In Chapter 6, the in situ optimization technique is used in combination with the concept of complementary split ring resonators to create highly miniaturized patch antennas. By optimizing the geometry of complementary split rings placed horizontally between the patch and the ground plane, sub-wavelength resonance of the patch antenna can be achieved with a good impedance match and radiation characteristics comparable to those of a traditional patch antenna on a finite ground plane. High levels of miniaturization are demonstrated through simulations and experiments, with antenna area reductions of a factor of more than sixteen.

Chapter 7 focuses on the design of tunable resonant structures that can be used to create reconfigurable metamaterials. A brief review of existing reconfigurable metamaterials is first presented, followed by new techniques developed by the Michigan State University Metamaterials Group to create widely tunable metamaterial structures.

A conclusion which proposes points of improvement and potential future applications of the work presented in Chapters 3-7 is presented in Chapter 8. An appendix containing codes for the Matlab-HFSS interface and various genetic algorithms is also provided at the conclusion of the dissertation.

CHAPTER 2

LITERATURE REVIEW

Metamaterials are known as artificially engineered materials that exhibit electromagnetic properties not readily found in nature. Although the interest in metamaterials has seen a significant increase over the past decade, the study of engineered materials (namely artificial dielectrics and magnetics) is well over a century old. Pioneers in the field include J. C. Bose, J. W. Strutt, W. E. Kock, S. A. Schelkunoff and H. T. Friis. Their work provided the foundation for the current developments in metamaterials. This chapter presents a brief historical review of metamaterials, discussing both the pioneering works on artificially engineered materials and their recent developments. The chapter also presents a review of the applications of metamaterials to the design of various RF components, such as highly miniaturized antennas, miniaturized waveguides and tunable metamaterials.

2.1   Historical review of metamaterials

The interest in metamaterials has increased tremendously since J. B. Pendry's work in the late 1990s on the design of negative permittivity ($\epsilon < 0$) and negative permeability ($\mu < 0$) media [1] – [3], and the successful experimental verification of such media by R. A. Shelby and D. R. Smith [4]. While many may consider the work of Pendry as the starting point of the metamaterial era, the concept and experimental realization of artificially engineered media is not new. In fact, it can be traced back over a century to the theoretical work of J. W. Strutt [5] on artificial dielectrics composed

of small spherical scatterers and the work of J. C. Bose [6] on twisted structures.

2.1.1 Artificial dielectrics

Some of the first experimental works on artificial dielectrics were presented by W. E. Kock in the mid 1940s [7] – [8]. Kock sought to realize lightweight and low-cost dielectric lens antennas by replacing homogeneous, high permittivity dielectric lenses with arrays of parallel metallic plates. The focusing of Kock's artificial lens is based on the property that electromagnetic waves traveling between parallel plates with the electric field polarized parallel to the plates experience a phase velocity higher than they would in free space. The higher phase velocity results in an index of refraction given as

$$n = \frac{v_0}{v_p} = \sqrt{1 - \left(\frac{\lambda_0}{2a}\right)^2},$$
(2.1)

which is less than unity and would suggest the design of the concave shaped converging lens shown in Figure 2.1. In (2.1), a is the separation between plates, λ_0 is the free space wavelength, v_0 is the phase velocity of the wave in free space and v_p is the phase velocity of the wave confined between the conducting plates.

Though Kock's artificial dielectric was shown to provide the same focusing effect as the bulky and more expensive homogeneous dielectric, it is frequency dependent and limited to narrow band applications. To overcome the frequency dependence, Kock introduced the concept of metallic delay lenses [8], which are artificial dielectrics designed based on the lattice structure of true dielectrics. The metallic delay lenses
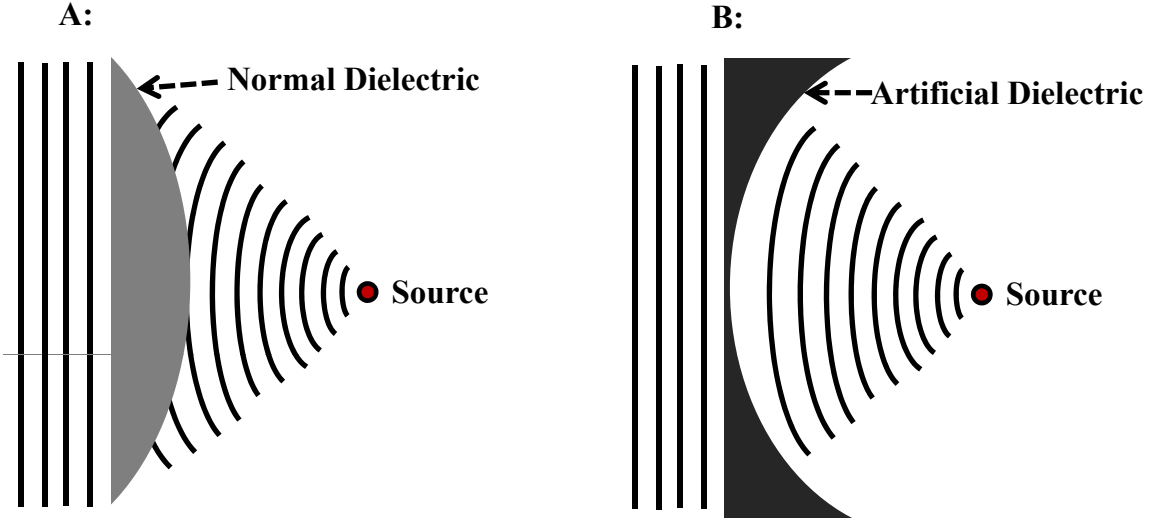
Figure 2.1. Concave shaped converging lenses. A: $n > 1$; B: $n < 1$. n represents the index of refraction. For interpretation of the references to color in this and all other figures, the reader is referred to the electronic version of this dissertation.

are made of three-dimensional arrays of sub-wavelength metallic elements such as spheres, disks or thin rods (shown in Figure 2.2) with element spacing much smaller than the smallest operating wavelength. The effective permittivity of these artificial dielectrics is dependent on the type of elements that constitute the medium and is given by

$$\epsilon = \epsilon_0 + N\alpha. \tag{2.2}$$

In (2.2), ϵ_0 is the free space permittivity, N is the number of elements per unit volume and α is the polarizability of each element. Near the resonance of the elements, α is highly frequency dependent. However, for very small elements (element size $\leq \lambda_o/4$), it is shown in [8] that α is fairly constant, leading to a frequency independent relative

permittivity.

Analytical studies of Kock's experimental work were later conducted by several researchers including S. B. Cohn, J. Brown and W. Jackson. In 1949, Cohn [9], showed that Kock's experimental work on arrays of metallic strips could be verified analytically using a transmission line model, and more importantly the parameters of the metallic strip medium could be selected appropriately such that the impedance of the artificial medium is matched to that of free space. In 1960, Brown [10] presented in detail the theory of artificial dielectrics, concluding that electrical performance similar to solid homogeneous material is achievable provided that the inclusions are very small compared to the wavelength and the ratio of the inclusion size to the lattice spacing is kept small enough.

Early examples of artificial dielectrics also includes artificial plasmas thanks to the work of W. Rotman. In [11], Rotman showed theoretically and experimentally that an artificial medium composed of arrays of H-plane parallel plate waveguides or an array of rods exhibits electrical characteristics similar to a plasma. The array of rods, now known as a wire medium, is widely used in the design of materials with $\epsilon < 0$ and $\mu < 0$. These materials are known as double negative metamaterials or left handed materials.

2.1.2 Artificial magnetic

The first artificial magnetic medium was presented by S. A. Schelkunoff and H. T. Friis in 1952 [12]. The motivation to achieve magnetic material properties at radio frequencies was driven by the desire to match the intrinsic impedance of Kock's delay
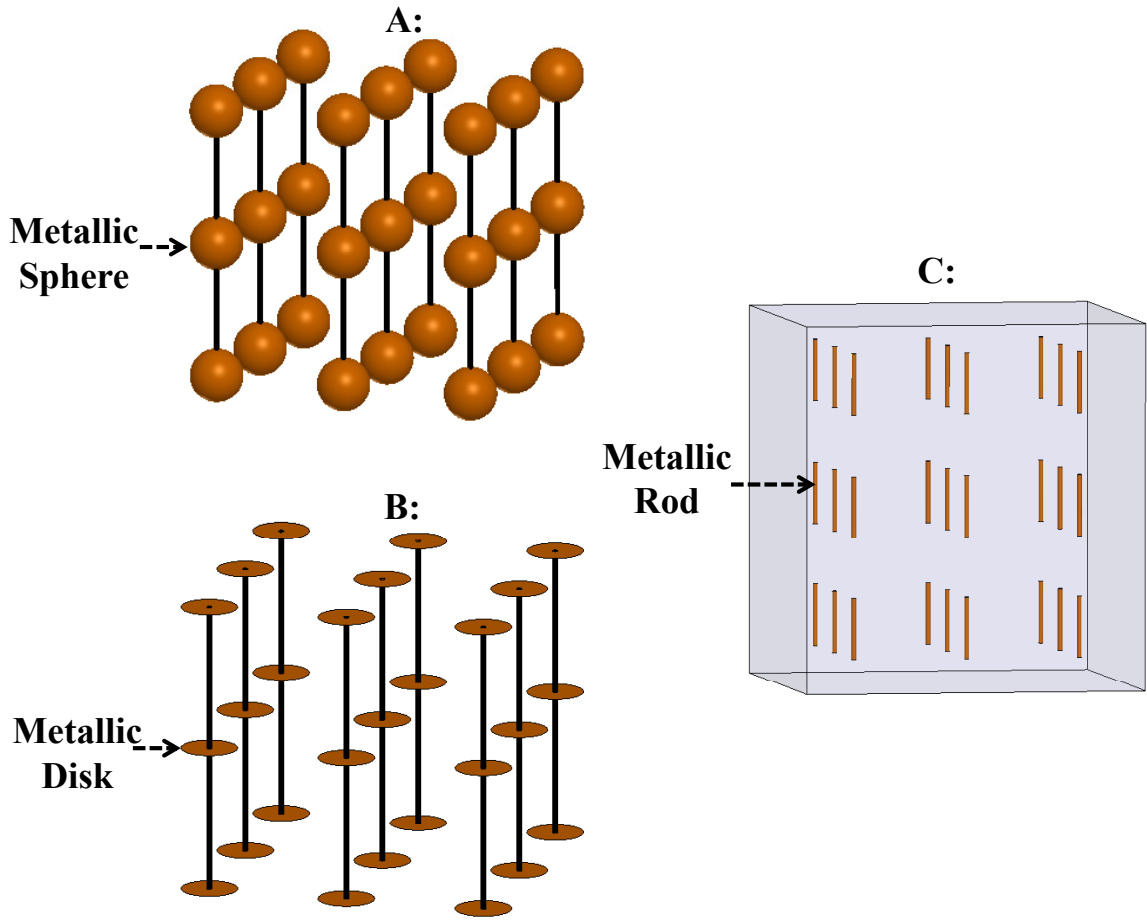
Figure 2.2. Arrays of metallic inclusions. The rods shown in A and B are non-conducting rods used to support the metallic spheres and metallic disks.

lenses to free space. Noting that the intrinsic impedance of a medium is given by the ratio between permeability and permittivity, and given that Kock's delay lenses have a permittivity greater than unity, a free space impedance match is realizable provided the permeability of the medium can be made greater than unity. Although gyrotropic magnetic materials can be used, they are heavy, expensive, and lose their magnetic response with increasing frequencies. In lieu of using gyrotropic materials, Schelkunoff and Friis suggested the use of the broken ring shown in Figure 2.3. A

conducting ring placed in an environment with the magnetic field aligned along the axis of the ring exhibits an impedance that is purely inductive. However, when capacitance is introduced into the structure (by placing a gap as in Figure 2.3), the resulting structure exhibits a magnetic polarizability given by

$$\chi_m^o = \frac{\omega^2 \mu_o^2 C S^2}{1 - \omega^2 LC}. \tag{2.3}$$

Here, L is the inductance of the broken loop, C is the capacitance, μ_O is the free space permeability, S is the surface area and ω is the frequency of operation. Unfortunately, the gap introduced on the structure does not provide enough capacitance to significantly lower the resonant frequency of the broken loop of Figure 2.3. A solution proposed in [12] is to place a lumped capacitor at the location of the gap.

After the publication of [12], the concept of artificial magnetic media was left dormant for nearly thirty years, until the rise of artificial bianisotropic materials in the late 1980s. This renewed interest led to the study of chiral structures and various metal loop shapes including the very popular concentric split ring resonator (SRR), [2], [13], and [14]. Sketches of the most popular metal loop shapes used to date are shown in Figure 2.4.
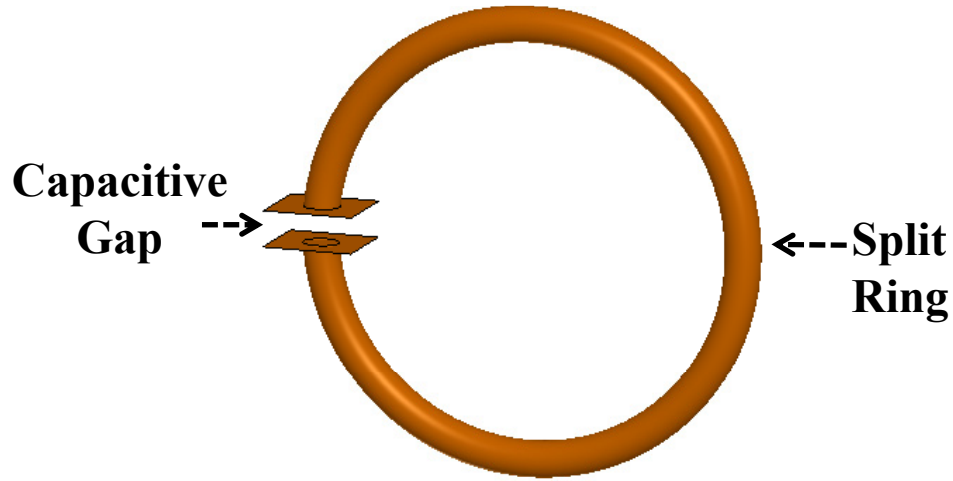
Figure 2.3. Split ring resonator proposed by Friis and Schelkunoff.

2.2 Selected applications of metamaterials

The pioneering works of W. E. Kock, S. A. Schelkunoff and H. T. Friis on the practical implementation of artificial dielectrics and magnetic materials have paved the way for what are now known as metamaterials. The range of applications of metamaterials is very broad and includes absorbers, antennas, cloaking, filters, focusing lenses, and tunable devices. Though each of these applications is very exciting and worth investigating, only the use of metamaterials with antennas and filters, and the design of tunable metamaterial inclusions, are discussed in this dissertation. The sections below address the need for small RF components, and provide a review of miniaturization techniques developed by various research groups to meet those needs. Both conventional and metamaterial-based antenna miniaturization techniques, waveguide filter design techniques, and the design of tunable metamaterials are reviewed.
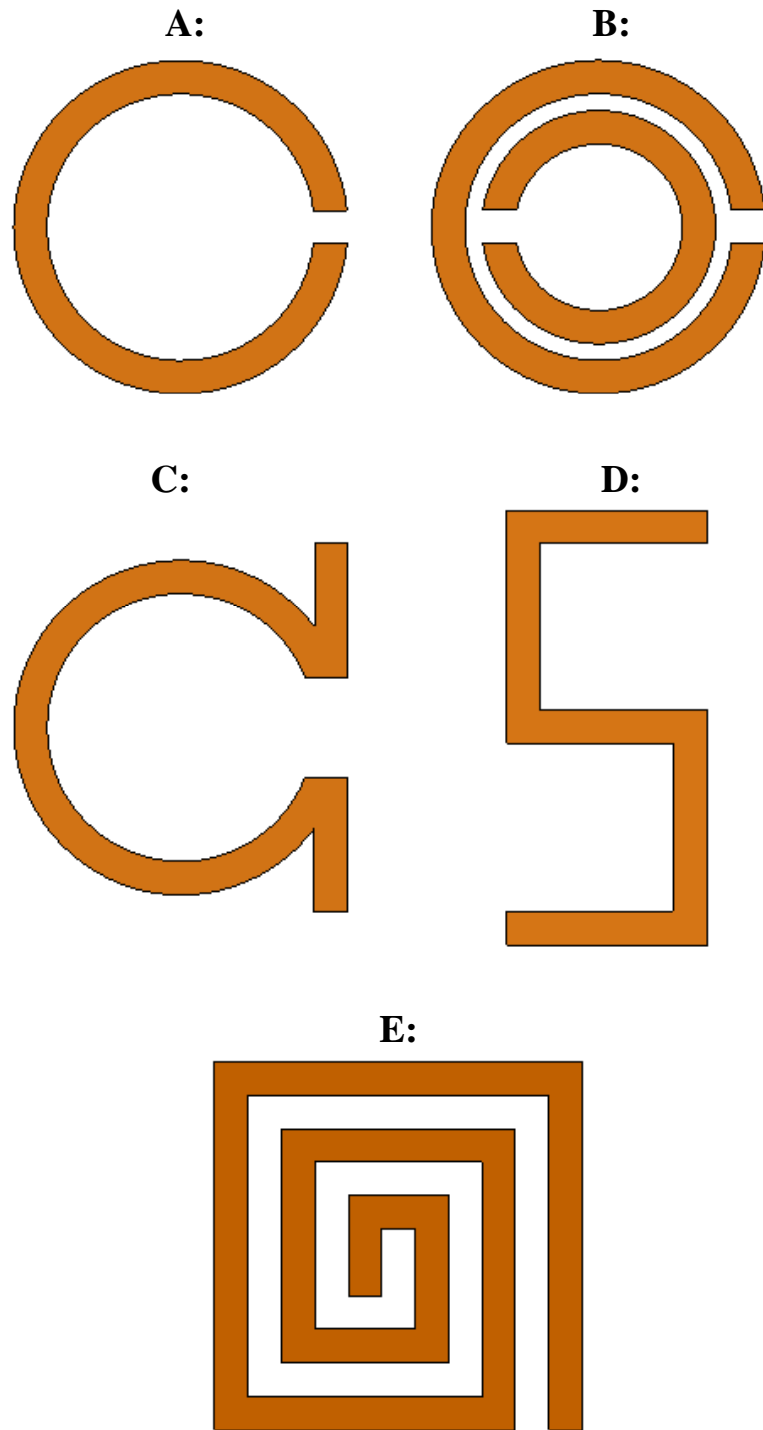
Figure 2.4. Variations of metallic inclusions used in the design of artificial magnetic media. A: SRR; B: edge coupled SRR; C: Omega ring; D: S-ring; E: Spiral.

2.2.1 Application of metamaterials to antenna miniaturization

In recent years, the demand for small, compact, and low cost planar antennas has increased tremendously, due to the need for miniaturized devices in both military and commercial applications. Not only is there a desire for increasingly smaller antennas but also a requirement for these small antennas to maintain acceptable electrical characteristics such as efficiency, bandwidth, and radiation pattern. These requirements present a big challenge for antenna engineers since the performance of an antenna is highly dependent on its physical dimensions and a reduction of those dimensions leads to significant performance degradation.

Among the multitude of antennas in existence, one that has received the most attention and continues to be the most used is the patch antenna. A patch antenna in its basic form is a very simple structure composed of a radiating element placed a certain distance above a ground plane, as shown in Figure 2.5. A dielectric is typically placed between the radiating element and ground plane both for support and also for miniaturization purposes. The low profile of patch antennas, their lightweight, and their planar nature make them suitable for embedded antenna applications such as: wireless devices (cellular phones, personal digital assistants (PDAs), radio frequency identification (RFID) tags, computers), airplanes, missiles and radars. They are also well suited for large planar array applications. Patch antennas also benefit from other advantages including ease of fabrication, the potential for multi-frequency operation, the capability of supporting both linear and circular polarizations, and robustness since they are not easily broken, unlike wire antennas.

Unfortunately, no antenna is perfect. Patch antennas suffer from multiple drawbacks including narrow bandwidth, low efficiency, and a large transverse dimension ($\approx \lambda_O/2$). The presence of the ground plane placed in close proximity to the radiating patch creates an image current of the electric current of the radiating patch. This image current gives rise to radiated fields that tend to cancel the fields radiated from the patch current, thus leading to a low radiation efficiency. The presence of the ground plane also leads to a significant increase in the stored energy of the near field of the antenna, which increases the radiation Q and lowers the bandwidth of the antenna. The efficiency and bandwidth can be significantly increased, by up to 90% and 35% respectively, by using very thick dielectrics [16]. However, the increase of the thickness of the antenna introduces undesirable surface waves which travel within the dielectric and scatter at discontinuities such as the boundary between the dielectric and free space. This scattering contributes to the degradation of the antenna radiation pattern and polarization [17] − [21].

Much work has been done using conventional techniques to miniaturize the large transverse dimension of patch antennas. The simplest and most straight forward approach is to use a high permittivity dielectric. Since the frequency of resonance of a patch antenna is inversely proportional to the square root of the relative permittivity $\sqrt{\epsilon_r}$ of the dielectric, it is possible to lower the resonance frequency of the patch by loading the patch cavity with a dielectric of high relative permittivity [22] − [24]. The patch cavity refers to the area between the radiating patch and the ground plane.

Commercially available high permittivity dielectrics such as ceramic-PTFE composites provide a dielectric constant of $\epsilon_r \approx 10$, producing an antenna size reduction
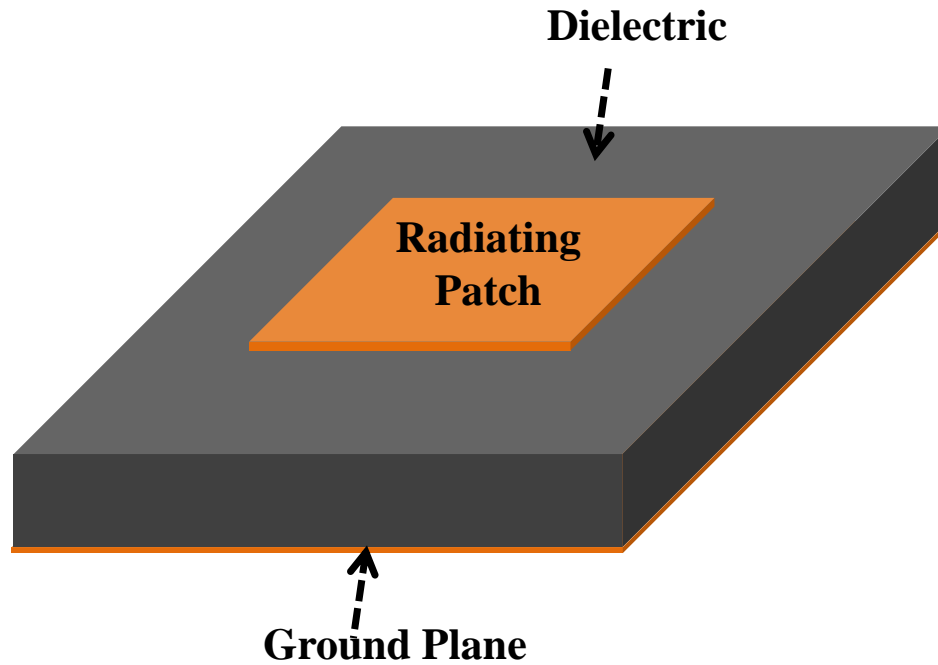
Figure 2.5. Patch antenna.

of about 50% compared to conventional circuit board materials such as RT/duroid with $\epsilon_r \approx 2.2$. Though much higher permittivity dieletrics ($\epsilon_r > 50$) are realizeable as presented in [25] – [27], they are not commercially available and suffer from multiple disadvantages including high cost, increased losses, low thermal conductivity and weak mechanical performance (e.g., they break very easily).

The miniaturization of patch antennas can also be achieved by using shorting pins, [28] – [32]. In this approach, the miniaturization is achieved by shifting the voltage null point of the excited dominant mode from the center of the patch to the edge of the patch by placing a shorting pin between the feed position and the edge of the radiating patch. The amount of miniaturization achievable is limited by the distance between the voltage null and the patch edge. A typical size reduction of 50% can be

achieved with this technique when applied to a circular or rectangular patch antenna, but larger reductions of 70% have been reported with a triangular patch antenna [33], [34].

Patch antennas can also be miniaturized by increasing the path length of the excited surface current. The path length of the current is increased by meandering or fractalizing the radiating patch, or by placing slots on the ground plane [35] – [38]. The achievable level of miniaturization depends on the length of the extended current path, and antenna size reductions as large as 38% have been reported [38]. Folding the patch into a multi-layered structure can yield a size reduction of about 50% at the cost of increased thickness [39].

It is important to note that by using the conventional techniques discussed above, the achievable size reduction is limited to about 70% which is typically achieved by combining several techniques (e.g., a shorting post and dielectrics with $\epsilon_r > 4.4$). The use of very high permittivity dielectrics with $\epsilon_r > 10$ should provide higher levels of miniaturization but their associated high cost make them undesirable. Another drawback of the techniques discussed above is the deterioration of the radiation pattern and the increase of the cross polarization in both E and H-planes [23].

The emergence of new artificial materials such as magnetodielectrics, high impedance surfaces, reactive impedance surfaces, and artificial magnetic conductors (all classified as metamaterials) provides new ways to achieve higher levels of miniaturization compared to using conventional techniques. It is shown in [40] and [45] that it is possible to match an electrically small dipole antenna to free space while maintaining excellent radiation characteristics by surrounding the dipole antenna with a

properly designed homogeneous and isotropic shell having a negative permittivity (ENG) as shown in Figure 2.6. The match between the dipole and ENG shell is possible since an electrically small dipole antenna has an impedance that is highly capacitive while a negative permittivity shell exhibits an impedance that is highly inductive. An LC resonance can therefore be achieved for any size dipole antenna if the proper parameters of the ENG shell are selected. Unfortunately, the design proposed in [40] and [45] assumes a homogeneous and lossless shell which cannot be implemented (at least not with current technology). A wire medium could be used to create an ENG shell but the complexity of the design, the presence of losses, and the large size of the shell can lead to a system design that does not provide any advantage when compared to a dipole the same size as the shell.

Using the concept of duality, it is shown in [47] that it is possible to create an electrically small planar loop antenna with good electrical characteristics by surrounding the loop antenna with a mu negative (MNG) layer. In this case, an array of SRRs is placed around the loop as shown in Figure 2.7 to create the MNG layer. The resonance of the antenna is lowered to that of the SRRs which typically occurs when the largest dimension of the SRR is approximately $\lambda_O/10$. Though the planar loop can be made very small, the overall structure (loop and array of SRRs) is fairly large and the largest dimension of the structure exceeds $\lambda_O/3$. A more compact design was proposed in [46] where a planar loop antenna is placed within a single SRR to achieve resonance. Though this approach produces a higher level of miniaturization than does the approach described in [47], the antenna suffers from a low efficiency, narrow bandwidth and requires the use of a large ground plane placed normal to the

17
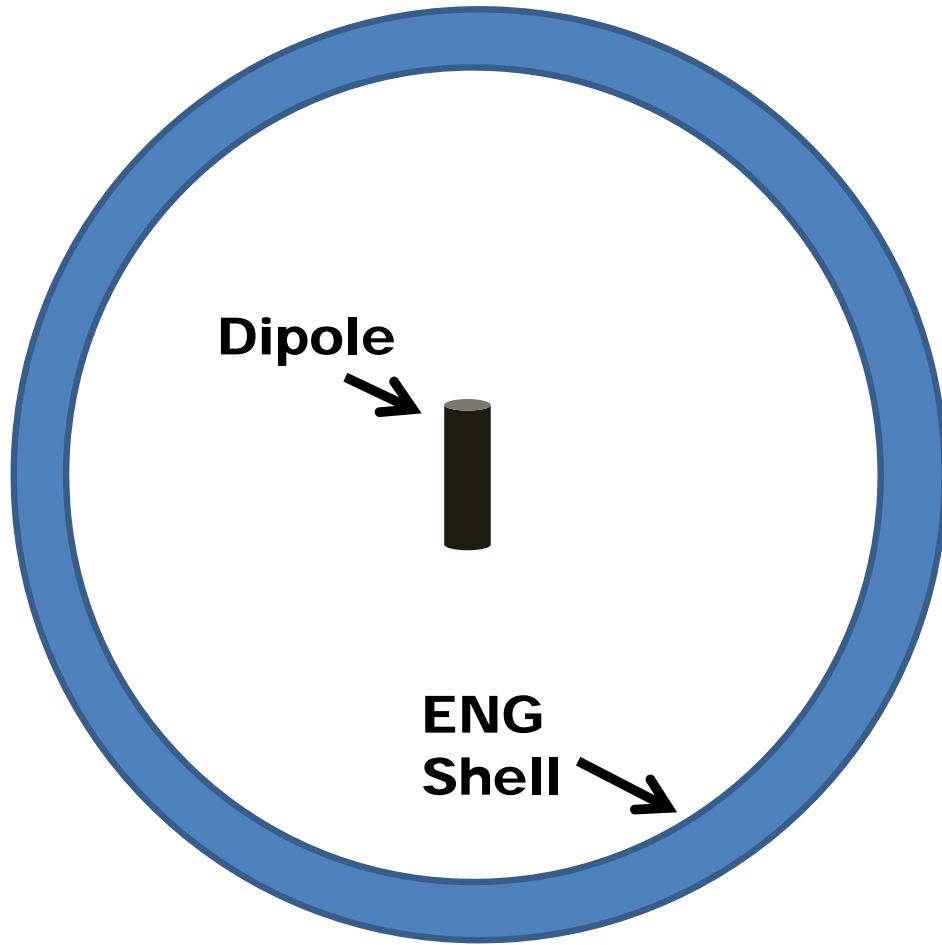
Figure 2.6. Dipole inside an ENG shell.

plane of the antenna.

The use of ENG or MNG metamaterials was later extended from linear antennas to the miniaturization of patch antennas [48] – [54]. It is reported in [52] that highly miniaturized patch antennas can be created by partially loading the patch cavity with a properly designed homogeneous, isotropic, MNG metamaterial. A practical implementation of this concept was later proposed in [53], where inclusions consisting of arrays of SRRs were used to create the required MNG medium, as shown in Fig-
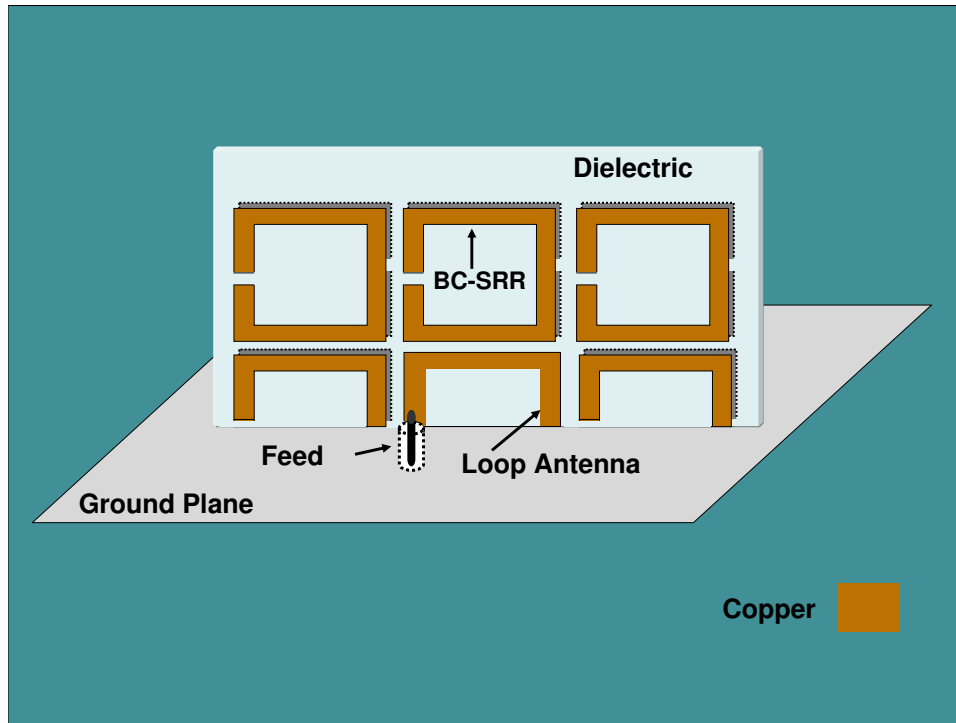
Figure 2.7. Planar loop surrounded by a layer of SRRs.

ure 2.8. This implementation is problematic since several arrays of planar resonant structures must be placed vertically within the patch cavity in order to be effectively excited by the horizontal dominant-mode magnetic field. Additionally, since the level of miniaturization achievable depends on the size of the inclusions (with larger inclusions producing lower resonance frequencies), very thick substrates are required to produce a meaningful reduction in size. The fabrication process of such designs requires high complexity and high cost.

Based on the concept of complementary SRRs introduced in [59], several authors [60] – [63] proposed the concept of a metamaterial ground plane as a means to reduce the size patch antennas. It is reported in [60] and [61] that by etching arrays of SRRs
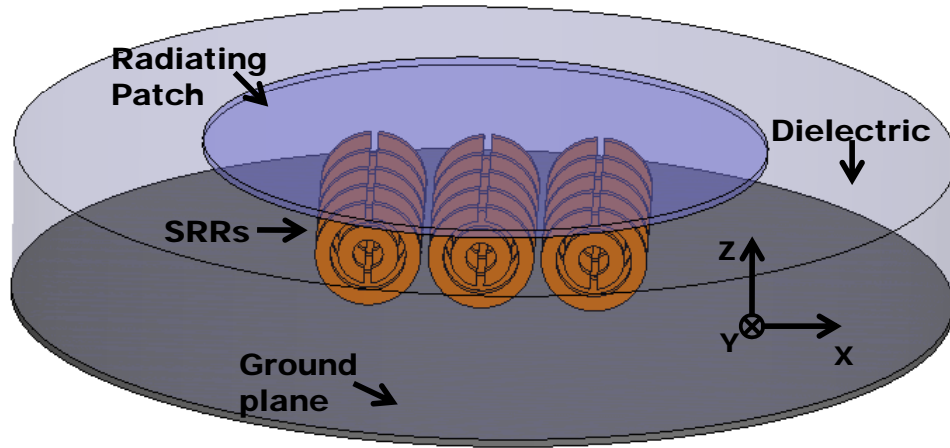
Figure 2.8. Patch antenna loaded with SRRs.

on the ground plane (creating complementary SRRs or CSRRs) it is possible to lower the resonant frequency of the patch to that of the CSRRs. Although this approach seems easier to implement than the approach in [53], it fails to provide significant size reduction. For instance, a size reduction of only 31% is reported in [60]. Additionally, placing a large number of slots on the ground plane deteriorates the radiation pattern, leading to a front to back ratio ≈ 0 and increases the cross-polarization to almost the same level as the co-polarization.

Besides the use of single negative metamaterials for antenna miniaturization, high impedance surfaces and reactive impedance surfaces have been proposed as alternative techniques for achieving antenna miniaturization $[55]-[58]$. High impedance surfaces (HIS) are used to create a medium with low permittivity and a very large permeability to emulate an artificial magnetic conductor (AMC). From electromagnetic theory, an electric current placed parallel to a magnetic conductor gives rise to an image current

which is in phase and parallel to the originating current. This leads to an antenna with good radiation characteristics and a high efficiency. The major drawback of HISs is the fact that they are very bulky and hard to manufacture. However, they can be miniaturized by using high permittivity dielectrics or resonant structures. In the latter case, the frequency of resonance of the antenna shifts down to that of the resonant structures. Unfortunately, when resonant structures are used, the efficiency and bandwidth of the antenna placed on the HIS deteriorate due to the narrow band and lossy nature of resonant structures.

Reactive impedance surfaces (RIS) introduced in [58], were proposed to reduce the mutual coupling between the radiating patch and ground plane of a patch antenna. In [58], it is shown that it is possible to design a surface with a purely reactive impedance that minimizes the mutual interaction between the fields of the image current and the fields of the source. The proposed RIS was made using an array of patches on a substrate that is 4 mm thick with a high permittivity of $\epsilon_r = 25$. A second dielectric layer that is 2 mm thick with a permittivity of $\epsilon_r = 6$ is placed between the radiating patch and the RIS surface. Though this approach reduces the transverse dimension of the patch antenna at resonance from $\lambda_o/2$ to $\lambda_o/10$ while producing a broad bandwidth of 6.71%, it requires a thick substrate with a high permittivity. The use of such high permittivity negates the miniaturization claim of the authors since a patch antenna on a substrate with a permittivity of $\epsilon_r = 21$ is resonant when the transverse dimension of the patch antenna is $\approx \lambda_o/10$. Typically, patch antennas designed on a 1.5 mm thick low loss substrate have a bandwidth that is approximately 1.2% and it is well known that the bandwidth of patch antennas

21

increase as the thickness of the substrate is increased. Thus, the bandwidth increase claim of the authors could just be the result of the 6mm thick substrate they used. Regardless, the front to back ratio is still low (about 5 dB) despite the fact that the width of the ground plane is almost three times the width of the radiating patch. The end result of the RIS approach is an antenna that is thick, complex, and expensive.

A technique that achieves high levels of miniaturization without the use of high permittivity dielectrics, thick substrates, and does not rely on complex design schemes is presented in Chapter 6 of this dissertation. Miniaturization is achieved by loading the patch cavity with CSRRs placed horizontally between the patch and the ground plane. By optimizing the geometries of the CSRRs in situ it is possible to create miniaturized patch antennas with transverse dimensions less than $\lambda_O/10$ while maintaining good radiation characteristics. The technique presented in Chapter 6 can also be found in [65] – [66].

2.2.2   Applications of metamaterials to waveguide filters

Rectangular waveguides are hollow metallic structures (Figure 2.9) that are used to convey electromagnetic waves. Their ability to carry high power signals along with their broad bandwidth and low loss nature have made them indispensable components in a variety of RF applications. Typical RF applications of rectangular waveguides include satellite communications, radar systems and microwave ovens. Because of the broad bandwidth of rectangular waveguides, it is often necessary to implement a filtering system with high in-band rejection and low out-of-band insertion loss.

Conventional E-plane and H-plane rectangular waveguide filters involve physical

Figure 2.9. Rectangular waveguide.

alterations of the waveguide structure. For instance, it shown in [73] – [82] that it is possible to create a waveguide filter by placing metallic inserts such as inductive strips or posts vertically inside the waveguide. The presence of the inserts create a discontinuity that leads to a stopband within the passband of the waveguide. The ability to achieve a wide stopband and a high in-band rejection with a rapid roll-off depend on the arrangement and the number of inserts. Typically, a larger number of inserts produces a wider stopband and a faster roll-off. Physical alterations of the waveguide structure results in complex filters that are several wavelengths long and hard to manufacture.

Rectangular waveguide filters can also be created using resonant type inserts or frequency selective surfaces (FSS) as suggested in [83] – [86]. Given that FSSs can be designed to operate as opaque surfaces near their frequency of resonance, it is possible

to create a band-stop filter by inserting an FSS screen normal to the direction of propagation of the wave within the waveguide. The stopband in this case occurs at the frequency of resonance of the FSS. Though easier to implement than altering the physical structure of the waveguide, FSS based filters suffer from a slow roll-off which is undesirable. Increasing the number of FSS screens along the longitudinal direction of the waveguide leads to a faster roll-off and a wider bandwidth but at the cost of increased fabrication complexity and increase length of the waveguide filter, since a typical spacing of $\lambda/4$ is required between inserts.

The use of isotropic and homogeneous MNG metamaterials has been suggested in [87] as an alternative and less complex means to produce miniaturized waveguide filters. A practical implementation of waveguide filters based on metamaterials was reported in [88] – [90], where it was shown that it is possible to create a stopband above the cutoff frequency of a rectangular waveguide by loading the waveguide with an array of SRRs. In this approach, SRRs are printed on a dielectric slab that is then inserted along the longitudinal axis of a waveguide. The stopband occurs near the frequency of resonance of the SRRs. Though the design is very simple and does not involve any physical alteration of the waveguide, the resulting bandwidth is fairly narrow, due to the narrow bandwidth of the SRRs.

The bandwidth issue is resolved in Chapter 4 of this dissertation using a topology optimization. A rectangular metallic patch on a dielectric slab is discretized into pixels and placed longitudinally inside the waveguide. An optimization tool such as a genetic algorithm is then used to alter the geometry of the pixelated metallic patch by turning pixels on or off. Through this design technique, it is possible to create alternate

24

resonant structures capable of meeting the filter requirements while maintaining a compact size. The design technique presented in Chapter 4 is easier to implement compared to the techniques described above and leads to smaller broadband filters that are easy to fabricate and at a low cost.

2.2.3   Tunable metamaterials

The resonant behavior of a metamaterial medium is dependent on the characteristics of both the inclusions and the host medium. Typical metamaterial inclusions are resonant structures that exhibit a narrow bandwidth at resonance, and it is very difficult to increase the bandwidth of the inclusions by altering the geometry. This represents a serious drawback since most applications require a bandwidth which often exceeds that of the resonant structures. Changing the properties of the host medium to make it lossier can slightly increase the bandwidth but at the expense of decreased efficiency. An alternative approach to overcome the narrow bandwidth issue is the use of tunable metamaterials.

For instance, it is reported in [92] – [97] that the frequency of resonance of an SRR can be varied up to 30% by loading the SRR with variable capacitors (varactors), diodes, or ferroelectric tunable capacitors. By changing the capacitance of the varactors, the effective capacitance of the SRR also changes. This alters the frequency of resonance of the SRR, with high capacitance values leading to lower resonant frequencies. The concept of tuning the frequency of resonance of SRRs with varactors was later extended to CSRRs for the construction of tunable transmission line filters, [98] – [99].

Using a ring broken into two symmetric structures as a metamaterial inclusion, the authors [100] showed that it is possible to create a dual-state switchable metamaterial by placing a micro-electromechanical switch (MEMS) at the location of one of the gaps. A closed switch state shorts the two symmetric structures at the location of the switch, leading to a ring with a single gap. An open switch state has no effect on the doubly broken ring. This approach leads to only two frequencies of operation. It was later reported in [101] that it is possible to achieve a 14% tuning range by varying the spacing between the two symmetric structures. In [101], one of the symmetric structures is maintained fixed while the other is moved back and forth using a MEMS systems.

Besides loading the resonant structures with lumped components, it is also possible to achieve frequency tuning of metamaterials by varying the characteristics of the host medium. For instance, the authors of [102] and [103] proposed using vanadium dioxide (VO_2) as a thin coating layer between the dielectric and the array of SRRs, creating a multi-layered structure. VO_2 is a material whose properties change with temperature. Changing the ambient temperature alters the effective permittivity of the host medium composed of dielectric and VO_2, which alters the frequency of resonance of the metamaterial. The use liquid crystals has also been reported as a means to create tunable metamaterials, [104] – [107]. Liquid crystals are anisotropic materials that are highly sensitive to external electric fields. Varying the intensity of the incident field alters the effective permittivity of the liquid crystals. By using liquid crystals as a host medium, it is therefore possible to tune the frequency of resonance of the metamaterial by changing the intensity of the incident field.

2.3 Conclusion

In this chapter, a brief review highliting the pioneering works of W. E. Kock, S. A. Schelkunoff and H. T. Friis, on the realization of artificial dielectrics and magnetic media has been presented. A review of the impact of metamaterials on the design of miniaturized planar antennas and rectangular waveguide filters has also been presented. A section discussing the narrow bandwidth limitation of the inclusions used in the design of metamaterials and how to overcome this limitation through the design of tunable metamaterials has also been presented. The next chapter addresses the resonance behavior of SRRs, their advantages and their limitations. The chapter also introduces new design methodologies capable of creating new resonant structures that are quite different from SRRs but with improved functionally.

CHAPTER 3

SYNTHESIS OF ALTERNATIVE RESONANT STRUCTURES

3.1   Introduction

The existence of double negative media and their properties was first postulated by V. Veselago in 1968 [15]. Although the natural occurrence of double negative media has not yet been reported, several authors have shown that they can be artificially engineered. In 1998, Pendry et al. established that it is possible to create an artificially engineered medium with a negative effective permittivity using arrays of thin metallic posts embedded in a host medium [1]. The authors of [1] later showed in 1999 that an artificially engineered medium with a negative effective permeability can be created by embedding arrays of sub-wavelength metallic split ring resonators into a host medium [2]. Based on the works of Pendry et al., Shelby et al. demonstrated experimentally that by properly arranging arrays of thin metallic strips and SRRs in the same host medium, an artificially engineered medium with simultaneous negative effective permittivity and permeability can be created [4].

The electrical and magnetic performance of these artificially engineered media depends on the geometry and the arrangement of the metallic inclusions relative to the orientation of the exciting electric and magnetic fields. Most inclusions used to date to create negative permeability media are resonant structures that are derived from SRRs and include broadside-couple SRRs, edge-couple SRRs, omega rings, S-rings, and spirals. Unfortunately, these resonant structures have limited flexibility

since their design involves very few parameters (ring radii, split and slot widths) that do not allow for much tuning of the material properties. Additionally, when a resonant structure is placed next to a device, the effects of mutual coupling usually compromise the performance of the combined structure. Therefore, additional tuning of the resonant structure becomes necessary to achieve the desired electrical and magnetic performance.

In this chapter, a methodology that can be used to synthesize new resonant structures for the design of negative permeability media is presented. A pixelization approach is introduced as an effective means to create new resonant structures quite different from SRRs and with improved functionality. Through the pixelization approach it will be shown that for prescribed unit cell dimensions it is possible to synthesize multiple structures, all resonating at the same frequency, but with different permeability values.

3.2   Resonance behavior of split ring resonators

The split ring resonator proposed by Pendry [2], consists of two concentric rings with gaps in opposite sides, as shown in Figure 3.1. When the SRR is placed in an environment where the magnetic field is aligned along the axis of the rings, simultaneous electric currents are induced on both concentric rings as shown in Figure 3.2, creating a capacitance between the rings. For an infinite array of SRRs, the capacitance along with the inductance of the rings leads to a resonant response that is characterized by a relative permeability that obeys a frequency dispersive Lorentz model derived in [2] as

$$\mu_r = \mu_r' + j\mu_r'' = 1 - \frac{\frac{\pi r^2}{a^2}}{1 + \frac{lj\sigma_1}{\pi f r \mu_0} - \frac{3l}{\pi^2 \mu_0 (2\pi f)^2 C_1 r^3}}. \tag{3.1}$$

In (3.1), μ_r' and μ_r'' are the real and imaginary parts of the relative permeability respectively, r is the radius of the inner ring, a is the lattice spacing of the SRRs lying in the same plane as shown in Figure 3.3, l is the spacing between planes, $j = \sqrt{-1}$, σ_1 is the resistance of the rings per unit length and depends on the thickness of the metal, f is the frequency of analysis, C_1 is the capacitance per unit length between the rings given by

$$C_1 = \frac{\epsilon_0}{\pi} \log \frac{2c}{d}. \tag{3.2}$$

In (3.2) c is the width of the metalization of the rings and d is the gap between concentric rings. In [2], f_o is defined as the frequency at which μ_r diverges and is given by

$$f_o^2 = \frac{3l}{4\pi^4 \mu_0 C_1 r^3}. \tag{3.3}$$
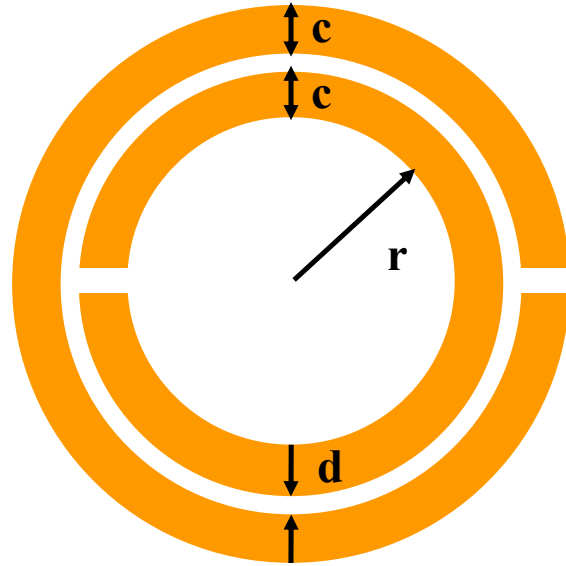
Figure 3.1. Split ring resonator.
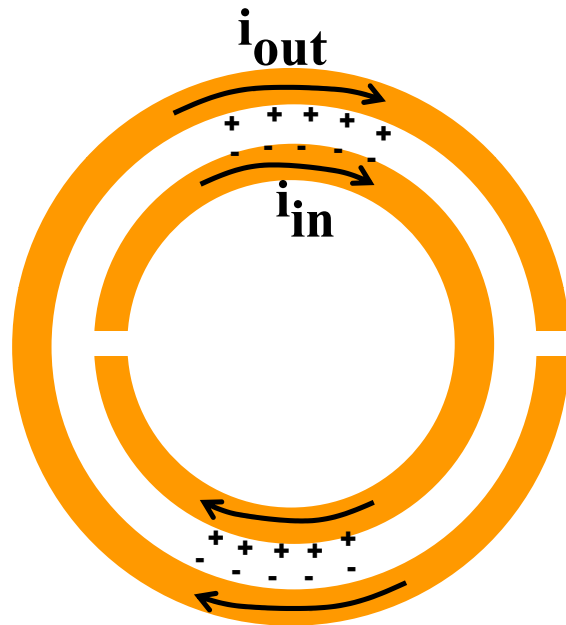
Figure 3.2. Electric currents induced on the SRR.
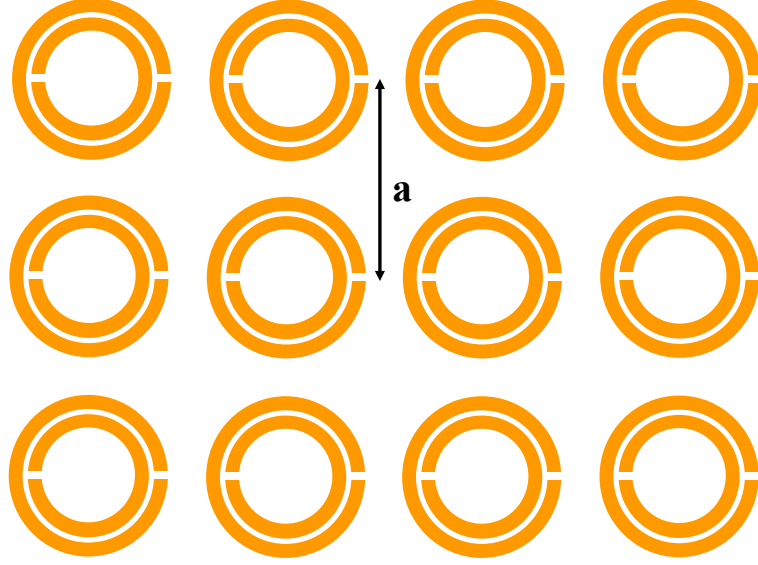
Figure 3.3. Array of SRRs.

Plots of μ_r' and μ_r'' generated using (3.1) are shown in Figure 3.4. The values of the parameters in (3.1) used to generate the plots of μ_r' and μ_r'' are shown in Table 3.1. These parameters were selected to ensure that resonance occurs at f_O = 5 GHz. Note from Figure 3.4 that far from f_o, μ_r' has unity value while μ_r'' is essentially zero. These values of μ_r' and μ_r'' are expected since a magnetic response is only expected near resonance. As one moves towards the frequency of resonance, μ_r' gradually increases until it reaches a peak value of 11.25 at f_o. The high positive values of μ_r', coupled with the near zero value of μ_r'', achieved over the frequency band slightly below resonance is ideal for the realization of magneto-dielectrics.

At f_o, μ_r' drops sharply to -9.1 but slowly increases until it reaches a zero value at 5.3 GHz, leading to a negative permeability bandwidth of 0.3 GHz or 6%. The

frequency at which μ'_r crosses the zero line for the second time (5.3 GHz in this case) is known as the magnetic plasma frequency f_p and is given by

$$f_p^2 = \frac{3l}{4\pi^4 \mu_0 C_1 r^3 (1 - \pi r^2/a^2)}.$$ (3.4)

The negative permeability bandwidth can be calculated from the resonant frequency and the plasma frequency as

$$BW_{MNG} = \sqrt{(2\pi f_0)^2 - (2\pi f_p)^2} = \sqrt{(2\pi f_p)^2 \left(\frac{1}{1 - \pi r^2/a^2} \right)}$$ (3.5)
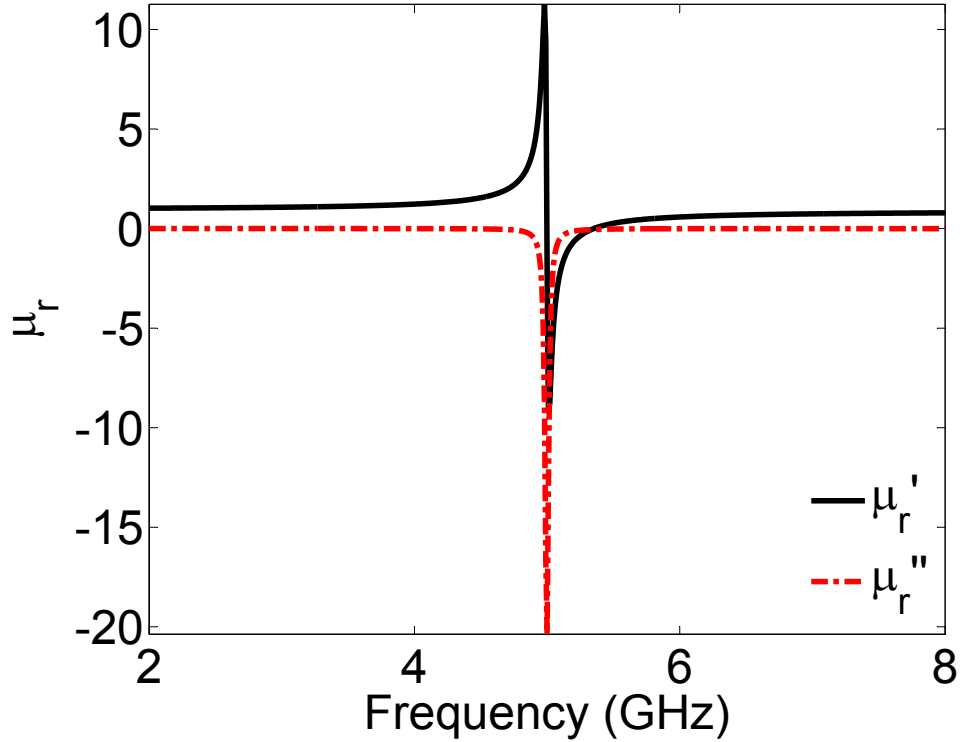
Figure 3.4. Real and imaginary plots of the relative permeability of (3.1). The values of the parameters are given in Table 3.1.

a	c	r	d	l	σ_1
2.0 x 10^{-2}	2.0 x 10^{-3}	4.2 x 10^{-3}	2.0 x 10^{-4}	2.55 x 10^{-3}	200

Table 3.1. Values of the parameters used to generate the plots of Figure 3.4. The dimensions of a, c, r, d, and l are in meters. σ_1 is given in Ω/m.

The frequency of resonance of SRRs can easily be altered by varying the parameters of the rings (r, c, d). For instance, increasing the radius r or the width of the metalization c increases the diameter of the SRRs and contributes to shifting the frequency of resonance downward. Increasing the gap d between concentric rings with fixed r also increases the diameter of the SRRs but results in an upward shift of the frequency of resonance.

Figure 3.5 and Figure 3.6 show plots of μ_r' and μ_r'' respectively, for different values of r. To create these plots, r is varied from 3.6 mm to 4.6 mm in increments of 0.2 mm while the values of the remaining parameters are kept the same as shown in Table 3.1. As expected, it can be seen from Figure 3.5 and Figure 3.6 that the frequency of resonance decreases as r is increased. Increasing r from 3.6 mm to 4.6 mm, which corresponds to a 27% increase in radius, results in a downward shift of the resonant frequency by 29.3% (from 5.8 GHz to 4.1 GHz). Note that the magnitudes of μ_r' and μ_r'' at resonance increase as the frequency is shifted down. The downward shift of the frequency of resonance is expected because increasing the radii of the rings increases not only the inductance of both concentric rings but also the capacitance accross the

gap between the two rings.

More plots of μ_r' and μ_r'', which are shown in Figure 3.7 and Figure 3.8 respectively, were created by varying the gap between concentric rings from 0.1 mm to 0.35 mm in increments of 0.05 mm. Although increasing d also increases the diameter of the SRRs, it can be seen from both figures that the effects of increasing d are an upward shift of the frequency of resonance and a change in the magnitudes of both μ_r' and μ_r''. The upward shift of the frequency of resonance is expected since increasing the gap between concentric rings reduces the capacitance which in turn increases the frequency of resonance.
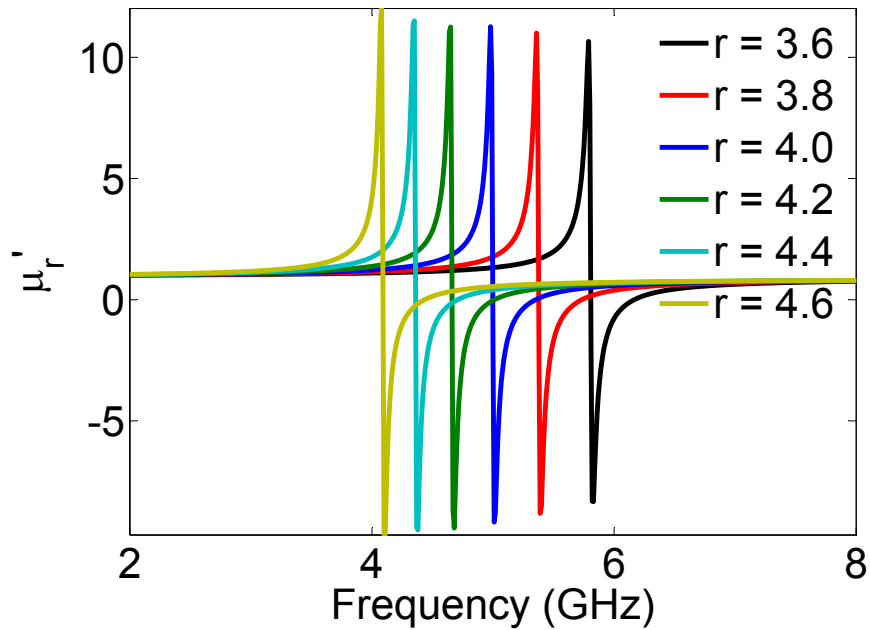
Figure 3.5. Real part of the relative permeability: effects of varying r (mm).
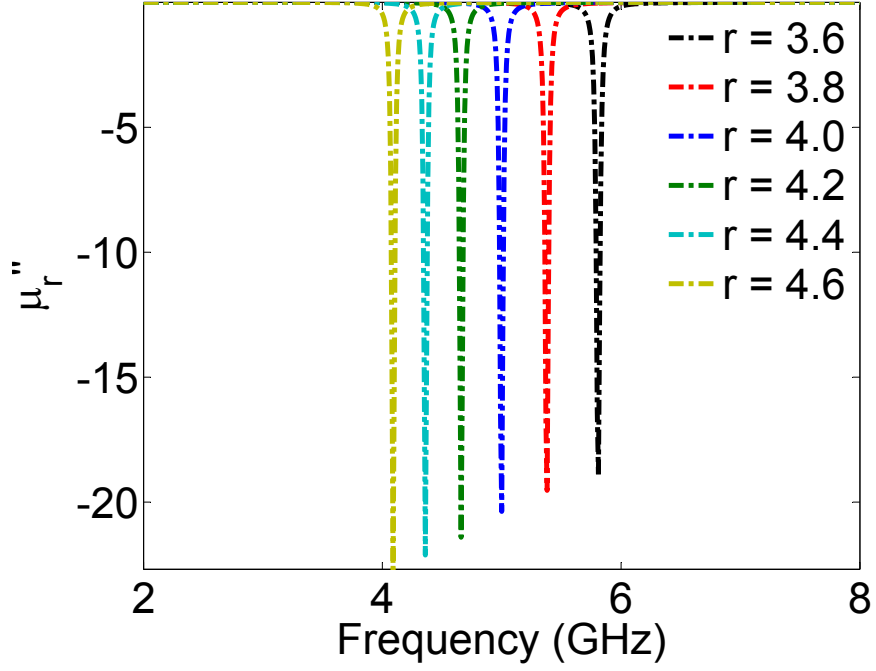
Figure 3.6. Imaginary part of the relative permeability: effects of varying r (mm).
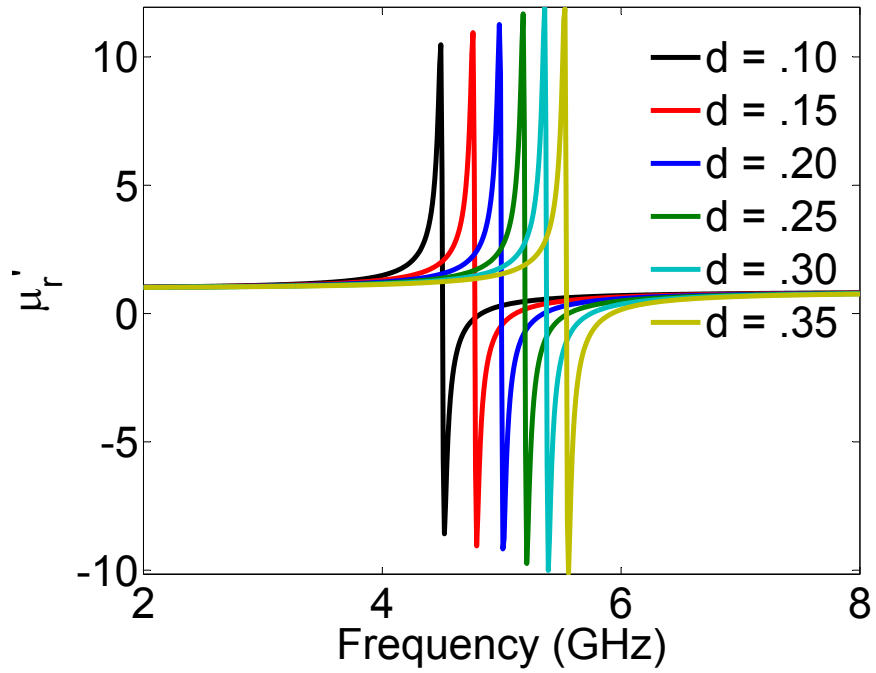
Figure 3.7. Real part of the relative permeability: effects of varying d (mm).
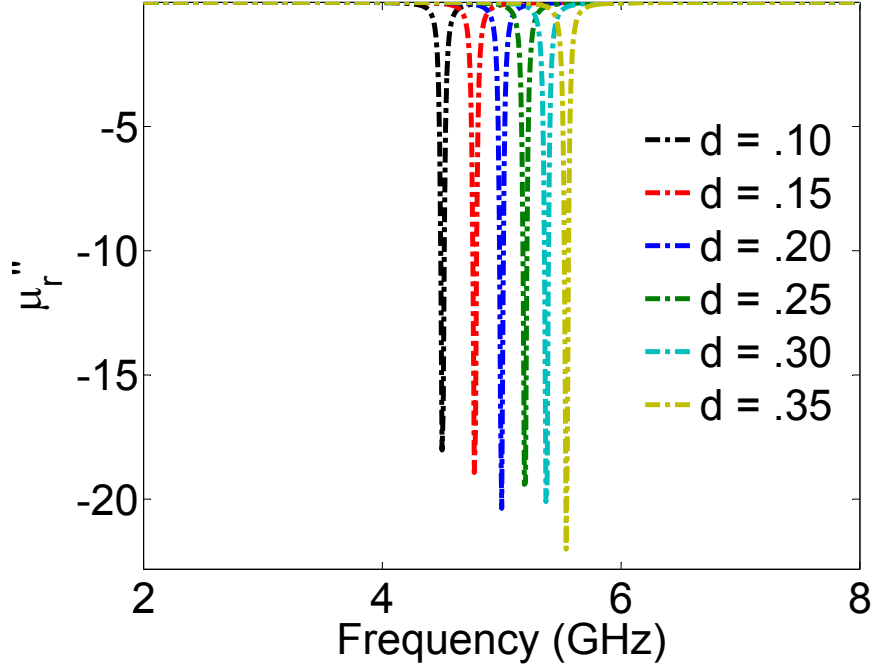
Figure 3.8. Imaginary part of the relative permeability: effects of varying d (mm).

Difficulties arise when the goal of the design is to create a negative permeability metamaterial with specific values of μ_r' and μ_r'' at a prescribed frequency. The easiest approach through which the frequency of resonance can be maintained fixed while the values of μ_r' and μ_r'' are varied is to change σ_1 as suggested by Pendry in [2]. Figure 3.9 and Figure 3.10 show plots of μ_r' and μ_r'' for different values of σ_1. These two plots were created by varying σ_1 from 200 Ω/m to 1200 Ω/m in increments of 200 while the rest of the parameters are kept identical to those shown in Table 3.1. σ_1 can be varied by using different types of metals or by changing the thickness of the metal. However, varying the thickness of the metal is not very practical since SRRs are typically etched onto circuit boards with a copper plating that is 17 or 34 μm

thick. Though it is possible to deposit other types of metals such as aluminum, gold, or silver on non plated dielectrics, it is an expensive, complex, and lengthy process that requires the use of specialized facilities.

In the next section, a design methodology based on a pixelization approach is presented as an effective means to create new resonant structures quite different from SRRs. It will be shown that for prescribed unit cell dimensions and metalization, it is possible to create multiple structures, all resonating at the same frequency but with different relative permeability values.
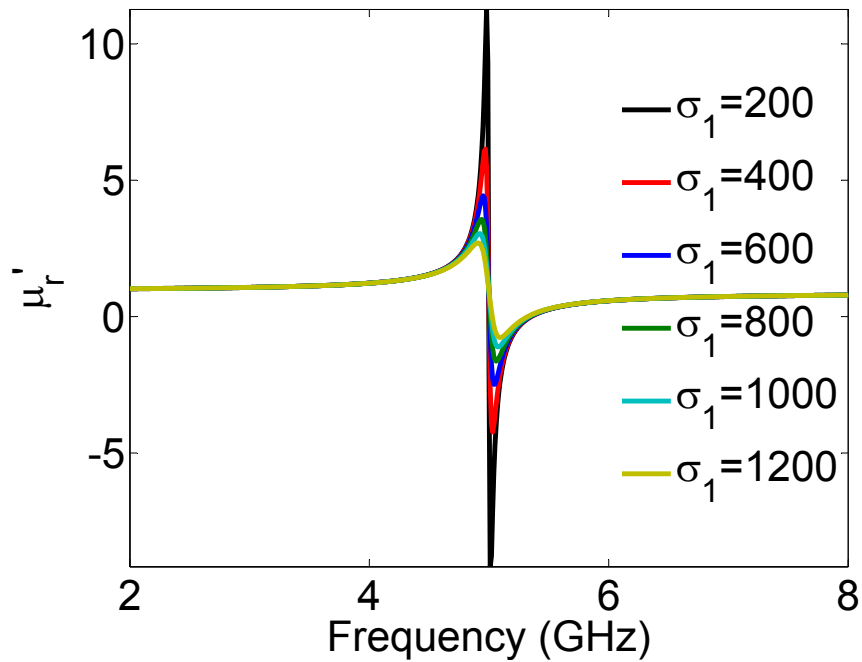
Figure 3.9. Real part of the relative permeability: effects of varying σ_1 (Ω/m).
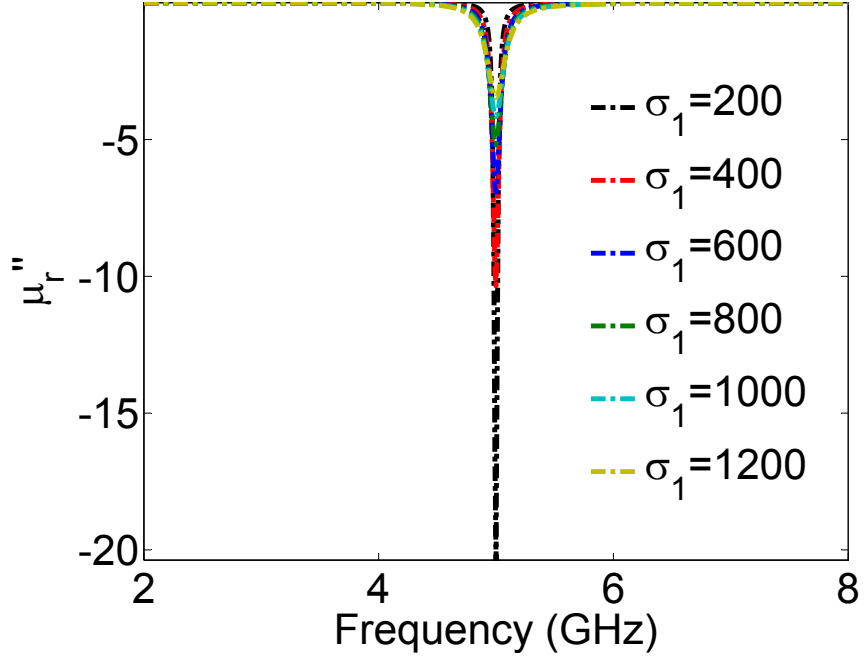
Figure 3.10. Imaginary part of the relative permeability: effects of varying σ_1 (Ω/m).

3.3 Synthesis of new resonant structures using a gradient based optimizer

In 2009, Diaz et al. proposed a methodology based on a topology optimization to synthesize new resonant structures that can be used to create negative permeability metamaterials [71]. The synthesis of new resonant structures in [71] was performed on a 3D unit cell containing a centrally located inclusion as shown in Figure 3.11.a. The inclusion is a dielectric slab backed by two thin metallic sheets that are symmetric about the y_1 axis. One sheet is on the front of the dielectric slab and the other is on the back. The back sheet is created by rotating the front sheet 180° about the vertical y_2 axis as shown in Figure 3.11.b. The sheets were discretized into pixels and a SIMP (Solid Isotropic Material with Penalization)-like model was used to find

the appropriate metal conductivity of each pixel. The conductivity of each pixel was varied between $\sigma = 0$ S/m and $\sigma = 5.8$ x 10^7 S/m, with $\sigma = 5.8$ x 10^7 S/m corresponding to the conductivity of copper. Pixels with $\sigma = 0$ S/m were labeled as white pixels and pixels with $\sigma = 5.8$ x 10^7 S/m were labeled as black pixels. Pixels with conductivities that are neither 0 S/m nor 5.8 x 10^7 S/m were referred to as gray pixels.
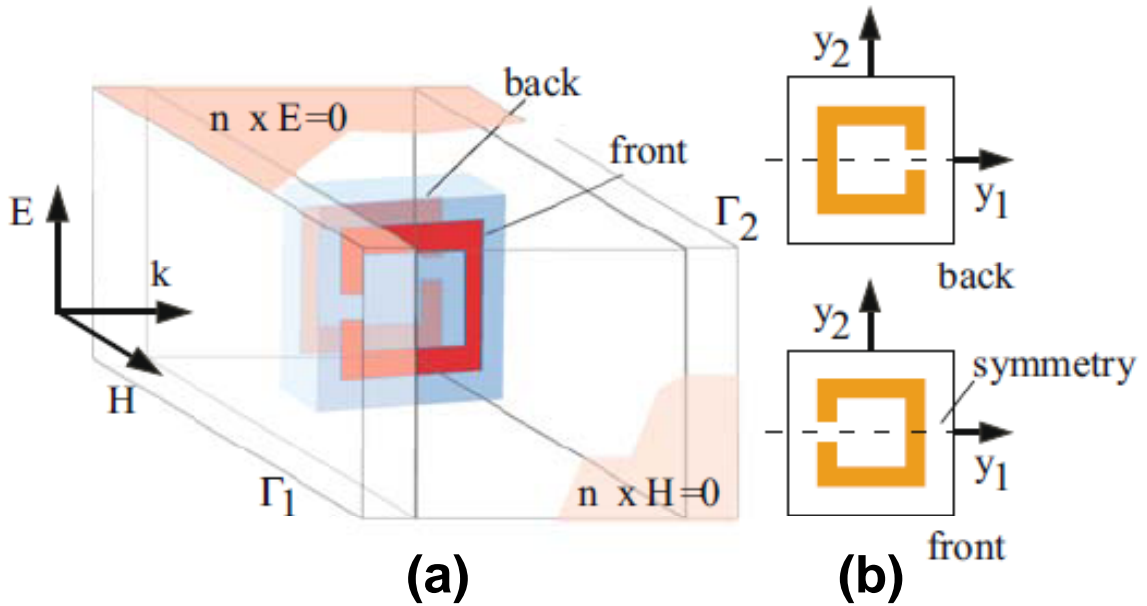
Figure 3.11. Representative unit cell (a) and symmetry (b). Picture taken from [71] with permission, see Appendix A.

A uniform plane wave was used to excite the unit cell while perfect electric ($\mathbf{n} \times \mathbf{E} = 0$) and perfect magnetic ($\mathbf{n} \times \mathbf{H} = 0$) boundary conditions were assigned to the side walls of the unit cell as shown in Figure 3.12.a. This particular analysis setup

is similar to having a medium composed of an infinite array of the unit cell in free space as shown in Figure 3.12.b. An effective medium theory was used to evaluate the relative permeability of the medium using the transmission and reflection coefficients obtained from ports Γ_1 and Γ_2 [71].
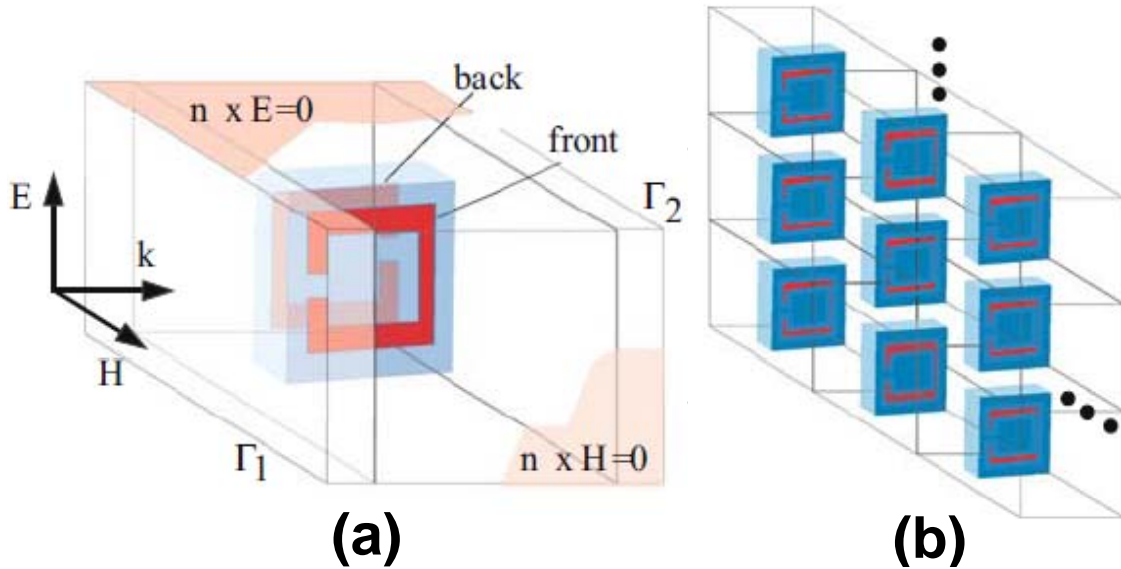
Figure 3.12. Representative cell (a) and infinite array representation (b). Picture taken from [71] with permission, see Appendix A.

Using a gradient based algorithm with the imaginary component of the relative permeability as the objective, Diaz et al. [71] showed that it is possible to synthesized new resonant structures that can be used to create negative permeability metamaterial media by varying the conductivity of the pixels. Examples of new resonant structures optimized to resonate at 2.2 GHz and their respective relative permeability plots are shown in Figure 3.13 and Figure 3.14.
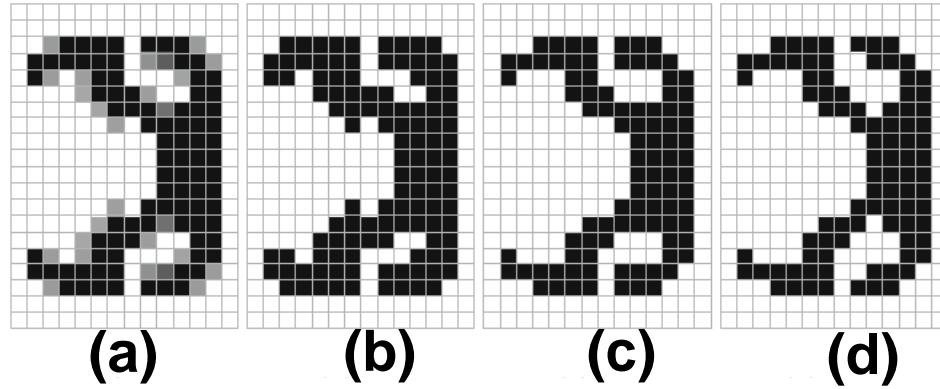
Figure 3.13. Examples of synthesized resonant structures. Picture taken from [71] with permission, see Appendix A.
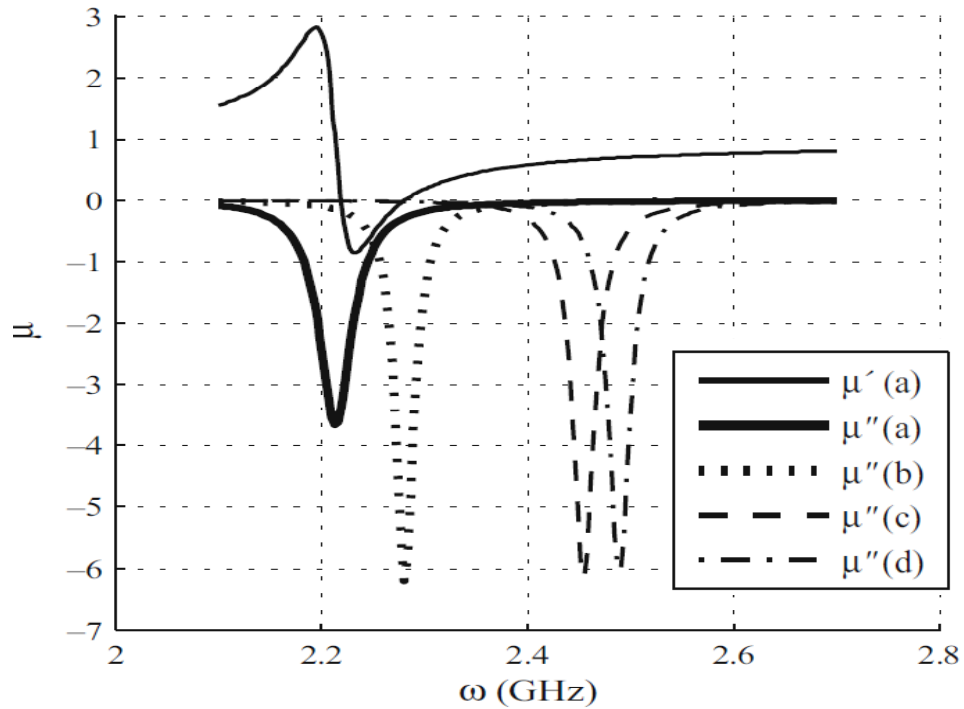
Figure 3.14. Plots of the relative permeability of the structures shown in Figure 3.13. Picture taken from [71] with permission, see Appendix A.

Although the methodology presented in [71] successfully creates new resonant structures, the optimized resonant structures contain gray pixels. These gray pixels are undesirable because they have a conductivity that is neither 0 S/m nor 5.8 x 10^7 S/m and thus cannot be fabricated. To make the new resonant structures more practical, several filtering techniques have to be used to convert the gray pixels to black or white pixels. The drawback of converting gray pixels to black or white pixels is a change in the characteristics of the resonant structure. As shown in Figure 3.14, the frequency of resonance shifts away from 2.2 GHz and the magnitude of the permeability at resonance changes.

The use of a gradient based optimizer requires knowledge of the gradient of the electric field at every location within the unit cell of Figure 3.11.a. Such knowledge may not be available to the designer when a commercial electromagnetic solver is used to perform the analysis. Additionally, since the analysis is performed in free space on an infinite representation of inclusions, a very large sample that is several wavelengths in length and width is required in the experimental setup in order to avoid diffraction at the edges of the sample. To fabricate a metamaterial sample with such large dimensions is a difficult and expensive task.

3.4   Synthesis of new resonant structures using a binary optimizer

An alternative design methodology that uses the pixelization approach of [71] with a binary optimization tool is presented here to overcome the difficulties associated with the use of a gradient based algorithm and the need of large samples in the experimental setup. It will be shown that if a genetic algorithm (GA) is used as a

binary optimizer, then for a given frequency and unit cell dimensions, it is possible to create multiple resonant structures, all resonating at the same frequency but with different permeability values at resonance. Since the optimizer is binary there are no gray pixels and filtering is not needed. Additionally, the GA optimization only requires knowledge of the transmission and reflection coefficients, which are readily accessible in all commercial EM solvers. Difficulties associated with manufacturing large samples and issues related to edge diffraction can be avoided by performing the analysis and experiment in a waveguide. In this case, a sample made of only a single unit cell is required in the experimental setup.

3.4.1   Design setup

The synthesis of new resonant structures is performed here considering an inclusion centrally located inside a rectangular waveguide as shown in Figure 3.15.a. The top, bottom, left and right walls of the waveguide are assumed to be perfect electric conductors while the front and back walls represent the two excitation ports where the transmission and reflection coefficients are evaluated. If only the dominant TE_{10} mode propagates inside the waveguide at the frequency of interest, and is polarized such that the electric field is normal to the top and bottom walls of the waveguide, an infinite symmetric representation of the inclusion can be obtained along the z axis using image theory. The resulting medium composed of an infinite array of inclusions is shown in Figure 3.15.b.

Under the infinite symmetric representation condition, if the size of the inclusion is much smaller than the operating wavelength, the medium behaves as a homoge-

neous slab characterized by a relative permittivity and permeability [71] – [109]. In general, it is typically required that the length and width of the inclusion be less than $\lambda_0/4$ since most structures radiate when they are approximately $\lambda_0/2$ or $\lambda_0/4$ long. Although radiation does not occur in a waveguide, the length and width of the inclusions are selected to be less than $\lambda_0/4$. The effective parameters can be calculated from the transmission and reflection coefficients computed at the two ports of the waveguide. The meaning of effective parameters should be interpreted with care since the infinite array of inclusions does not represent a true homogeneous material. In fact, the values of the extracted effective parameters depend on the polarization of the imping wave, the number of inclusions and the arrangement of the inclusions within the host medium. The extracted effective parameters discussed in the next sections are only valid for the setup of Figure 3.15.
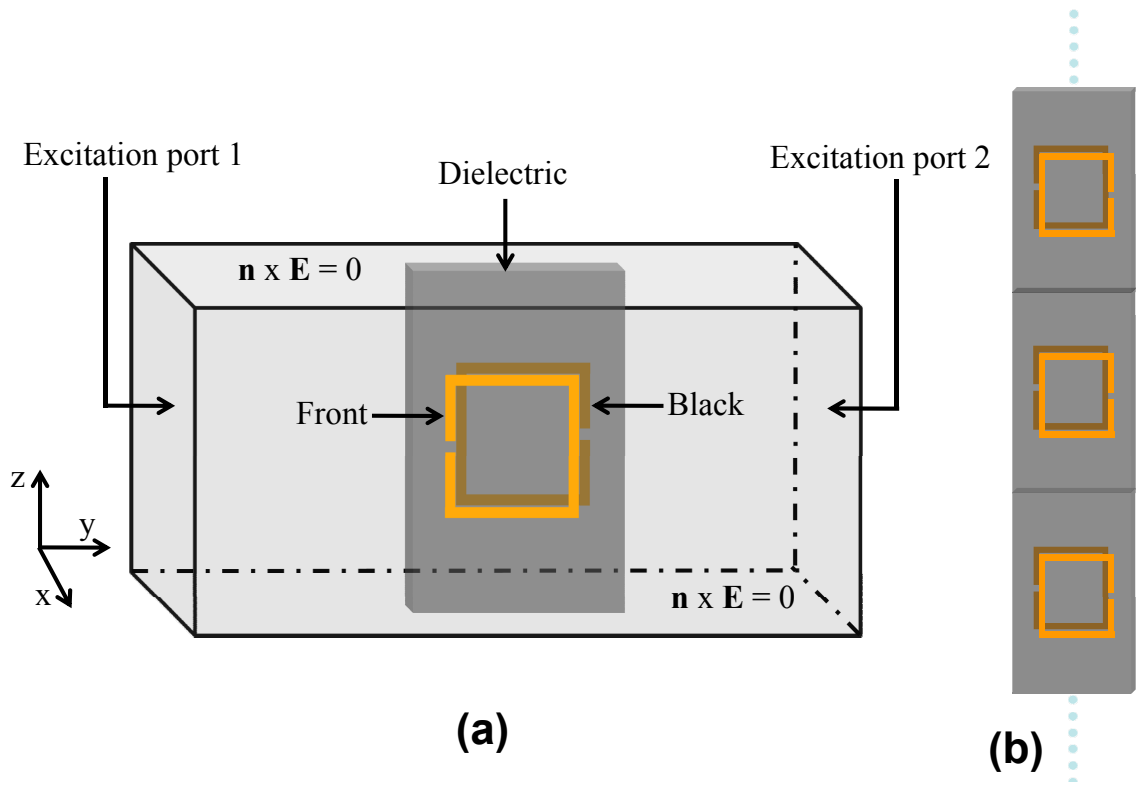
Figure 3.15. Rectangular waveguide loaded with an inclusion (a) and equivalent infinite array representation (b).

The inclusion used here is a dielectric slab backed by two symmetric metallic sheets. The two metallic sheets are created following the layout of Figure 3.16. Half of the front metallic sheet is pixelated and each pixel is randomly assigned a conductivity of 0 S/m (white pixel) or 5.8×10^7 S/m (black pixel). The half pixelated sheet is rotated $180°$ about the y axis to create the full front sheet which is shown in Figure 3.16.b. The second pixelated metallic sheet, which is on the back of the dielectric, is obtained by rotating the front pixelated sheet $180°$ about the z axis.

The characteristics and geometry of the inclusion can be altered by turning pixels

black or white. Changing the characteristics of the inclusion alters the magnitude
and phase of the transmission and reflection coefficients, which in turn affect the
values of the extracted effective parameters. The goal of the binary optimizer is thus
to determine which pixels to turn black or white such that the desired extracted
parameters can be obtained.
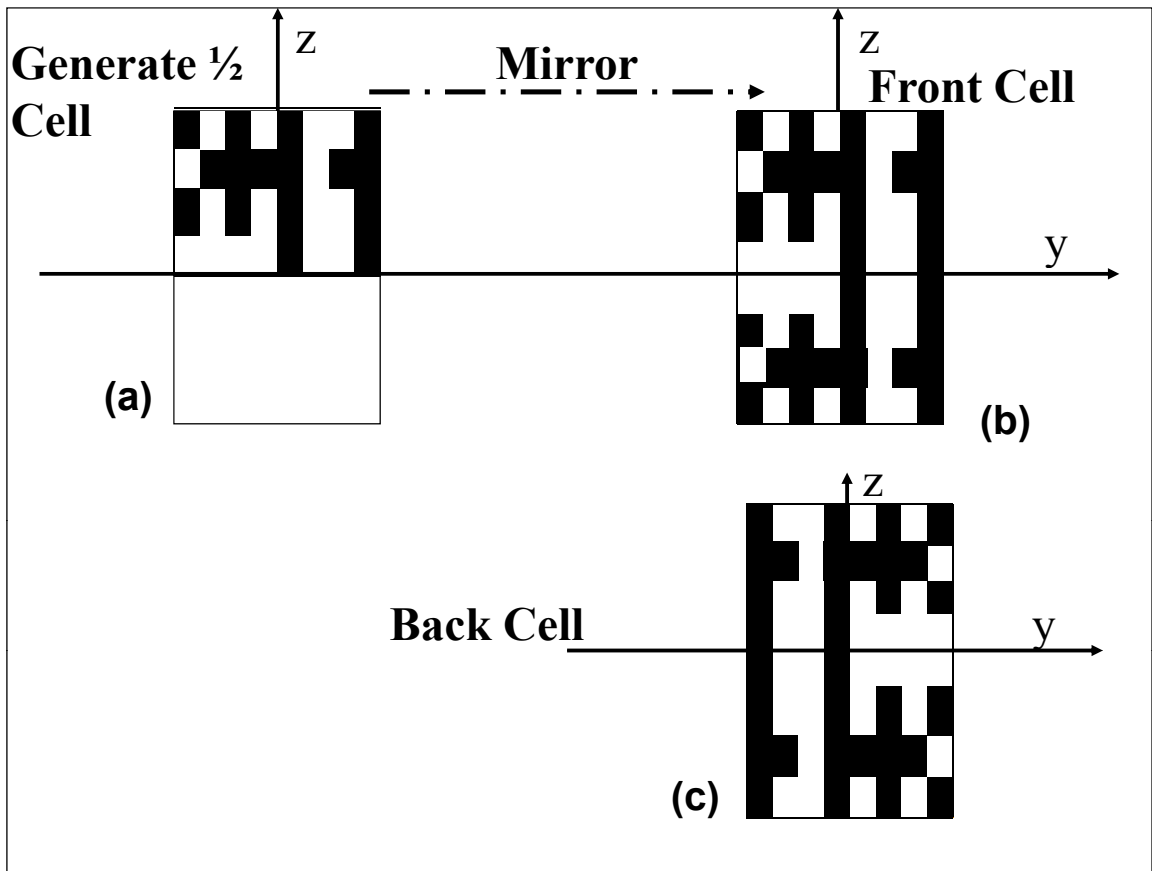
Figure 3.16. Symmetry used to create the pixelated metallic sheets placed on either
side of the dielectric slab.

The analysis and optimization are performed by integrating the commercial full

wave solver HFSS [114] with the numerical computing software Matlab [115], following the outline of Figure 3.17. The waveguide and the inclusion are created in Matlab and exported to HFSS for analysis. Once the analysis is completed, desired output parameters such as the transmission and reflection coefficients are exported back to Matlab for post-processing and optimization. Post-processing involves using the transmission and reflection coefficients obtained from HFSS to calculate the effective parameters of the analyzed inclusion. The calculated effective parameters are compared against a stopping criterion. The stopping criterion is typically a set value of the real part of the relative permeability. If the stopping criterion is not met, the optimizer creates a new inclusion based on the performance of the inclusion that was just analyzed. The newly created inclusion is loaded in a waveguide and exported to HFSS for analysis. This process is repeated until the desired effective permeability value is obtained or the optimizer reaches a predetermined number of iterations.

To integrate Matlab with HFSS, a set of Matlab functions have to be generated in order to create a script that HFSS can execute. This is not an easy task since HFSS has over one hundred commands and a script is needed to execute each of these commands. Appendix A.1 provides a step by step explanation of how to integrate Matlab with HFSS. Details of how to write Matlab functions to create scripts that HFSS can execute are also provided in Appendix A along with a list of more than seventy Matlab functions that have already been written. These Matlab functions can be found on the MSU electromagnetics group web page.
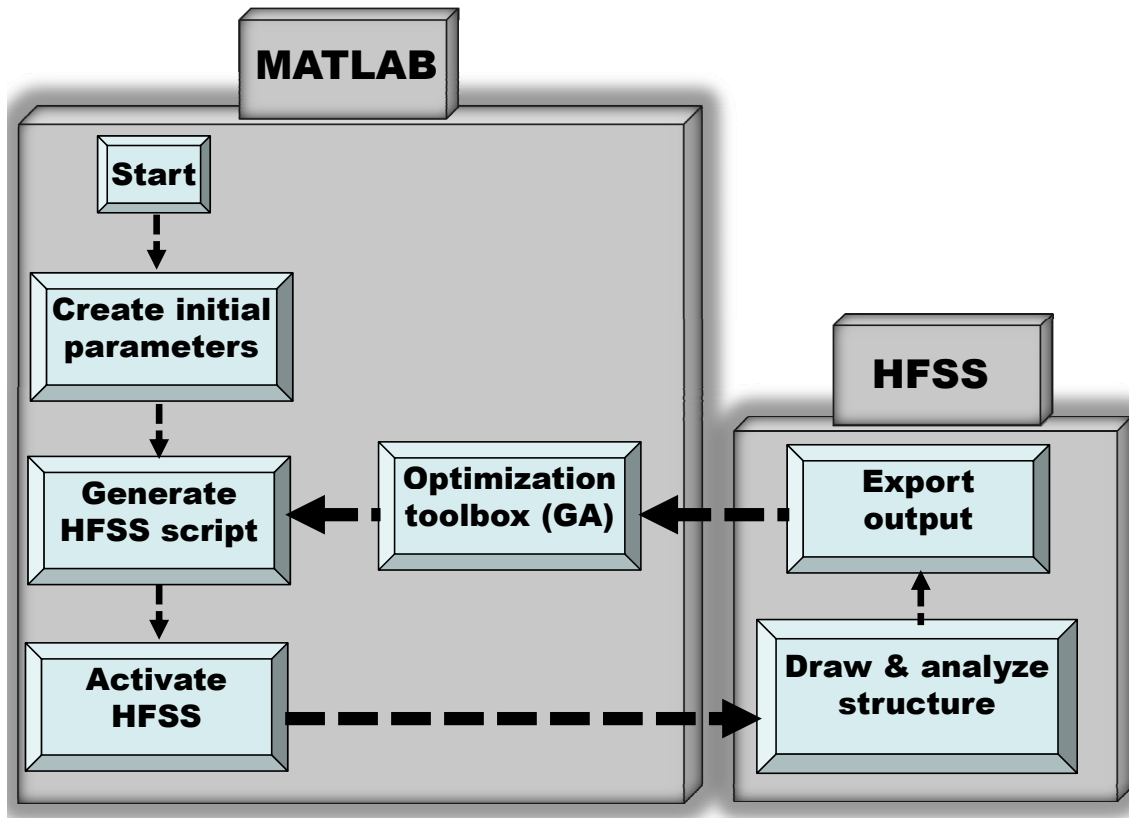
Figure 3.17. Matlab HFSS interface.

3.4.2 Optimization tool

The optimization tool used in this dissertation is a proprietary genetic algorithm written in Matlab by the author. A GA is a stochastic search algorithm based on the principles of genetics and natural evolution. Within a given population, individuals who are the most fit have the highest probability of survival. Allowing only the fittest individuals to mate increases the probability of producing new generations composed of offspring that are as fit as the parents. One would hope for offspring that are more fit than the parents but that depends on the genes inherited by the offspring and gene

mutation.

The concept of natural evolution is mimicked in GAs through selection, crossover and mutation. An initial population is randomly selected and the chromosome of each individual within the population is encoded into a binary string. The fitness of each individual is evaluated using a fitness function. Individuals with the highest fitness values are selected into a mating pool. Mating involves two or more individuals who share parts of their chromosomes through crossover to create a new generation of individuals or offspring. To increase the level of diversity in the new generation, several offspring are selected and one or more of their genes are mutated.

The fitness of each offspring is evaluated and compared to a stopping criterion. If the stopping criterion is met, the GA stops. On the other hand, if the stopping criterion is not met, the offspring undergo the same process of selection and crossover as their parents to create a newer generation of offspring. The fitness of each offspring in the newer generation is evaluated and compared to the stopping criterion. This process is repeated until the stopping criterion is met or a set number of generations has been evaluated. A block diagram of the steps involved in a basic genetic algorithm is shown in Figure 3.18.
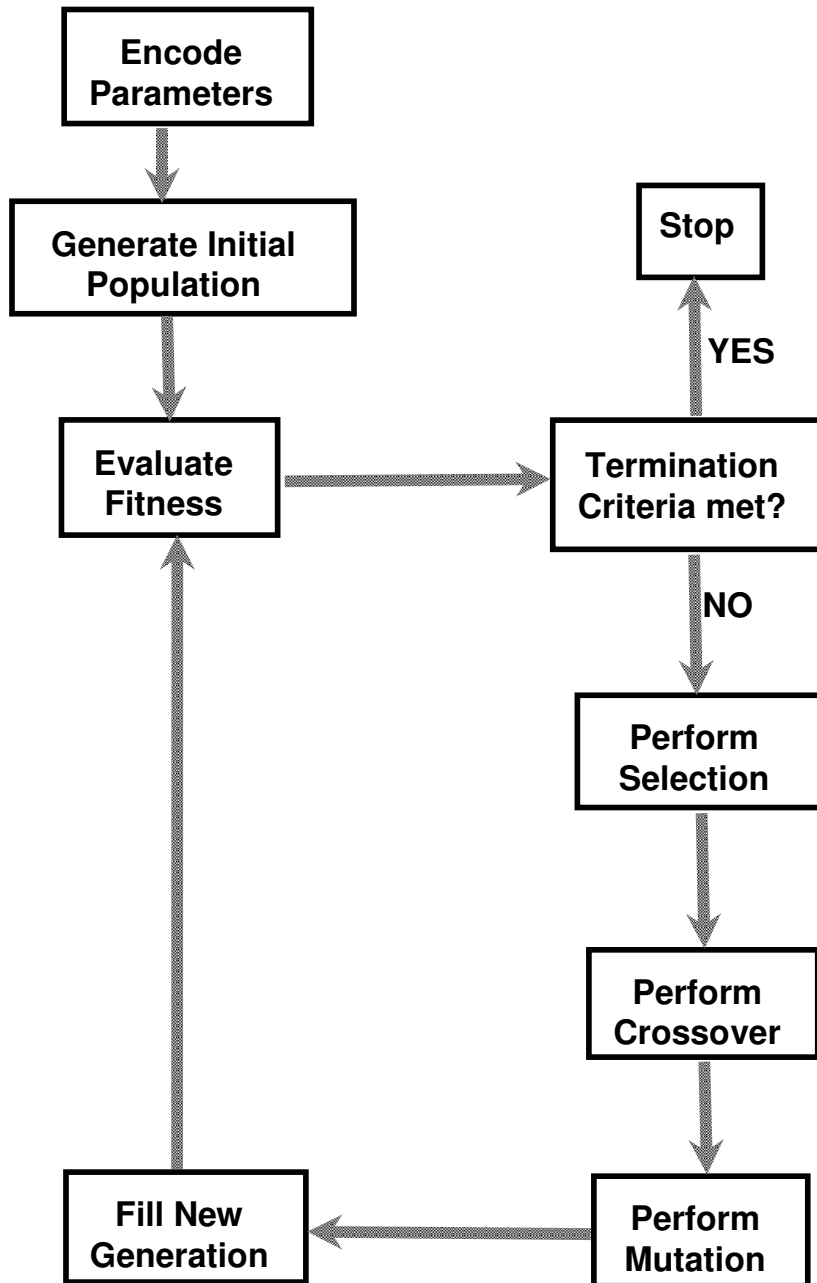
Figure 3.18. Block Diagram of a basic genetic algorithm.

3.4.2.1 Encoding parameters

The parameters to be optimized need to be encoded into chromosomes. The lengths of the chromosomes determine the search space and longer chromosomes are needed for more complex problems. With reference to the pixelated sheets, the geometry of each sheet is encoded into a chromosome as a binary string of '0's and '1's. A '1' is used to represent a black pixel, while a '0' is used for a white pixel. Because of the symmetry of Figure 3.16, the chromosome length is equal to the number of pixels on a half sheet.

3.4.2.2 Initial population

The initial population represents the first set of chromosomes to be evaluated. The initial population is usually generated randomly but a pre-existing pool of chromosomes can be used as the starting population.

3.4.2.3 Evaluating the fitness

The fitness of each individual is evaluated using a fitness function. In nature, the fitness of an individual might be determined based on its endurance, its life expectancy, or a combination of several criteria. Since the goal of the present optimization is to create a medium with $\mu_r' < 0$, information about μ_r' should be included in the formulation of the fitness function. Often, terms such as cost function or objective function are used in lieu of fitness function. Extra caution should be exercised when substitut-

ing these terms because they might be opposites of one another. For instance, fitness is maximized while cost is minimized.

3.4.2.4   Mating pool selection

The mating pool is composed of individuals that have been selected to pass their genetic information to the next generation. Selection of the mating pool can be done through various methods among which are elitist, thresholding, roulette wheel and tournament selection:

- Elitist: the chromosomes are ranked based on their fitness and a number of chromosomes, counting from the fittest, are selected.

- Thresholding: a preselected fitness value or a ratio between a chromosome fitness and the average fitness is used as selection criterion.

- Roulette wheel: chromosomes with higher fitness values have higher probabilities to be selected compared to chromosomes with lower fitness values. The roulette wheel method allows for more diversity in the mating pool.

- Tournament: two or more chromosomes are selected randomly from the population and the chromosome with the highest fitness value is selected for the mating pool. This process is repeated until the mating pool is filled.

3.4.2.5 Crossover

After the selection process is completed, the selected chromosomes or parents are paired and crossovers are performed with crossover probability P_{cross}. Crossover can be performed at one or multiple points between two or multiple chromosomes. A simple one point crossover performed between two chromosomes is demonstrated below.

Assume two parents C_1 and C_2, each n bits long given as

$$C_1 = X_0 X_1 X_2 X_3 X_4 X_5 .... X_{n-1}, \tag{3.6}$$

$$C_2 = Y_0 Y_1 Y_2 Y_3 Y_4 Y_5 .... Y_{n-1}. \tag{3.7}$$

A crossover point X_n is randomly selected between 1 and n and the chromosomes of the two parents are split into two strings at that specific crossover point. The strings are then swapped, creating two new chromosomes or offspring O_1 and O_2 as shown below.

Assuming $X_n = 5$,

$$O_1 = X_0 X_1 X_2 X_3 X_4 Y_5 .... Y_{n-1}, \tag{3.8}$$

$$O_2 = Y_0 Y_1 Y_2 Y_3 Y_4 X_5 .... X_{n-1}. \tag{3.9}$$

3.4.2.6 Mutation

Once the crossover is completed, random mutations are performed with mutation probability P_{mut}. Mutation is carried on by toggling a random bit within the binary string of the chromosome. For instance, a chromosome with binary string {111111} will have the following binary string {110111} if mutation is performed on the third bit of its string. After the mutation process, the generation of offspring then becomes the new generation of parents and their fitness values are evaluated once again.

3.4.2.7 Stopping criterion

The GA is sometimes stopped after a set number of generations has been evaluated. More often, a stopping condition can be imposed when a chromosome with a fitness value higher than a preselected value is found.

3.4.3 Synthesized structures and corresponding μ plots

The design methodology described in the previous sections is used here to show that for a given frequency and unit cell dimensions, it is possible to create multiple examples of resonant structures, all resonating at the same frequency, but with different values of μ'_r at the frequency of resonance. Multiple examples including a variation of the unit cell dimensions and a variation of the number of pixels are investigated. In all the examples, the unit cells are analyzed in an F-band waveguide. The width and height of the waveguide are 0.0404 m and 0.0202 m, respectively. In order to determine the operating frequency band of the dominant TE_{10} mode, the cutoff frequency

of the TE_{10} mode and that of the next higher order mode need to be calculated. The cutoff frequency of any TE_{mn} mode in a rectangular waveguide is given by [113]

$$f_{cmn} = \frac{1}{2\sqrt{\epsilon_0 \mu_0}} \sqrt{\left(\frac{m}{a}\right)^2 + \left(\frac{n}{b}\right)^2}. \tag{3.10}$$

In (3.10), a and b are the width and height of the waveguide respectively and, m and n are integers. Note that in the present case, $a = 2b$ and (3.10) can be simplified to

$$f_{cmn} = \frac{1}{2a\sqrt{\epsilon_0 \mu_0}} \sqrt{(m)^2 + 4\,(n)^2}. \tag{3.11}$$

With $a = 0.0404$ m, the cutoff frequency of the TE_{10} mode is $f_{c10} = 3.71$ GHz. The next higher order modes are the TE_{01} and TE_{20} modes. These two modes are known as degenerate modes since their cutoff occurs at the same frequency $f_{c01} = f_{c20} = 2f_{c10} = 7.42$ GHz.

It is common practice to select an operating frequency band that starts approximately 25% above the cutoff frequency of the dominant mode and stops before the cutoff frequency of the next higher order mode in order to avoid any phase distortion. As such, the operating frequency band of the F-band waveguide is designated as $4.95 - 7.05$ GHz [113].

The ability to create new resonant structures using the pixelization approach is first demonstrated by considering a unit cell of dimensions 6 mm by 6 mm. The desired frequency of resonance is arbitrarily selected to be 5.5 GHz. At 5.5 GHz, the dimensions of the unit cell are $\lambda_0/9.1$ by $\lambda_0/9.1$. The unit cell is parameterized into a uniform pixelated grid containing 144 square pixels such that the dimensions of each

pixel are 0.5 mm by 0.5 mm. Recall from Section 3.4.1 that the unit cells considered here are double sided structures which are designed following the symmetry of Figure 3.16. The backing substrate used is a 0.78 mm thick Rogers 5870 RT/duroid with dielectric constant $\epsilon_r = 2.33$ and loss tangent $\delta_t = 0.0012$ [116]. The same substrate is used for all the examples discussed below.

The GA optimization is performed by selecting an initial random population of 200 binary strings. Each binary string is 72 bits long and the state of the bits are used to specify the conductivity of the pixels on the top half of the front sheet of the unit cell. Note that each binary string has only 72 bits instead of 144 bits because of the symmetry of Figure 3.16. When the state of a bit is "0", the corresponding pixel is assigned a conductivity of 0 S/m (white pixel). On the other hand, when the state of the bit is "1", the pixel is assigned a conductivity of 5.8 x 10^7 S/m (black pixel). Since the bits are binary, 72 bits lead to a total of 2^{72} or over 10^{21} possible pixel combinations. Given this large number of combinations, it is evident that a directed search is needed to ensure convergence to acceptable solutions within an acceptable amount of time.

The initial random population of 200 binary strings is created in Matlab using the following command sequence:

```
for ip = 1:200
    for jp = 1:72
      if rand() > 0.5
        Pop(ip, jp) = 0;
      else
        Pop(ip, jp) = 1;
       end
```

57

```
        end
    end
```

From the Matlab command lines above, ip is an integer used to specify the index of each individual, jp is an integer used to specify the index of the bits within each binary string, rand() is a pseudo-random number generator that generates numbers between 0 and 1, and Pop(ip, jp) is a 200 x 72 matrix that is used to store the 200 binary strings.

Once the 200 binary strings have been generated, the corresponding unit cell geometries of all the binary strings are created. Each of the 200 unit cells is loaded in an F-band waveguide and exported to HFSS for analysis. Once the analysis is completed, the transmission and reflection coefficients are exported back to Matlab for post processing. In the post processing stage, the transmission and reflection coefficients are used to calculate μ_r', μ_r'', ϵ_r' and ϵ_r'' as

$$\mu_r = \mu_r' + j\mu_r'' = \frac{Z_r c \log(U)}{jW\omega}\sqrt{1 - \frac{f_c^2}{f^2}} \tag{3.12}$$

$$\epsilon_r = \epsilon_r' + j\epsilon_r'' = \frac{\log(U)\sqrt{1 - \frac{f_c^2}{f^2}}}{\frac{jW Z_r \omega}{c}} + \frac{c^2}{4a^2 f^2 \mu_r} \tag{3.13}$$

$$U = \frac{1 - P(S_{11} + S_{21})}{S_{11} + S_{21} - P} \tag{3.14}$$

$$Z_r = \frac{P+1}{1-P} \tag{3.15}$$

$$P = \frac{S_{11}^2 - S_{21}^2 + 1}{2S_{11}} \pm \sqrt{(\frac{S_{11}^2 - S_{21}^2 + 1}{2S_{11})^2} - 1} \tag{3.16}$$

where W is the thickness of the unit cell, f_c is the cutoff frequency, f is the frequency of operation, and Z_m is the wave impedance within the unit cell. The equations provided above are derived in [112] using the Nicholson Ross Weir technique.

Since the goal of the optimization is to synthesize resonant structures that can lead to $\mu_r' < 0$, the cost function is simply defined as

$$Cost = \mu_r'. \tag{3.17}$$

Once all the unit cells have been analyzed, their respective cost values are evaluated and ranked. The binary strings of the best 20 unit cells are selected into a mating pool. Note that the best unit cells are those with the lowest cost value. A new population of 80 individuals is created by performing a two point and three point crossover using the individuals in the mating pool. Forty offspring are created through a 2 point crossover while the other 40 are created using a 3 point crossover. Crossover is performed using parents selected from the mating pool. Two types of selections are implemented:

- Select the best from three parents who are randomly selected from the mating pool

- Select a parent randomly from the mating pool

Once crossover is completed, a single bit mutation is performed with a mutation probability of 0.2. After the mutation process is completed, the corresponding unit cell geometries of the 80 offspring are created. Each created unit cell geometry is loaded in an F-band waveguide and exported to HFSS for analysis. Once the analysis is completed, cost values are evaluated once again and the processes of selection, crossover and mutation are repeated. For this first example and the other two discussed below, the stopping criterion is the maximum number of generations which is set to 80.

The optimizations are performed at a single frequency point which is 5.5 GHz. The best unit cell found at the end of each generation is loaded in the F-band waveguide and a frequency sweep is performed in HFSS from 5 GHz to 6 GHz using 200 frequency points. The goal of the frequency sweep is to determine the performance of each unit cell at frequencies other than the optimized frequency. All the analyses are performed on a desktop computer with an Intel i7 quad core processor and 12 Gb of RAM. The run time for each iteration is approximately 75 seconds. An iteration involves creating the structure in Matlab, loading the structure in HFSS, running an HFSS simulation, exporting the output data from HFSS to Matlab and processing the data in Matlab. More than 95% of each iteration time is spent on the HFSS simulation. The complete Matlab code used to perform the optimization is provided in Appendix C.

A convergence plot showing the best cost found by the GA at the end of each generation is shown in Figure 3.19. It can be seen from the figure that the value of the best cost at the end of the first generation is 0.92. Figure 3.20 shows plots of μ'_r

and μ_r'' with respect to frequency. Observe that μ_r' is maintained between 0.9 and 0.95 while μ_r'' is essentially zero throughout the frequency band. The expected values of μ_r' and μ_r'' for an empty waveguide are one and zero respectively. This shows that the structures from the initial population of 200 had no values of μ_r' and μ_r'' that showed resonance properties. It is therefore left to the GA to find structures that can produce negative values of μ_r' at 5.5 GHz.
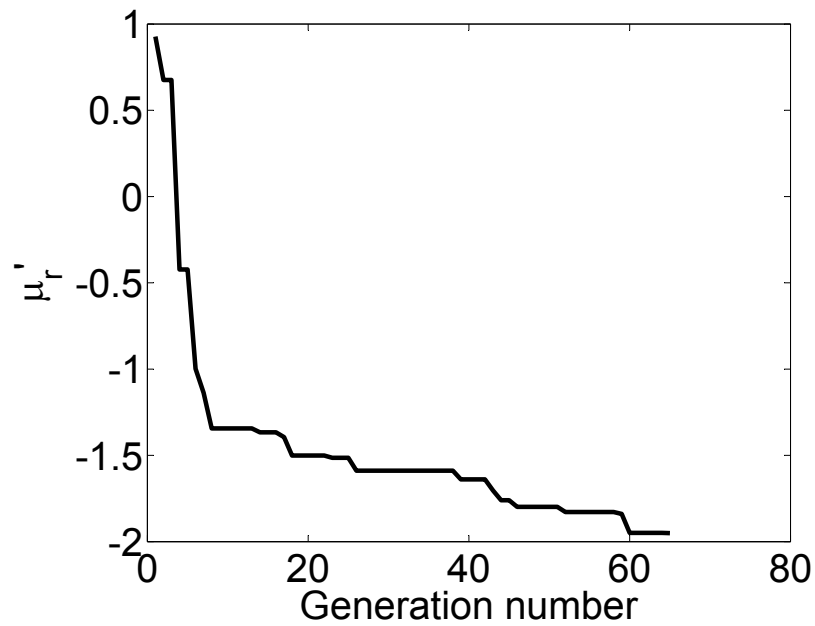
Figure 3.19. Convergence plot showing the best cost at the end of each generation: 1st example.
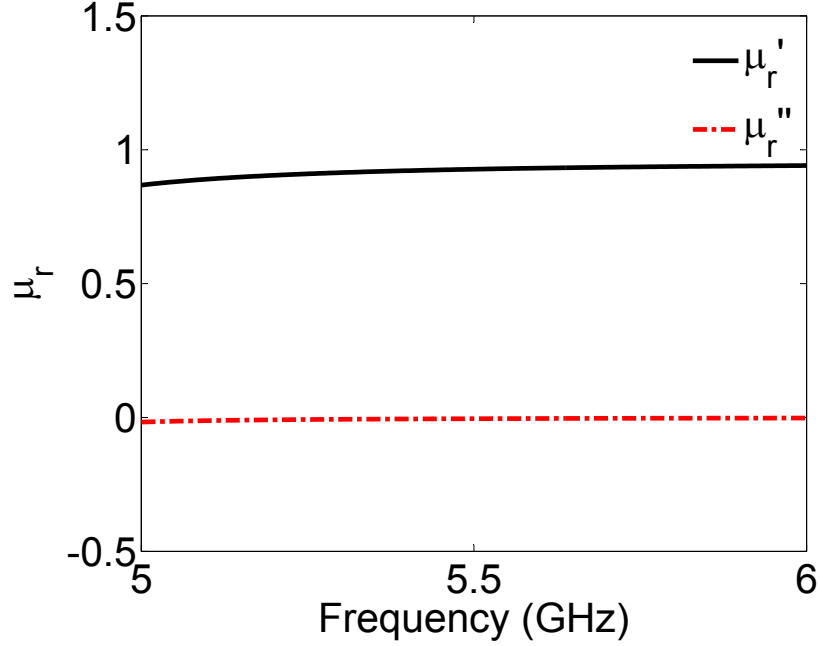
Figure 3.20. Real and imaginary parts of the relative permeability of the best structure found at the end of the 1st generation: 1st example.

By the end of the fourth generation, the best structure found at the GA has a cost of -0.428. This is very interesting because the total number of structures investigated by the end of the fourth generation is 440. Of the 440 structures, 200 are created randomly and the remaining 240 are created by the GA. Plots of μ'_r and μ''_r as a function of frequency for the best structure found at the end of the fourth generation are shown in Figure 3.21. Note that resonance does occur at the desired frequency of 5.5 GHz and the curves of μ'_r and μ''_r are similar to those created in Section 3.2 using (3.1).
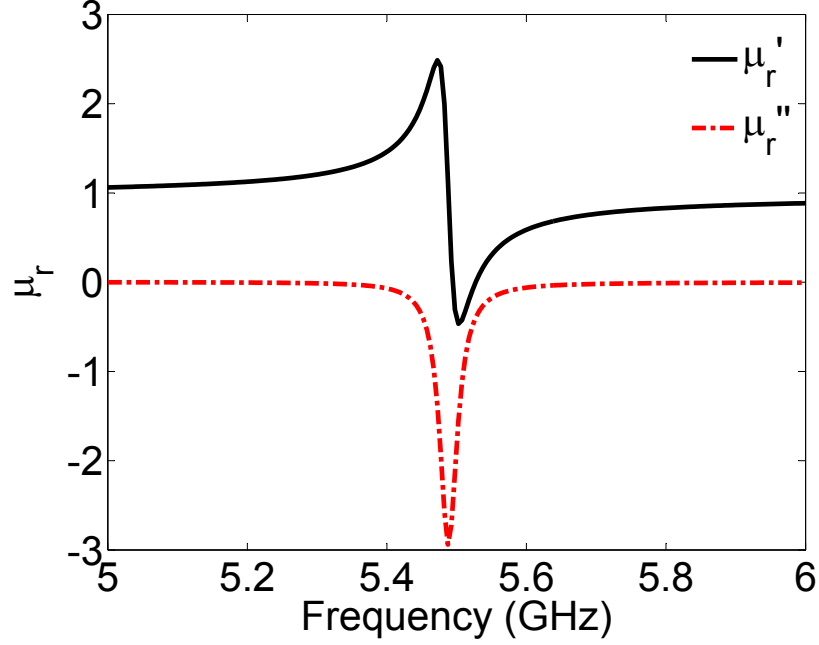
Figure 3.21. Real and imaginary parts of the relative permeability of the best structure found at the end of the 4th generation: 1st example.

By the end of the sixth generation, the best structure found has a cost of -1.01. With reference to [3], a medium with $\mu'_r = -1$ can be used to create perfect flat lenses provided $\epsilon'_r = -1$. Plots of μ'_r and ϵ'_r with respect to frequency are shown in Figure 3.22. Though ϵ'_r shows a dip near the same frequency of resonance as μ'_r, it remains positive throughout the frequency band. The plots shown in Figure 3.22 are encouraging even though negative values of ϵ'_r were not obtained because the optimization was only performed to create negative values of μ'_r at 5.5 GHz. With SRRs, the resonances of μ'_r and ϵ'_r typically occur at frequencies that are far apart from each other. What is seen in Figure 3.22 suggests that by reformulating the cost function to include information about ϵ'_r , it should be possible to drive the values of μ'_r and ϵ'_r to -1 at the same frequency.
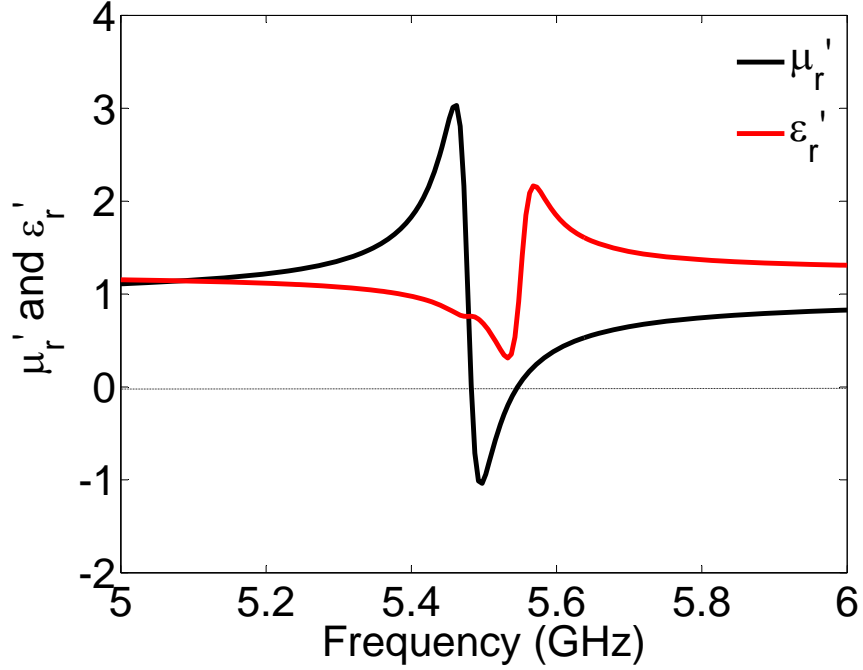
Figure 3.22. Real parts of the relative permeability and permittivity of the best structure found at the end of the 6th generation: 1st example.

The best structure found at the GA by the end of the 65th generation has a cost of -1.95. Plots of μ'_r and μ''_r with respect to frequency are shown in Figure 3.23. Note that the minimum value of μ'_r is still maintained at the desired frequency of 5.5 GHz. A plot of ϵ'_r with respect to frequency, as shown in Figure 3.24, reveals a narrow frequency band (5.548 – 5.565 GHz) where $\epsilon'_r < 0$. This narrow frequency band overlaps with the frequency band over which $\mu'_r < 0$. The overlap between μ'_r

and ϵ'_r is unexpected since ϵ'_r was not included in the formulation of the cost function.
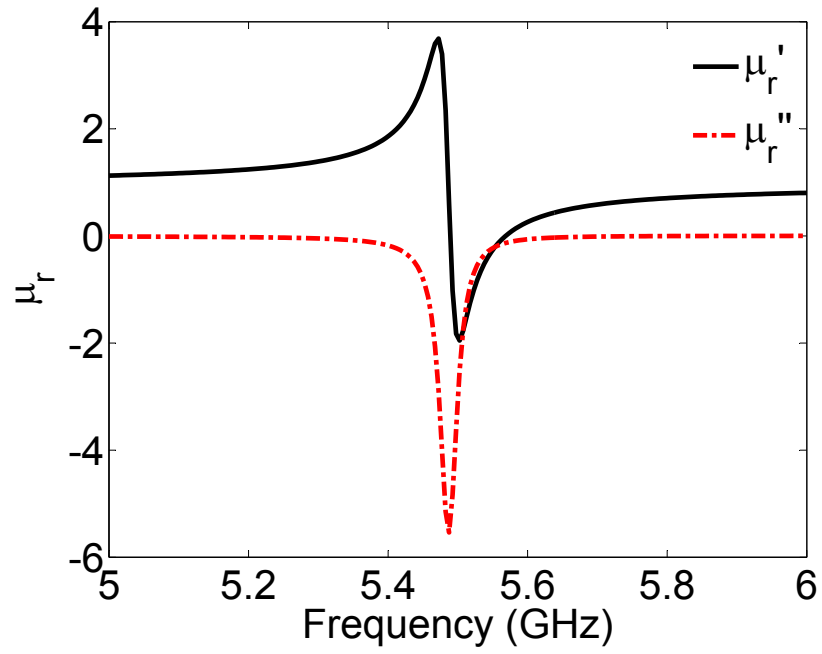
Figure 3.23. Real and imaginary parts of the relative permeability of the best structure found at the end of the 65th generation: 1st example.
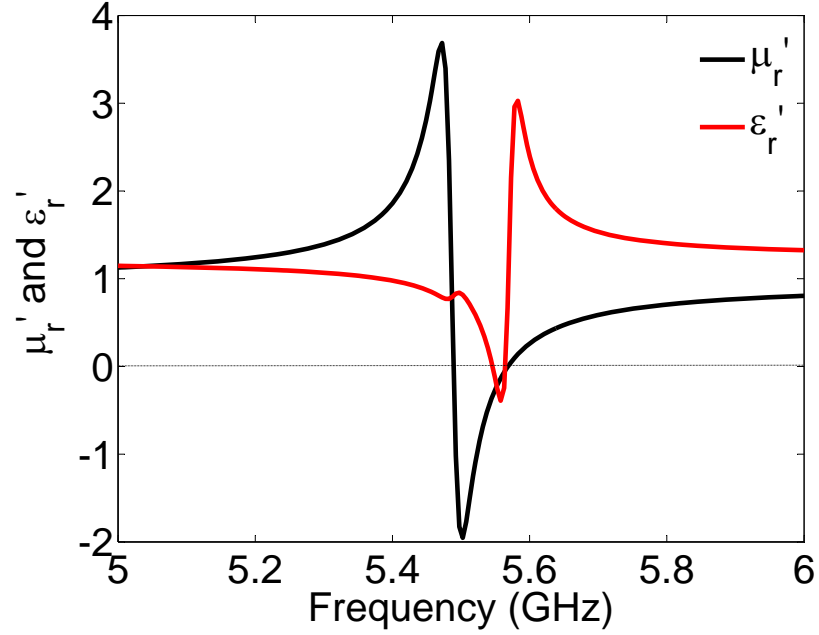
Figure 3.24. Real parts of the relative permeability and permittivity of the best structure found at the end of the 65th generation: 1st example.

Recall that the objective of the optimization is to show that for a given unit cell dimensions it is possible to synthesize several resonant structures that resonate at the same frequency but exhibit different values of μ'_r at the frequency of resonance. Therefore, several plots of μ'_r with respect to frequency are overlapped and shown in Figure 3.25. These plots are created using the best structures at the end of the 4th, 6th, 30th and 65th generations. Screen shots of these structures are shown in Figure 3.26. It can be seen from the overlapping plots that the minimum of μ'_r occurs at the optimized frequency of 5.5 GHz for all the four plots. It can also be seen that the magnitude of μ'_r at 5.5 GHz is different for all the four plots.

Analyses of the intensity of the electric and magnetic fields tangential to the synthesized structures at resonance show characteristics similar to what is observed on SRRs. At resonance, the intensity of the electric field on the SRR surface is more pronounced near the gaps of the rings because of the accumulation of free charge at the location of the gaps. The magnetic field on the other hand tends to be strongest on the side of the rings opposite to the gaps.

The synthesized structures show similar field patterns at resonance. For instance, Figure 3.27 and Figure 3.28 show plots of the intensity of the electric and magnetic fields on the surface of the best structure found at the end of the 65th generation. The intensity of the electric field is strongest at the location of the gaps which are on the right side of the structure while the magnetic field is strongest on the opposite side (left side of the structure).

Although the intensity of the electric and magnetic fields seem to be weaker on the four floating pixels located on the far right side of the structure of Figure 3.27, deleting these pixels affects the resonant frequency and and the magnitude of μ'_r as shown in Figure 3.29.
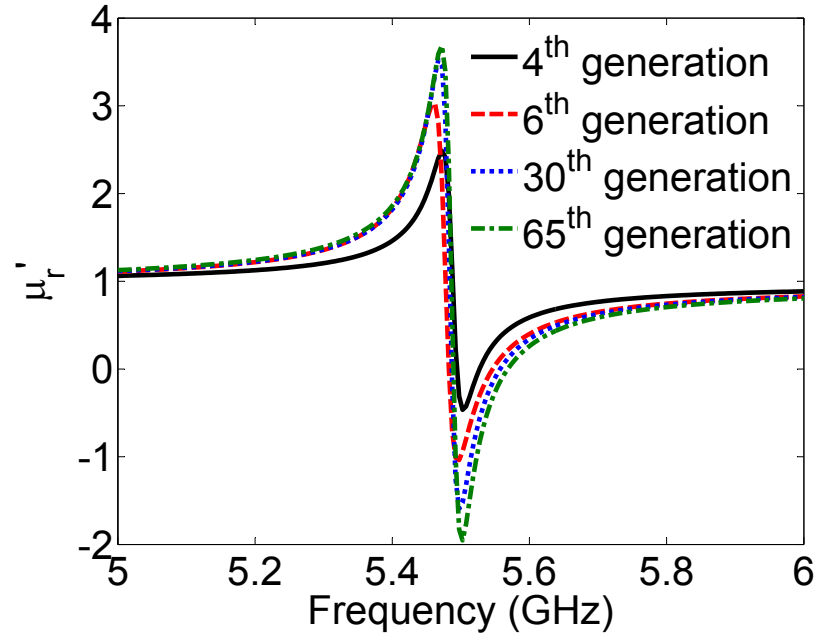
Figure 3.25. Real parts of the relative permeability of the best structures at the end of the 4th, 6th, 30th, and 65th generations: 1st example.

Dielectric **Copper**

(a) **(b)** **(c)** **(d)**
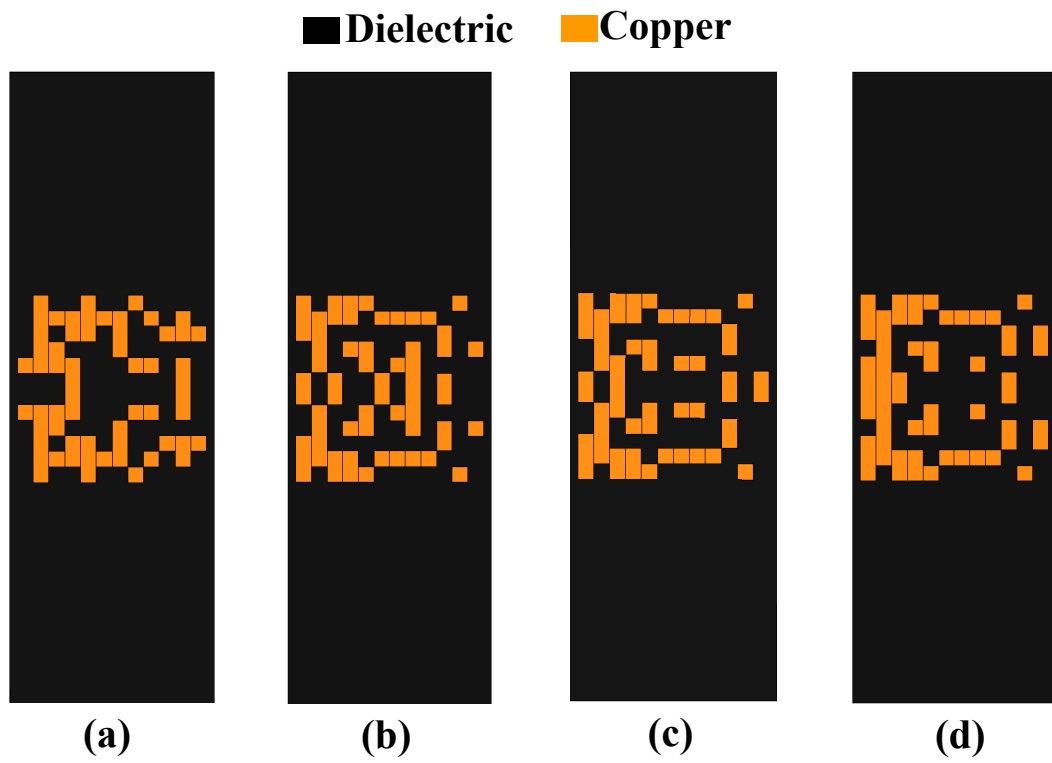
Figure 3.26. Best structures at the end of the 4th (a), 6th (b), 30th (c), and 65th (d) generations: 1st example.
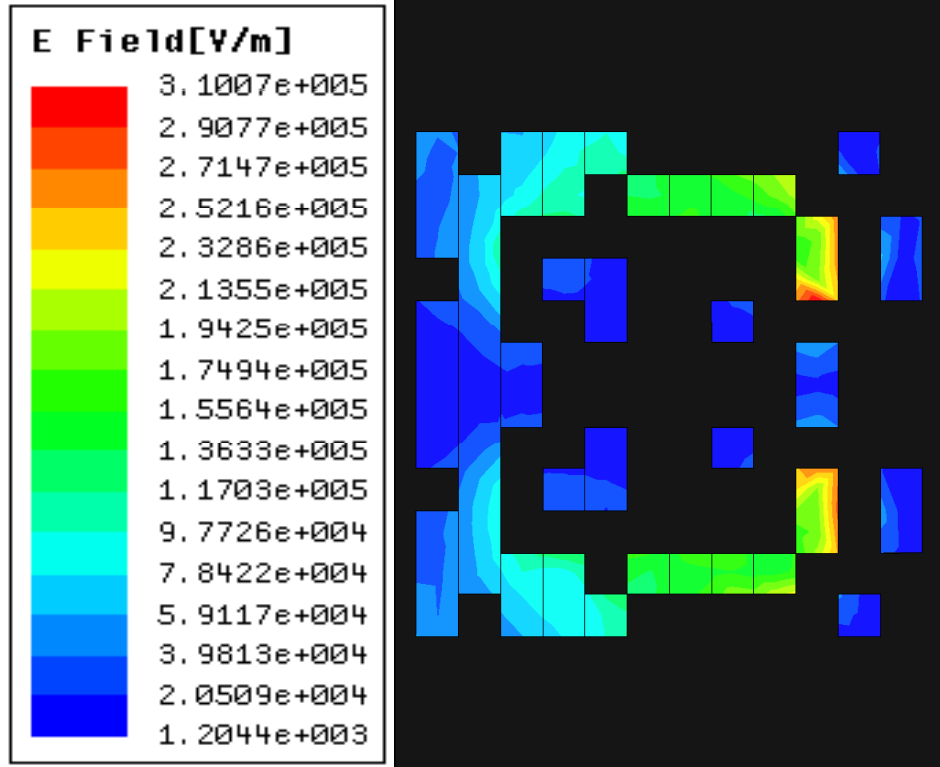
Figure 3.27. Intensity of the electric field tangential to the best structure found at the end of the 65th generation.
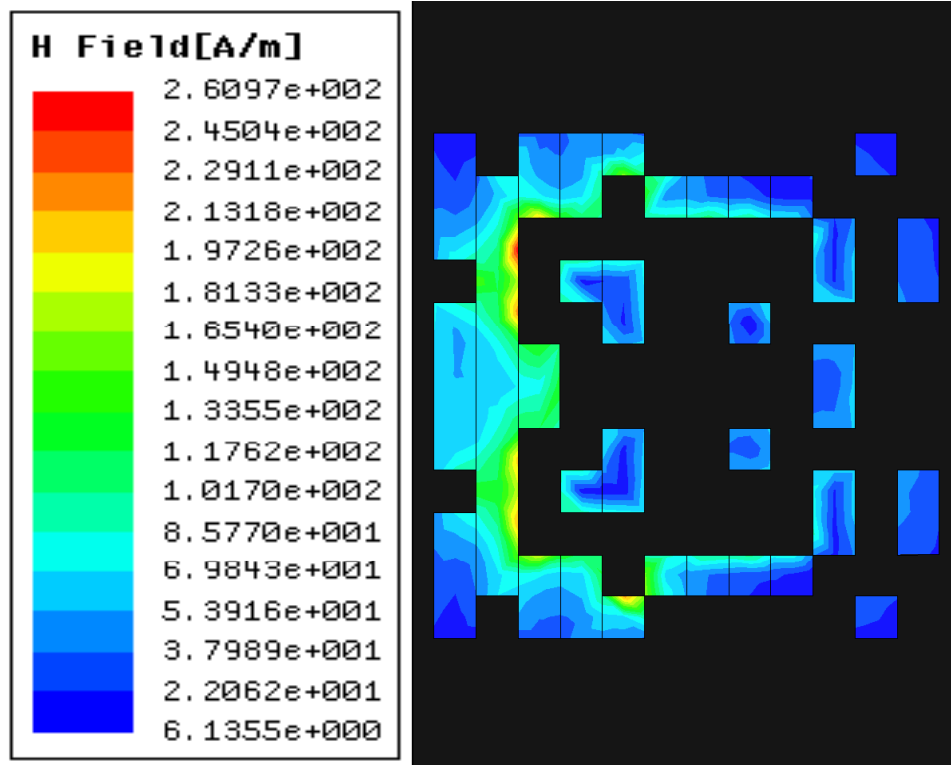
Figure 3.28. Intensity of the magnetic field tangential to the best structure found at the end of the 65th generation.
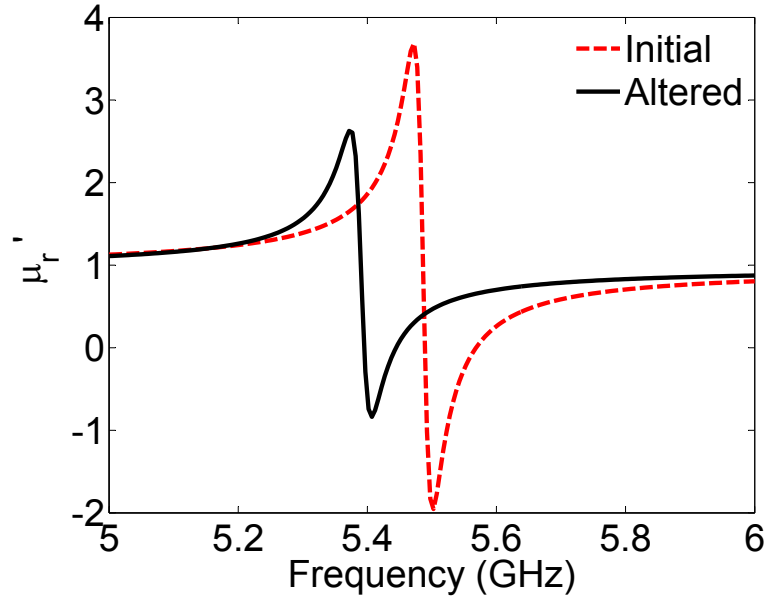
Figure 3.29. Real and imaginary parts of the relative permeability of the best struc-
ture found at the end of the 65th generation: Effect of deleting floating pixels.

The second example investigated is similar to the first example except that the
dimensions of the unit cell are increased from 6 mm by 6 mm to 7.2 mm by 7.2 mm.
The dimensions of the pixels are also increased from 0.5 mm by 0.5 mm to 0.6 mm
by 0.6 mm such that the total number of pixels per sheet is maintained at 144. The
setup of the GA remains identical to the one described in the first example. The
target frequency is 5.5 GHz

A convergence plot showing the best cost found at the end of each generation for
the second example is shown in Figure 3.30. Observe from the figure that the value of
the best cost decreases rapidly from a value of 0.913 at the end of the 1st generation
to -2.074 obtained by the end of the 11th generation. Note also that the best cost

found after just 11 generations in the second example is better than the one obtained after 65 generations in the first example. However, after the 16th generation, the performance of the GA does not improve for 32 generations. The optimization was stopped at the end of the 50th generation with a best cost value of -2.42. A screen shot of the best structure found at the end of the 50th generation is shown in Figure 3.31. Plots of μ'_r and μ''_r as a function of frequency for the best structure are shown in Figure 3.32 where it can be observed that the minimum value of μ'_r is obtained at the desired frequency of 5.5 GHz.

Although the best structure found at the end of the 50th generation in the second example has a better cost than the one at the end of the 65th in the first example, ϵ'_r remains positive throughout the frequency band in the second example as shown in Figure 3.33. This suggests that a stronger resonance of μ'_r does not correlate to a stronger nearby resonance of ϵ'_r. From the convergence plot, it can be assumed that the larger the size of the unit cell, the faster the convergence towards lower values of μ'_r at the optimized frequency.
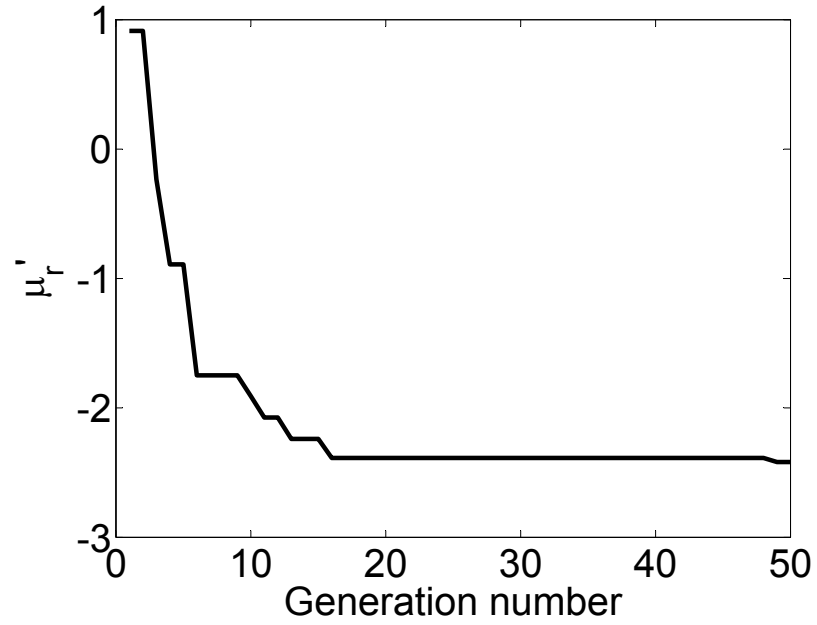
Figure 3.30. Convergence plot showing the best cost at the end of each generation: 2nd example.
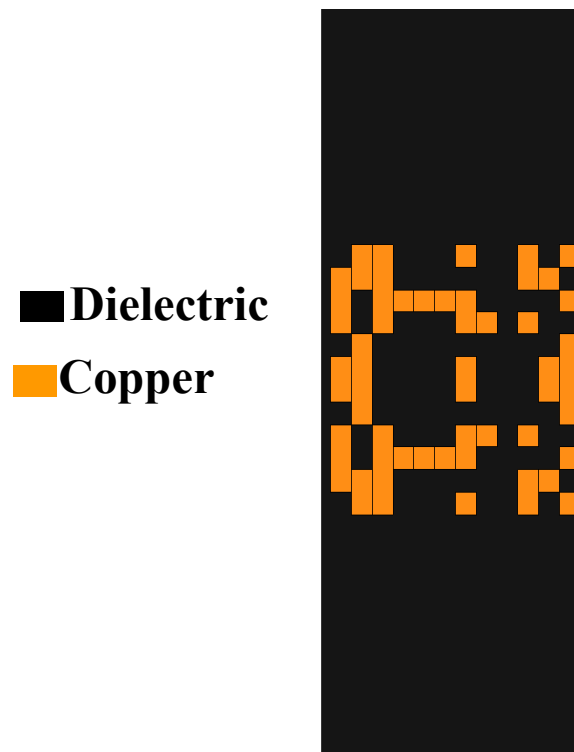
Figure 3.31. Best structures at the end of the 50th generation: 2nd example.
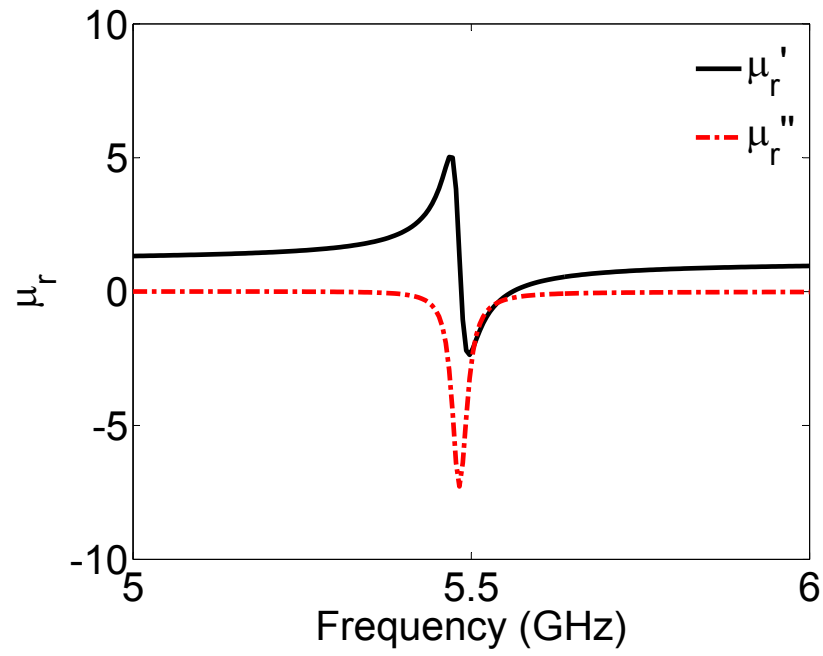
Figure 3.32. Real and imaginary parts of the relative permeability of the best structure found at the end of the 50th generation: 2nd example.
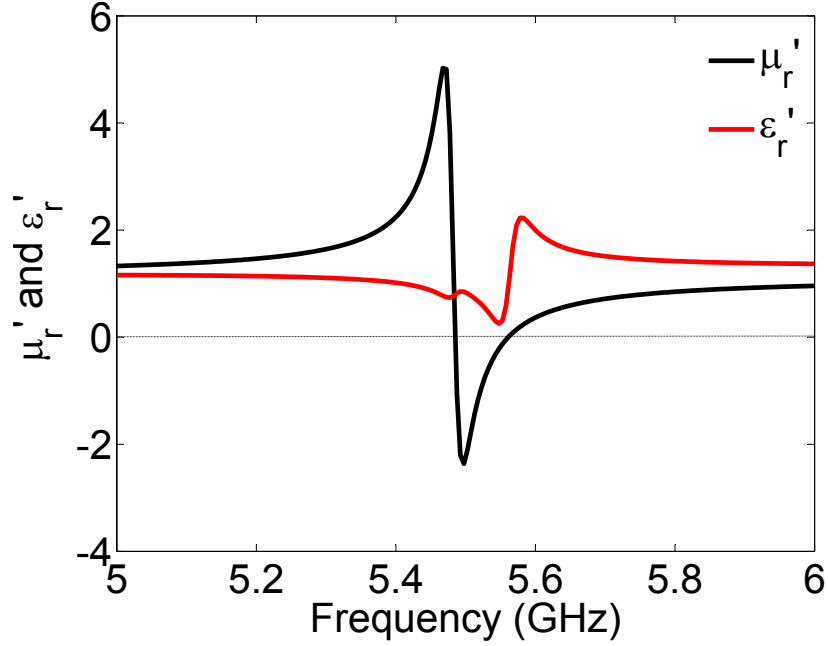
Figure 3.33. Real parts of the relative permeability and permittivity of the best structure found at the end of the 50th generation: 2nd example.

The third example investigated considers a unit cell with dimensions 8 mm by 8 mm. Note that the unit cell dimensions in the third example are larger than the ones used in the previous two examples. Each side of the unit cell is discretized into uniform pixels of dimensions 0.5 mm by 0.5 mm, leading to a total of 256 pixels. The parameters of the GA remain the same as previously described.

A convergence plot showing the best cost at the end of each generation is shown in Figure 3.34. As anticipated, convergence towards negative values of μ_r' is faster in this case compared to the previous cases due to the larger dimensions of the unit cell. At the end of the first generation the best structure found has a cost value of 0.9. This cost value is similar to the best cost values obtained by the end of the first

generation of the previous two examples.

Note from Figure 3.34 that the best cost at the end of the fifth generation in the third example is better than the one obtained by the end of the 65th generation of the first example. It took fifteen generations for the GA in the third example to find a structure with a better cost than the one found at the end of the 50th generation of the second example. The GA was stopped here after 30 generations with a best cost of -3.24. The best structure found at the end of the 30th generation is shown in Figure 3.35. Plots of μ'_r and μ''_r with respect to frequency for the best structure are shown in Figure 3.36. Once again, the minimum value of μ'_r is obtained at the desired frequency of 5.5 GHz.

Similar to the first example, several plots of μ'_r with respect to frequency are overlapped and shown in Figure 3.37. These plots are created using the best structures found at the end of the 5th, 10th, 20th and 30th generations. Once again, it can be seen that the resonances of μ'_r for all four structures occurs at 5.5 GHz with different magnitudes.
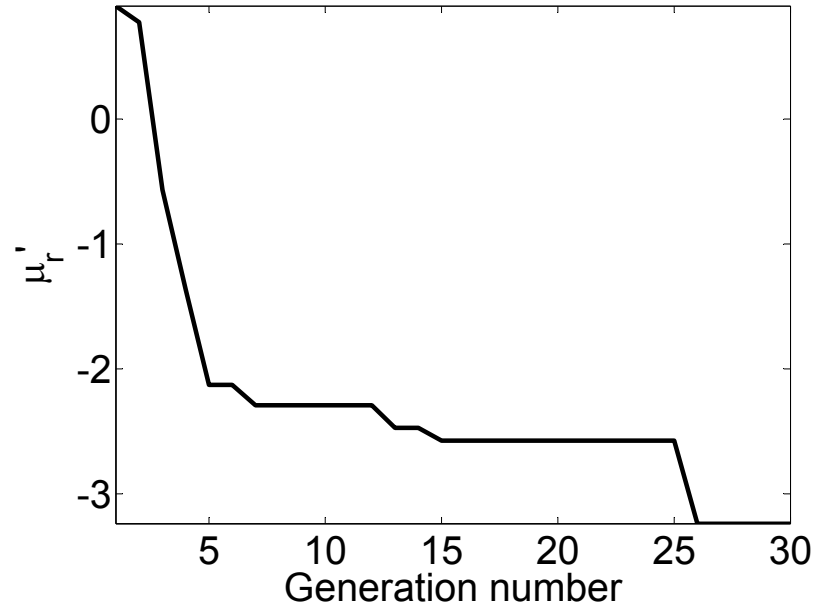
Figure 3.34. Convergence plot showing the best cost at the end of each generation for the third example investigated
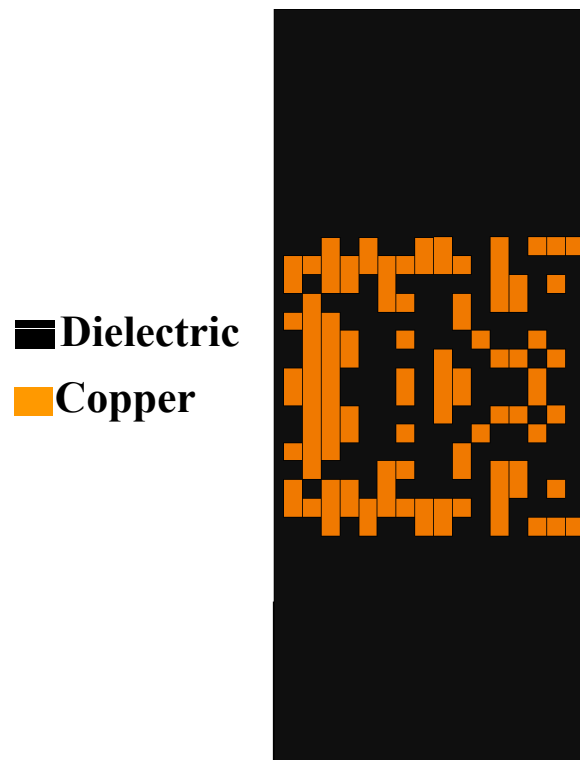
Figure 3.35. Best structure found at the end of the 30th generation: 3rd example.
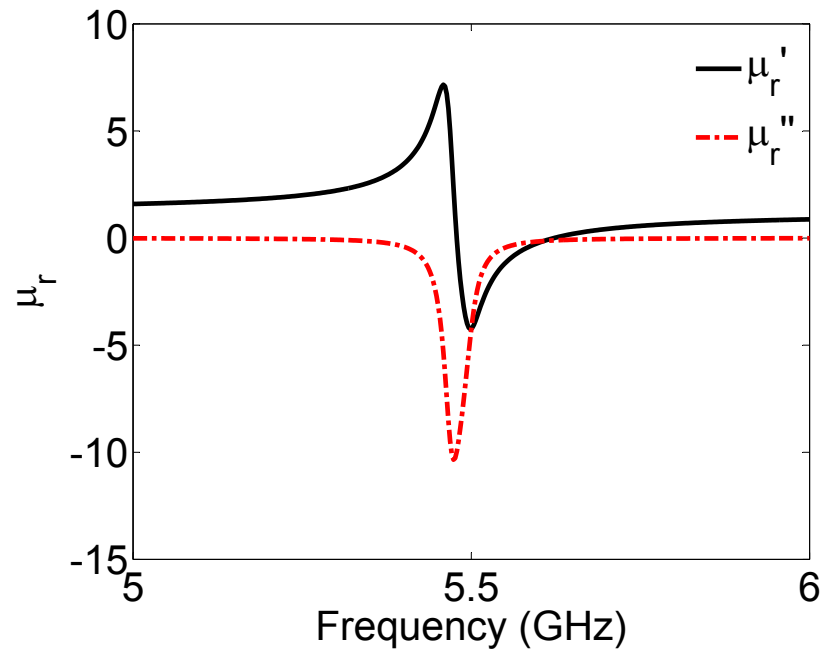
Figure 3.36. Real and imaginary parts of the relative permeability of the best structure found at the end of the 30th generation: 3rd example.
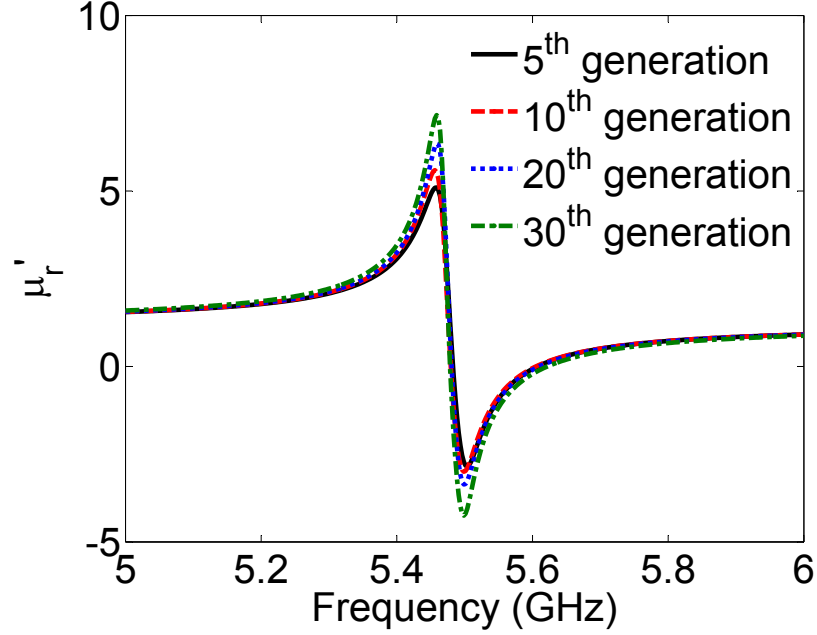
Figure 3.37. Real parts of the relative permeability of the best structures at the end of the 5th, 10th, 20th, and 30th generations: 3rd example.

3.5   Conclusion

In this chapter, a methodology that can be used to synthesize new resonant structures for the design of negative permeability media has been presented. A pixelization approach is combined with a binary search algorithm such as a GA to create new resonant structures quite different from SRRs and with improved flexibility. Using the proposed methodology, it is shown that for prescribed unit cell dimensions it is possible to synthesize multiple structures, all resonating at the same frequency, but with different permeability values.

CHAPTER 4

WAVEGUIDE BAND-STOP FILTER DESIGN USING OPTIMIZED PIXELATED INSERTS

The pixelization approach introduced in Chapter 3 is used in this chapter to create waveguide filters. By optimizing a grid of metallic pixels on a dielectric sheet placed longitudinal to the waveguide axis, compact broadband waveguide filters that are easy to fabricate may be produced. Measured and simulated performance of an F-band waveguide filter show strong rejection in the stopband with a rapid roll off at the band edges, and low insertion loss outside the stopband.

4.1 Motivation

Rectangular waveguides are hollow metallic structures that are used to convey electromagnetic waves. Their ability to carry high power signals along with their broad bandwidth and low loss nature have made them indispensable components in a variety of RF applications. Typical RF applications of rectangular waveguides include satellite communications, radar systems and microwave ovens. Because of the broad bandwidth of rectangular waveguides, it is often necessary to implement a filtering system with high in-band rejection and low out-of-band insertion loss.

Conventional E-plane and H-plane rectangular waveguide filters involve physical alterations of the waveguide structure. For instance, it shown in [73] – [82] that it is possible to create a waveguide filter by placing metallic inserts such as inductive strips or posts vertically inside the waveguide. The presence of the inserts create a

discontinuity that leads to a stopband within the passband of the waveguide. The ability to achieve a wide stopband and a high in-band rejection with a rapid roll-off depend on the arrangement and the number of inserts. Typically, a larger number of inserts produces a wider stopband and a faster roll-off. Physical alterations of the waveguide structure results in complex filters that are several wavelengths long and hard to manufacture.

Rectangular waveguide filters can also be created using resonant type inserts or frequency selective surfaces (FSS) as suggested in [83] – [86]. Given that FSSs can be designed to operate as opaque surfaces near their frequency of resonance, it is possible to create a band-stop filter by inserting an FSS screen normal to the direction of propagation of the wave within the waveguide. The stopband in this case occurs at the frequency of resonance of the FSS. Though easier to implement than altering the physical structure of the waveguide, FSS based filters suffer from a slow roll-off which is undesirable. Increasing the number of FSS screens along the longitudinal direction of the waveguide leads to a faster roll-off and a wider bandwidth but at the cost of increased fabrication complexity and increase length of the waveguide filter, since a typical spacing of $\lambda/4$ is required between inserts.

It has recently been suggested that metamaterials with negative permeability could be used as an alternative means for creating compact waveguide filters [87]. For instance, it is reported in [88] – [90] that it is possible to create a stopband above the cutoff frequency of a rectangular waveguide by loading the waveguide with an array of SRRs. The stopband occurs near the frequency of resonance of the SRRs and the bandwidth of the stopband is inherently that of the SRRs that compose the

filter.

Unfortunately, since SRRs exhibit a narrow bandwidth at resonance, SRR-based filters are limited to applications that require a narrow band of operation. In Chapter 3 it is shown that is is possible to synthesize new resonant structures that can be used in the design of negative permeability metamaterials by optimizing the geometry of a pixelated metallic patch placed longitudinal to the waveguide axis. By employing the in situ optimization technique described in [72] and also presented in Chapter 5, it is possible to design wide-band rectangular waveguide band-stop filters with a specified bandwidth. As an example, a three-element linear array of resonant structures is designed to produce an F-band filter centered at 6 GHz with 500 MHz bandwidth. The resulting rectangular waveguide filter has a compact size of 30 mm corresponding to $\lambda_0/1.6$ at the center frequency of 6 GHz, reasonably sharp band-edges, high reflection within the stopband, and small out-of-band insertion loss.

4.2   Theoretical foundation

The underlying principle behind metamaterial waveguide filters is explained in [87] and [88]. Consider a rectangular waveguide of height a along the y-axis and width b along the x-axis ($a < b$) and filled with a homogeneous biaxial medium described by the dyadics

$$
\overline{\epsilon} = \begin{bmatrix} \epsilon_x & 0 & 0 \\ 0 & \epsilon_y & 0 \\ 0 & 0 & \epsilon_z \end{bmatrix}, \quad \overline{\mu} = \begin{bmatrix} \mu_x & 0 & 0 \\ 0 & \mu_y & 0 \\ 0 & 0 & \mu_z \end{bmatrix}. \tag{4.1}
$$

For a TE mode with the electric field polarized along y, the only nonzero field components are E_y, H_x, and H_z. Consequently, the relevant parameters from (4.1) are ϵ_y, μ_x, and μ_z, and the dispersion relation may be written as

$$\frac{k_x^2}{\epsilon_y \mu_z} + \frac{k_z^2}{\epsilon_y \mu_x} = k_0^2.$$

(4.2)

Here, $k_x = n\pi/b$ is the transverse wave number with n an integer, $k_0 = \omega\sqrt{\mu_0 \epsilon_0}$ is the free space wave number, ω is the frequency with time convention $e^{j\omega t}$. The longitudinal wavenumber, k_z, determines the propagation behavior of the guided wave. A stopband requires a large imaginary value of k_z, and this is achievable in a low-loss guide only when the wave is evanescent. Ordinarily this occurs only at frequencies below cutoff, but the resonance behavior of a metamaterial may be used to introduce evanescence above cutoff.

Equation (4.2) may be rearranged to determine k_z:

$$k_z = \sqrt{\epsilon_y \mu_x \left(k_0^2 - \frac{k_x^2}{\epsilon_y \mu_z} \right)}.$$

(4.3)

The region of evanescence is obviously dependent on the values of ϵ_y, μ_x, and μ_z. Although a typical metamaterial is far from homogeneous, these parameters are useful abstractions because they can be related to the resonant properties of metamaterial inserts, such as SRRs. If an empty guide is loaded using an array of SRRs placed longitudinally (along the z axis), the relevant parameter is μ_x since H_x is the only field component present that will excite a current in the SRRs. The other two parameters,

ϵ_y and μ_z, will be positive and equal to those of the host medium. Assuming lossless inserts as in [87], above the cutoff frequency of the guide the condition $k_0^2 - k_x^2/\epsilon_y\mu_z > 0$ holds, and the wave propagates unattenuated as long as $\mu_x > 0$. However, near the resonant frequencies of the SRRs a negative permeability effect is encountered such that $\mu_x < 0$, and thus k_z becomes imaginary, producing an evanescent wave and creating a stopband.

Unfortunately, SRRs are narrowband and provide little flexibility for designing stopbands with specific bandwidth characteristics. In contrast, it is shown in [72] – [71], and also in Chapter 3 of this dissertation, that metamaterial structures may be designed to have resonances with desired properties using a topology optimization procedure. When these structures are optimized in situ, a metamaterial-inspired filter can be produced with desirable characteristics such as wide bandwidth, sharp band edges, and low out-of-band insertion loss.

4.3 Design procedure

The proposed filter insert consists of a dielectric sheet with copper pixels etched onto one side, placed along the longitudinal axis of a rectangular waveguide as shown in Figure 4.1. The shape of the etched structure begins with a rectangular metal patch that is pixelated using a rectangular grid, as shown in Figure 4.2. The topology of the grid is optimized by turning pixels on (copper) or off (no copper) based on the results of a full-wave simulation tool such as HFSS. The optimization routine is a genetic algorithm written in Matlab and integrated with the simulator as described in Chapter 3. Optimization is done in situ by modeling the waveguide with a three-

element array of pixelated patches inserted into the guide. Note that arrays with more elements can be used to produce sharper band edges, but at the expense of greater length.

The GA is implemented using a single bit mutation with a two point crossover and tournament selection. An initial population of 200 different binary strings are selected randomly with each string representing the encoding of a specific pixelated patch geometry. The geometry of each pixelated patch, along with that of the dielectric sheet and rectangular waveguide, are created in Matlab and exported to HFSS for simulation. The simulated transmission coefficient of the loaded waveguide is exported back to Matlab and the cost of each pixilated patch geometry is evaluated as

$$Cost = \sum_{n=1}^{N} S_n C_n, \qquad (4.4)$$

where

$$S_n = 20 \log_{10} |S_{21}(f_n)|, \qquad (4.5)$$

and

$$C_n = \begin{cases} 1, & S_n > -10 \text{ dB} \\ -10/S_n, & S_n \leq -10 \text{ dB} \end{cases}. \qquad (4.6)$$

Here the transmission coefficient, S_{21}, is computed at $N = 100$ equally-spaced frequencies f_n in the stopband $f_{min} \leq f \leq f_{max}$.

Once the costs of all 200 initial pixelated patch geometries have been evaluated, they are ranked and the top 20% (those with the lowest cost values) are selected for crossover and mutation until a new population of 200 pixelated patch geometries are

created and evaluated. This process is repeated until a cost value of -1000 is obtained (which equates to a transmission coefficient no greater than -10 dB at all frequency points for the example considered below) or until a set maximum number of iterations (typically twenty) is completed.

The key to increasing the bandwidth of the filter lies in (4.6). Formulating the cost function to minimize the sum or the average of the transmission coefficient evaluated at each frequency point as given by

$$Cost = \sum_{n=1}^{N} 20 \log_{10} |S_{21}(fn)|. \tag{4.7}$$

would not guarantee a wide bandwidth. For instance, consider two structures A and B where structure A has a -10 dB bandwidth of 50 MHz while structure B has a -10 dB bandwidth of 70 MHz. If the minimum value of the transmission coefficient of structure A is -50 dB and that of structure B is -15 dB, structure A will be preferred over structure B even though structure B has a wider -10 dB bandwidth. By using (4.6), transmission coefficient values that are lower than -10 dB are assigned a cost of -10. The value -10 is selected here to create a filter with a broad -10 dB bandwidth. If a broad -20 dB bandwidth was the target, then -20 would have be used in (4.6) instead of -10.

The Matlab code used to create the waveguide filters is very similar to the code shown in Appendix C. The main differences lie in the formulation of the cost function and the fact that the structure used in this chapter has three elements. Because of these similarities, the full Matlab code used to create the filters is not provided in this

chapter. Only the Matlab code showing how the cost function is written is provided below.

```matlab
%%%%%%%%%%%%%%%%%%%%%%%%%%%%%%%%%%%%
Fit1=0;

 for np=1:nPoints

    S21(np)=20*log10(abs(S(np, 1, 3)));

    if S21(np)>-10

        Cn=1;

    else

        Cn=-10./S21(np);

    end

    Fit1=Fit1+Cn*S21(np);

 end

 fitness(ip)=Fit1;

 %%%%%%%%%%%%%%%%%%%%%%%%%%%%%%%%%%%%
```

In the Matlab code above, nPoints is the number of frequency points.
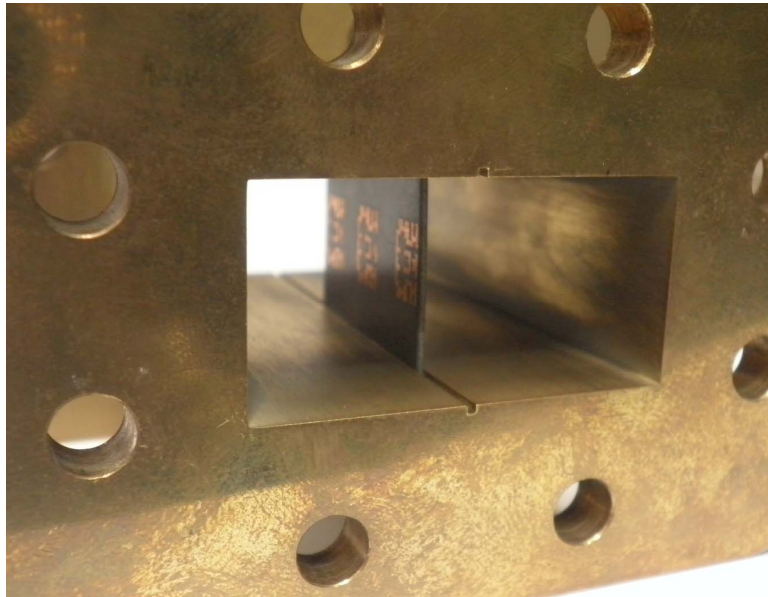
Figure 4.1. Rectangular waveguide with resonant structure inserted along the longitudinal axis.
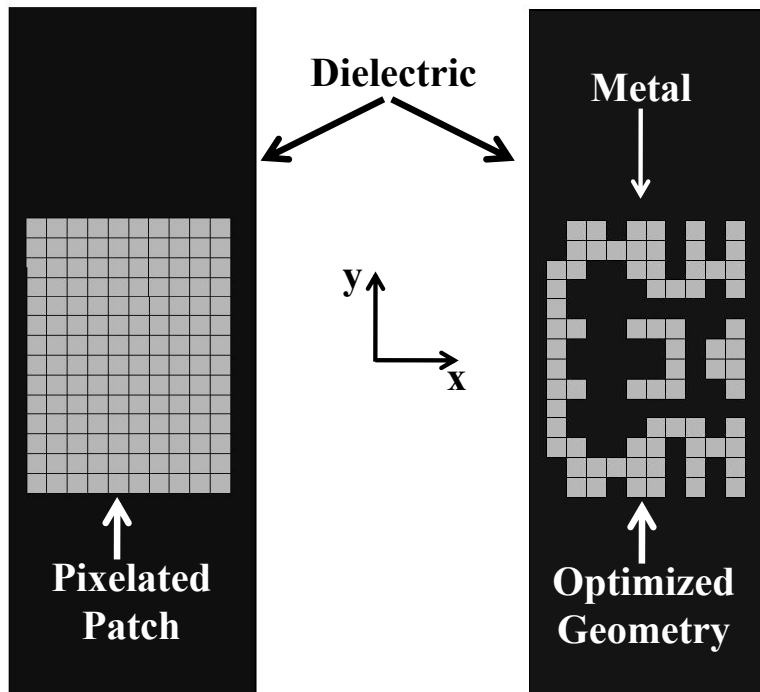
Figure 4.2. Initial pixelated grid and optimized resonant structure.

4.4 Example design and test

The design scheme discussed above was used to create an F-band rectangular waveg-uide filter with the rejection band from $f_{min} = 5.75$ GHz to $f_{max} = 6.25$ GHz. The F-band rectangular waveguide has cross sectional dimensions of 40.4 mm by 20.2 mm and an operational frequency band from 4.9 GHz to 7.05 GHz. The dielectric sheet is a 0.78 mm thick Rogers RT duroid 5870 substrate with dielectric constant $\epsilon_r = 2.33$ and loss tangent $\delta = 0.0012$. A rectangular copper patch of dimensions 6 mm by 8.4 mm was inscribed on one side of the substrate, and discretized into a 10 by 14 grid of square pixels (each pixel is 0.6 mm by 0.6 mm) as shown in Figure 4.2. The patch geometry was cascaded into a three element linear array with an element cen-ter to center spacing of 12 mm such that the total length of the structure is 30 mm corresponding to $\lambda_0/1.6$ at the center frequency of 6 GHz. The GA optimizer was then used to search for pixel arrays that minimize (4.4).

One structure located by the optimizer is that shown in Figure 4.2. The opti-mization was completed within sixteen generations with a transmission coefficient no greater than -10 dB at all desired frequency points (5.75 GHz – 6.25 GHz). The sim-ulated transmission and reflection coefficients for the resulting filter performed over a frequency band from 5 GHz – 7 GHz are shown in Figure 4.3. Note that near perfect transmission of the signal is achieved across the operating band of the waveguide ex-cept within the desired stopband, where $|S_{21}|$ is maintained at less than -18 dB. As expected, the filter also demonstrates near complete reflection ($|S_{11}| \approx 0$ dB) within the stopband due to the low loss of the substrate. Analysis of $|S_{21}|$ outside the op-

timized frequency band shows a wider -10 dB bandwidth of 5.7 GHz – 6.35 GHz. The wider bandwidth is expected since the structure of Figure 4.3 met the stopping criteria of $|S_{21}| \leq -10 \ dB$ for all frequency points within 5.75 GHz – 6.25 GHz. As a result, the minimum -10 dB bandwidth is 5.75 GHz – 6.25 GHz.

Also shown in Figure 4.3 are measured transmission and reflection coefficients for a prototype fabricated through photolithography. The fabricated structure is shown in Figure 4.4, and is also shown installed into the rectangular waveguide in Figure 4.1. Excellent agreement is observed between simulations and measurement, thus validating the feasibility of the proposed filter design procedure.
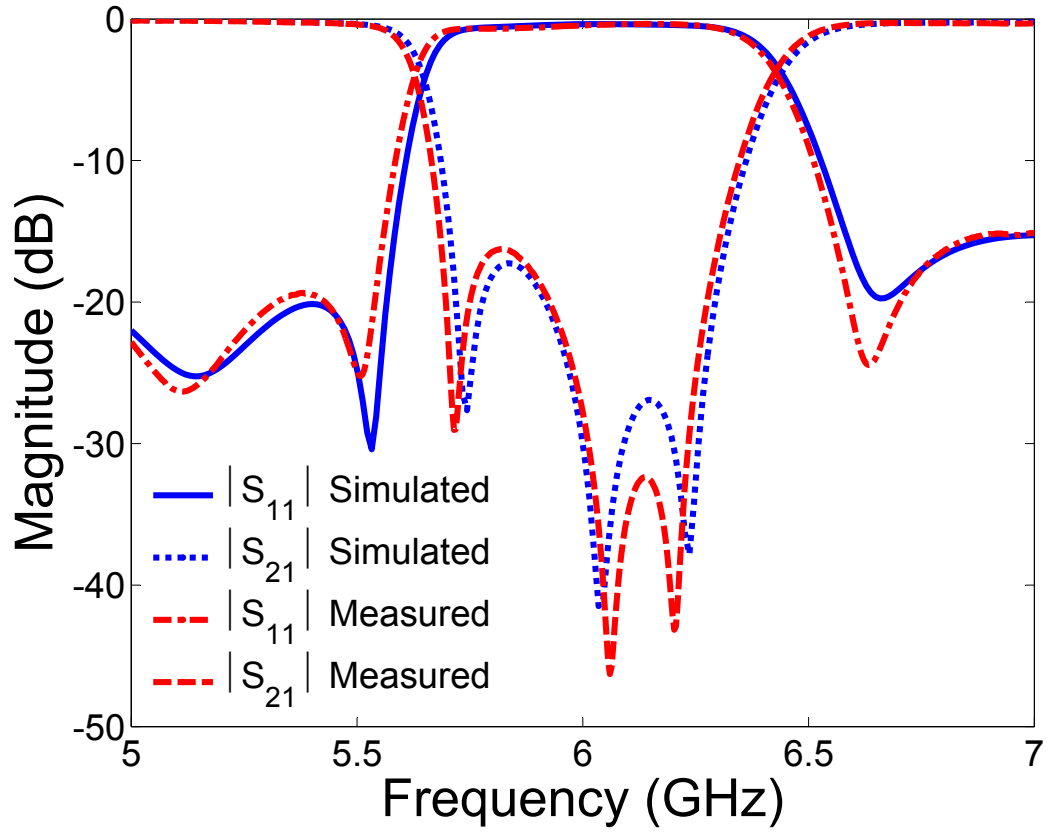
Figure 4.3. Simulated and measured transmission and reflection coefficients of a rectangular waveguide loaded with the prototype resonant structure shown in Figure 4.4.
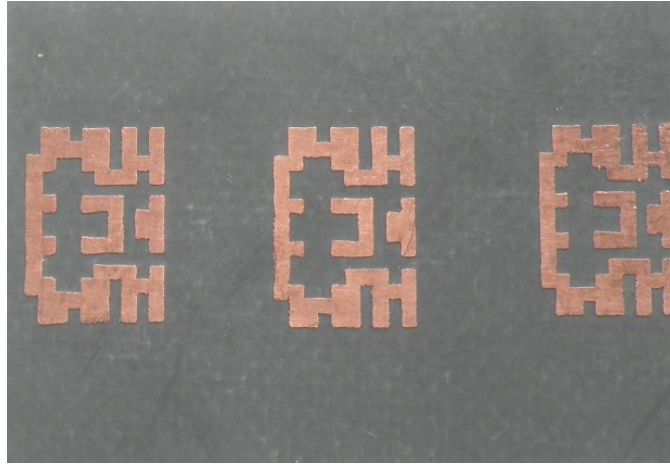
Figure 4.4. Prototype of a three element array fabricated through photolithography.

The performance of a single element of the optimized three element array was investigated both in simulations and measurements. Figure 4.5 shows plots of the transmission and reflection coefficients of the simulated and measured single element of Figure 4.6. Observe from Figure 4.5 that the resonance of the single element occurs around 6 GHz but the -10 dB bandwidth is less than one third that of the three element array. Note how the slope of $|S_{21}|$ at the edges of the band is much higher in Figure 4.3 for the three element array compared to Figure 4.5 for the single element. A filter with band edges sharper than those of Figure 4.3 can be created by increasing the number of elements beyond three but at the expense of an increased length of the filter. It might be possible to reformulate the cost function to optimize for sharper band edges as well, but this has not yet been investigated .
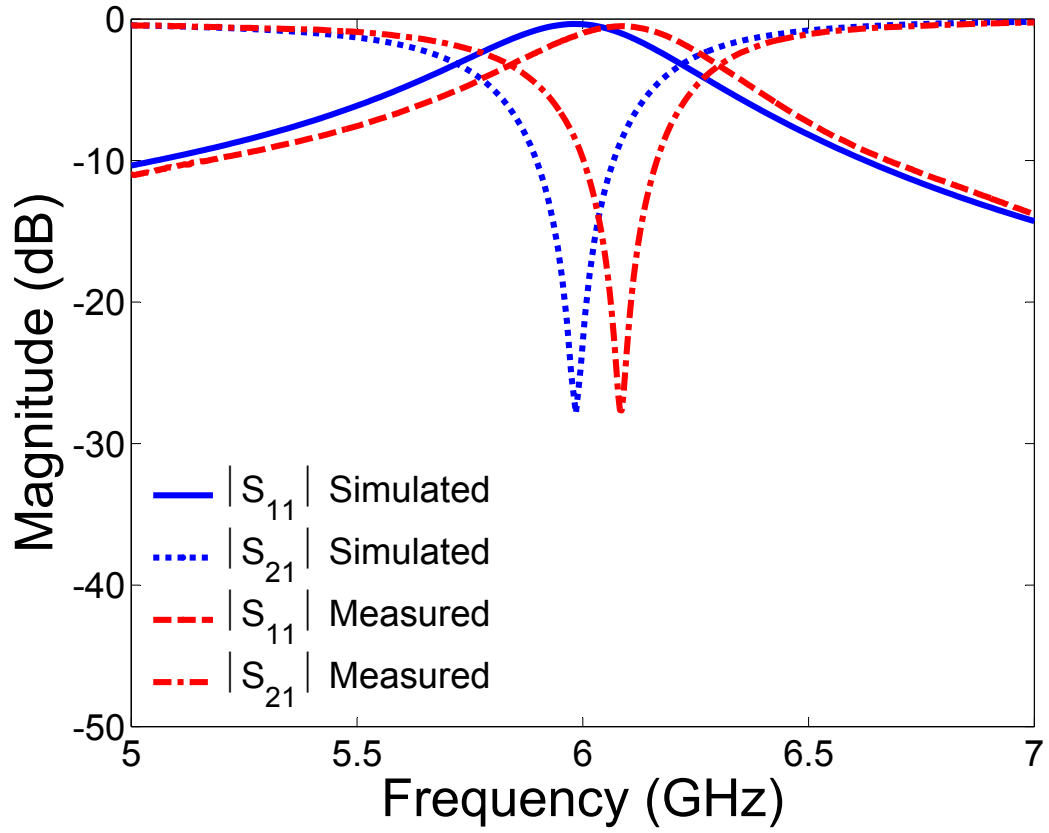
Figure 4.5. Simulated and measured transmission and reflection coefficients of a rectangular waveguide loaded with the prototype resonant structure shown in Figure 4.6.

Figure 4.6. Prototype of a single element fabricated through photolithography.

4.5 Conclusions

The pixelization approach introduced in Chapter 3 is used here to create rectangular waveguide filters. The design is easy to implement and leads to small broadband filters that are easy to fabricate and at a low cost. Both simulations and measurements of the filters demonstrate strong rejection of the transmitted signal within the stopband, with high insertion loss and sharp band edges. The next chapter demonstrates how the in situ design technique and the pixelization approach can be combined to create miniaturized planar loop and monopole antennas suitable for integrated applications.

CHAPTER 5

IN SITU OPTIMIZATION OF METAMATERIAL-INSPIRED ANTENNAS

In this chapter, an in situ optimization technique is combined with the pixelization approach presented in Chapter 3 to create miniaturized metamaterial-inspired monopole and loop antennas. Antenna miniaturization is demonstrated through two design examples. In the first example, a loop antenna initially resonant at 4.8 GHz is made resonant at 0.96 GHz by optimizing the geometry of a pixelated area adjacent to the loop, thus providing an 80% downward shift of the resonant frequency. In the second example, the in situ optimization technique is used to create an ultra compact folded monopole antenna that fits into a hemisphere of radius 5.73 mm, which is approximately $\lambda_0/29$ at the resonance frequency of 1.8 GHz, making the antenna ideal for integrated device and on-chip applications.

5.1 Introduction: metamaterial-inspired antennas

An electrically small antenna is defined as an antenna that can be contained within a sphere of radius a such that $ka \leq 0.5$, where k is the free space wavenumber ($k = 2\pi/\lambda_0$). Considering a loop antenna for instance, the first natural resonance of the loop occurs when the circumference of the loop is $2\pi a \approx \lambda_0/2$. This corresponds to $a \approx \lambda_0/12.5$ or $ka \approx 0.5$. Although the loop can be considered as electrically small, its radius remains too large for applications such as cellular phones. As the radius

of the loop is made smaller, assuming the frequency of resonance remains fix such that $ka < 0.5$, the self capacitance of the loop decreases and the loop becomes highly inductive [22]. To maintain an impedance match in this case, lumped components such as capacitors have to be used.

An alternative approach to maintain a good impedance match for $ka < 0.5$ is to use artificial materials. For instance, it is shown in [45] and [40] that by incorporating homogeneous metamaterials into the structures of antennas (creating "metamaterial-based antennas"), various properties such as size, gain, and impedance may be dramatically improved. Similar results can also be achieved by loading the antenna with one or more metallic inclusions such as SRRs. These antennas are referred to as "metamaterial-inspired" since the design of the inclusions is based on their performance as a unit cell within a metamaterial [41] - [46].

The resonance behavior of the unit cell, which produces a negative permeability when used to compose a metamaterial, is utilized to alter the resonance behavior (particularly the resonant frequency) of the metamaterial-inspired antenna through coupling between the structures. When a metamaterial unit cell is placed adjacent to an antenna, mutual coupling causes the resonance frequency of the system to shift away from the resonance frequency of the unloaded antenna and also away from that of the unit cell. However, experience shows that a resonance of the metamaterial-inspired antenna often occurs near that of the metamaterial comprising arrays of the same unit cell, which is generally much lower than that of the isolated antenna. It is this effect that provides for the miniaturization properties of metamaterial-inspired antennas.

Unfortunately, it is difficult to predict the precise shift in resonance frequency produced by a particular inclusion, and design thus becomes trial and error. Also, the resulting metamaterial-inspired antenna might not meet the performance criteria of the original antenna, and additional tuning thus becomes necessary to achieve the desired properties.

In this chapter, the in situ optimization technique and the pixelization approach are used to demonstrate that it is possible to achieve a good impedance match for a monopole or loop antenna with $ka < 0.5$ by synthesizing a resonant structure adjacent to the antenna. By designing the resonant structure in place, the performance of the metamaterial-inspired antenna is directly optimized without separate consideration of the isolated antenna or unit cell.

5.2 Example 1: loop antenna miniaturization

It is reported in [47] that by properly arranging an array of SRRs in the plane of a small loop antenna, a layer of MNG metamaterial can be created around the loop to provide an impedance match to the antenna. The array of SRRs is excited by the near-zone magnetic field components H_θ and H_r of the loop antenna which is in the x-y plane. From [22], the near-zone magnetic field components of a circular loop are given as

$$H_r \approx \frac{a^2 I_0 \exp^{-jkr}}{2r^3} \cos\theta \qquad (5.1)$$

$$H_\theta \approx \frac{a^2 I_0 \exp^{-jkr}}{4r^3} \sin\theta \qquad (5.2)$$

where I_O is the current on the loop and a is the radius of the loop. In the plane of the

loop antenna where $\theta = 90^O$, H_θ reaches it maximum while H_r is at its minimum.

It is established in Chapter 3 that SRRs are excited when placed in an environment

where the magnetic field is aligned along their axes. Thus, to properly excite the

SRRs in this particular case, they have to be placed in the plane of the loop as shown

in Figure 5.1.
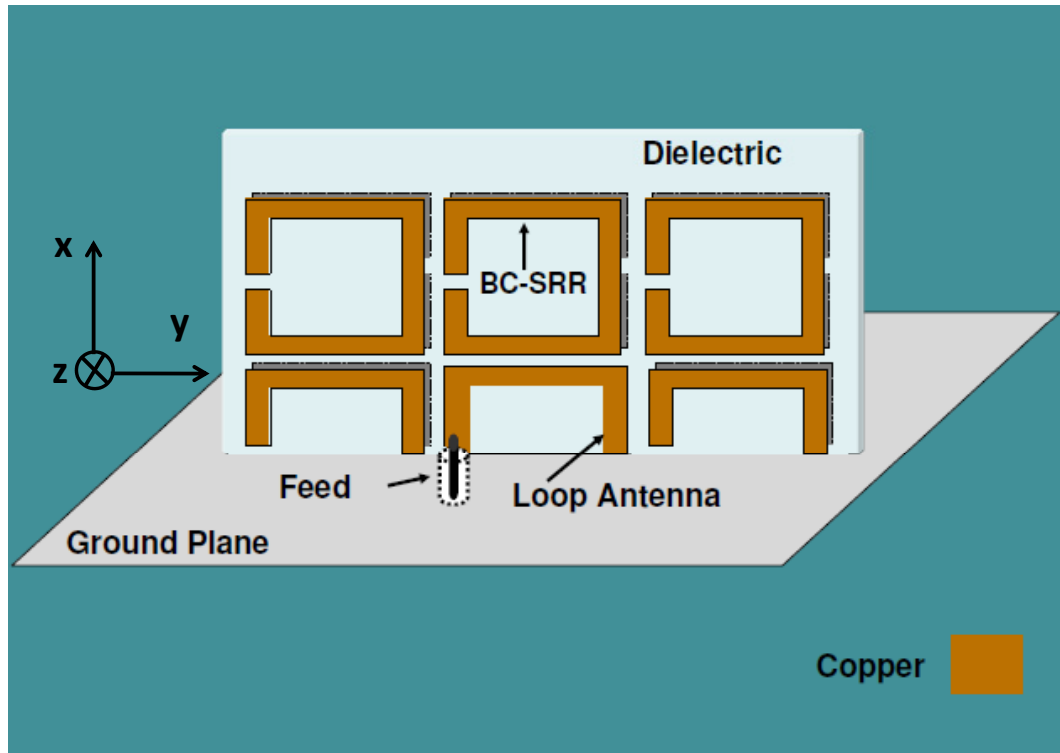
Figure 5.1. Loop antenna surrounded by an array of SRRs.

The dimensions of the small loop antenna reported in [47] are 11.4 mm by 5.7 mm and the frequency of resonance of the antenna without the array of SRRs is around 7.25 GHz. The dimensions of the SRRs were selected to be 10 mm by 10 mm with a separation between elements of 1 mm (edge to edge) such that the negative permeability resonance occurs at 2 GHz. When the small loop antenna is loaded with the array of SRRs, the resonance of the antenna shifts from 7.25 GHz to 2.08 GHz. Although this downward frequency shift confirms that loading a loop antenna with SRRs leads to significant size reduction of the loop antenna, the overall dimensions of the entire structure consisting of the loop loaded with SRRs are 32 mm by 16 mm, or $\lambda_0/4.68$ by $\lambda_0/9.37$.

Given that a loop antenna with dimensions of 32 mm by 16 mm is resonant around 2.4 GHz, it can be concluded that no significant size reduction is achieved in [47]. However, the main goal of the work reported in [47] is to show that an array of SRRs can be used as a MNG layer to significantly lower the frequency of resonance of the enclosed loop. By using different types of resonant structures or a different arrangement of the resonant structures, it might be possible to reduce the size of the overall structure while still being able to achieve a significant downward shift of the frequency of resonance of the antenna.

In [72], it is reported that a small loop antenna initially resonant at 4.8 GHz can be made resonant at 0.96 GHz by synthesizing a single resonant structure adjacent to the loop, creating a metamaterial-inspired loop antenna. It is also reported in [72] that a loop antenna with the same dimensions as the metamaterial-inspired loop antenna is resonant at 2.4 GHz, and the area of the loop would have to be increased by

a factor of seven in order to lower the frequency of resonance to 0.96 GHz. The work presented in [72] is reproduced in this section with permission and a letter granting permission to reuse the content of [72] is shown in Appendix D.

5.2.1 Design procedure

The geometry of a single pixelated unit cell is optimized in close proximity to a loop antenna to produce an impedance match at a frequency well below the initial resonance frequency of the loop. The unit cell is a double-sided symmetrically pixelated structure that has the symmetry of Figure 5.2. The front of the cell is first created using left-right symmetry. The front is then flipped top to bottom to create the back side of the cell.

The optimization procedure is based on the integration of a full-wave solver (HFSS) with a proprietary GA written in Matlab. The geometries of the combined pixelated cell and loop antenna are created in Matlab and exported to HFSS for simulation. The reflection coefficient of the simulated structure is exported back to Matlab for post-processing and optimization. The goal of the optimization is to determine a metalization geometry that produces an acceptable impedance match for the metamaterial-inspired loop antenna at a specific frequency. Since the cell is parameterized as a pixelated grid, its electrical characteristics can be altered by turning each pixel "ON" (copper) or "OFF" (no copper).
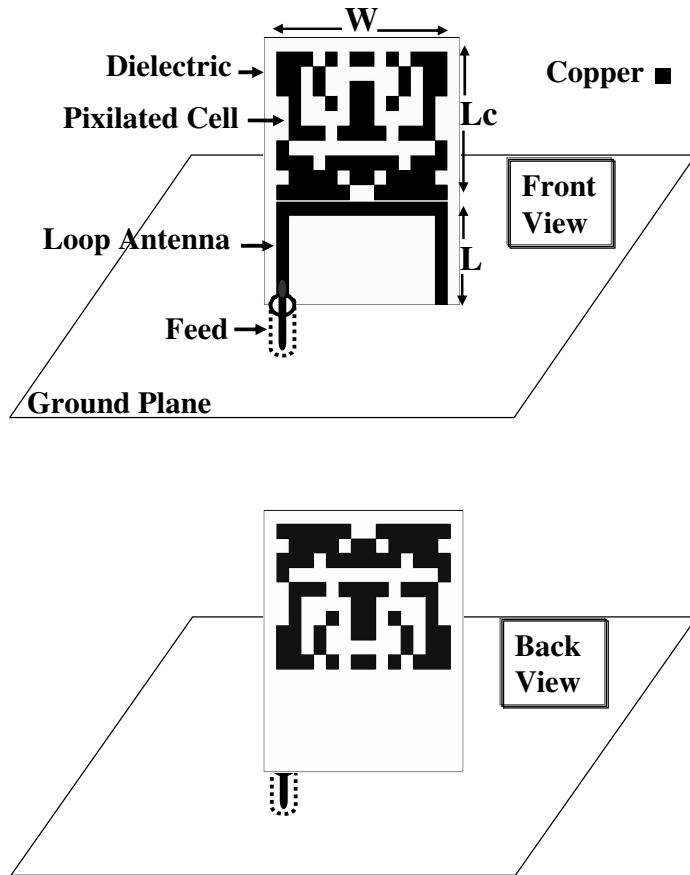
Figure 5.2. Optimized pixelated structure in close proximity to a loop antenna over a ground plane.

For given cell dimensions, the number of unknowns and the number of possible geometries (pixel combinations) are determined by the pixelization of the unit cell. In this example, a cell with a total of 140 pixels on each side of the substrate is used. Because of the assumed left-right symmetry, 140 pixels lead to a total of 2^{70}, or over

10^{21}, possible solutions. Thus, an efficient binary search algorithm such as a GA is needed to quickly find a pixel combination that produces an acceptable impedance match.

5.2.2 HFSS analysis

The analysis is performed in HFSS on the computational domain Ω, which is a radiating box containing the monopole, the feed, the ground plane, and the pixelated cell, as shown in Figure 5.3.
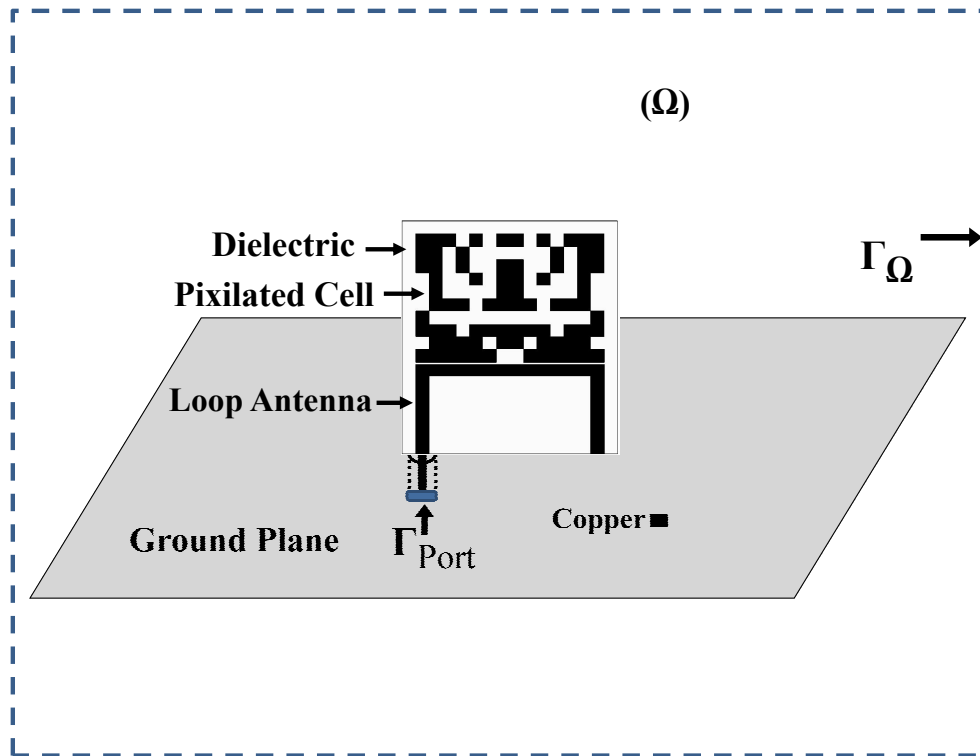
Figure 5.3. Radiating box containing the metamaterial-inspired antenna.

The vector Helmholtz equation is solved for the electric field $\mathbf{E}$ using the finite element method with tetrahedral elements. The vector Helmholtz equation is written as

$$\nabla \times (\frac{1}{\mu_r}\nabla \times \mathbf{E}) - k_0^2(\epsilon_r - \frac{j\sigma}{\omega\epsilon_0})\mathbf{E} = \mathbf{0} \quad \text{in} \quad (\Omega) \tag{5.3}$$

where μ_r and ϵ_r are the relative permeability and dielectric constant respectively, k_0 and ϵ_0 are vacuum wavenumber and vacuum permittivity, ω is the angular frequency and σ is the electrical conductivity. At the surface of the radiating box Γ_Ω, the scattering boundary condition

$$\mathbf{n} \times (\nabla \times \mathbf{E}) - (jk + \frac{1}{r})\mathbf{n} \times (\mathbf{E} \times \mathbf{n}) = \mathbf{0} \quad \text{at} \quad \Gamma_\Omega \tag{5.4}$$

is applied. Here the wave number is k and the position vector is $\mathbf{r} = x\hat{\mathbf{x}} + y\hat{\mathbf{y}} + z\hat{\mathbf{z}}$ with length $r = |\mathbf{r}|$. An incident electric field $\mathbf{E}_{inc}$ is applied at the input boundary of the feed, Γ_{port}, and the reflection coefficient is evaluated as

$$S_{11} = \frac{\int_{\Gamma_{port}} (\mathbf{E} - \mathbf{E}_{inc}) \cdot \mathbf{E}_{inc}^* d\Gamma}{\int_{\Gamma_{port}} \mathbf{E}_{inc} \cdot \mathbf{E}_{inc}^* d\Gamma}. \tag{5.5}$$

The radiation efficiency of the antenna is calculated as

$$\eta_{rad} = \frac{P_{rad}}{P_{acc}}. \tag{5.6}$$

The radiated power P_{rad} can be approximated if the radius of the radiating box extends to the farfield as

$$P_{rad} = \frac{\int_{\Gamma_\Omega} \|\mathbf{E}\|^2 d\Gamma}{\eta_o} \tag{5.7}$$

where η_o is the free space intrinsic impedance. The accepted power P_{acc} is

$$P_{acc} = P_{in} \left(1 - |S_{11}|^2\right) \tag{5.8}$$

where P_{in} is the input power.

The farfield of an antenna is the region for which

$$r \geq 2\frac{D^2}{\lambda_0} \tag{5.9}$$

where D is the maximum dimension of the antenna. In all the examples discussed in this dissertation, the dimensions of the radiation box are selected such that the sides of the box are at least $\lambda_0/2$ away from the edges of the structure.

5.2.3 GA optimization

The GA is configured for tournament selection with a two point crossover and self evolving mutation probability. An initial population of 160 different pixel combinations is selected randomly. For each pixel combination, an equivalent geometry is generated in Matlab and exported to HFSS for simulation. Once the HFSS simulation is completed, the complex reflection coefficient is exported from HFSS back to

Matlab and the corresponding cost is evaluated using the cost function

$$cost = 20 \log_{10}(|S_{11}|) \ dB. \tag{5.10}$$

Here S_{11} is the complex reflection coefficient exported from HFSS. Minimizing the cost function is thus equivalent to minimizing the magnitude of the reflection coefficient, which translates to an improved impedance match. Once all initial geometries have been simulated and their costs evaluated and ranked, the best 25% are selected for mutation and crossover until a new population of 160 pixel combinations is generated and evaluated. This process is repeated until a cost value of -20 dB or lower is obtained or the maximum number of generations (set to 100 in this example) is reached. When the optimization is performed on a 3-GHz desktop computer with 3 Gb of RAM, each iteration (HFSS simulation and fitness evaluation) requires approximately 60 seconds.

5.2.4   Results

In this section, the miniaturization of a loop antenna is demonstrated by optimizing a pixelated cell in close proximity to the loop. A planar loop antenna of width W = 22.4 mm, length L = 5.3 mm and strip width 1.6 mm was designed using a 0.78 mm thick Rogers 5880 RT/duroid substrate with dielectric constant ϵ_r = 2.2 and loss tangent δ_t = 0.0009. The pixelated cell was selected to have a width W = 22.4 mm, a length Lc = 16 mm and parameterized as a pixelated grid with 140 square pixels on each side of the substrate. Each pixel is 1.6 mm by 1.6 mm. The

gap between the edge of the cell and the edge of the loop antenna is 0.2 mm and a coaxial probe is used to feed the loop as shown in Figure 5.2. The coaxial probe is modeled as an SMA connector with an outer conductor, an inner conductor, and a teflon material with $\epsilon_r = 2.1$ providing support for the inner conductor. The outer conductor is a hollow cylindrical tube of inner radius 2.4 mm and outer radius 2.6 mm. The teflon is also a hollow tube of inner radius 0.635 mm and outer radius 2.4 mm. The inner conductor is a cylinder of radius 0.635 mm. The overall dimensions of the metamaterial-inspired antenna are 22.4 mm by 21.5 mm and the antenna can be contained in a sphere of radius $a = 13.6$ mm or $(a = \lambda_0/22.9)$ leading to $ka = 0.27$.

For comparison, a loop of the same dimensions is simulated using the same dielectric properties, and a plot of its reflection coefficient is shown in Figure 5.4. From this figure, it can be seen that the loop with the same dimensions as the metamaterial-inspired antenna has its fundamental resonance occurring around 2.4 GHz. Also shown in Figure 5.4 is the reflection coefficient of the small loop antenna of dimensions 22.4 mm by 5.3 mm. Observe from the figure that the small loop is resonant at 4.8 GHz and is not well matched at resonance with a reflection coefficient of -8.5 dB. By optimizing the pixelated grid adjacent to the small loop antenna, the goal is therefore not only to achieve a downward frequency shift, but also improve the impedance match. The optimization was performed to shift the frequency of resonance of the small loop to 0.96 GHz.
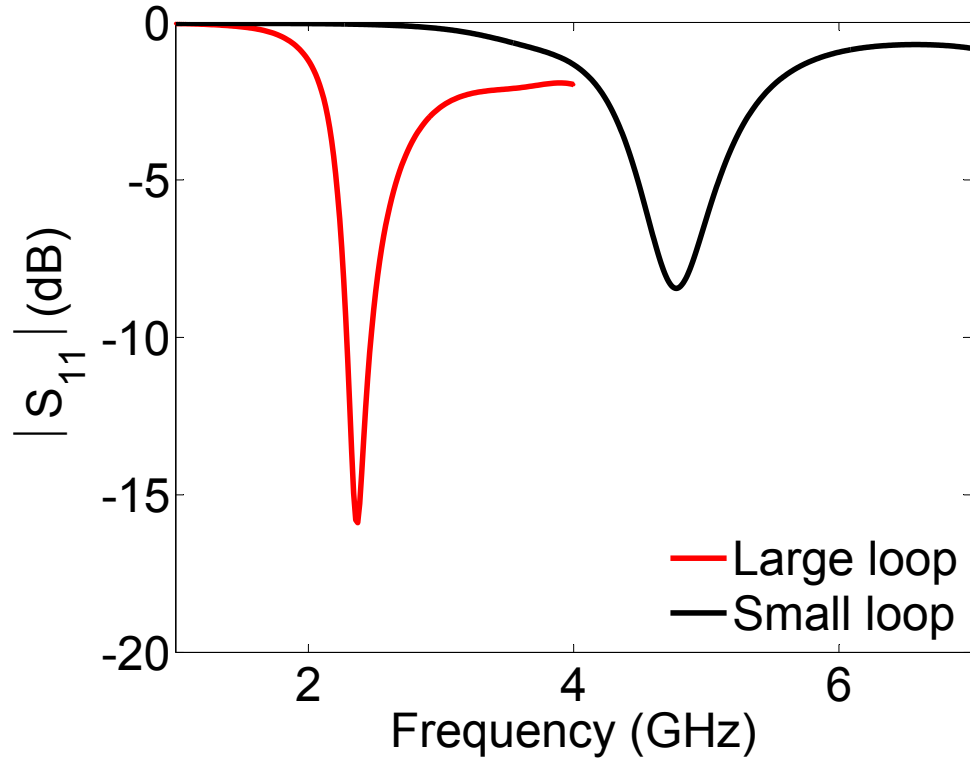
Figure 5.4. Simulated reflection coefficients of the small loop and a large loop which has the same dimensions as the metamaterial-inspired antenna.

Using the design methodology discussed above, a reflection coefficient of -29 dB at 0.96 GHz was obtained in twelve generations, corresponding to a total of 1600 cost evaluations and a total run time of approximately 26 hours. At the end of the twelfth generation, six different structures had costs less than -20 dB at 0.96 GHz and over 60% of the population had a cost less than -10 dB, attesting to the good performance of the present design methodology. The structure with the lowest cost of -29 dB is shown in Figure 5.2, and a plot of its reflection coefficient as a function of frequency is shown in Figure 5.5. It can be seen from the reflection coefficient plot

that the optimized metamaterial-inspired antenna has a narrow -10 dB bandwidth of 0.6%. Such low bandwidth can be useful in wireless communication when used at the receiving end because it is less prone to intermadulation noise [67]. A radiation efficiency of 37.5% and a peak directivity of 5.27 dB were obtained for the structure of Figure 5.2.

Though the radiation efficiency of the conventional loop antenna is 2.5 times that of the metamaterial-inspired antenna, the overall dimensions of the metamaterial-inspired antenna are 22.4 mm by 21.5 mm, which is seven times smaller than the loop antenna. Additionally, the reflection coefficient of the loop antenna at 0.96 GHz is -0.02 dB. Even if the loop had a radiation efficiency of 100%, the radiatate power would be close to 0 since almost all the input power is reflected at the feed. It should be mentioned that the metamaterial-inspired antenna was optimized for the lowest reflection coefficient only, which does not guarantee that the unit cell geometry with the lowest reflection coefficient also has the highest efficiency. For instance, it was observed that some geometries with a reflection coefficient less than -20 dB produced efficiencies as high as 44%. Therefore, performing an optimization where both reflection coefficient and efficiency are considered should lead to designs with improved results.

Plots of the simulated E-plane and H-plane realized gain patterns of the metamaterial-inspired antenna are shown in Figure 5.6 and Figure 5.7. Both the E-plane and H-plane patterns are nearly identical to the patterns of a typical small loop antenna, showing that the field patterns are not significantly altered by the presence of the metamaterial.

A prototype of the metamaterial-inspired antenna shown in the inset in Figure 5.5 was fabricated through photolithography using a Rogers 5880 duroid substrate with the same properties and dimensions as those used in the simulation. The measured reflection coefficient is shown in Figure 5.5 along with the simulated reflection coefficient. A comparison of the two plots shows a very good match between simulation and measurement. Figure 5.6 and Figure 5.7 show the measured E-plane and H-plane patterns of the prototype metamaterial-inspired antenna. A good match is seen in Figure 5.6 between the simulated and measured E-plane pattern. The measured H-plane pattern shown in Figure 5.7 is slightly different from the simulated H-plane realized gain pattern, possibly due to fabrication errors leading to a prototype with properties that are slightly different from the simulated metamaterial-inspired antenna.

It was mentioned in Section 5.1 that if an SRR is placed adjacent to an antenna to create a metamaterial-inspired antenna, the resonance of the metamaterial-inspired antenna will be different from the resonance of the isolated SRR. This statement was verified by simulating the pixelated unit cell of Figure 5.2 in a WR1000 waveguide using HFSS. The WR1000 has a width of 253.3 mm and a height of 123.8 mm. The operation frequency band of the WR1000 waveguide is 0.75 GHz to 1.1 GHz.

The material parameter extraction technique was used to obtained the real and imaginary values of the relative permeability as a function of frequency. These are shown in Figure 5.8. It can be seen that the μ-resonance of the isolated pixelated cell occurs at 0.94 GHz while the resonance of the metamaterial-inspired antenna occurs at 0.96 GHz. The difference between the resonance frequency of the isolated

pixelated cell and that of the metamaterial-inspired antenna is mainly due to the mutual coupling between the two structures. The proposed in situ optimization technique accounts for the coupling effects, leading to an optimized metamaterial-inspired antenna with the desired performance criteria.
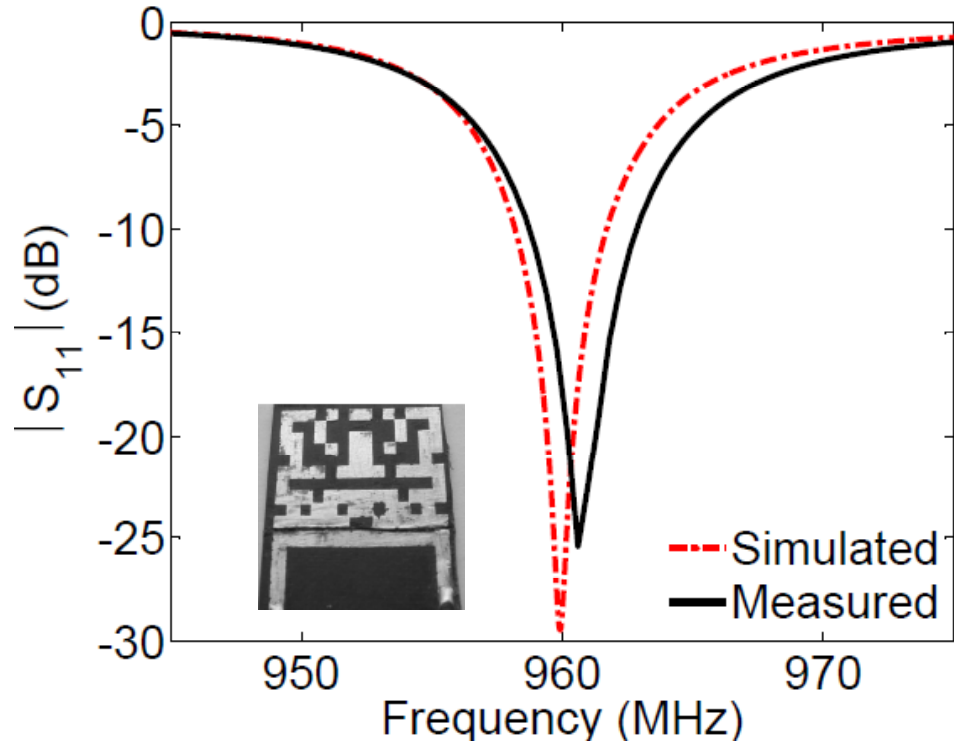
Figure 5.5. Simulated and measured reflection coefficients of the optimized antenna. The prototype is shown as inset.
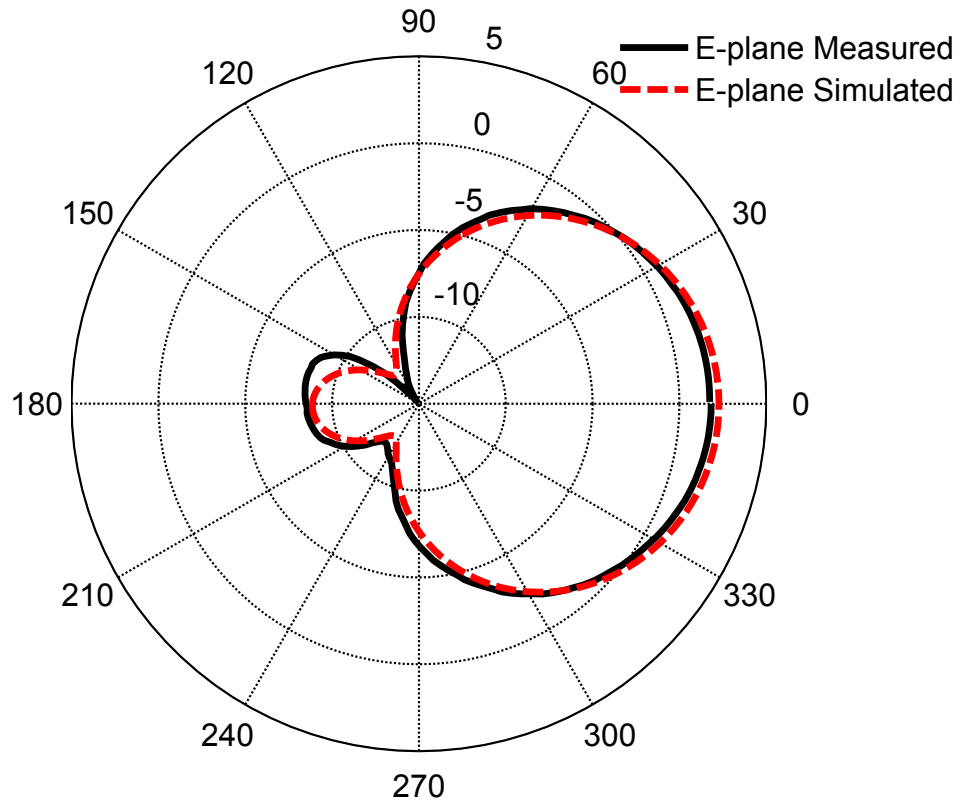
Figure 5.6. Simulated and measured E-plane realized gain pattern (dB).
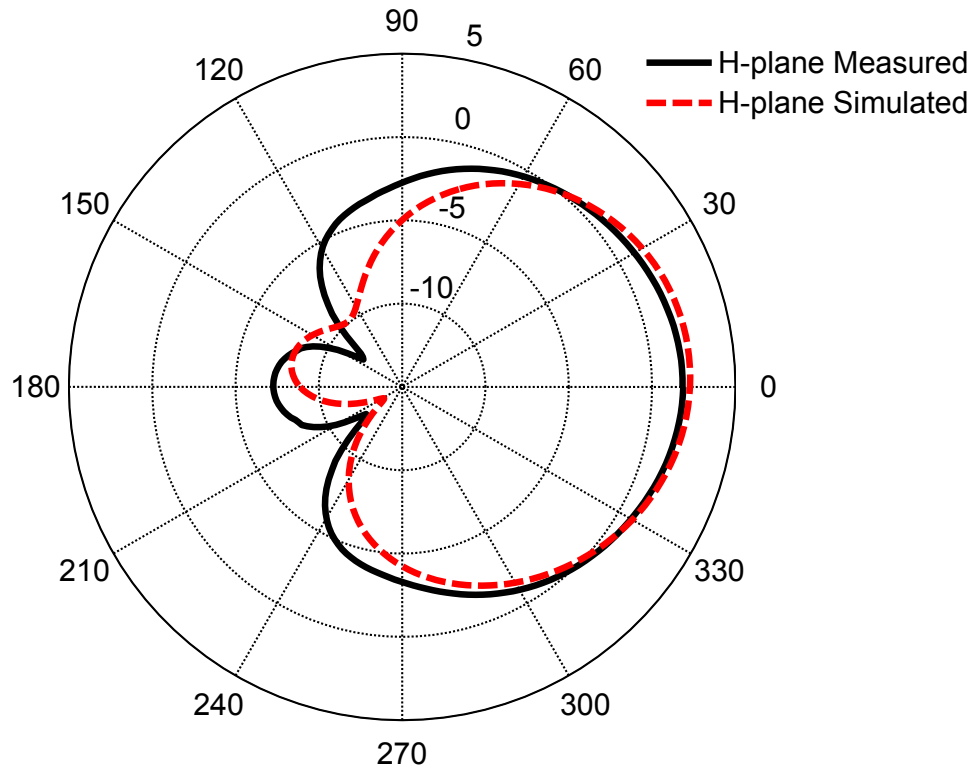
Figure 5.7. Simulated and measured H-plane realized gain pattern (dB).
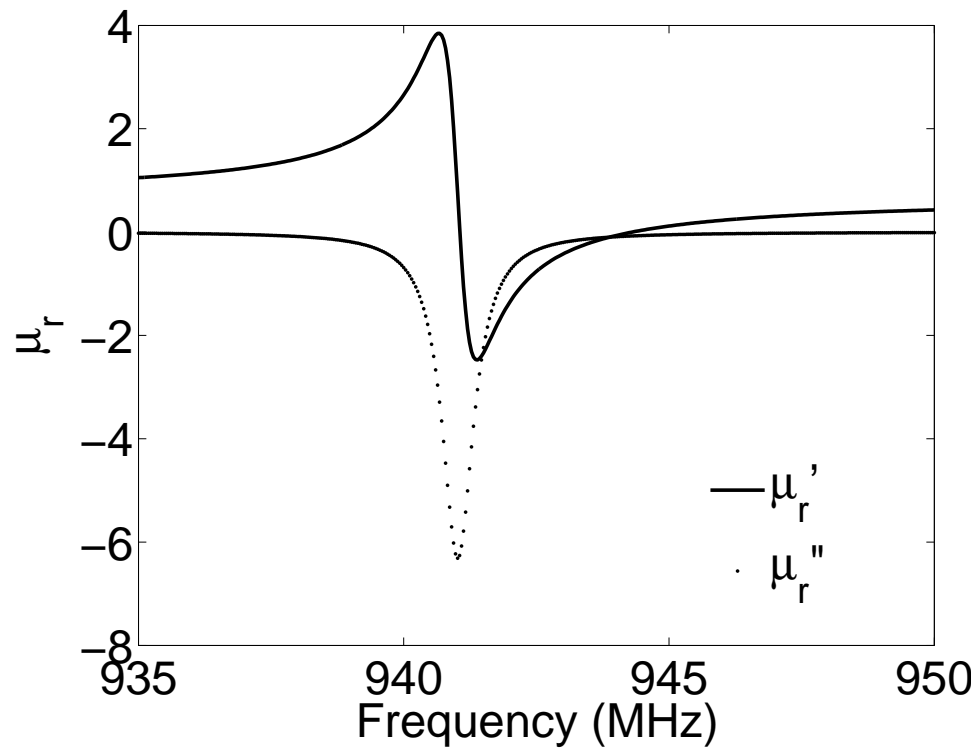
Figure 5.8. Relative permeability of the pixelated cell placed in a waveguide, extracted from simulation.

5.3 Example 2: ultra-compact folded monopole antenna for integrated applications

Although the metamaterial-inspired loop antenna presented in the first example is electrically small with $ka = 0.27$, it requires the use of a large ground plane placed perpendicular to the plane of the antenna as shown in Figure 5.2. The presence of the large ground plane makes the antenna unsuitable for integrated applications. In this example, the in situ optimization technique and pixelization approach are used on a different antenna structure to create an ultra-compact metamaterial-inspired antenna that is suitable for antenna on-chip applications.

5.3.1 Design

A monopole antenna is used in this example and a pixelated patch is placed around the antenna, whereas in the first example the pixelated patch is placed adjacent to the antenna. The pixelated patch is placed above a small ground plane and a coplanar waveguide (CPW) is used to excite the monopole as shown in Figure 5.9. The use of the CPW enables the ground plane, monopole, and pixelated patch to be in the same coordinate plane, thus providing a convenient connection between the antenna and the rest of the circuitry. A copper sheet is placed on the back side of the substrate as shown in Figure 5.10. Note from the figure that the copper sheet does not extend all the way to the feed. The distance between the edge of the copper sheet and the edge of the outer conductor of the feed is 1 mm. The purpose of the copper sheet is to minimize the effects of neighboring circuit components on the resonance frequency

of the antenna. Similar to the first example of this chapter, the objective is to find a pixelization geometry that results in a downward shift of the frequency of resonance of the antenna to a specified frequency.

To investigate the potential of the design described in this example, a semi-circular patch of radius 5.2 mm is parameterized into a pixelated grid with 154 square pixels of side length 0.52 mm each. A folded monopole antenna of dimensions W1 = 2.6 mm, W2 = 0.728 mm, L1 = 4.94 mm and L2 = 1.42 mm is inscribed in the middle of the pixelated patch as shown in Figure 5.9. Note that the 24 pixels located in the middle of the pixelated patch are turned off by default to allow enough space for the monopole antenna. The dimensions of the ground plane are GL1 = 3.12 mm and GL2 = 10.4 mm and the gaps between the ground plane and the monopole antenna are G1 = 0.4 mm and G2 = 0.15 mm. The ground plane, monopole antenna and pixelated patch are backed by a thin Rogers 4003 substrate of thickness 0.5 mm, with a dielectric constant $\epsilon_r = 3.55$ and a loss tangent $\delta_t = 0.0027$. The objective of the optimization is to create structures that produce a reflection coefficient below -10 dB at 1.8 GHz. At 1.8 GHz, the antenna fits into a hemisphere of radius $a = 5.73$ mm or $(a = \lambda_0/29.2)$ leading to $ka = 0.211$.

The configuration of the GA is similar to that of the first example except that a population size of 200 is used here. The goal of the GA is to find geometries that minimize the cost function

$$cost = c_1[20\log_{10}(|S_{11}|)] - c_2\eta_{rad}, \quad c_1, c_2 > 0 \qquad (5.11)$$

where c_1 and c_2 are parameters used to scale the two contributions of the cost function, and S_{11} and η_{rad} are defined in (5.5) and (5.6), respectively. In this particular example, $c_1 = 1$ and $c_2 = 50$.
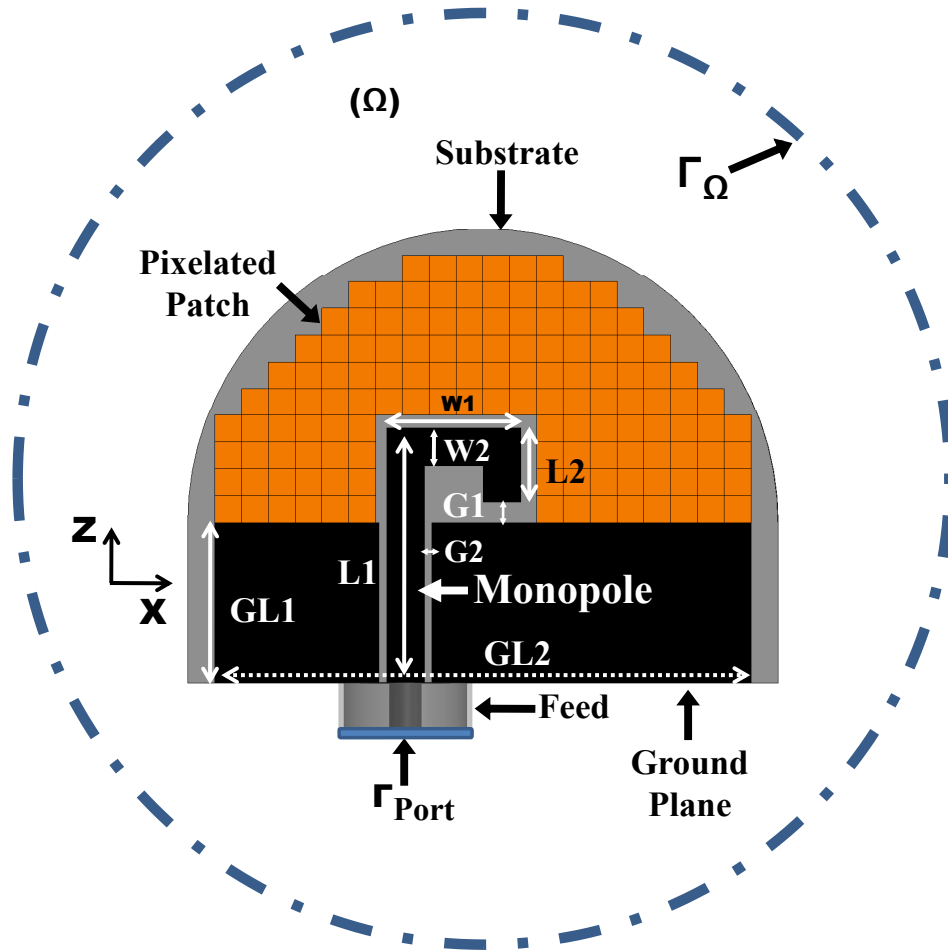
Figure 5.9. Analysis domain of the monopole antenna surrounded by the pixelated patch.
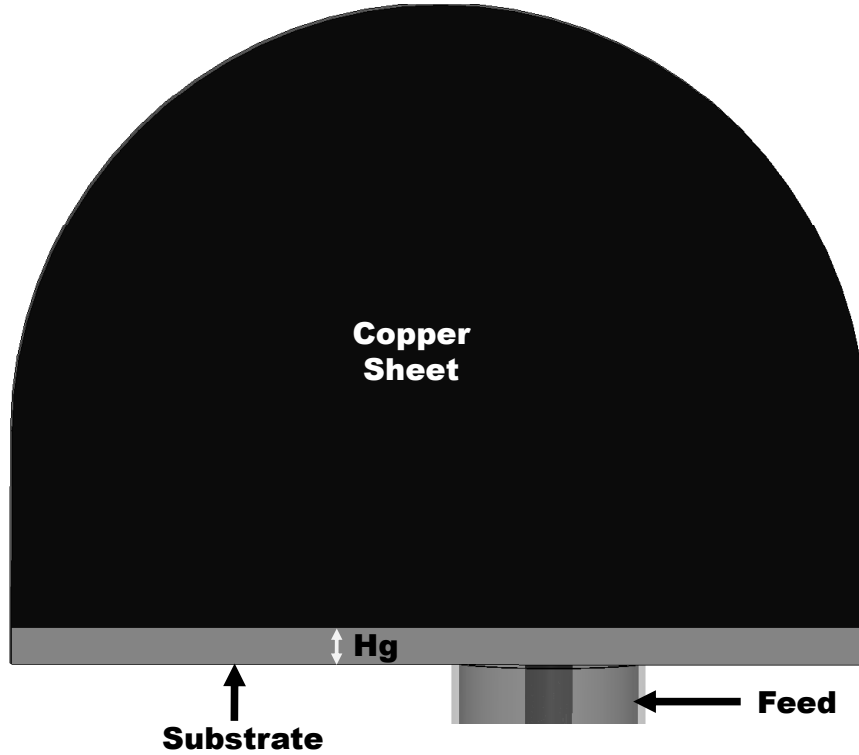
Figure 5.10. Back view of the substrate showing the copper sheet. Note that the copper sheet does not extend all the way to the outer conductor of the feed.

5.3.2 Results

The optimizer found pixel geometries that meet the design requirements within 20 generations. A screen shot of the best structure found by the GA is shown in Figure 5.11 and a prototype fabricated through photolithography is shown in Figure 5.12. Also shown in Figure 5.12 is a U.S. penny which is placed next to the prototype for reference. Plots of both simulated and measured reflection coefficients are shown in Figure 5.13. It can be seen that a very good reflection coefficient of -23 dB with a -10 dB bandwidth of 1.4% are achieved for both simulation and measurement. The

simulated efficiency of the antenna is 20%. Figure 5.14 shows plots of the radiation pattern in the horizontal and vertical planes of the antenna. Notice that the doughnut shape of the radiation pattern of the monopole antenna is maintained despite the presence of the copper pixels around the monopole.

It is possible to increase both the efficiency and bandwidth to almost double their current values by removing the copper sheet placed on the back of the substrate. However, without the copper sheet the antenna becomes highly sensitive to the presence of neighboring circuitry. Increasing the spacing between the antenna and the copper sheet to 1 mm increases the bandwidth and efficiency to above 2.5% and 30%, respectively. Using a Rogers 5870 substrate, which has $\epsilon_r = 2.33$ and $\delta_t = 0.0012$, instead of the present substrate which has $\epsilon_r = 3.55$ and $\delta_t = 0.0027$, increases the radiation efficieny to 38% but the frequency of resonance shifts to 2.13 GHz. Given that the antenna is very small, it might be worth it in an actual application to slightly increase the dimensions of the antenna to achieve a higher efficiency and bandwidth. The substrate used in this example was selected because it is one of the most commonly used in industry.

Since the main purpose of the design is to create an ultra-compact antenna suitable for integrated applications, the effects of placing circuit components next to the antenna was investigated in both simulations and measurements. Rectangular copper pads that are 0.5 mm thick were placed around the antenna as shown in Figure 5.15 to simulate the presence of circuit components. The copper pads were generated randomly since in most cases the antenna engineers have no knowledge of the arrangement of the circuit components within a given device. A 0.3 mm thick polyethylene

119

substrate with dielectric constant $\epsilon_r = 2.25$ and loss tangent $\delta_t = 0.001$ was placed above the antenna and copper pads to simulate the presence of a plastic cover.

A plot of the reflection coefficient of the monopole antenna loaded with the copper pads and the plastic cover is shown in Figure 5.16. It can be seen from the figure that the frequency of resonance of the antenna is shifted from 1.8 GHz to 1.69 GHz. Since the initial resonance at 1.8 GHz was obtained by turning pixels on or off, it should be possible to tune the antenna loaded with the copper pads and plastic cover to resonate at 1.8 GHz by turning pixels on or off. Also shown in Figure 5.16 is the reflection coefficient of the antenna tuned to its initial resonance of 1.8 GHz. Note that the reflection coefficient is below -20 dB at 1.8 GHz after the antenna was tuned. Tuning of the antenna was performed by deleting pixels 1 and 3 following the numbering of Figure 5.11. Note that without the copper sheet, the frequency of resonance shifts by more than 300 MHz when circuit components such as those shown in Figure 5.16 are placed next to the antenna.

The effect of neighboring circuitry on the prototype antenna was investigated experimentally by placing the prototype on a Blackberry Curve, as shown in Figure 5.17. The original antenna of the Blackberry was removed and replaced by the prototype of Figure 5.12. Figure 5.18 shows a plot of the reflection coefficient of the antenna after it was loaded on the Blackberry. Note that the frequency of resonance of the prototype is shifted from 1.8 GHz to around 1.7 GHz. Similar to the simulations case, deleting pixels 1 and 3 shifted the frequency of resonance back to 1.8 GHz. The reflection coefficient of the tuned antenna is not as low as in Figure 5.13 but it is still maintained below -10 dB.
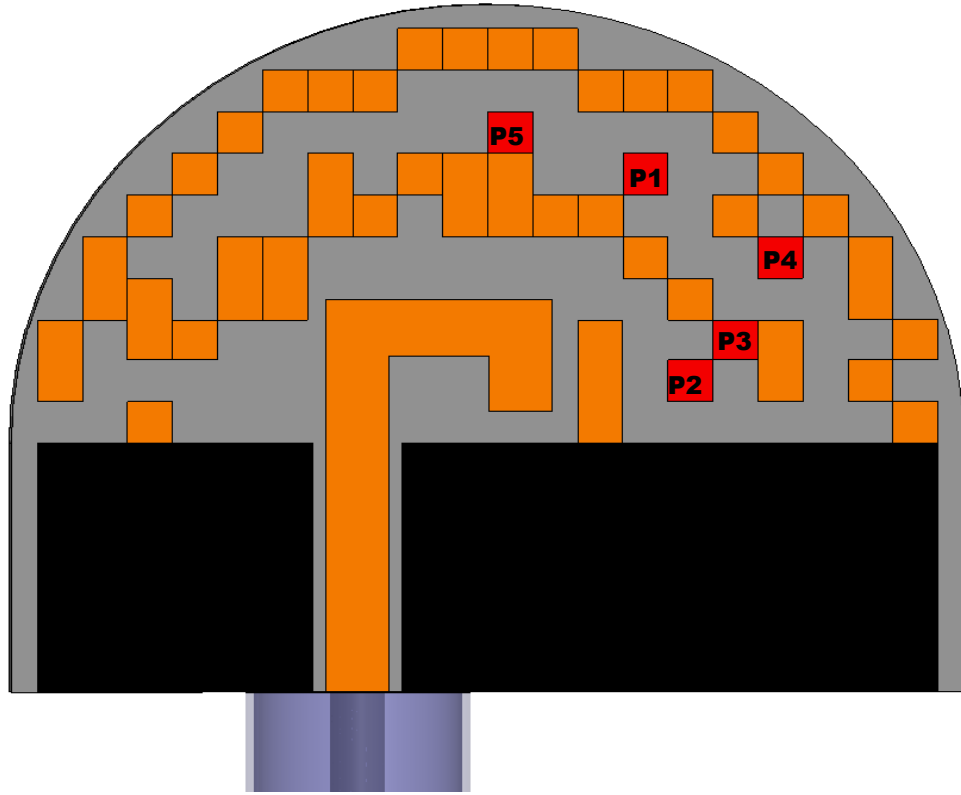
Figure 5.11. Best structure found by the GA.
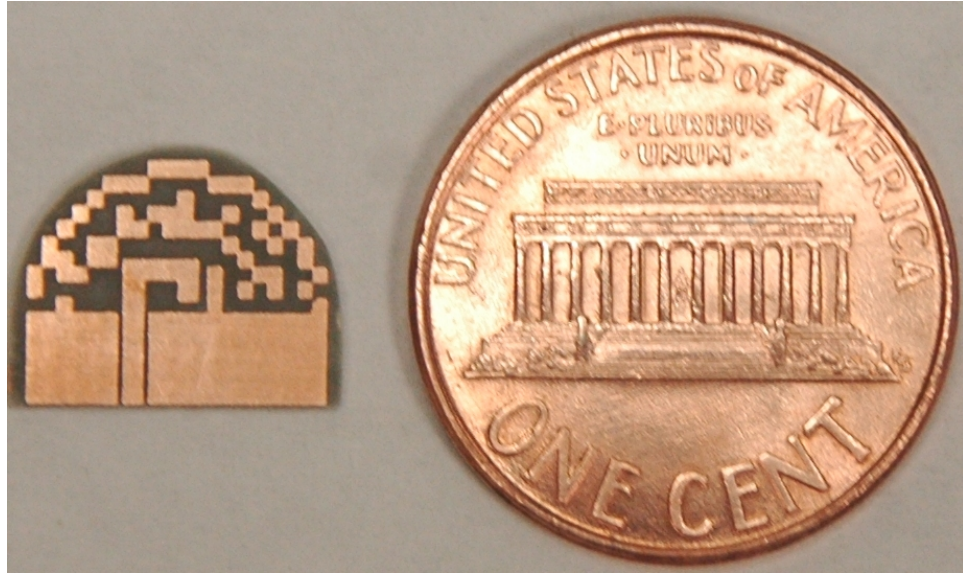
Figure 5.12. Prototype antenna fabricated through photolithography. U.S. penny shown for reference.
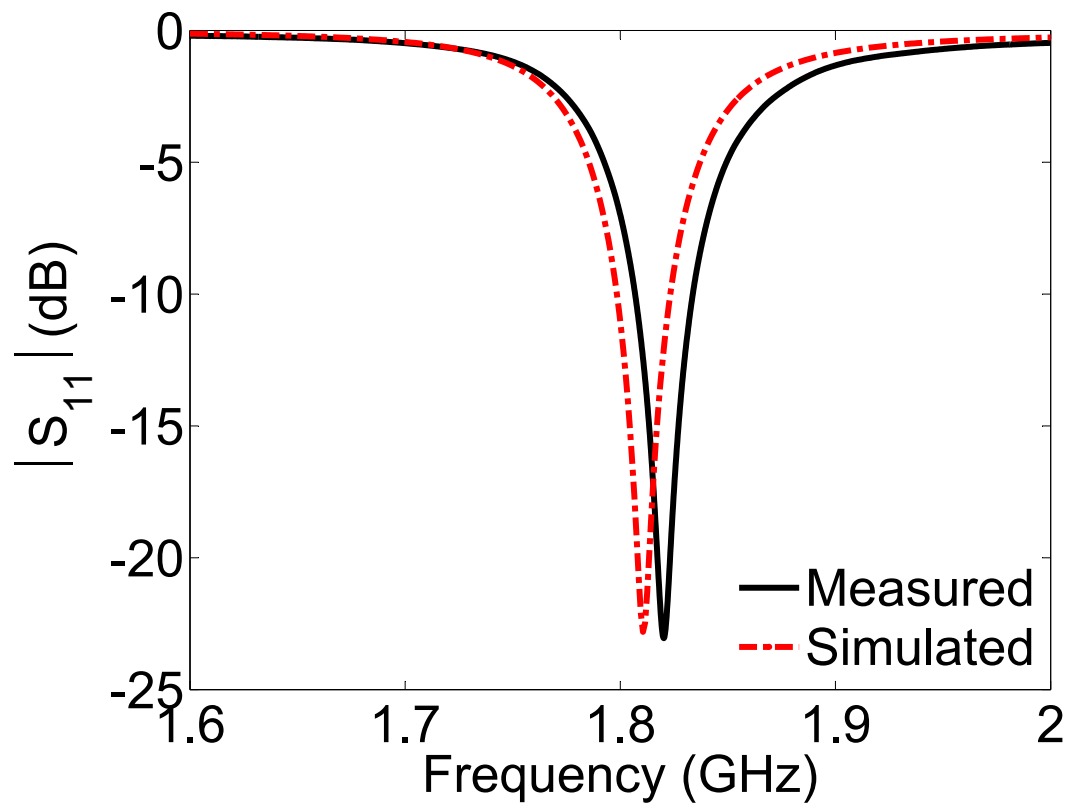
Figure 5.13. Simulated and measured reflection coefficients of the antenna shown in Figure 5.12.
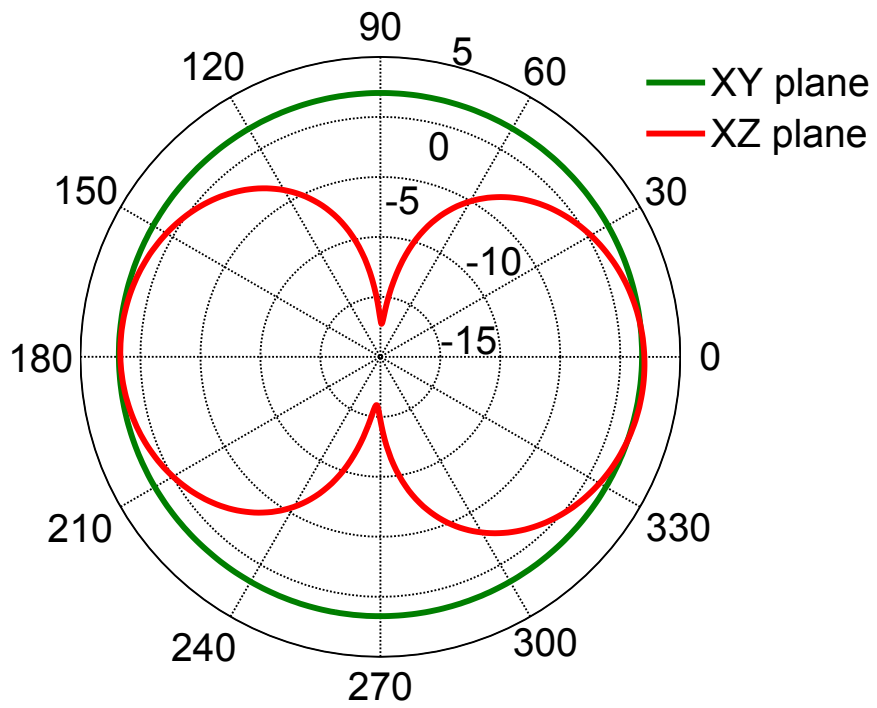
Figure 5.14. Simulated radiation pattern (dB) of the antenna shown in Figure 5.11.
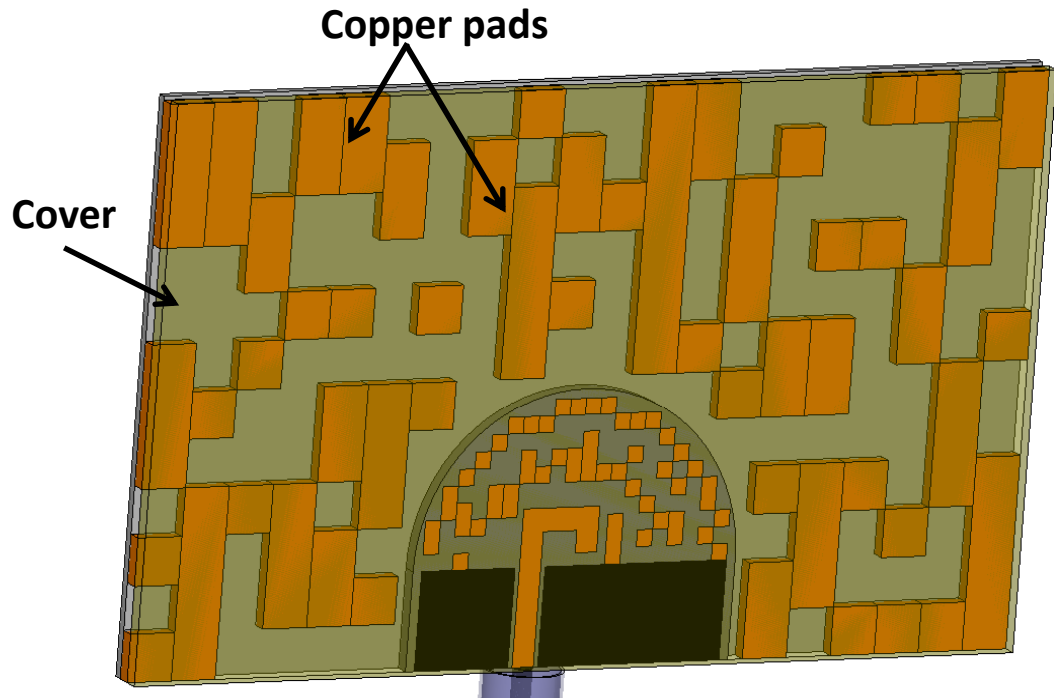
Figure 5.15. Antenna loaded with copper pads and a plastic cover.
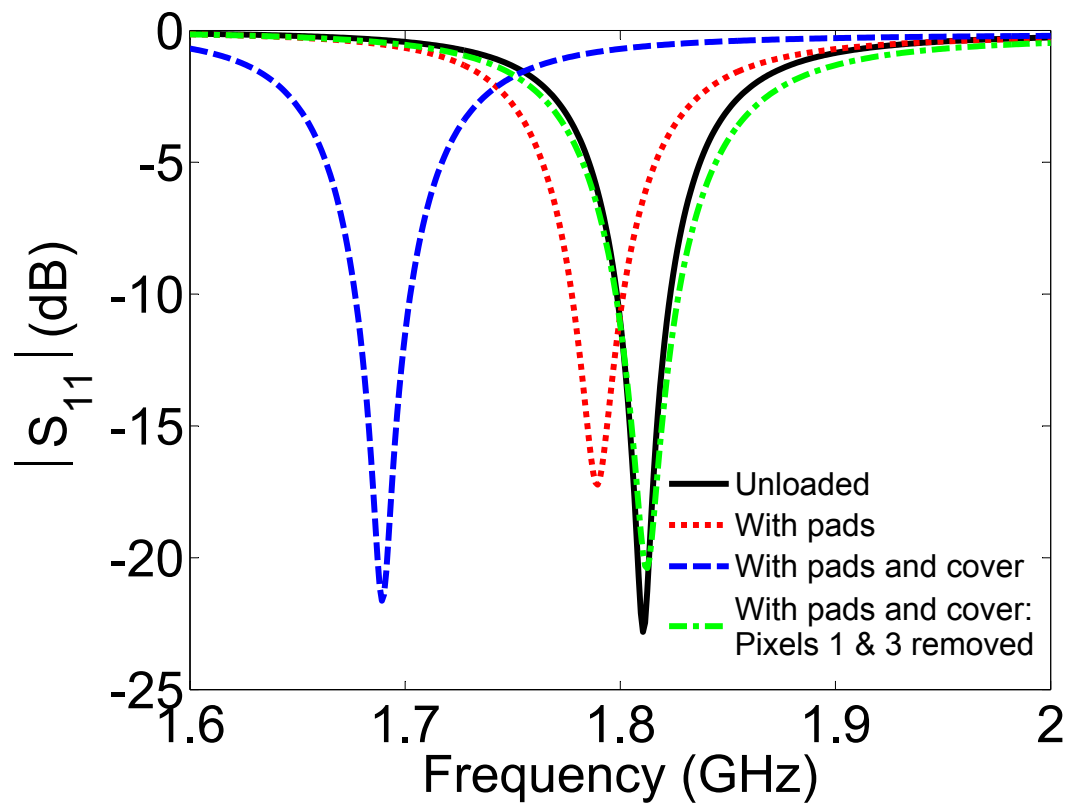
Figure 5.16. Effects of neighboring circuit components on the reflection coefficient of the antenna. Unloaded represents the antenna without the copper pads and plastic cover.
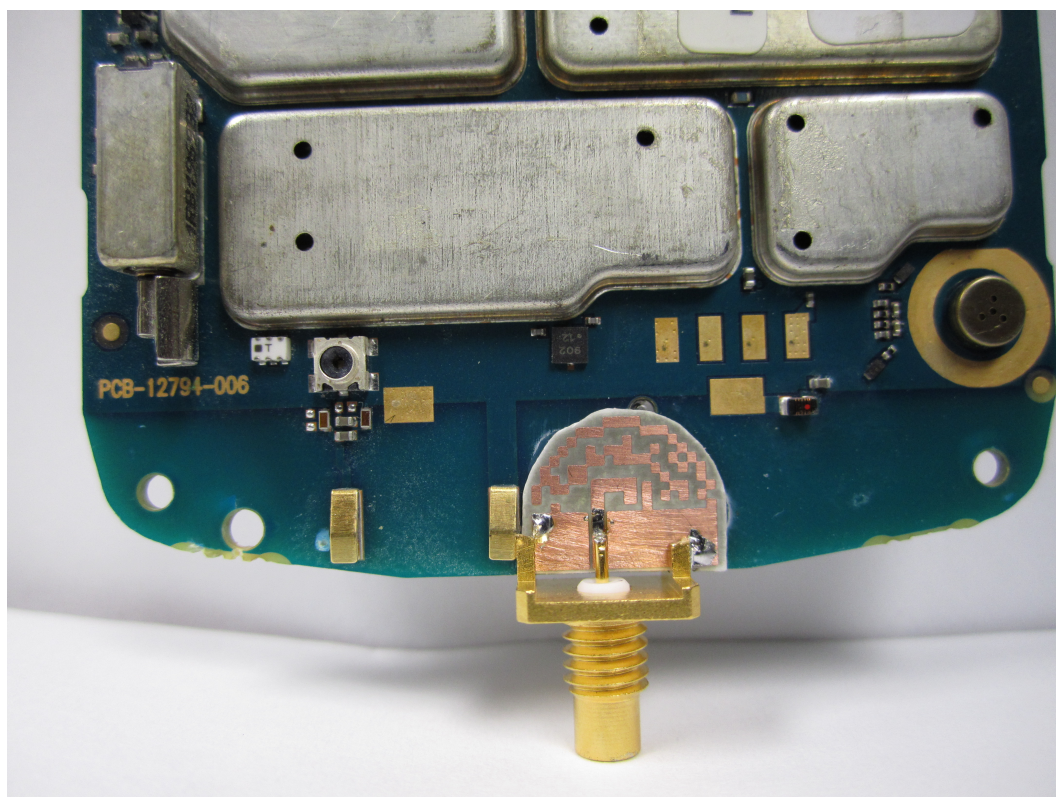
Figure 5.17. Prototype antenna placed on a Blackberry.
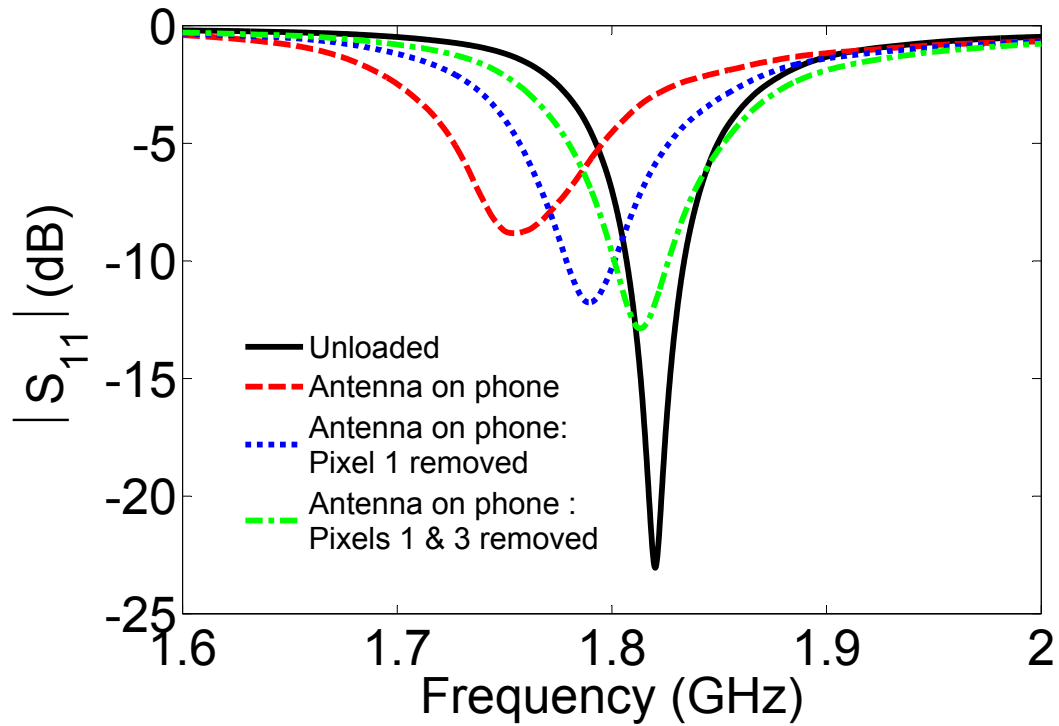
Figure 5.18. Effects of the Blackberry on the reflection coefficient of the antenna. Unloaded represents the antenna without the Blackberry.

5.4 Conclusion

The in situ optimization technique and the pixelization approach are used in this chapter to create highly miniaturized monopole and loop antennas. Antenna miniaturization was achieved in both cases by optimizing the geometry of a pixelated patch in close proximity to the antennas. Simulation and measurement results show that this approach can be used to create ultra-compact antennas that are suitable for integrated device and on-chip applications. Both simulated and measured patterns show

that the field patterns of the loop or monopole antenna are maintained despite the presence of the pixelated patch and the high levels of miniaturization.

CHAPTER 6

IMPLEMENTATION OF THE IN SITU OPTIMIZATION TECHNIQUE TO THE DESIGN OF MINIATURIZED PATCH ANTENNAS

The in situ optimization technique presented in Chapter III is used in this chapter in combination with the concept of complementary split ring resonators to create miniaturized patch antennas. By optimizing the geometry of complementary split rings placed horizontally between the patch and the ground plane, sub-wavelength resonance of the patch antenna can be achieved with a good impedance match and radiation characteristics comparable to those of a traditional patch antenna on a finite ground plane. Construction of the optimized antenna is straightforward, requiring only the sandwiching of two etched circuit boards.

High levels of miniaturization are demonstrated through simulations and experiments, with reductions of a factor of more than four in transverse dimension achieved for a circular patch resonant at 2.45 GHz. Although miniaturization is accompanied by a decrease in antenna efficiency and a loss of fractional bandwidth, antenna performance remains acceptable even for a 1/16 reduction in patch area.

6.1 Motivation

The demand for small, compact, low cost antennas has increased tremendously over the past years, due to the need for reduced antenna size in both military and commercial spheres. Microstrip patch antennas, though popular for these applications, are

difficult to miniaturize since their resonant frequency is determined by the dominant mode of the patch cavity. Nevertheless, much work has been done to find ways to miniaturize patch antennas.

One of the most common techniques is to use shorting plates [32] or shorting pins [28] to shift the voltage null away from the center of the patch. The level of miniaturization achieved with this technique depends on the placement position of the shorting element relative to the voltage null of the unloaded patch. By placing the shorting element at the edge of the patch, a maximum shift of the voltage null can be achieved and the transverse dimension of the antenna can be reduced by 60%.

Other well known miniaturization techniques involve placing slots on the radiating patch [35]-[23] or fractalizing the radiating edge [38], thereby increasing the length of the current path and consequently reducing the resonant frequency of the antenna. The achievable level of miniaturization depends on the length of the extended current path, with a typical size reduction of about 38% [38]. Folding the patch into a multi layered structure can be used to reduce the transverse dimension of the patch by 50% [39], but at the cost of increased thickness, such that the overall volume of the antenna is unchanged. Each of these methods is limited in the amount of miniaturization that may be achieved, and each is associated with a dramatic drop in radiation efficiency and a degradation of the radiation pattern in both the E and H planes.

Patch antennas can also be miniaturized by using a high permittivity or artificial dielectric substrate. Loading an empty patch cavity with a dielectric of relative permittivity ϵ_r produces a reduction in the resonant frequency proportional to roughly $\sqrt{\epsilon_r}$. Readily available high permittivity dielectrics such as aluminum oxide

(Al_2O_3) provide a dielectric constant of $\epsilon_r \approx 10$ and thus may be used to produce size reductions of about 50% compared to conventional circuit board materials such as RT/duroid. Though dielectrics with much higher dielectric constants exist, their increased cost makes them unsuitable for low-cost consumer applications.

The emergence of new artificial materials such as high impedance surfaces (HISs), reactive impedance surfaces (RISs), magneto-dielectrics, and metamaterials provide new ways to achieve higher levels of miniaturization than more conventional techniques [55]-[63]. For instance, it is reported in [57] that an RIS can be used to both miniaturize (down to a size of $\lambda_0/10$) and increase the bandwidth of a patch antenna. However, the implementation of the RIS requires the use of high permittivity dielectrics ($\epsilon_r = 25$) and thick substrates to achieve the desired level of miniaturization and bandwidth. Unfortunately, the exorbitant cost of high permittivity dielectrics and the use of thick substrates render the RIS approach unsuitable for low-cost or low-profile applications.

In [52], it is reported that sub-wavelength resonance of a patch antenna can be achieved by partially loading the patch cavity with a properly designed homogeneous, isotropic, negative permeability metamaterial. A practical implementation of this idea was later proposed in [54] and [53], where inclusions consisting of arrays of resonant structures such as split-ring resonators were used to create the required $\mu < 0$ medium. However, this implementation is problematic since several arrays of planar resonant structures must be oriented vertically within the patch cavity in order to be effectively excited by the horizontal dominant-mode magnetic field. Since the level of miniaturization achievable depends on the size and the number of inclusions

132

(with larger inclusions producing lower resonant frequencies), very thick substrates are required to produce a meaningful reduction in size. Additionally, the fabrication process of such structures results in high cost and complexity.

In [60]-[63] it is reported that by etching arrays of SRRs into the ground plane, creating CSRRs, it is possible to lower the resonant frequency of the patch to that of the CSRRs. However, this approach only provides modest size reductions. For instance, only 32% reduction of the transverse dimension of the patch is reported in [60]). Additionally, the presence of the array of large slots on the ground plane significantly reduces the front-to-back ratio (FBR) to almost 0 dB while increasing the cross-polarization to the same level as the co-polarization in both E and H planes.

In this chapter, the in situ optimization technique described in Chapter III and also presented in [72], is used to produce highly miniaturized patch antennas that are thin, low cost, and easy to fabricate. Importantly, miniaturization is accompanied by a very good impedance match, with a return loss of more than 20 dB in all cases, and without significantly compromising the radiation pattern. At least a 4.5 dB front-to-back ratio is maintained for a 75% size reduction, with excellent isolation between the co- and cross-polarized fields in both the E and H planes. There is a trade off, however, since increased levels of miniaturization result in a reduction of the bandwidth and efficiency of the antenna. But even with a miniaturization to 1/16 the area of a traditional patch, the reductions in bandwidth and efficiency remain acceptable.

Miniaturization is achieved by loading the patch cavity using CSRRs. By duality with SRRs, these are excited by the vertical electric field of the patch cavity mode,

and thus may be oriented horizontally between the patch and the ground plane. The geometries of the CSRRs are optimized in place to produce appropriate antenna characteristics at frequencies much lower than the resonant frequency of the unloaded patch cavity. Since the sizes of the horizontal CSRRs may be much larger than those used in [60] – [63], as well as the vertical inclusions used in [54] and [53] (up to the size of the ground plane), higher levels of miniaturization are possible. Moreover, the simple construction of the antenna and the use of low permittivity dielectrics can lead to lower production cost compared to designs based on high permittivity dielectrics and other complex approaches using a HIS, RIS or magneto-dielectrics.

Preliminary simulations of the work presented here were used in an earlier conference paper [65] to explore the underlying principle of the patch miniaturization technique. The effectiveness of the proposed technique is demonstrated in this chapter with detailed discussions of the design, optimization procedure and the impact of the technique on the bandwidth, efficiency, front to back ratio, and cross polarization of the antenna. Miniaturized antennas with a surface area reduction of more than a factor of sixteen are achieved in simulations without serious degradation of impedance or pattern, and measurements of the performance of several prototypes are used to validate the results obtained from the simulations. Details of the design and the optimization procedure are provided below.

6.2   Basic concept

It is established in Chapter II that by placing an array of properly designed SRRs in an environment where the magnetic field is polarized along the axis of the rings, the

effective permeability of the resulting composite medium may be made to resonate at a frequency determined by the capacitance and inductance of the ring structure. The resonant frequency of an SRR may be lowered significantly by increasing its effective capacitance and inductance through the use of multiple concentric split rings as presented in [64]. Falcone et al. [59] showed using the concepts of duality and complementarity that the effective permittivity of a medium composed of CSRRs can be tailored to desirable values if the medium is excited with an electric field polarized along the axes of the CSRRs. Given that the electric field of the dominant mode within a patch cavity is polarized normal to the ground plane, it is possible to excite properly designed CSRRs placed horizontally between the ground plane and radiating patch and thus lower the resonant frequency of the patch to that of the CSRR.

In a dual to the multiple concentric SRR approach of [64], the resonant frequency of a complimentary structure can be lowered by using multiple slots. Similarly, it is possible to maintain the resonant frequency of a complimentary structure while the dimensions of the disk are reduced by placing multiple concentric slots on the disk. This approach allows high levels of miniaturization of the CSRR with the highest level of miniaturization determined by the total number of slots that can be placed on the disk.

By using the in situ optimization technique, the geometry of the CSRRs within the patch cavity can be optimized by varying the number of slots and the dimensions of each slot to produce an antenna resonance at a frequency well below that of the unloaded antenna. Equivalently, the frequency of resonance can be kept fixed and the size of the loaded antenna can be reduced to desired levels of miniaturization. The

use of the optimizer is crucial for finding CSRR geometries that couple well with the antenna to produce the desired output parameters. As is shown in the results section, several CSRR geometries can lead to the same frequency of resonance but produce different antenna reflection coefficients and efficiencies, many combinations of which are unacceptable.

6.3 Antenna design

Figure 6.1 illustrates the proposed geometry of a miniaturized circular patch antenna. A radiating circular patch is placed above a circular dielectric substrate backed by a circular ground plane of the same diameter as the substrate. A microstrip feed line is used to excite the patch. A conducting disk is placed horizontally between the patch and ground plane and complementary split-rings of various radii are created by removing metal from the disk. The geometry of the disk, shown in Figure 6.2, is optimized by varying the number of complementary split rings, the radius of the largest ring R_2, the slot width W, the metalization width S, and the gap width G. To reduce optimization costs, the values of W, G, and S are chosen to be the same for all of the complementary split rings, and the radius of the disk, R_1, is fixed by choice.

6.3.1 Proof of concept design

Consider a traditional patch antenna consisting of a circular copper patch of radius 23.1 mm etched on top of a circular Rogers RT/duroid 5870 substrate of thickness 2.34 mm and radius 46.2 mm, backed by a copper ground plane also of radius 46.2 mm.
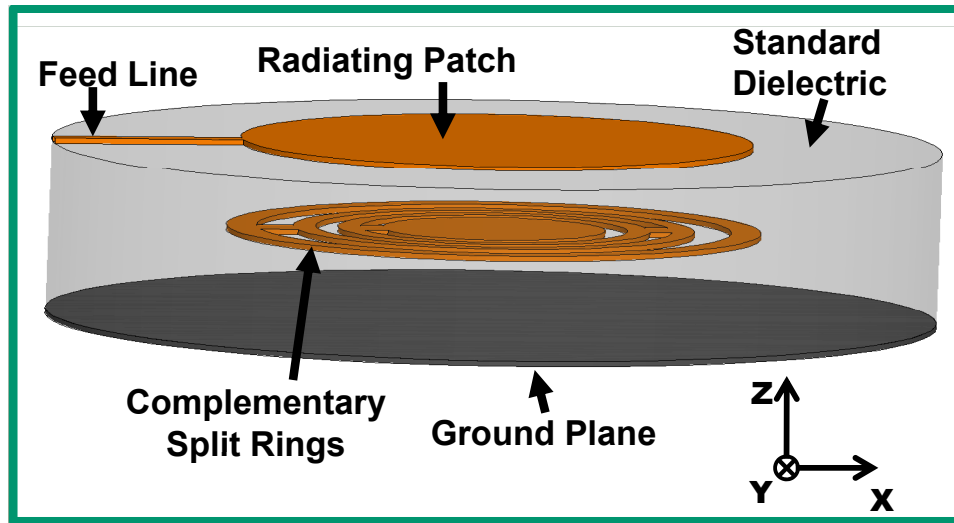
Figure 6.1. Geometry of the miniaturized patch antenna.

The dielectric constant of the substrate is $\epsilon_r = 2.33$ and the dielectric loss tangent is $\delta = 0.0012$. Both dielectric and copper losses are included in the analysis of the performance of the antenna and form the basis for determining the antenna efficiency. A 50Ω copper microstrip line of width 1.5 mm is used to feed the patch, with an SMA connector placed at the edge of the substrate. The radius of the patch is chosen such that the antenna resonates at 2.45 GHz. The goal of this design is to produce miniature versions of the antenna that achieve performance similar to the traditional patch at the 2.45 GHz operational frequency.

Three miniaturized patch antennas were designed. The radii of the patches were chosen to be 12 mm, 8 mm and 6 mm, which represent reductions in patch area to 1/4, 1/9, and 1/16, respectively, of the traditional patch (i.e., radius reduction of 1/2, 1/3, and 1/4). In each case, the ratio of patch radius to ground plane radius was held at 1:2, the substrate thickness was fixed at 2.34 mm, and the width of the microstrip line

was kept at 1.5 mm to achieve a 50Ω characteristic impedance; these are all identical to the corresponding properties of the traditional patch. Miniaturization was achieved by placing a copper disk containing CSRRs 0.78 mm below the radiating patch. The radius R_1, of this disk in each case was chosen to be slightly smaller than the ground plane to avoid contact with the SMA connector. The values of R_1 used in each case are provided in Table 6.1. Finally, the geometry of the CSRRs was optimized in simulations using an in-house genetic algorithm, as described below.
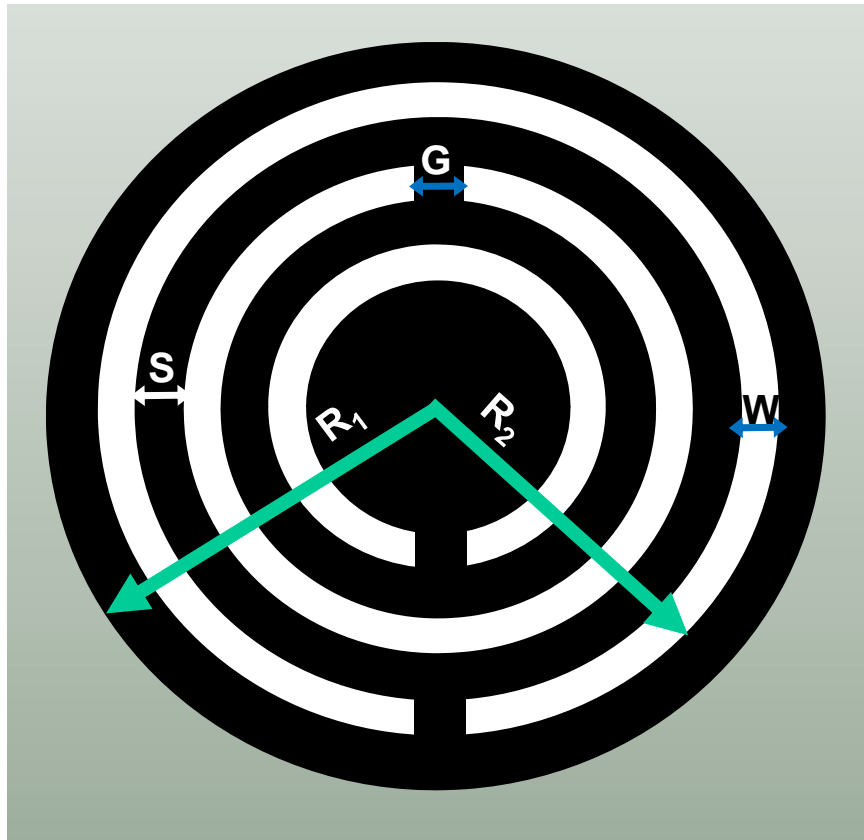
Figure 6.2. Geometry of the disk containing the CSRRs.

6.3.2 Optimization method and analysis

The geometry of the CSRRs appropriate for a desired level of miniaturization was determined in simulations by integrating the full wave solver HFSS with an in-house GA written in Matlab. The dimensional parameters R_2, W, S and G are encoded into a 21-bit binary string ρ, and the number of rings is determined by

$$N = \left\lfloor \frac{R_2}{S + W} \right\rfloor, \qquad (6.1)$$

where the floor operator $\lfloor x \rfloor$ rounds the positive number x to the largest integer less than x. For a given 21-bit binary string, the value of R_2 is determined by performing a binary to decimal conversion of the first six bits of the string.

The values of W, S and G are determined by performing a similar conversion of the remaining fifteen bits with five bits used for each parameter. The ranges of values allowed for each of the four parameters are shown in Table 6.2 and Table 6.3 for each desired level of miniaturization. Note from the tables that the largest value of R_2 is always smaller than R_1 and the value of $W + S$ is also always smaller than R_2. These values are selected to ensure that there is always at least one ring on the circular disk. To illustrate how the encoding is done, assume a 21-bit binary string given as {110101100110001101101}. The value of R_2 is determined by converting the first six bits starting from the left {110101} to a decimal number. The conversion is performed as

$$R_2 = 5 + 0.1 \cdot \left[(2^0) \cdot 1 + (2^1) \cdot 1 + (2^2) \cdot 0 + (2^3) \cdot 1 + (2^4) \cdot 0 + (2^5) \cdot 1 \right], \quad (6.2)$$

139

where 5 and 0.1 are the initial and incremental values of R_2 as shown in Table 6.3. The value of S is determined using the seventh through the eleventh bits {10011}, the value of W is determined using the twelfth through the sixteenth bits {00011} and the last five bits {01101} are used to determine the value of G.

The goal of the optimization is to produce a good impedance match without seriously compromising the efficiency of the antenna. This is done by seeking low values of the cost function

$$F(\rho) = \eta_{\text{rad}} \times \left[20 \log_{10}(|S_{11}|) \right], \tag{6.3}$$

where $|S_{11}|$ is the magnitude of the reflection coefficient referenced to 50Ω and η_{rad} represents the radiation efficiency of the antenna. Note that $F(\rho)$ is always negative. The GA is configured for a 2-point crossover with an evolving single bit mutation. An initial population of 500 different binary strings is selected randomly and the corresponding antenna geometries are created in Matlab and exported to HFSS for simulation. Note that only the geometries of the CSRRs differ between simulation runs; the patch does not change. The cost of each binary string is then evaluated and ranked. The top 25% is selected for crossover and mutation until a new population of 100 binary strings (1/5 the starting population size) is generated. This process is repeated until the preset optimization goal of $20 \log_{10}(|S_{11}|) < -10$ dB and $\eta_{\text{rad}} > \gamma$ are reached. The value of γ is selected to be 1/2, 1/3 and 1/4 for the respective radii reductions to 1/2, 1/3 and 1/4. The time to complete a full-wave simulation for a given antenna geometry is approximately 150 seconds using an intel quad core i7

computer with 12 Gb of RAM.

A Matlab code used to create patch antennas loaded with a CSRR layer is provided in Appendix E. The code generates a random 21 bit binary string and performs a binary to decimal conversion to determine the values of R_2, S, W and G. The values are then used to create the CSRR layer. The code also creates a patch antenna of radius 6 mm and loads the CSRR layer between the radiating patch and ground plane as shown in Figure 6.1.

Patch Radius	N	R_1	R_2	W	G	S
12	1	23	7.1	1.5	1.15	–
8	1	15	6.2	1.6	1.75	–
6	3	11.5	9.9	1.65	1.9	1.05

Table 6.1. Parameter values of the CSRRs for each level of miniaturization (dimensions in mm).

Parameter	Start	Step	End
R_2	5	0.15	14.45
G	0.1	0.075	2.425
S	0.3	0.1	3.4
W	0.3	0.1	3.4

Table 6.2. Parameter values used to optimize the CSRRs to miniaturize the patch antenna to 1/4 and 1/9 the area of the traditional patch (dimensions in mm).

Parameter	Start	Step	End
R_2	5	0.1	11.3
G	0.1	0.075	2.425
S	0.3	0.075	2.65
W	0.3	0.075	2.65

Table 6.3. Parameter values used to optimize the CSRRs to miniaturize the patch antenna to 1/16 the area of the traditional patch (dimensions in mm).

6.4 Results

For each desired level of miniaturization, the GA successfully found several sets of design parameters that produce a reflection coefficient lower than -10 dB. The parameters of the CSRRs that produce the best identified cost values for each miniaturization level are provided in Table 6.1, and frequency sweeps of the reflection coefficients for each optimized antenna are shown in Figure 6.3 – Figure 6.5. A plot of the reflection coefficient of a traditional patch antenna designed on the same substrate is also shown in each figure for reference. It can be seen that a very good impedance match of $|S_{11}|$ less than -20 dB is achieved for each desired level of miniaturization.

While it is to be expected that the bandwidth and the efficiency of the miniaturized antennas will be reduced compared to the traditional patch antenna (due to the reduction in antenna volume), the properties of the three optimized antennas remain quite good. From the simulations, the -10 dB bandwidths of the antennas with area reductions to 1/4, 1/9 and 1/16 of the traditional patch antenna are 1.2%, 0.81% and 0.4%, respectively, compared to 1.3% for the traditional patch antenna; the corresponding efficiencies are 84.7%, 49.8% and 28.1% respectively, compared to

94% for the traditional patch antenna.

A plot of reflection coefficient versus efficiency obtained from the last generation of the GA optimization performed to produce a 1/16 area miniaturization is shown in Figure 6.6. It can be seen that while several CSRR geometries produce patch antennas resonant at a given frequency, the performances of the antennas vary. The reflection coefficient ranges from below -25 dB to near 0 dB, while the efficiency ranges from 10% to 80%. These results show that using an optimizer is crucial to finding the CSRR geometries that produce acceptable performance. Note also that more than fifteen different CSRR geometries produce a reflection coefficient less than -10 dB, each with a different efficiency. This suggests that the data presented here might not be the best achievable through the proposed design methodology and that further optimization or the use of a more sophisticated optimizer may lead to even better results. Similar conclusions can be drawn by observing Figure 6.7 which is a plot of the reflection coefficient versus efficiency obtained from the last generation of the GA optimization performed to produce a 1/9 area miniaturization.

When an SRR is placed in an environment with a time varying normal magnetic field, an electric current is induced on the metal, reaching its peak at the frequency of resonance of the SRR. By duality, one would expect that a magnetic current is induced in the slots of a CSRR when the CSRR is placed in an environment with a time varying normal electric field. The magnetic current should reach its peak at the frequency of resonance of the CSRR. This effect is clearly seen in Figure 6.8 which shows a plot of the intensity of the electric field on the surface of the CSRR disk for a resonant patch antenna miniaturized to 1/16 of the area of a traditional antenna.

It can be seen that at resonance the electric field in the slots is very strong, with the intensity of the field greatest at the edges of the slots. This behavior is the expected edge singularity of the slot magnetic current. The intensity of the field is strongest in the middle slot, which has a diameter of $\lambda_0/9.6$. This diameter is comparable to those of the single slots found by the optimizer for patch areas of 1/4 and 1/9 of the traditional antenna (shown in Figure 6.19). Plots of the intensity of the electric field on the surface of the CSRR disk for a resonant patch antenna miniaturized to 1/9 and 1/4 of the area of a traditional antenna are shown in Figure 6.9 and Figure 6.10 respectively. These two plots also show that the electric field in the slots is very strong with the intensity of the field greatest at the edges of the slots.

As the size of the conducting disk is reduced, more concentric slots must be created in order to maintain the same frequency of resonance and a good impedance match. Further optimizations to miniaturize the patch area to 1/64 that of a traditional antenna (resulting in a patch radius of 3 mm) produce a CSRR with five concentric slots and a reflection coefficient of -14 dB. Unfortunately, the efficiency drops to only 5% and given that the ground plane is significantly reduced to less than $\lambda_0/10$, the front-to-back ratio decreases to almost 0 dB.

The simulated E-plane and H-plane realized gain patterns of the various miniaturized patch antennas are shown in Figure 6.11 and Figure 6.12, respectively. The radiation patterns of the traditional patch antenna are also shown in these figures for comparison. Note from the two figures that the broadside nature of the radiation pattern is maintained in both planes, but the realized gain is reduced as the antenna is made smaller, primarily due to the decrease in efficiency. Note also that the size of

the backlobe increases as the antenna size is reduced, because the ground plane size is reduced in tandem with the patch. The smallest FBR is 4.5 dB and corresponds to the FBR of the antenna miniaturized to 1/16 the area of the traditional patch. This FBR is higher than the one reported in [54] (3 dB for an area reduction to 1/16) and [28] (2 dB for an area reduction to 1/9).

The directivity of the miniaturized antennas remains very good as well despite the large reduction in antenna area. For instance, the directivity of the simulated antennas with area reductions to 1/4, 1/9 and 1/16 of the traditional patch antenna are 5.96 dB, 4.86 dB and 4.23 dB, respectively, compared to 7.34 dB for the traditional patch antenna. The lack of symmetry of the E-plane pattern (Figure 6.11) is due to the presence of the microstrip feed and the CSRR gaps, which are aligned along the x axis as shown in Figure 6.1. If desired, the asymmetry can be reduced somewhat by rotating the CSRRs by 90 degrees.

The isolation between the co-polarization minimum and cross-polarization maximum remains excellent for all three miniaturized antennas with over 35 dB in the E-plane and 20 dB in the H-plane. It should be mentioned here that the isolation between co-polarization minimum and cross-polarization maximum of the miniaturized patch antennas is higher than the isolation between co-polarization minimum and cross-polarization maximum of the traditional patch antenna as shown in Figure 6.13 – Figure 6.18. The level of the cross-polarization of a patch antenna is affected by the thickness of the substrate, with thicker substrates leading to higher cross polarization levels. Although the traditional antenna and the miniaturized antennas have the same substrate thickness, there is a slotted conducting disk placed between the radi-

ating patch and ground plane which contributes to the radiation of the miniaturized antennas.

The CSRR layer position is determined by available board thicknesses. The value of 0.78 mm used here is a standard substrate thickness manufactured by Rogers Corp. Additional optimizations with the CSRRs placed 1.56 mm from the radiating patch produced results similar to those obtained for a distance of 0.78 mm. Note however that moving an optimized CSRR from the position where it was optimized alters the performance of the antenna, due to the change in coupling between the CSRR structure and its surroundings, and additional optimization would be needed to return the performance of the altered antenna to an acceptable level. It is also expected that antenna performance depends on the distance between the CSRRs and the ground plane. This emphasizes the need for an optimizer to find appropriate CSRR structures for a given geometry.

Prototypes of the traditional and miniaturized antennas were fabricated through photolithography using a 0.78 mm thick double-sided Rogers 5870 duroid substrate and a 1.56 mm single-sided Rogers 5870 duroid substrate. The properties of the substrates are the same as those used in the simulations. The radiating patch was etched on one side of the 0.78 mm thick substrate and the CSRRs were etched on the other side. The ground plane was provided using the single-sided 1.56 mm substrate. The final prototypes were produced by gluing the two substrates such that the CSRRs are between the patch and the ground plane. The traditional patch was constructed the same way, except without the CSRR structures. Figure 6.19 shows the top and bottom views of the etched 0.78 mm substrate.

The measured reflection coefficients of the miniaturized antennas are shown in Figure 6.3 – Figure 6.5, where they are compared to the results from simulations. In each case excellent agreement is seen between measurement and simulation. Figure 6.20 – Figure 6.22 compare the simulated and measured H-plane realized gain patterns of the miniaturized patch antennas. Good agreement is again observed between simulations and measurements, thus attesting to the feasibility of the proposed miniaturization technique.
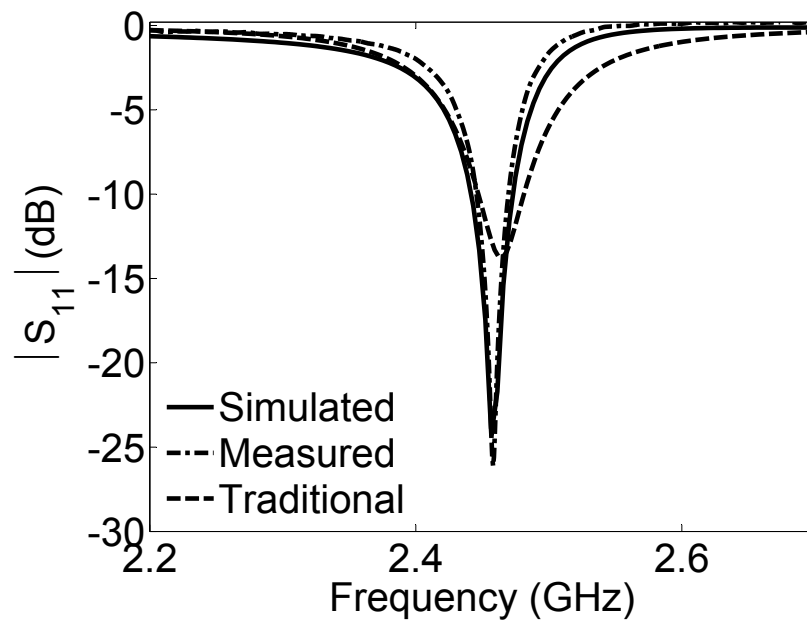
Figure 6.3. Reflection coefficient of the patch antenna miniaturized to 1/4 the area of the traditional patch (traditional patch reflection coefficient added for reference).
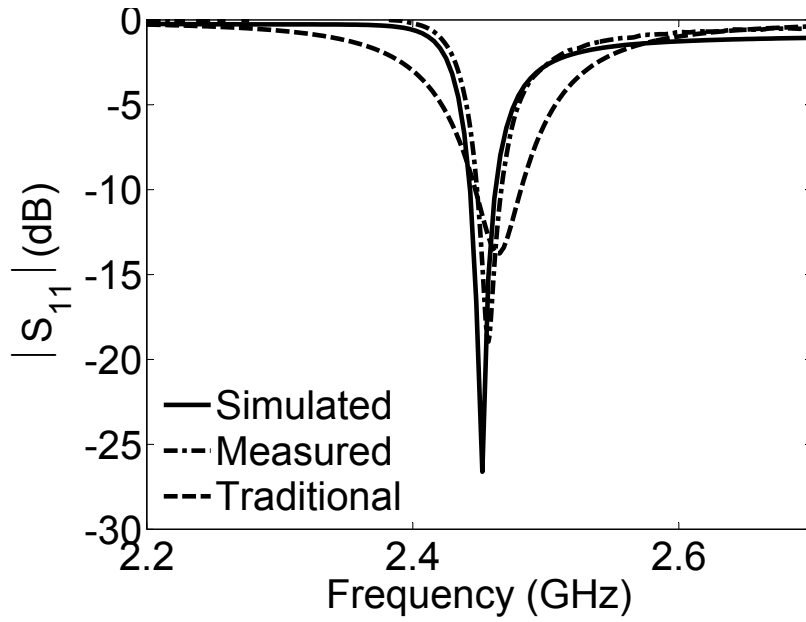
Figure 6.4. Reflection coefficient of the patch antenna miniaturized to 1/9 the area
of the traditional patch (traditional patch reflection coefficient added for reference).
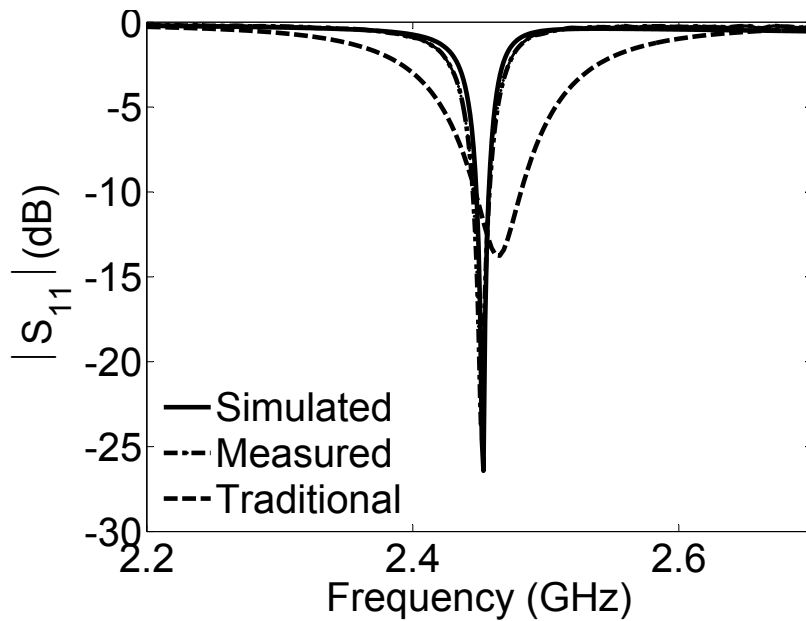
Figure 6.5. Reflection coefficient of the patch antenna miniaturized to 1/16 the area
of the traditional patch (traditional patch reflection coefficient added for reference).
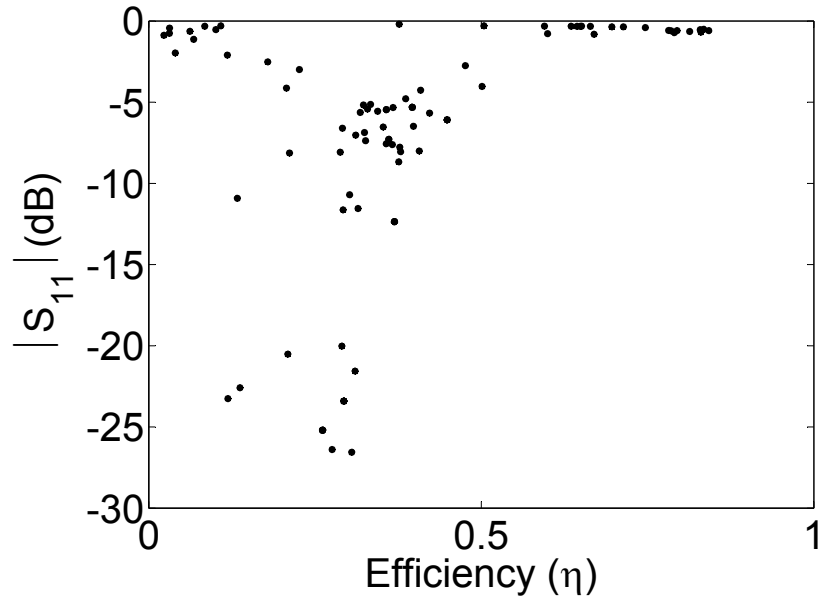
Figure 6.6. Reflection coefficient vs. radiation efficiency of the last population for optimization of a patch antenna miniaturized to 1/16 the area of the traditional patch.
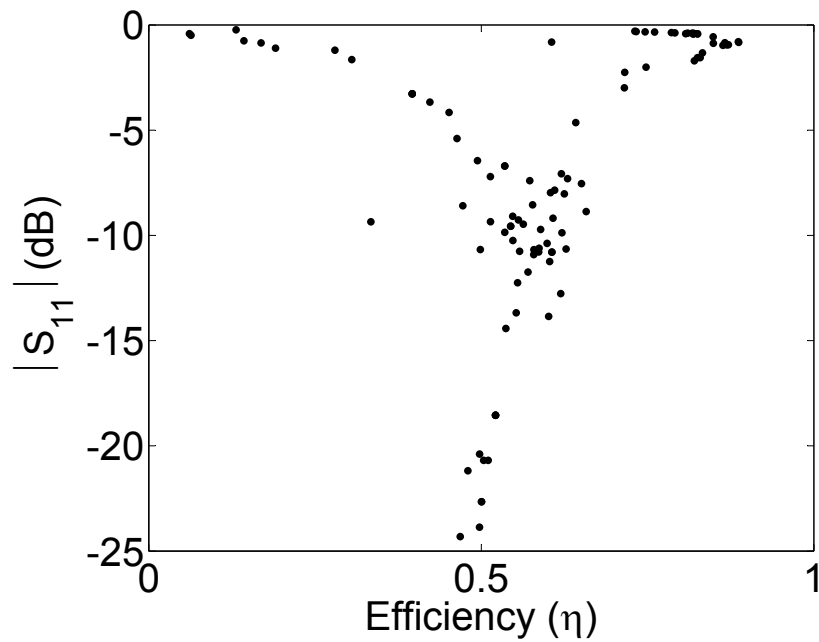
Figure 6.7. Reflection coefficient vs. radiation efficiency of the last population for optimization of a patch antenna miniaturized to 1/9 the area of the traditional patch.
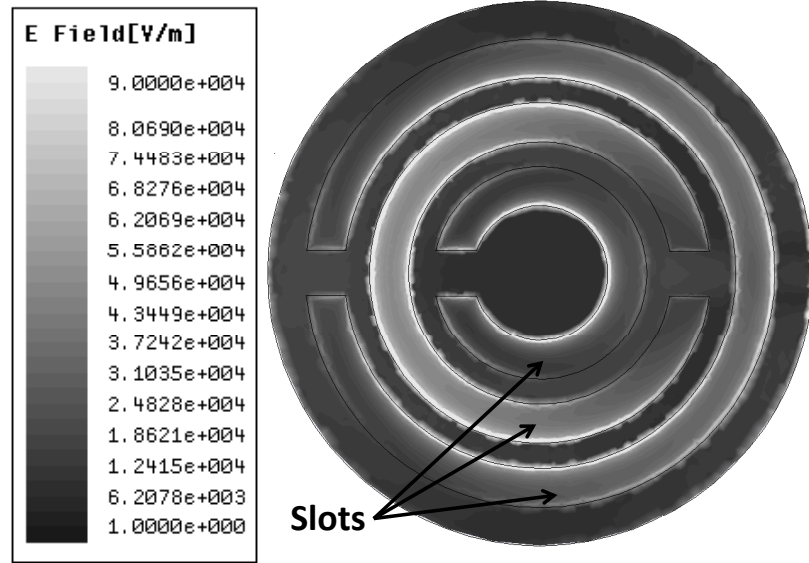
Figure 6.8. Intensity of the electric field on the CSRR structure of the patch antenna miniaturized to 1/16 the area of the traditional patch.
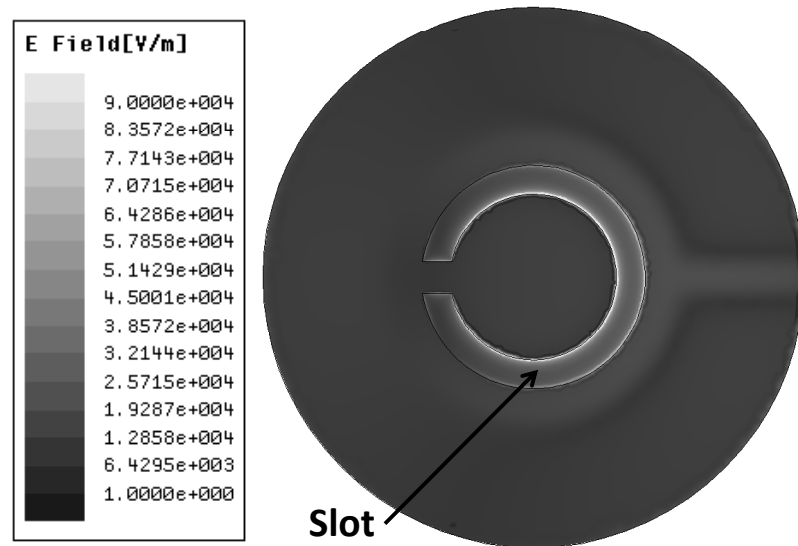
Figure 6.9. Intensity of the electric field on the CSRR structure of the patch antenna miniaturized to 1/9 the area of the traditional patch.
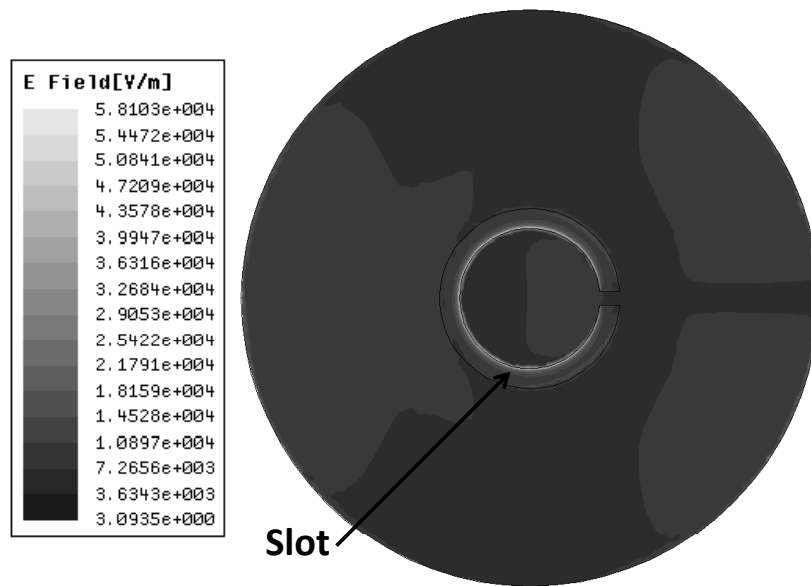
Figure 6.10. Intensity of the electric field on the CSRR structure of the patch antenna

miniaturized to 1/4 the area of the traditional patch.
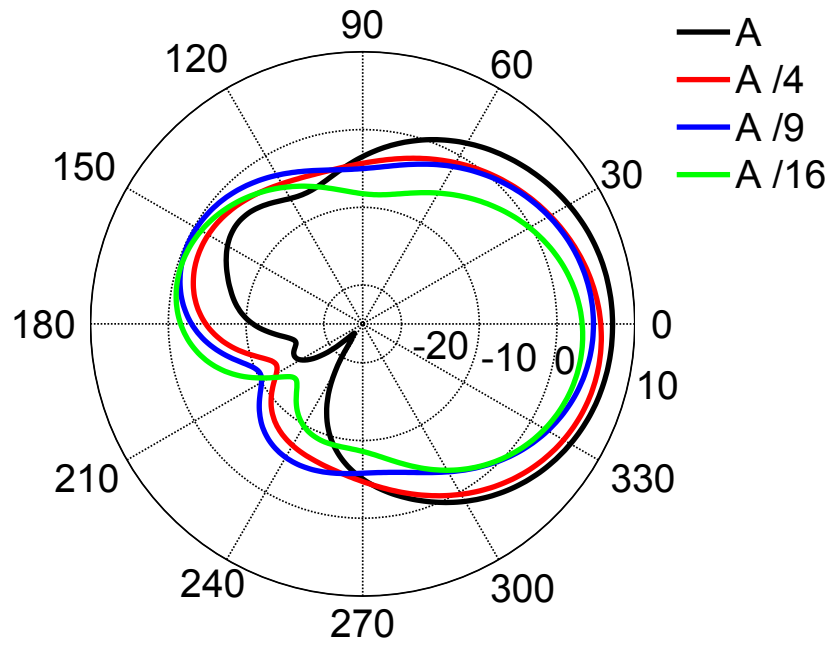
Figure 6.11. Simulated E-plane realized gain patterns of the traditional and minia-
turized patch antennas (10 dB / div). Size reduction is relative to the area of a
traditional patch, A.
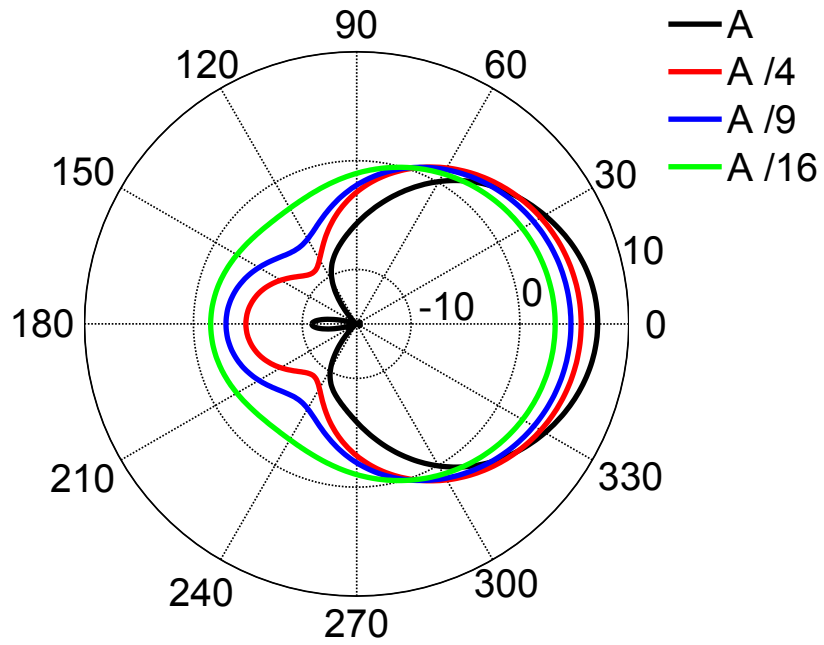
Figure 6.12. Simulated H-plane realized gain patterns of the traditional and minia-turized patch antennas (10 dB / div). Size reduction is relative to the area of a traditional patch, A.
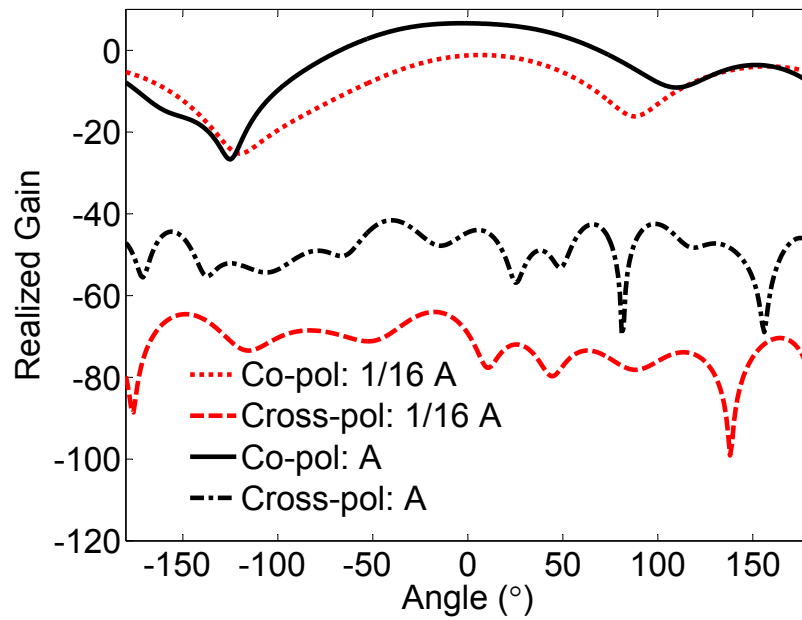
Figure 6.13. Simulated co-polarization and cross-polarization field patterns in the xz plane of the traditional patch antenna and patch antenna miniaturized to 1/16 the area of the traditional patch antenna. Size reduction is relative to the area of a traditional patch, A.
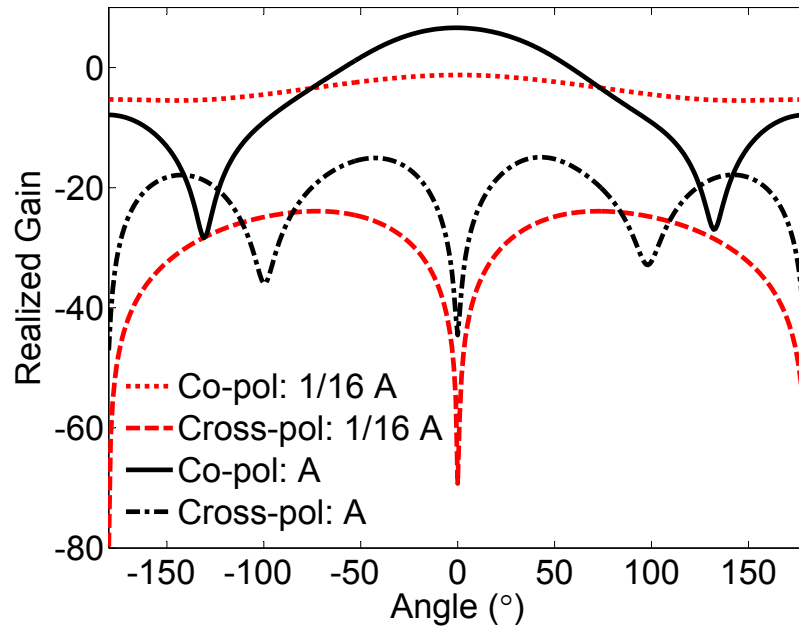
Figure 6.14. Simulated co-polarization and cross-polarization field patterns in the *yz* plane of the traditional patch antenna and patch antenna miniaturized to 1/16 the area of the traditional patch antenna. Size reduction is relative to the area of a traditional patch, A.
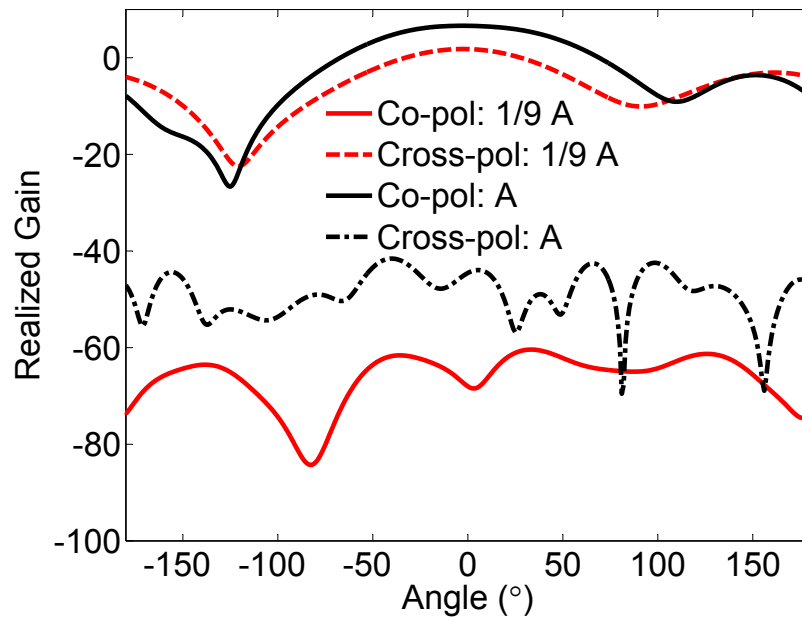
Figure 6.15. Simulated co-polarization and cross-polarization field patterns in the xz plane of the traditional patch antenna and patch antenna miniaturized to 1/9 the area of the traditional patch antenna. Size reduction is relative to the area of a traditional patch, A.
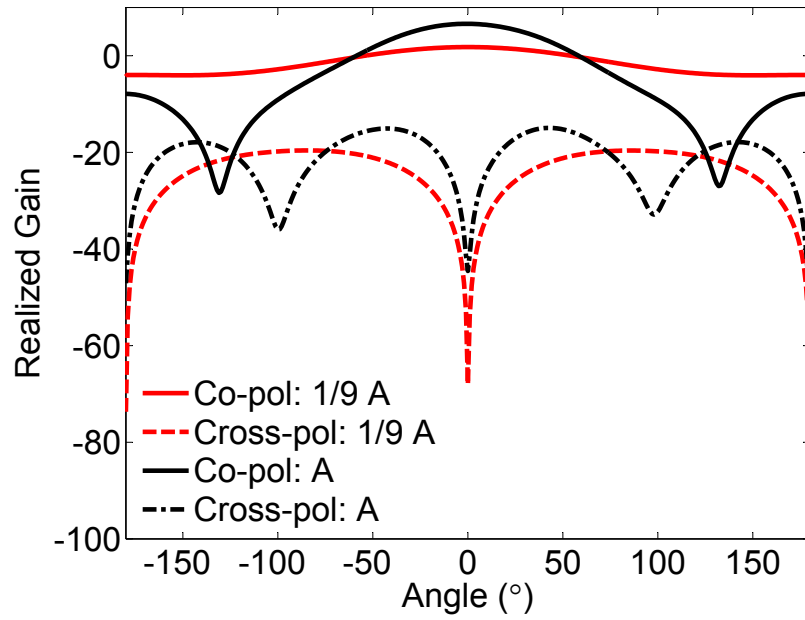
Figure 6.16. Simulated co-polarization and cross-polarization field patterns in the yz plane of the traditional patch antenna and patch antenna miniaturized to 1/9 the area of the traditional patch antenna. Size reduction is relative to the area of a traditional patch, A.
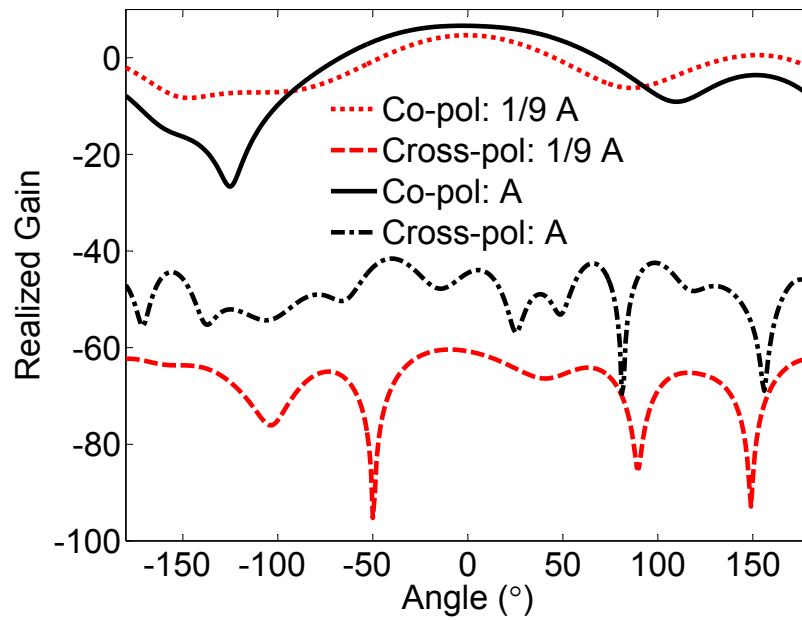
Figure 6.17. Simulated co-polarization and cross-polarization field patterns in the xz plane of the traditional patch antenna and patch antenna miniaturized to 1/4 the area of the traditional patch antenna. Size reduction is relative to the area of a traditional patch, A.
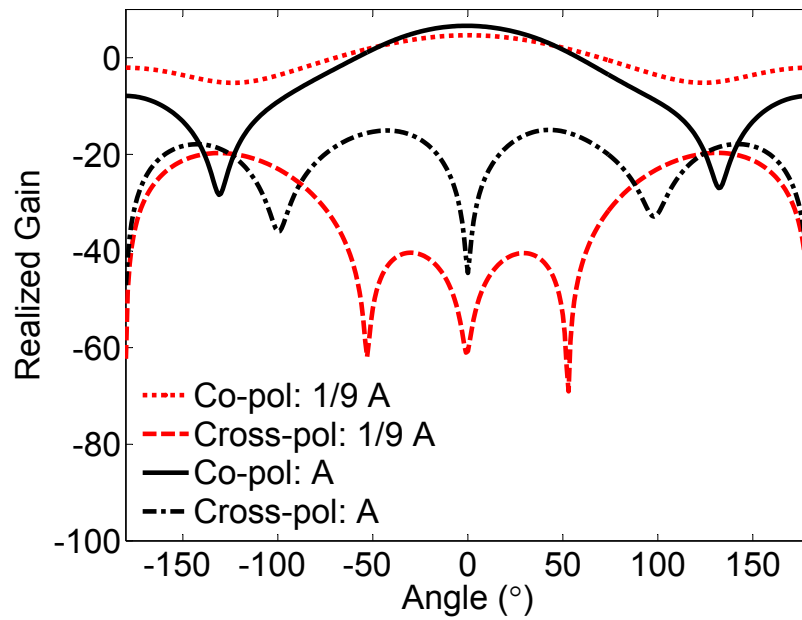
Figure 6.18. Simulated co-polarization and cross-polarization field patterns in the yz plane of the traditional patch antenna and patch antenna miniaturized to 1/4 the area of the traditional patch antenna. Size reduction is relative to the area of a traditional patch, A.
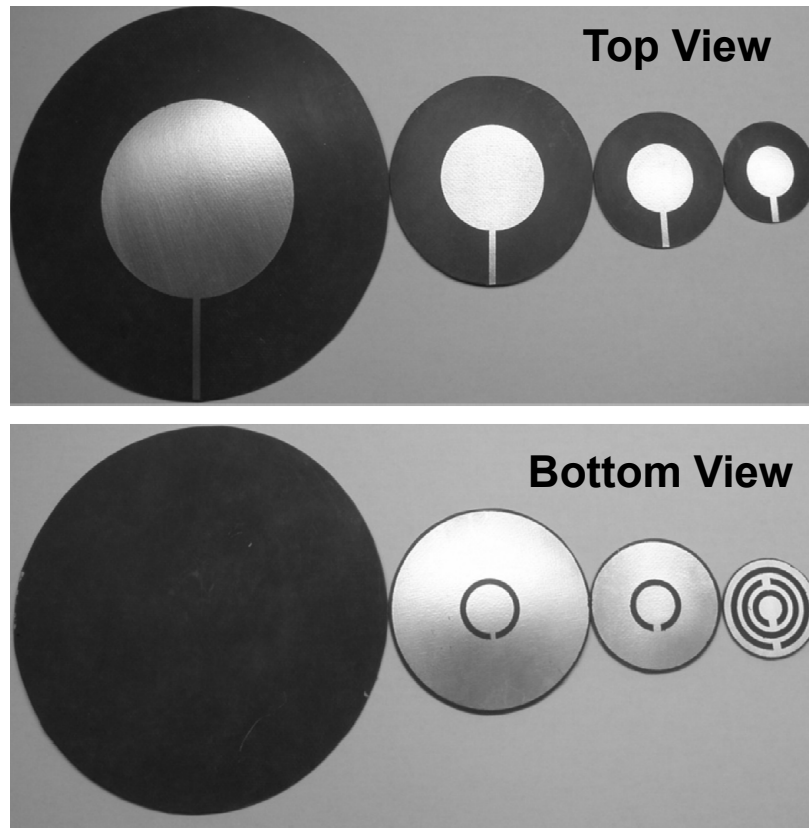
Figure 6.19. First layer of the fabricated traditional circular patch antenna and miniaturized prototypes showing reductions to 1/4, 1/9, and 1/16 of the traditional patch area. The second layer, which includes the ground plane, is not shown.
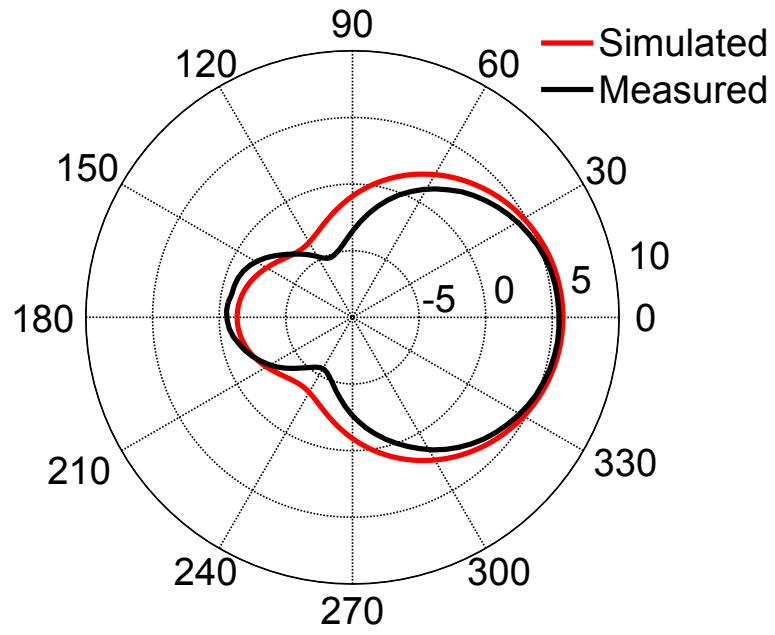
Figure 6.20. Simulated and measured H-plane gain patterns of the patch antenna miniaturized to 1/4 the area of the traditional patch (5 dB / div).
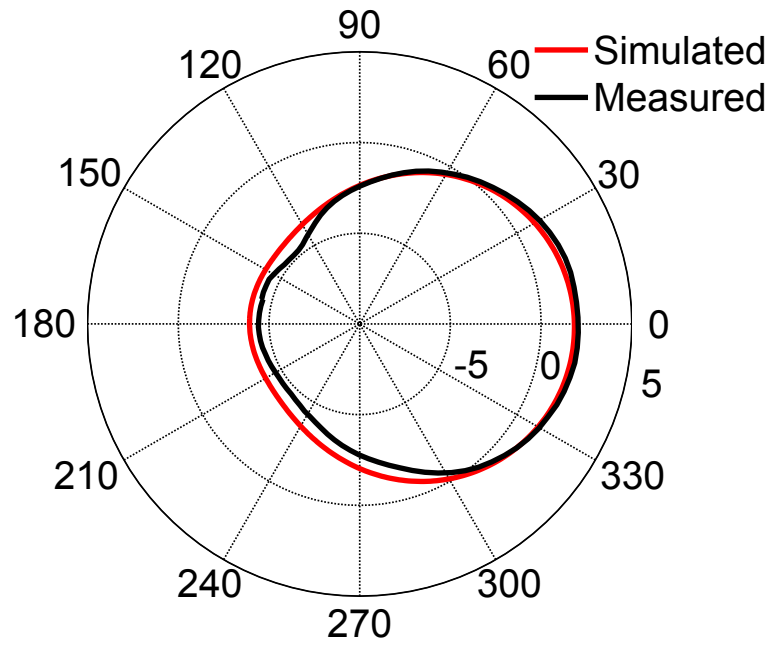
Figure 6.21. Simulated and measured H-plane gain patterns of the patch antenna miniaturized to 1/9 the area of the traditional patch (5 dB / div).
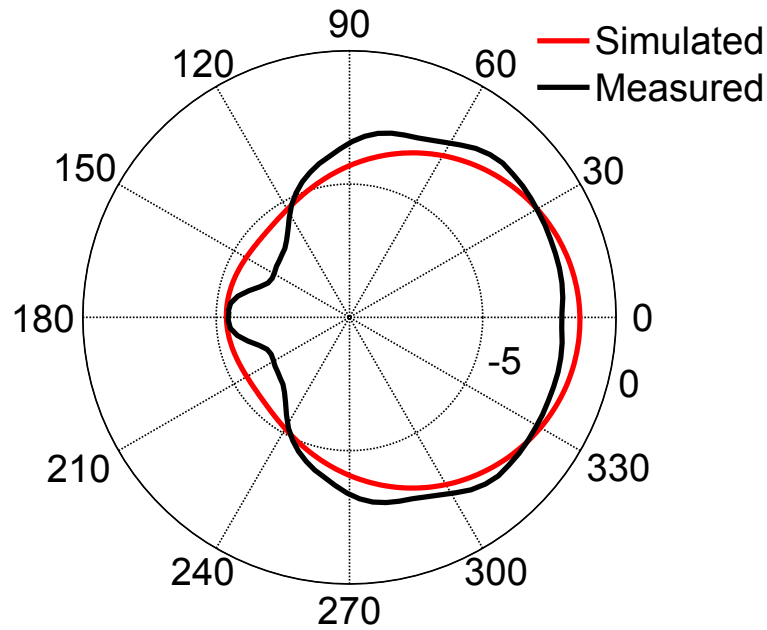
Figure 6.22. Simulated and measured H-plane gain patterns of the patch antenna miniaturized to 1/16 the area of the traditional patch (5 dB / div).

6.5 Conclusion

In this chapter, an in situ optimization technique is used to produce highly miniaturized patch antennas. By adding a single layer containing complementary split-ring resonators to a traditional patch structure, the size of the antenna can be reduced significantly while maintaining the impedance match and the structure of the field pattern. Because the construction is simple, the miniaturized antennas can be produced with little effort at low cost. Feasibility of the proposed technique has been validated by fabricating several miniaturized patch antennas with surface areas as small as one sixteenth that of a traditional patch antenna. Measurements of reflection coefficient

163

and antenna pattern agree well with simulations. Even smaller antennas are possible, but with further size reduction comes a reduction in efficiency and fractional bandwidth that may prove undesirable. Note that although the work presented in this chapter focuses on miniaturization of a circular patch antenna, the proposed design technique can also be used to create broadband or multiband miniaturized patch antennas.

CHAPTER 7

WIDELY TUNABLE METAMATERIAL STRUCTURES BASED ON SPIRALS

In chapters 5 and 6, resonant structures such as complementary split ring resonators and pixelated structures are used as inclusions to miniaturize various types of planar antennas. Although antenna size reductions of 80% or more are demonstrated in each chapter, the miniaturized antennas suffer from a loss of fractional bandwidth. The bandwidth of planar antennas can be increased by using lossier substrates. However, the use of lossy subtrates on miniaturized antennas is not recommended given that most miniaturized antennas also suffer from low radiation efficiencies. An alternative approach to overcome the narrow bandwidth issue is to use tunable resonant structures as inclusions. This chapter investigates the implementation of widely tunable resonant structures that can be used to create reconfigurable metamaterial devices.

7.1 Existing techniques for tuning resonant structures

Numerous techniques have already been proposed by several research groups to create reconfigurable metamaterials. For instance, it is reported in [92] – [97] that the frequency of resonance of an SRR can be varied up to 30% by loading the SRR with varactors (variable capacitors), diodes, or ferroelectric tunable capacitors. Figure 7.1 shows a sketch of an SRR loaded with a varactor at the gap of the outer ring. By changing the capacitance of the varactor, the effective capacitance of the SRR also changes. This alters the frequency of resonance of the SRR, with high capacitance

values leading to lower resonant frequencies.

Using a ring broken into two symmetric structures as shown in Figure 7.2, the authors of [100] showed that it is possible to create a dual-state switchable metamaterial by placing a micro-electromechanical systems switch at the location of one of the gaps. A closed switch state shorts the two symmetric structures at the location of the switch, leading to a ring with a single gap. An open switch state has no effect on the doubly broken ring. This approach leads to only two frequencies of operation.

Mechanical systems have also been used to create tunable metamaterials. It is reported in [101] that it is possible to achieve a 14% tuning range by varying the spacing between two concentrics rings as shown in Figure 7.3. One of the rings is maintained fixed while the other ring is moved back and forth using MEMS. The back and forth movement of the movable ring changes the physical dimensions of the structure leading to different resonant frequencies.

Besides loading the resonant structures with lumped components, it is also possible to achieve frequency tuning of metamaterials by varying the characteristics of the host medium. For instance, the authors of [102] and [103] proposed using vanadium dioxide (VO_2) as a thin coating layer between the dielectric and the array of SRRs, creating a multi-layered structure. VO_2 is a material whose properties change with temperature. Changing the ambient temperature alters the effective permittivity of the host medium composed of the dielectric and VO_2, which alters the frequency of resonance of the metamaterial.

The use of liquid crystals has also been reported as a means to create tunable metamaterials [104] – [107]. Liquid crystals are anisotropic materials that are highly

166

sensitive to external electric fields. Varying the intensity of the incident field alters the effective permittivity of liquid crystals. By using liquid crystals as a host medium, it is possible to tune the frequency of resonance of the metamaterial by changing the intensity of the incident field.

Most of the techniques described above use SRRs as resonant inclusions, and the maximum tunable bandwidth is approximately 30%. Although SRRs are electrically small, since their resonance occurs when the side length of the outer ring is approximately $\lambda_0/10$, they remain physically large at low frequencies. For instance, an SRR resonating at 300 MHz has an outer ring with a side length of approximately 10 cm, and to create a 10 x 10 array of SRRs at 300 MHz would result in a structure that is more than 1 m in size. In this chapter, the tuning of more compact resonant structures such as spiral resonators is investigated. By loading a three turn spiral resonator with a switch and a varactor it shown that a 65% tunable bandwidth can be achieved while maintaining the length of each side of the spiral to less than $\lambda_0/22$ across the tunable band.
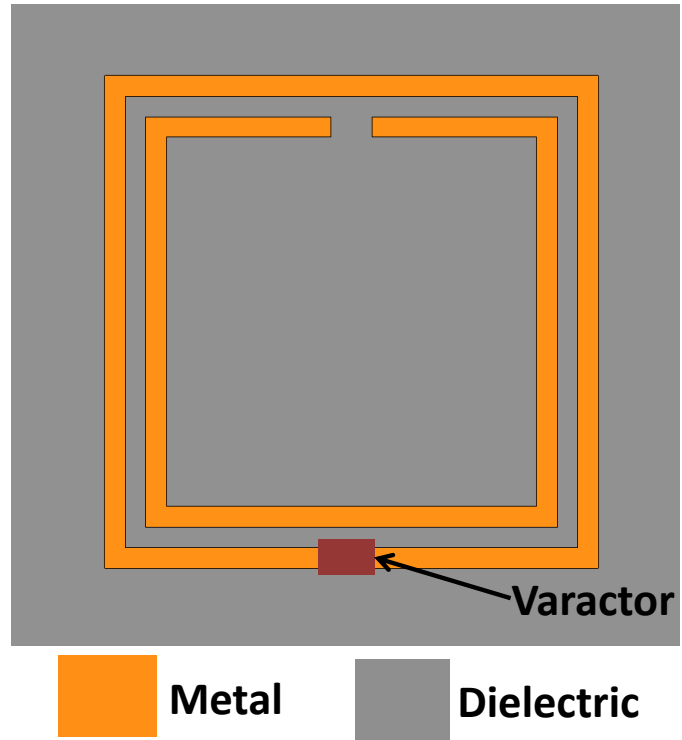
Figure 7.1. Split ring resonator loaded with a varactor.
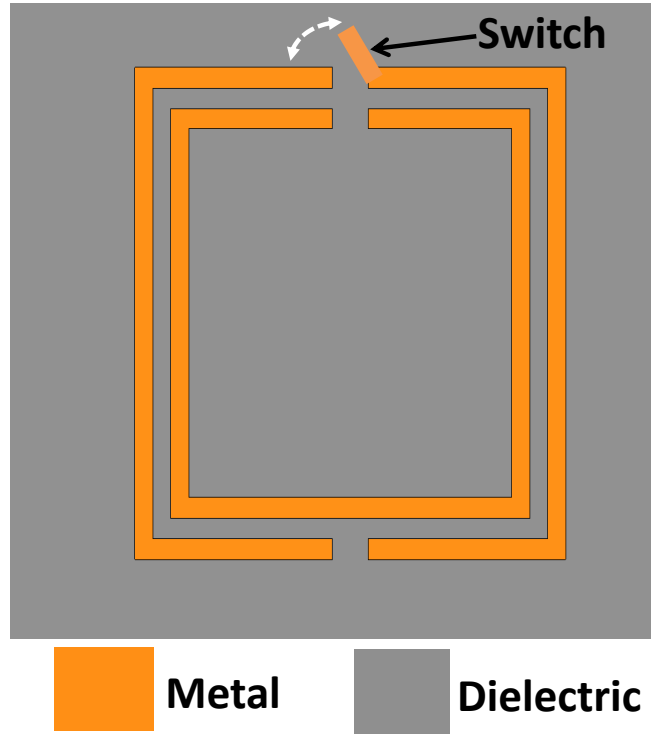
Figure 7.2. Doubly broken SRR with a switch on the outer ring.
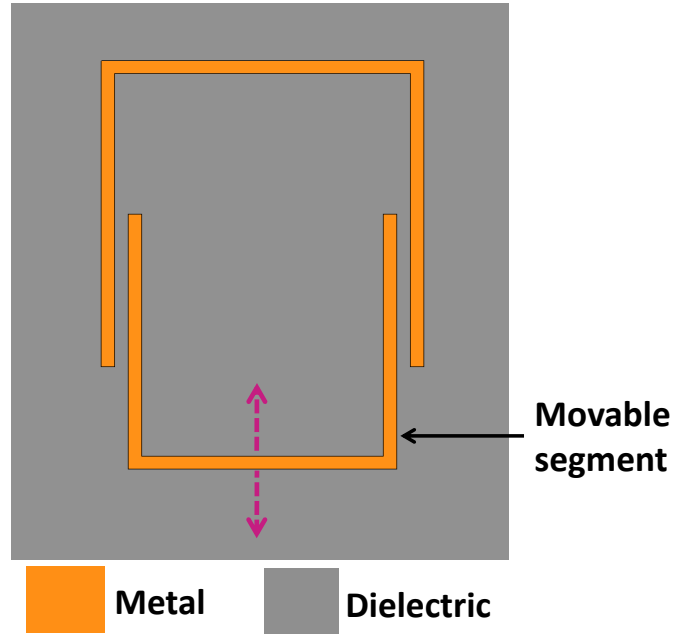
Figure 7.3. SRR with movable inner ring.

7.2   Spiral resonators for the design of reconfigurable metamaterials

A spiral resonator is a planar conducting strip that winds around a fixed center point as shown in Figure 7.4. It was first presented in [2] as an alternative to SRRs for the synthesis of metamaterial media requiring inclusions with dimensions much less than $\lambda_0/10$. The frequency of resonance of the spiral resonator depends on the number of turns of the conducting strip, the width of the strip and the width of the slots between adjacent strips. Increasing the number of turns of the spiral increases both the length of the strip and the length of the slot. This contributes to increasing the effective inductance and capacitance of the spiral, resulting in a downward shift of the frequency of resonance. Besides changing the physical properties of the spirals

to shift the frequency of resonance, any perturbation such as placing capacitors or switches across the slots of the spiral will also alter the spiral's electrical performance and its resonant frequency.

Strip   **Slot**
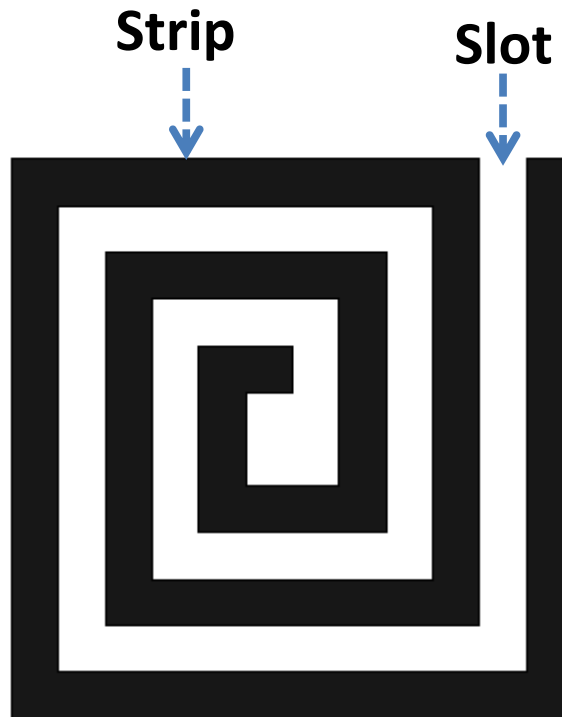
Figure 7.4. Three turn spiral resonator.

7.2.1 Frequency tuning of a spiral resonator using switches

The frequency of resonance of a spiral resonator can be altered by placing switches across the slots of the spiral. A closed switch creates a short between adjacent metalized strips of the spiral, changing the spiral's electrical performance and its resonant frequency. In contrast, an open switch has no effect on the performance of the spiral.

It is difficult to place a large number of switches on the structure of an SRR since

the SRR has a single slot. With spirals, however the number of slots can be increased by increasing the number of turns, and so a larger number of switches can be placed on the spiral. Having a large number of switches increases the possibility of finding switch combinations that can create a spiral resonance at any desired frequency within a reasonable range.

Similar to SRRs, spiral resonators are excited when placed in an environment where the magnetic field is aligned along their axes. Recall from Chapter IV that when an SRR is placed along the longitudinal axis of a rectangular waveguide, a stopband is created within the passband of the waveguide at the frequency of resonance of the SRR. Consequently, frequency tuning of a spiral resonator can be investigated by placing the spiral loaded with the switches along the longitudinal axis of a rectangular waveguide.

Although feasible, placing switches inside a rectangular waveguide might not be ideal in practice since each switch needs to be connected to a minimum of three wires (control, ground, input power) and all three wires have to be extended outside of the rectangular waveguide. This implies that a large hole or several small holes have to be drilled through one of the waveguide walls to create a passage for the wires.

An alternative approach is to use a transmission line as shown in Figure 7.5. In this case, the spiral is connected to the transmission line, creating a transmission line filter. The transmission line without the spiral has near perfect transmission with $|S_{21}| \approx 0$ dB. When the spiral is connected to the transmission line, a stopband occurs near the frequency of resonance of the spiral. Thus, frequency tuning of the spiral can be investigated by monitoring the shift of the frequency at which the stopband occurs as

172

the states of the switches are changed. One of the drawbacks of the transmission line approach is that radiation from the wires connected to the switches can drastically affect the performance of the filter. Radiation from the wires can be suppressed by using lumped components such as inductors.
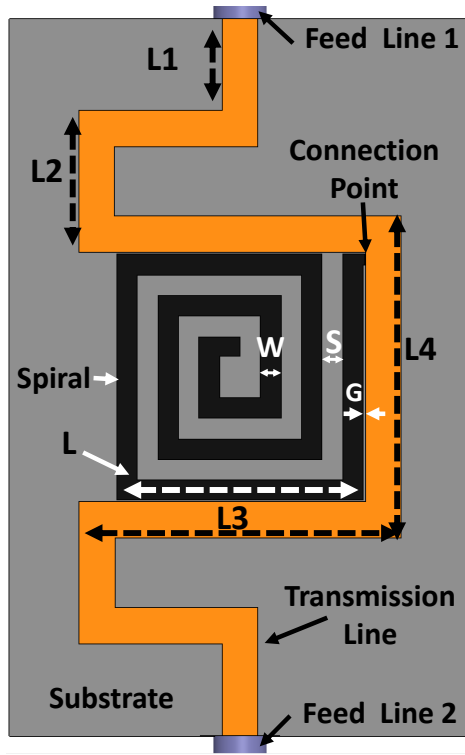
Figure 7.5. Three turn spiral resonator connected to a transmission line.

Simulations of the three turn spiral connected to a transmission line as shown in Figure 7.5 were conducted in HFSS to first determine the resonance of the unloaded spiral. The term unloaded spiral is used here implying the spiral without any switches. The spiral has a strip width $W = 2$ mm and a slot width $S = 2$ mm. The length of the first segment of the spiral is $L = 24$ mm. The width of the strip of the transmission

line is 3.5 mm and the lengths of the segments are $L1 = 12.5$ mm, $L2 = 12.5$ mm and $L3 = L4 = 31.3$ mm. The gap between the spiral and the transmission line is $G = 0.2$ mm. The substrate is a 1.56 mm thick Rogers 5870 RT/duroid with dielectric constant $\epsilon_r = 2.33$ and loss tangent $\delta_t = 0.0013$. A ground plane is placed on the back of the substrate. The two feed lines are modeled as SMA connectors. The simulations were performed from 200 MHz to 1000 MHz with 500 data points.

Figure 7.6 shows a plot of the simulated transmission and reflection coefficients of the structure shown in Figure 7.5. Also shown in Figure 7.6 is a plot of the transmission coefficient of the transmission line without the spiral. As expected the transmission coefficient of the transmission line is near 0 dB throughout the simulated frequency band. However, the transmission coefficient of the transmission line loaded with the spiral shows a stopband centered at 382.4 MHz, which corresponds to the resonance of the spiral. At that frequency, the value of the transmission coefficient is -28.52 dB and the -10 dB bandwidth of the stopband is 10.9 %. It should be pointed out that the largest dimension of the spiral is 24 mm, which corresponds to $\lambda_0/32.7$

at the resonance frequency of 382.4 MHz.
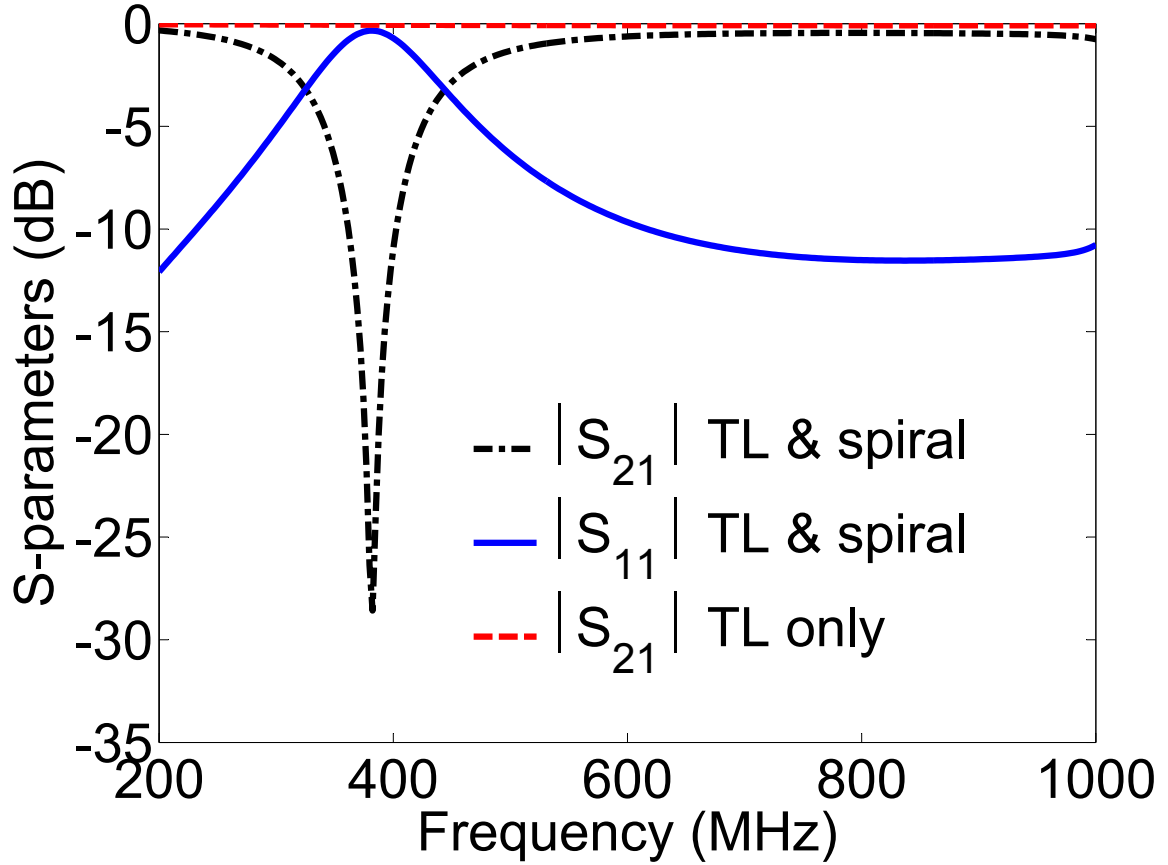
Figure 7.6. S-parameters of the transmission line (TL) connected to the spiral. The transmission coefficient of the transmission line is added for reference.

To investigate the impact of creating a short between two adjacent strips of the spiral resonator, eleven conducting strips are placed across the slots of the spiral as shown in Figure 7.7. All eleven strips are identical and have dimensions of 2 mm by 0.5 mm. To simulate the presence of switches at the location of the strips, the conductivity of each strip is assigned a value of 0 S/m or 5.8×10^{7} S/m. A value of 0 S/m represents an open switch and has no impact on the spiral while a value

of 5.8 x 10^7 S/m creates a short at the location of the strip, representing a closed switch. Given that each switch has two states, eleven switches lead to a total of 2^{11} or 2048 switch states or switch combinations. Before running an exhaustive search to determine the frequency shifts caused by all 2048 switch combinations, eleven simulations were performed. In each simulation, only one switch was closed while the remaining ten were left open.

Figure 7.8 shows plots of the transmission coefficients obtained from all eleven simulations. Also shown in Figure 7.8 is the transmission coefficient of the spiral with all switches open. The frequency of resonance of the spiral with all switches open is 382.4 MHz. The figure shows an interesting trend. The closer a switch is to the center of the spiral, the least effect it has on the frequency of resonance of the spiral. This is expected since large turns of the spiral lead to bigger frequency shifts compared to smaller turns. For instance, closing switch 1 only shifts the frequency of resonance from 382.4 MHz to 385.01 MHz, leading to a frequency shift of just 2.61 MHz or 0.68 %. On the other hand, closing switch 11 shifts the frequency of resonance from 382.4 MHz to 718.4 MHz, resulting in a frequency shift of 336 MHz or 61.04 %.

To run the exhaustive search, a Matlab code was written to generate all 2048 switch combinations as binary strings that are eleven bits long. In each binary string, the first bit starting from the left is used to encode the state of switch 1 or P1 as shown in Figure 7.7, the second bit from the left is used to encode the state of switch 2 or P2, and so on until the last bit which is used to encode P11. The conductivity of each strip is determined by the value of the corresponding bit within each binary string. For instance the binary string 10000000000 corresponds to switch 1 closed

176

and all remaining ten switches open. As such, strip P1 is assigned a conductivity of 5.8×10^7 S/m while the remaining strips are assigned a conductivity of 0 S/m. For each switch combination, the structures of the transmission line, spiral and conducting strips with their equivalent conductivity assignments are created in Matlab and exported to HFSS for simulation. Once the simulation is completed, the transmission coefficient is exported back to Matlab and stored into a 2048 x 500 matrix.

Figure 7.9 shows a plot of the minimum value of the transmission coefficient and the frequency at which the minimum occurred for all 2048 switch combinations. Observe from the figure that the minima of the transmission coefficients are grouped into eight main clusters and the transmission coefficients are maintained below -25 dB. The largest cluster contains 1024 data points spread over a frequency span from 718.4 MHz to 796.6 MHz. Note that 718.4 MHz is the frequency of resonance of the spiral with just switch 11 closed and 1024 is equivalent to 2^{10}. This suggests that while switch eleven is closed, closing any other switch contributes to shifting the frequency of resonance higher than having just switch eleven closed. The fact that the total number of data points within the cluster is 1024 suggests that the largest cluster corresponds to all the switch combinations with switch eleven closed.

The second largest cluster contains 512 data points spread over a frequency span from 622.0 MHz to 663.7 MHz. The frequency of resonance of 622.0 MHz corresponds to the resonance of the spiral with just switch 10 closed and 512 is equivalent to 2^9. This suggests that the second largest cluster corresponds to all the switch combinations with switch 10 closed and switch eleven open. A count of the number of data points in the remaining cluster reveals that the sizes of the clusters decrease by a

factor of two. That is, the third largest cluster contains 256 data points, the fourth largest cluster contains 128 data points and so on.

From Figure 7.9 it can also be seen that there are frequency gaps where there is no resonance. It is possible to fill these gaps by reducing the spacing between the switches or increasing the number of switches on the spiral. Reducing the spacing between switches will result in a smaller tuning range.
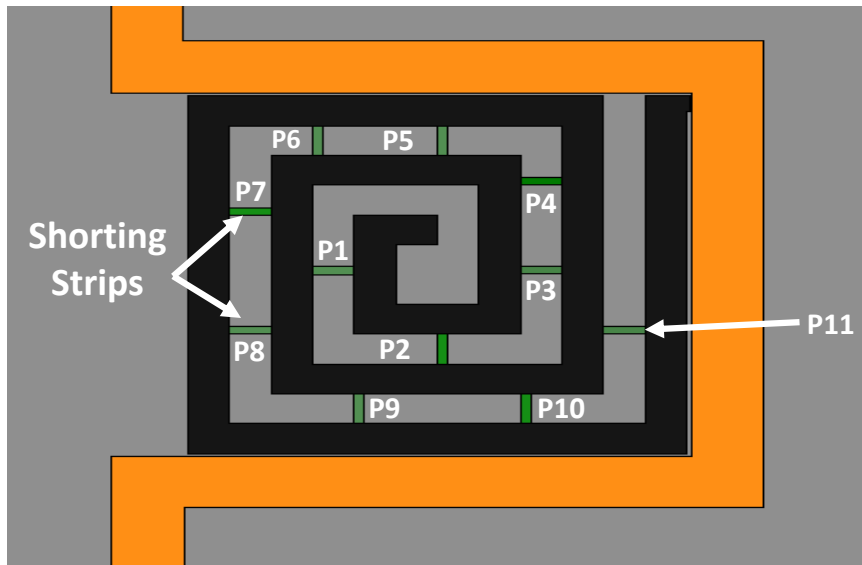
Figure 7.7. Spiral loaded with eleven conducting strips. The conducting strips are used as switches.
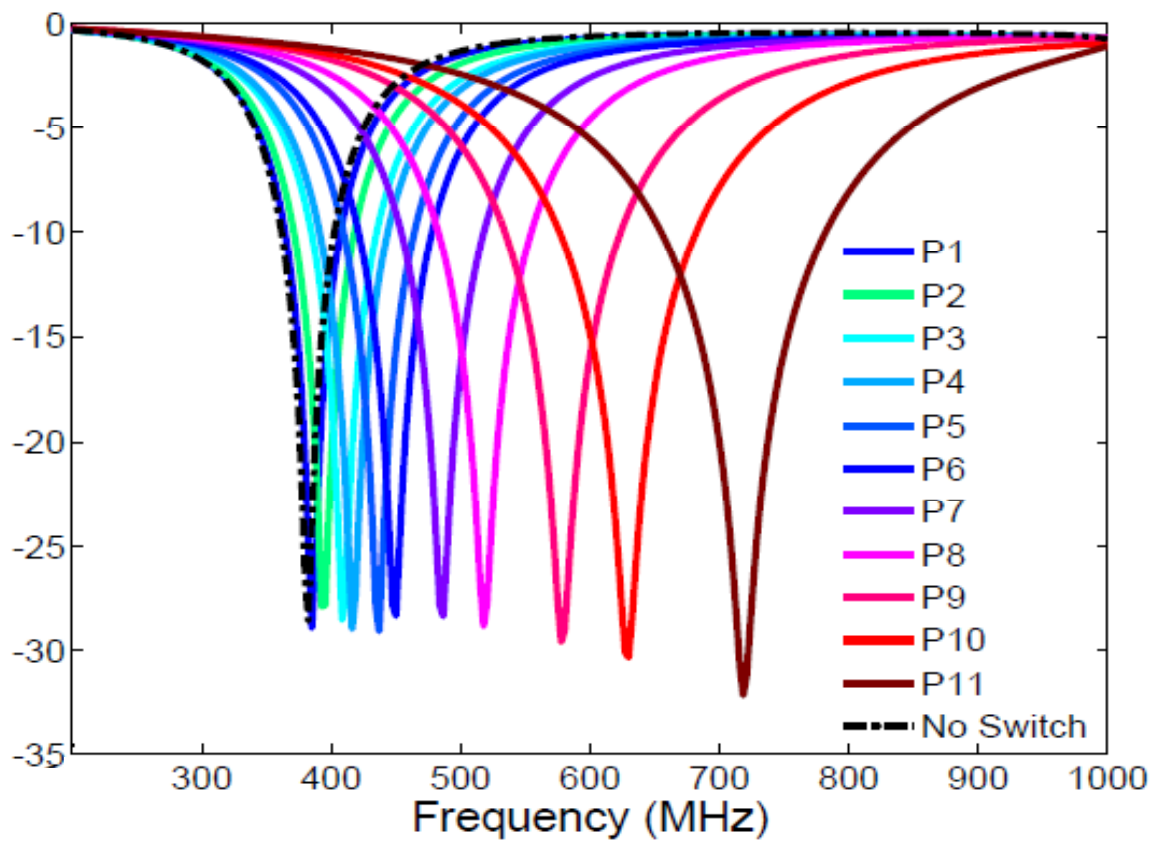
Figure 7.8. Transmission coefficient of the loaded spiral with the switches closed one at a time.
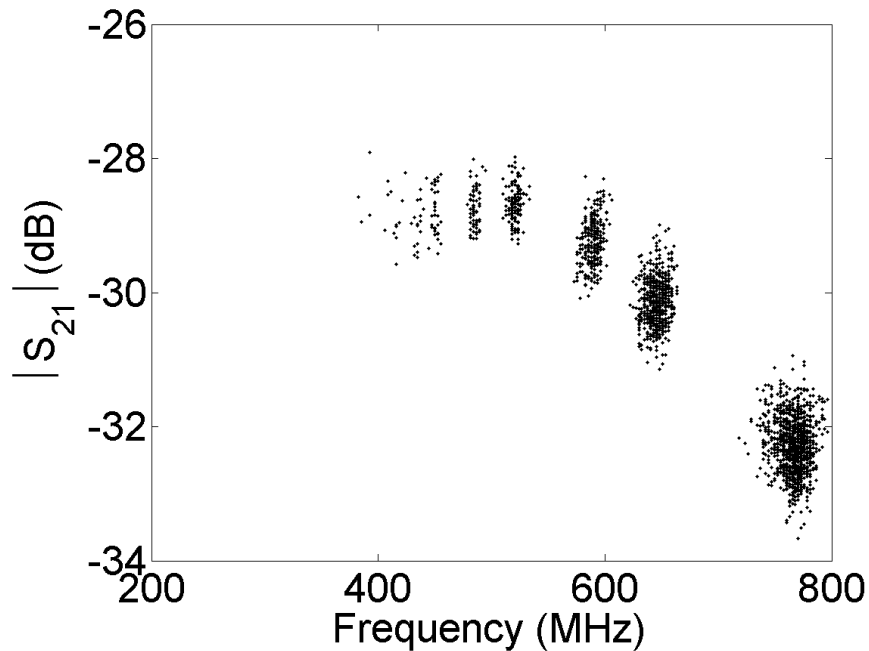
Figure 7.9. Frequency of resonance and corresponding transmission coefficient values for all 2048 switch combinations. (I still have to annotate this plot based on what we discussed).

7.2.2 Spiral tuning through varactor loading

The simulations were performed assuming switches modeled as simple strips of copper. Practical switches introduce approximately a 1 dB loss into the system for each switch and using a very large number of switches could lead to a very lossy system. Another issue is the small size of the spiral. The smallest switches available to the author are surface mount switches which are approximately 2.5 mm by 1.5 mm and to place a large number of these switches on a spiral that is just 24 mm by 24 mm is not an easy task. Moreover, several lumped components such as capacitors and resistors have

to be used with each switch, thus increasing both the complexity and surface area required to properly implement each switch. For these reasons, the use of varactors was investigated.

A three turn spiral with the same dimensions as provided in Section 7.2.1 is used and a varactor is placed across one of the slots of the spiral as shown in Figure 7.10. In practice, the two pins of the varactor are also connected to a DC ground and a power supply. To prevent the varactor from shorting, it is necessary to create a gap on the strip of the spiral to isolate the two pins of the varactor. Placing a gap on the strip of the spiral prevents RF current from flowing on the entire length of the strip. However, it is possible to maintain DC isolation between the two pins of the varactor while allowing the RF current to flow by placing a capacitor at the location of the gap. The value of the capacitor is selected such that the impedance of the capacitor is infinite at DC and near zero at the frequency of interest. In the present case, a 100 pF capacitor is used.

The impedance of a capacitor is $Z_C = \dfrac{1}{j2\pi fC}$ Ω where f is the frequency and C is the capacitance. At DC, $f = 0$ and the impedance of the capacitor is $Z_C = \infty$ which is equivalent to having an open circuit. At the frequency of interest, which is around 400 MHz, $Z_C = -j3.9$ Ω and the capacitor is approximately a short.

The capacitance of the varactor was varied from 2 pF to 9 pF in increments of 0.5 pF. The range of 2 pF to 9 pF was selected based on the characteristics of a varactor available to the author. More information about the varactor is provided in the next section. Figure 7.11 shows plots of the transmission coefficients of the structure of Figure 7.10 for each value of capacitance used for the varactor. As the

capacitance of the varactor is increased, the frequency of resonance of the spiral shifts downwards. The downward shift is expected since the varactor is place in parallel with the slot of the spiral. Increasing the capacitance of the varactor also increases the capacitance of the spiral, which results in a downward shift of the frequency of resonance.

The advantage of using varactors over switches is that a single varactor can be used to achieve a continuous tuning of the frequency of resonance of the spiral. The tuning range is determine by the range of capacitance values of the varactor. The capacitance of the varactor used in this example can be varied from 2 pF to 9 pF and the resulting tunable bandwidth of the spiral is 26.2 %.
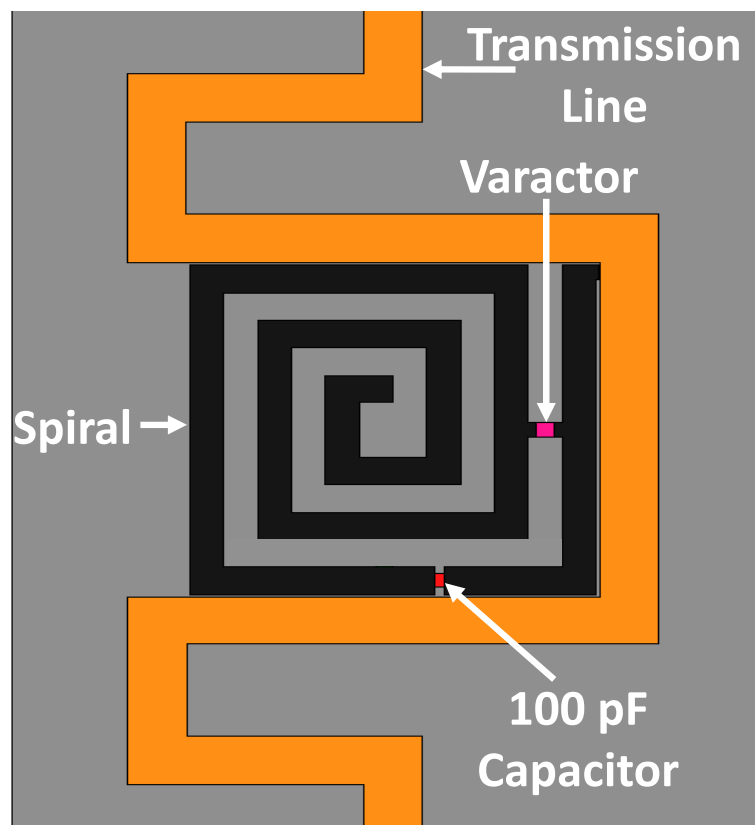
Figure 7.10. Three turn spiral loaded with a varactor.
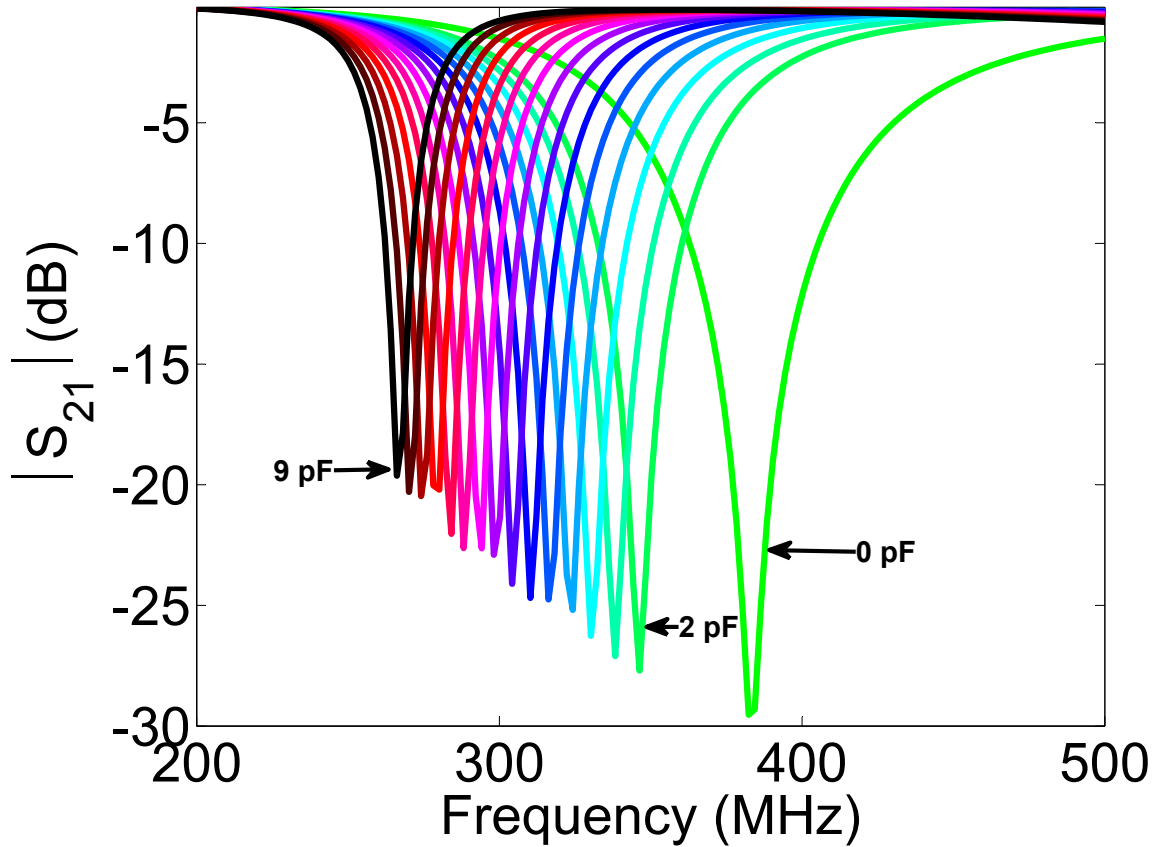
Figure 7.11. Simulated transmission coefficients of the structure of Figure 7.10 for different capacitance values.

7.2.3 Spiral tuning using a switch and a varactor

It is possible to achieve a continuous frequency tuning over a frequency range wider than what can be achieved with eleven switches by using a single switch and a varactor. From Figure 7.8 and Figure 7.11 it can be seen that changing the states of the switches shifts the frequency of resonance of the spiral up while increasing the capacitance of the varactor shifts the frequency of resonance of the spiral down. By

loading the spiral with a varactor and a switch as shown in Figure 7.12, the frequency of resonance of the spiral can be tuned continuously over a wide frequency range.

For instance, assume a spiral resonator with an initial frequency of resonance of 500 MHz. If loading the spiral with a varactor can provide a continuous frequency tuning over a 100 MHz span, then the location of the switch on the spiral should be selected such that when the switch is closed, the frequency of resonance of the spiral shifts from 500 MHz to 600 MHz. Therefore, when the switch is open, the frequency of resonance of the spiral can be tuned from 500 MHz to 400 MHz by varying the capacitance of the varactor. When the switch is closed, the frequency of resonance of the spiral shifts to 600 MHz and continuous frequency tuning can be achieved from 600 MHz to 500 MHz by varying the capacitance of the varactor. Thus by combining a switch and a varactor, continuous tuning of the spiral can be achieved from 600 MHz to 400 MHz. Frequency tuning of the three turn spiral using this approach was investigated experimentally.

Figure 7.13 and Figure 7.14 show a front view and a back view, respectively, of a prototype three turn spiral loaded with a varactor and a switch. The prototype is a multi-layered structure composed of two different circuit boards which were etched through a photolithographic process and glued together using cyanoacrylate (super glue). The first circuit board is a 1.56 mm thick Rogers 5870 RT/duroid with dielectric constant $\epsilon_r = 2.33$ and loss tangent $\delta_t = 0.0013$. The second circuit board is a 1.56 mm thick FR4 epoxy with a dielectric constant $\epsilon_r = 4.4$ and loss tangent $\delta_t = 0.02$.

The spiral and the transmission line were etched onto the top layer of the Rogers board as shown in Figure 7.13. The dimensions of the spiral and transmission line are

the same as those used in the simulations. Also shown on the top layer of the Rogers board is a 100 pF capacitor and a varactor. The varactor used is model SMV1413-SC-79 from Skyworks Inc. [117]. Figure 7.15 shows a larger view of the varactor and a graph providing the different capacitance values of the varactor as a function of the input voltage. The bottom layer of the Rogers board (not shown) is just copper and serves as a ground plane for the transmission line. The FR4 epoxy is a single sided board on which the traces needed for the switch were etched as shown in Figure 7.14. Note that several traces were etched so that the switch can be placed in one of several locations. The switch shown is a PE-4242 Cmos switch from Peregrine Semiconductors [118]. The capacitor and resistor shown in Figure 7.14 have values of 100 pF and 100 kΩ, respectively. The control voltage of the switch is 3 V.

The transmission coefficient of the spiral loaded with both the switch and varactor was measured with the switch open and closed. For each state of the switch, the input voltage of the varactor was varied from 0 V to 2 V in increments of 0.25 V and from 2 V to 20 V in increments of 2 V. Although Figure 7.15 shows that the input voltage of the varactor can go up to 30 V, it was observed that increasing the input voltage beyond 20 V produced very little shift of the frequency of resonance of the spiral. A 200 Ω resistor was placed in series with the input voltage line of the varactor as a preventive measure.

Figure 7.16 shows plots of the measured transmission coefficients of the prototype. When the switch is open and the input voltage of the varactor is 20 V, the capacitance of the varactor is approximately 2 pF and the resonance of the spiral occurs at 339.4 MHz, with a transmission coefficient of -23.3 dB. The simulated spiral loaded

with a 2 pF capacitor (Figure 7.11) has a resonance frequency of 346.3 MHz with a transmission coefficient of -27.7 dB. There is a frequency shift of just 5.9 MHz between the measured and simulated resonances. This small shift in resonance is acceptable given that the simulations were performed assuming an ideal environment.

With an input voltage of 0 V, the capacitance of the varactor changes to approximately 9 pF, which results in a shift of the frequency of resonance of the spiral from 339.4 MHz to 261.9 MHz with a transmission coefficient value of -14.88 dB. In the simulation, changing the capacitance from 2 pF to 9 pF shifts the frequency of resonance from 346.3 MHz to 266.1 MHz. The frequency tuning range of the measured spiral with the switch open is from 261.9 MHz to 339.4 MHz, resulting in a tunable bandwidth of 77.5 MHz, or 25.77 % at the center frequency of 300.65 MHz. The tunable bandwidth from the simulation is 26.2%.

The measured transmission coefficients of the spiral with the switch closed are also shown in Figure 7.16. When the input voltage of the varactor is 0 V, producing a 9 pF capacitance, the frequency of resonance of the spiral occurs at 370.6 MHz with a transmission coefficient value of -13.04 dB. As the input voltage is increased, the capacitance produced by the varactor decreases and the resonance of the spiral increases. At 20 V, the capacitance of the varactor is 2 pF and the frequency of resonance of the spiral occurs at 509.4 MHz with a transmission coefficient of -26.99 dB. The tunable bandwidth achieved with the switch closed is 138.8 MHz or 31.5 % at the center frequency of 440 MHz. Overall, the frequency of resonance of the spiral loaded with just a switch and a varactor can be continuously tuned from 261.9 MHz to 509.4 MHz, producing a tunable bandwidth of 247.5 MHz which corresponds to

65.4 % at the center frequency of 378.45 MHz. This tunable bandwidth is wider than

the one achieved with all eleven switches. Note from Figure 7.16 that there is a small

gap around 350 MHz, which is 16 MHz wide. The gap can be avoided by changing

moving the switch closer to the center of the spiral.
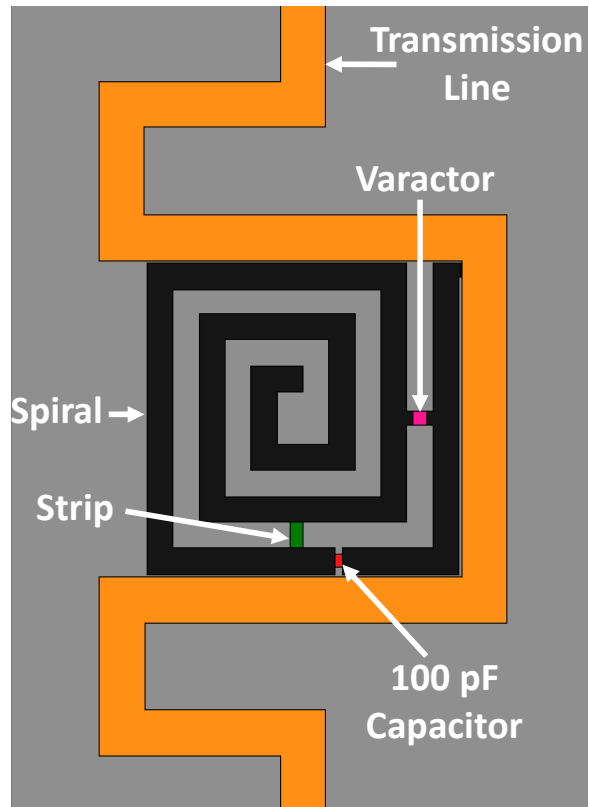
Figure 7.12. Spiral loaded with a switch and a varactor.
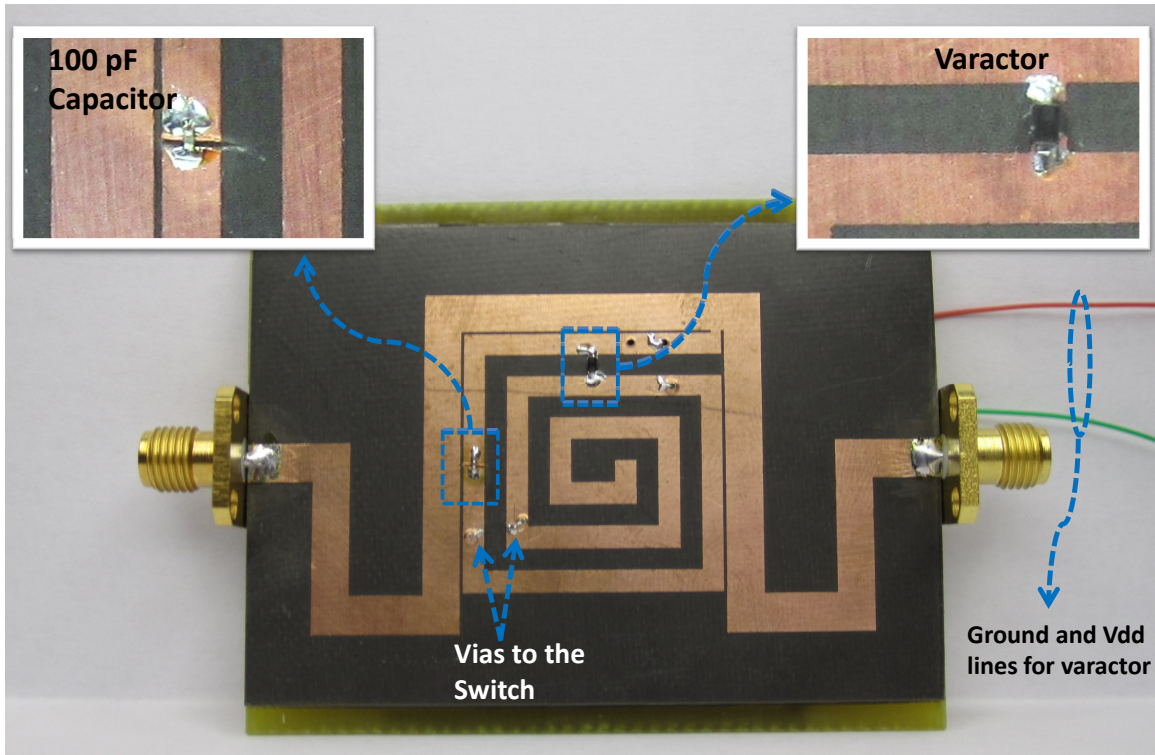
Figure 7.13. Top view of the prototype showing the transmission line, the spiral, the 100 pF capacitor, the varactors and the vias connecting the spiral to the switch (the switch is not shown).
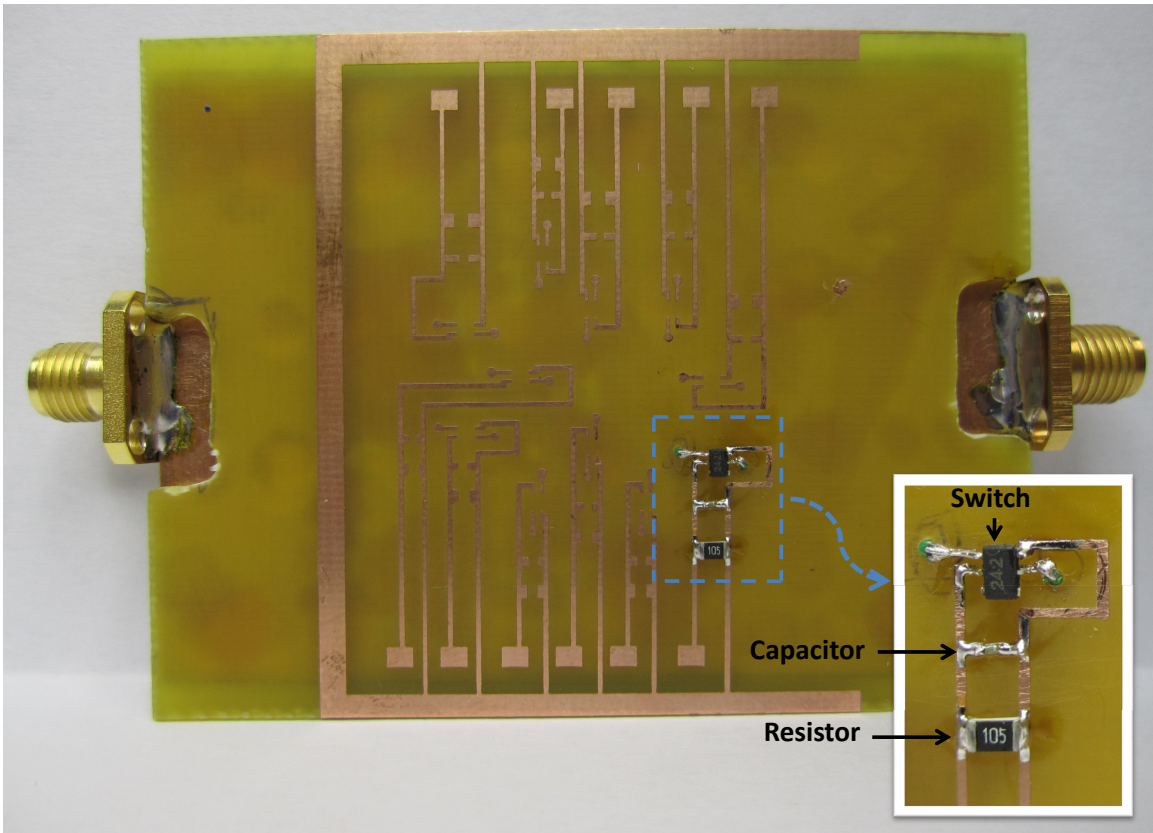
Figure 7.14. Bottom view of the prototype showing the switch.
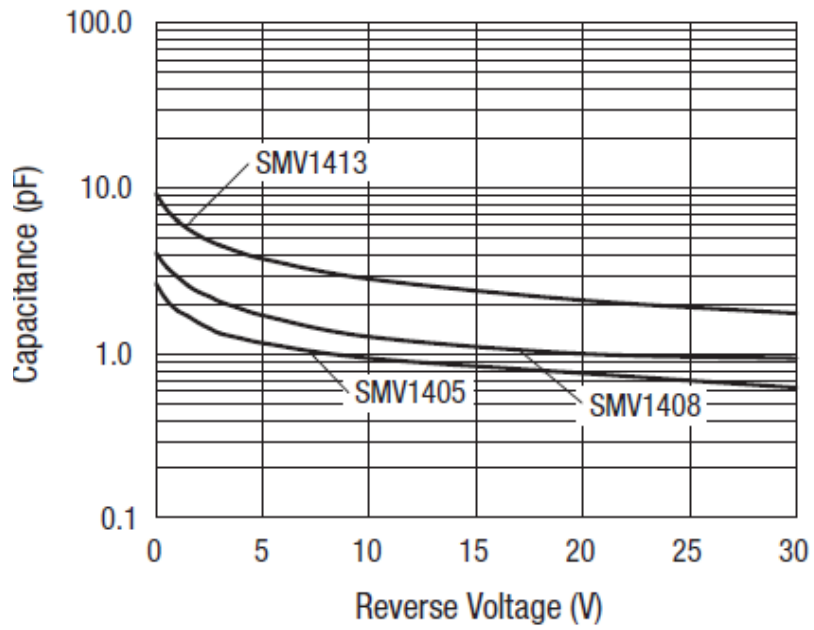
Figure 7.15. Data sheet showing the capacitance of the varactor as a function of voltage. Image taken from http://www.skyworksinc.com/.
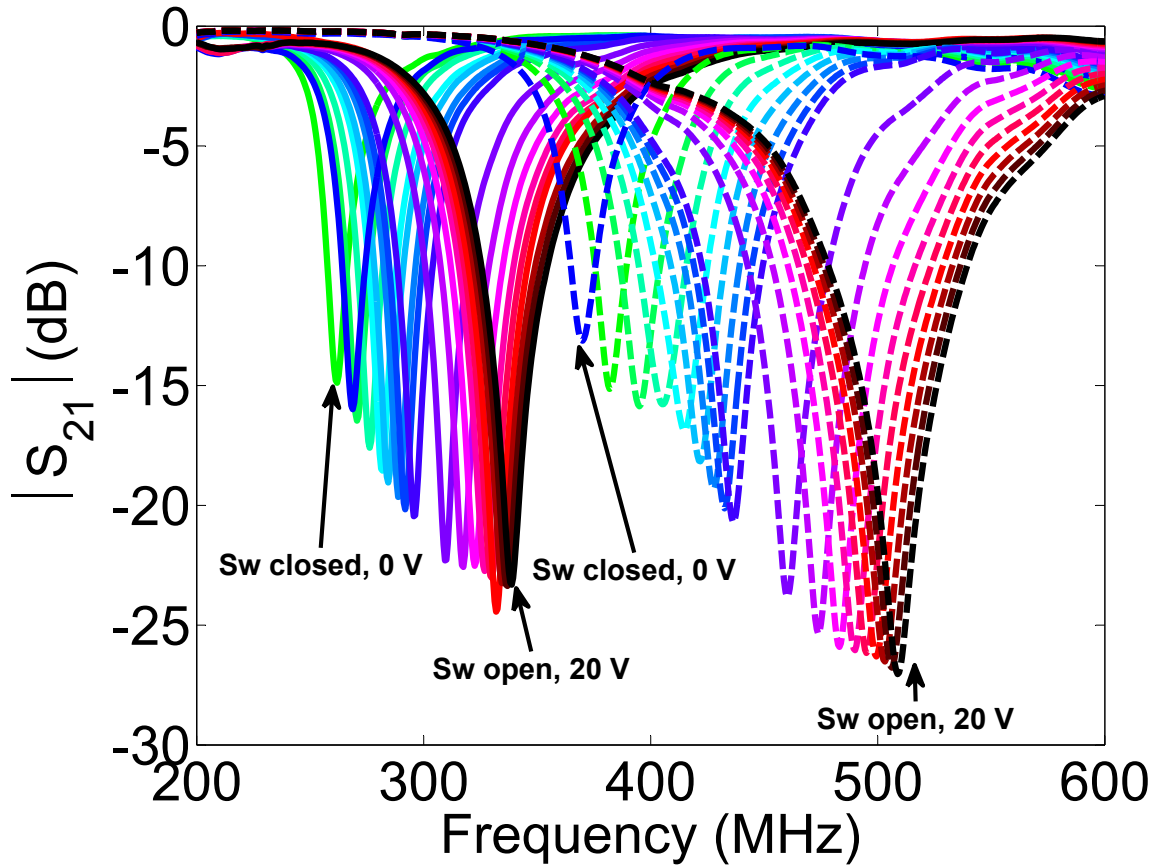
Figure 7.16. Measured transmission coefficients of the prototype. Sw is short for switch.

7.3   Conclusion

Frequency tuning of a spiral resonator is demonstrated in this chapter. By loading the spiral with a switch and a varactor at the right locations, it is possible to continuously tune the frequency of resonance of the spiral over a broad frequency range. Experiments performed using a three turn spiral resonator show that it is possible to tune the frequency of resonance of the spiral from 261.9 MHz to 509.4 MHz, resulting in a 65.4 % tunable bandwidth. At 509.4 MHz, the side length of the spiral is $\lambda_0/24.5$

compare to $\lambda_0/47.7$ at 261.9 MHz. The tuning approach presented in this chapter could be impleted with other resonant structures such as SRRs.

CHAPTER 8

CONCLUSION

In this dissertation, a new design methodology that can be used to synthesize new resonant structures for the design of metamaterial media has been introduced. By using a pixelization approach with a binary optimizer such as a genetic algorithm, it is shown that for prescribed unit cell dimensions it is possible to synthesize multiple structures, all resonating at the same frequency, but with different permeability values. Also introduced in this dissertation is an in situ optimization technique which can be used as an effective means to naturally compensate for the mutual coupling between metamaterial elements and the surrounding RF components.

The pixelization approach, the genetic algorithm and examples of synthesized resonant structures are presented in Chapter 3. In Chapter 4, the pixelization approach is used to create compact stopband waveguide filters with strong rejection of the transmitted signal within the stopband, with high insertion loss and sharp band edges. In Chapter 5, the in situ optimization technique and the pixelization approach are used to create ultra-compact folded monopole and loop antennas that fit into a hemisphere of radius $a = \lambda_0/29.2$ by optimizing the geometry of a pixelated metallic patch in close proximity to the antennas.

In Chapter 6, the in situ optimization technique is used to create sub-wavelength patch antennas with surface areas that are at least sixteen times smaller than the area of a traditional patch antenna while maintaining good impedance match and radiation

characteristics comparable to those of the traditional patch antenna on a finite ground plane. The miniaturized patch antennas are created by optimizing the geometry of complementary split rings placed horizontally between the radiating patch and the ground plane. In Chapter 7, it is shown that frequency tuning of a spiral resonator can be achieved over a 65.4 % bandwidth with a very good impedance match by the spiral with a single switch and a varactor.

The design methodologies presented in this dissertation lead to miniaturized RF components that are simple, easy to fabricate and at a low cost. Several prototypes fabricated through a photolithographic process are presented in chapters 4, 5, 6, and 7, with a very good agreement between simulated and measured data.

APPENDICES

APPENDIX A

LETTER GRANTING PERMISSION TO REUSE THE FIGURES OF

THE PAPER "A TOPOLOGY OPTIMIZATION METHOD FOR

SPRINGER LICENSE
TERMS AND CONDITIONS

Jun 15, 2011

This is a License Agreement between raoul O Ouedraogo ("You") and Springer ("Springer") provided by Copyright Clearance Center ("CCC"). The license consists of your order details, the terms and conditions provided by Springer, and the payment terms and conditions.

All payments must be made in full to CCC. For payment instructions, please see information listed at the bottom of this form.

License Number	2690210868953
License date	Jun 15, 2011
Licensed content publisher	Springer
Licensed content publication	Structural and Multidisciplinary Optimization
Licensed content title	A topology optimization method for design of negative permeability metamaterials
Licensed content author	Alejandro R. Diaz
Licensed content date	Jan 1, 2009
Volume number	41
Issue number	2
Type of Use	Thesis/Dissertation
Portion	Figures
Author of this Springer article	No
Order reference number	
Title of your thesis / dissertation	Metamaterials
Expected completion date	Aug 2011
Estimated size(pages)	200
Total	0.00 USD

Figure A.1. Copyright letter I.

APPENDIX B

MATLAB-HFSS INTERFACE

The design and optimization of the structures presented in this dissertation are performed by integrating the commercial full wave solver HFSS [114] with the numerical computing software Matlab [115]. The structures to be optimized are created in Matlab and exported to HFSS for analyses. Once the analyses are completed, desired output parameters such as S-parameters and farfield components are exported back to Matlab for post-processing and optimization. To interface Matlab and HFSS, a set of Matlab functions have to be generated in order to create a script that HFSS can execute. This is not an easy task since HFSS has over one hundred commands and a script is needed to execute each of these commands. The sections below discuss the advantages of interfacing Matlab with HFSS and provide details on how to create Matlab functions to generate HFSS scripts. A step by step description of an example design of a circular patch antenna is also presented.

B.0.1 Why create a Matlab-HFSS interface

HFSS is an interactive software for analyzing in detail the electromagnetic behavior of a structure. Creating a complete design in HFSS follows very basic steps as shown in Figure B.1. Drawing a structure such as the circular patch antenna of Figure B.2 is fairly simple and straight forward. It consists of a disk (radiating patch) on top of a cylinder (substrate) which is backed by another disk (ground plane). The feed

structure consists of three cylinders that are the outer conductor, the inner conductor and the teflon. For such a simple structure, spending several weeks creating Matlab functions to generate an HFSS script seems unwise. However, those familiar with the graphical interface of HFSS know how complicated it is to draw complex 3-D structures or equation based curves. To draw a structure which is composed of hundreds of objects could take hours to complete from the graphical interface. However, this task can easily be performed from Matlab using simple iterative statements such as for-loops.

The use of a Matlab-HFSS interface is most advantageous for optimization problems. Though HFSS has its own set of built-in optimizers such as quasi Newton, pattern search, and genetic algorithm, they are very limited in terms of the total number of variables that can be optimized. Additionally, the cost function can only be constructed using simple combinations of the output parameters. This can be a bit problematic when the cost function involves extensive post processing of the output parameters.

B.0.2 Creating the necessary Matlab functions

Interfacing Matlab with HFSS is a simple and powerful way of controlling HFSS from Matlab. A set of Matlab functions are written to create objects in HFSS by generating a set of scripts that HFSS can execute. For instance, a minimum of two Matlab functions are required to draw the substrate of the circular patch of Figure B.2. One function generates a script for a cylinder and the other generates a script for assigning the material characteristics of the cylinder. Other functions can also be
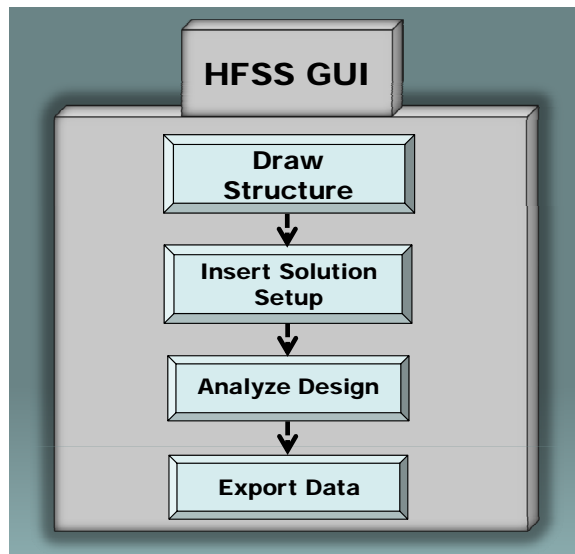
Figure B.1. Steps to create a design in HFSS.

used to specify the transparency and color of the cylinder. but they are just used of aesthetic purposes. Writing Matlab functions to create scripts that HFSS can execute is similar to solving an inverse problem. HFSS has a built-in scripting command that enables users to record all actions performed in the graphical interface to a script and the goal is to write Matlab functions that can generate the same scripts.

B.0.3   HFSS script

All actions performed within HFSS can be recorded into a script. By default, the script command is inactive and only actions performed after it has been activated are recorded. The script command is activated by clicking 'Record script' under the 'Tools' menu and specifying a script file name and a location to store the file. Once the script is activated, all subsequent actions are recorded into the file specified unless
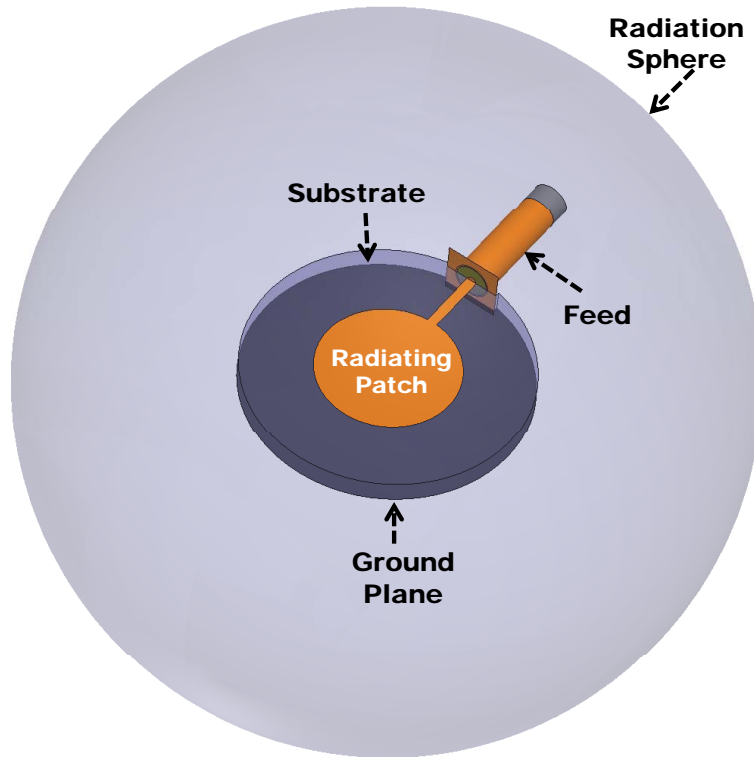
Figure B.2. Geometry of a circular patch antenna surrounded by a radiating sphere.

the script is deactivated. Deactivating the script is performed by clicking on 'Stop script' under 'Tools' or by closing HFSS. An example script generated by HFSS when a cylinder of radius 12.5 mm, height 0.78 mm with center coordinates (0, 0, 0) and directed along the z axis is shown below.

```
oEditor.CreateCylinder Array("NAME:CylinderParameters", _
  "XCenter:=",  "0mm", "YCenter:=", "0mm", "ZCenter:=", "0mm", _
  "Radius:=", "12.5mm", "Height:=",  "0.78mm", "WhichAxis:=", _
  "Z", "NumSides:=", "0"), Array("NAME:Attributes", "Name:=",  _
  "Cylinder1", "Flags:=", "", "Color:=", "(132 132 193)", _
  "Transparency:=", 0, "PartCoordinateSystem:=",  "Global", _
  "MaterialName:=", "vacuum", "SolveInside:=", true)
```

Note that the script contains two sections or arrays: one specifying the parameters (coordinates) of the cylinder and another describing the attributes of the cylinder. In this particular example, the only characteristics of the cylinder that were specified in the graphical interface are the parameters. The attributes which are the name of the cylinder, the material type, the color and the transparency are default values assigned by HFSS. If the user returns to the graphical interface and assigns a material type (e.g. Rogers RT/duroid 5870) to the cylinder, the following lines are automatically added to the script file:

```
oEditor.AssignMaterial Array("NAME:Selections", "Selections:=", _
  "Cylinder1"), Array("NAME:Attributes", "MaterialName:=", _
  "Rogers RT/duroid 5870 (tm)", "SolveInside:=", true)
```

Note that the material assignment has been changed from "Vacuum" (first script) to "Rogers RT/duroid 5870 (tm)". It is important to point out that all the scripts generated by HFSS follow the same format and they are somewhat similar. This information comes as relief because if all the scripts are similar, their equivalent Matlab functions ought to be similar as well. Thus, even though HFSS has over a hundred commands, all their equivalent Matlab functions can be derived from a single successfully written Matlab function. An example Matlab function written to create the script of the cylinder is discussed below. Basic knowledge of Matlab is required.

B.0.4 Creating the equivalent Matlab functions

Once a script is generated from HFSS, the next step is to write a Matlab function that can reproduce the same script. An example Matlab function that creates the script of the cylinder is shown below.

```
<1> function hfssCylinder(fid, Name, Axis, Center, Radius, Height...
, Units)
% Cylinder Parameters.
<2> fprintf(fid, '\n');
<3> fprintf(fid, 'oEditor.CreateCylinder _\n');
<4> fprintf(fid, 'Array("NAME:CylinderParameters", _\n');
<5> fprintf(fid, '"XCenter:=", "%f%s", _\n', Center(1), Units);
<6> fprintf(fid, '"YCenter:=", "%f%s", _\n', Center(2), Units);
<7> fprintf(fid, '"ZCenter:=", "%f%s", _\n', Center(3), Units);
<8> fprintf(fid, '"Radius:=", "%f%s", _\n', Radius, Units);
<9> fprintf(fid, '"Height:=", "%f%s", _\n', Height, Units);
<10> fprintf(fid, '"WhichAxis:=", "%s"), _\n', upper(Axis));

% Cylinder Properties.
<11> fprintf(fid, 'Array("NAME:Attributes", _\n');
<12> fprintf(fid, '"Name:=", "%s", _\n', Name);
<13> fprintf(fid, '"Flags:=", "", _\n');
<14> fprintf(fid, '"Color:=", "(132 132 193)", _\n');
<15> fprintf(fid, '"Transparency:=", 0, _\n');
<16> fprintf(fid, '"PartCoordinateSystem:=", "Global", _\n');
<17> fprintf(fid, '"MaterialName:=", "vacuum", _\n');
<18> fprintf(fid, '"SolveInside:=", true)\n');
<19> fprintf(fid, '\n');
```

The first statement given by line $< 1 >$ defines the function name ('hfssCylinder') and takes as inputs the parameters of the cylinder. The parameters are specified as variables which are defined in a main Matlab file from which the function 'hfssCylinder' is also invoked. These parameters are self explanatory by their names. For instance, the parameter 'Center' is a 3x1 array that specifies the center coordinates

(XCenter, YCenter, Zcenter) of the cylinder. 'fid' is used to specify the file where the script is be written to. The third statement given by line < 3 > writes the string 'oEditor.CreateCylinder' into the script file. Note that the script generated by HFSS starts with the same string.

The fifth statement writes the string 'Xcenter:=' followed by a comma, a single space, the first entry of the array Center, immediately followed by the unit symbol. The rest of the statements are somewhat identical to at least one of the three statements discussed above and need not be explained. As mentioned in the previous section, once a single function is successfully written, all the remaining function can be easily derived. A collection of Matlab-HFSS scripting functions can be found from (I need to find a place to upload the files for everyone to download).

B.0.5   The Main File

Once the necessary functions have been written, they can be called from a main Matlab file where all the required variables are defined. The main file replaces the graphical interface of HFSS. All the commands that would have been executed in the graphical interface are now performed in the main Matlab file by invoking the equivalent functions. Consequently, this file is written following the same basic steps discussed in Section B.0.1. An example Matlab file that creates and analyzes a circular patch antenna is shown below. The content of the file can be divided into three main sections:

- define the design variables

- design the structure by invoking the necessary function

- execute and export the desired output data.

The first section, which includes lines 1 through 25, defines all the parameters that are used in the design. Those parameters include the dimensions of the patch antenna given in lines 9 through 14, the dimensions of the feed structure given in lines lines 16 through 24, and the radius of the radiation sphere given by line 15. The feed structure is modeled as a coaxial feed and the dimensions are selected to match those of an actual SMA connector. Also defined in the variables section are the frequency range over which the analysis is performed (lines 4 and 5), the frequency point at which the mesh is generated (line 7) and the number of frequency points in the analysis (line 6).

The second section is the most involved and includes specifying the locations of various temporary folders and invoking the required functions. Each of these functions creates a script and all the scripts are written to a single script file. The location of all the functions written to generate HFSS scripts is specified by line 25. When the main file is executed, it generates a script and prompts the HFSS executable to execute the script. The executable creates a project file, analyzes the project and exports the data. It is therefore necessary to specify the location of the HFSS executable (line 26) and a folder where the script file, project file and data file need to be stored (lines 27 through 29).

Once these files have been defined, the next step is to open the script file to write all the necessary scripts. The script file is opened with the statement of line 30.

Lines 31 through 69 are all function calls and the functions are invoked following the same steps that one would follow to design a structure from the graphical interface. First insert a new design and specify the type of analysis to be performed (line 31). Next, draw the objects that make-up the structure (lines 32 through 63). There is no specific order as to which object is drawn first. For instance the radiation sphere (lines 32 through 34) which is drawn first could have been drawn after the radiating patch (lines 58 through 63) without causing any execution error. It is important to note that the order of the attributes of an object are not important. For instance three functions are invoked to specify the conductivity, color and transparency of the radiating patch (lines 61 through 63). In this particular case, the conductivity is specified first (line 61) and the color is specified last. Reversing this order would not have any effect on the execution of the project.

Once the structure is drawn, the following step is to insert a solution setup, specify the data to be exported and close the script. In this example, a fast sweep (line 65) is selected and the data to be exported are the S-parameters (line 68) and the efficiency (line 69). The script is closed with the statement of line 70. The final step is to execute the script by invoking the HFSS executable as specified on line 71. This statement prompts HFSS to open a new project called "CircPatch.hfss" and execute the script contained in the file "CircPatchScript.vbs". When the analysis is completed, HFSS exports the S-parameters to the file "CircPatchData.m", the efficiency to "XYfarField.m", but keeps the project file open. While the project file is open, Matlab is unable to perform any additional tasks (e.g. post processing of the exported data). This can be solved by deleting the inputs "True, false" from

206

the function hfssExecuteScript (invoked on line 71). Lines 72 – 80 are used for post

processing of the data exported by HFSS.

```
%%%%%%%%%%%%%%%%%%%%%%%%%%%%%%%%%%%%%%%%%%%%%%%%%%%%%%%%%%%%%%%%%%%%%%%%%%%
%This M file has been created by Raoul Ouedraogo
%to design a circular patch antenna in HFSS
%%%%%%%%%%%%%%%%%%%%%%%%%%%%%%%%%%%%%%%%%%%%%%%%%%%%%%%%%%%%%%%%%%%%%%%%%%%

clc
clear all;
format long
%%%%%%%%%%%%%%%%%%%%%%%%%%%%%%%%%%%%%%%%%%%%%%%%%%%%%%%%%%%%%%%%%%%%%%%%%%%%
%                         I: Define Parameters
<1> eps_o=8.8541878176e-12;  %Permittivity
<2> mu_o= 4*pi*1e-7;          %Mu
<3> Co=1/sqrt(eps_o*mu_o); %Speed of light in free space
<4> fLow =2e9;      %Simulation start frequency
<5> fHigh =3e9;     %Simulation end frequency
<6> nPoints = 200;  %frequency range discretization
<7> fC =(fHigh+ fLow)/2; % Mesh frequency
<8> Wv = (Co/fC)*1000; % Wavelength.

%Patch parameters
<9> Gnd_Ra=40; %Radius of the ground plane
<10> Sub_Ra=Gnd_Ra; %Radius of the dielectric
<11> Sub_Th=1.56; %Height of the substrate
<12> Patch_Ra=23; %Radius of the radiating patch
<13> StrX=1.5; %Feed line width
<14> StrY=Gnd_Ra; %Feed line length

%Radiation sphere radius
<15> Rad_Ra =Wv/2+Gnd_Ra ;

%Feed parameters (dimensions of an SMA connector)
<16> R_oc=2.6; %Radius of the outer conductor
<17> Th_oc=R_oc-.2;  %Radius of the outer Teflon
<18> R_feed=.635;    %Radius of the inner conductor
<19> Hi_feed=25;     %Height of the feed
<20> CapZ=3;         %Radius of the waveport cup
<21> Deembed=Hi_feed; %Deembedding distance
<22> Feed_X=-Gnd_Ra+1;% Start coordinate of the feed (X axis)
<23> Feed_Y=0;        % Start coordinate of the feed (Y axis)
```

```
<24> Feed_Z=Sub_Th;  % Start coordinate of the feed (Z axis)

%%%%%%%%%%%%%%%%%%%%%%%%%%%%%%%%%%%%%%%%%%%%%%%%%%%%%%%%%%%%%%
%II: Location of sub-functions
<25> addpath('C:\MatlabHFSS\MatHfssDis\Files');

%II: Location of HFSS executable
<26> hfssExePath = 'C:\"Program Files (x86)"\Ansoft\HFSS11\hfss.exe';

%II: Where to store the temporary files
<27> tmpPrjFile = 'C:\MatlabHFSS\MatHfssDis\CircPatch.hfss';
<28> tmpDataFile = 'C:\MatlabHFSS\MatHfssDis\CircPatchData.m';
<29> tmpScriptFile = 'C:\MatlabHFSS\MatHfssDis\CircPatchScript.vbs';
%FarFieldpath='C:\MatlabHFSS\MatHfssDis\XYfarField.m' ;

%%%%%%%%%%%%%%%%%%%%%%%%%%%%%%%%%%%%%%%%%%%%%%%%%%%%%%%%%%%%%%
% Open the temporary scrip file to write necessary scripts
<30> fid = fopen(tmpScriptFile, 'wt');

% Create a new design called GA_Loop
<31> hfssInsertNewDesign(fid, 'DualComp', 'DrivenModal');

%Draw Radiation sphere and assign it a  radiation boundary
<32> hfssSphere(fid, 'AirBox', [0, 0, 0], Rad_Ra, 'mm');
<33> hfssAssignRadiation(fid, 'Box_Rad', 'AirBox');
<34> hfssSetTransparency(fid, {'AirBox'}, 0.9);

%%%%%%%%%%%%%%%%Draw the Feed Structure%%%%%%%%%%%

%Draw outer conductor of the feed
<35> hfssHollowCylinder(fid, 'Outer_C', 'X', [Feed_X, Feed_Y,...
Feed_Z], Th_oc, R_oc, -Hi_feed, 'mm');
<36> hfssAssignPE(fid, 'PEC_oc',  {'Outer_C'});
%Draw the teflon of the feed
<37> hfssHollowCylinder(fid, 'Tef', 'X', [Feed_X, Feed_Y,...
Feed_Z], R_feed, Th_oc, -Hi_feed, 'mm');
<38> hfssAssignMaterial(fid, 'Tef', 'Neltec NX9294 (tm)');
%Draw inner conductor of the feed
<39> hfssCylinder(fid, 'Inner_C', 'X', [Feed_X, Feed_Y,...
Feed_Z], R_feed, -Hi_feed, 'mm');
<40> hfssAssignPE(fid, 'PEC_Ic',  {'Inner_C'});
%Draw waveport
<41> hfssCircularPort(fid, 'LPort', 'port1', 'X',...
[Feed_X-(Hi_feed), Feed_Y, Feed_Z], Th_oc,Deembed, 'mm');
%Draw the waveport Cap
```

```
<42> hfssCylinder(fid, 'PortCup', 'X', [Feed_X-(Hi_feed),...
Feed_Y, Feed_Z], R_oc, -CapZ, 'mm');
<43> hfssAssignMaterial(fid, 'PortCup', 'pec');

<44> hfssRectangle(fid, 'FeedRec', 'X', [-Gnd_Ra+1, -4, -4],...
8, 8, 'mm');
<45> hfssCircle(fid, 'FeedRec2', 'X', [-Gnd_Ra+1, 0, Feed_Z],...
R_oc , 'mm');
<46> hfssSubtract(fid, {'FeedRec'}, {'FeedRec2'});
<47> hfssAssignFiniteCond(fid, 'PEC_FeedRec', 0, 'um',  {'FeedRec'});

%%%%%%%%%%%%%Draw patch antenna structure%%%%%%%%%
%Draw substrate
<48> hfssCylinder(fid, 'Sub_Patch', 'Z', [0, 0, 0], Sub_Ra,...
Sub_Th , 'mm');
<49> hfssBox(fid, 'Sub_del', [-Sub_Ra,-4, 0], [ 1,8, Sub_Th], 'mm');
<50> hfssSubtract(fid, {'Sub_Patch'}, {'Sub_del'});
<51> hfssAssignMaterial(fid, 'Sub_Patch',...
'Rogers RT/duroid 5870 (tm)');
<52> hfssSetTransparency(fid, {'Sub_Patch'}, 0.8);

%Draw ground plane
<53> hfssCircle(fid, 'Gnd', 'Z', [0, 0, 0],Gnd_Ra , 'mm');
<54> hfssRectangle(fid, 'Gnd_Sub', 'Z', [-Gnd_Ra, -4, 0], 1, 8, 'mm');
<55> hfssSubtract(fid, {'Gnd'}, {'Gnd_Sub'});
<56> hfssAssignFiniteCond(fid, 'PEC_Gnd', 0, 'um',  {'Gnd'});
<57> hfssSetTransparency(fid, {'Gnd'}, .3);

%Draw radiating patch
<58> hfssCircle(fid, 'PatchP', 'Z', [0, 0, Sub_Th],Patch_Ra , 'mm');
<59> hfssRectangle(fid, 'stripF', 'Z', [ -Gnd_Ra+1,-StrX/2,...
Sub_Th], StrY, StrX, 'mm');
<60> hfssUnite(fid, 'PatchP' ,'stripF');
<61> hfssAssignFiniteCond(fid, 'PatP', 0, 'um', {'PatchP'});
<62> hfssSetTransparency(fid, {'PatchP'}, .5);
<63> hfssSetColor(fid, 'PatchP', [255, 128, 0]);

%%%%%%%%%%%%%%%%% Add solution setup%%%%%%%%%%%%%%%%%%%%%%%%%%%%%
<64> hfssInsertSolution(fid, 'Setup', fC/1e9, 0.001, 6);
<65> hfssFastSweep(fid, 'Sweep', 'Setup', fLow/1e9,...
fHigh/1e9, nPoints);
<66> hfssInsertFarField(fid, 'Infinite Sphere1',0,0,0,0,0,0,'deg');

%Solve and and specify the type of data to be exported as an m-file.
<67> hfssSolveSetup(fid, 'Setup');
```

```
<68> hfssSParameters(fid, tmpDataFile, 'Setup', 'Sweep');
<69> hfssFarFieldReport(fid, fC*(1e-9), 'GHz')


% Close the HFSS Script File.
<70> fclose(fid);

% Execute the Script by starting HFSS.
disp('Solving using HFSS ..');
<71> hfssExecuteScript(hfssExePath, tmpScriptFile, true, false);
disp('HFSS analysis completed ...');
%%%%%%%%%%%%%%%%%%%%%%%%%%%%%%%%%%%%%%%%%%%%%%%%%%%%%%%%%%%%%%%%%%%%%%%
%Post processing
<72>[heffi, FarField] = hdrload('eff1.m');
<73>f=FarField(:,1);
<74>Gr=FarField(:,2); %Get the efficiency

<75>run(tmpDataFile);
<76>  for np=1:nPoints
<77>    S1r(np)=20*log10(abs(S(np,:,:)));
<78>  end
<79> figure(2)
<80> plot(f, S1r, 'k','LineWidth',1.5)
```

APPENDIX C

MATLAB CODE USED TO CREATE NEW RESONANT

STRUCTURE

```
%%%%%%%%%%%%%%%%%%%%%%%%%%%%%%%%%%%%%%%%%%%%%%%%%%%%%%%%%%
%Created by Raoul ouedraogo to synthesize new resonant
% structure that can be used to create negative mu media
%%%%%%%%%%%%%%%%%%%%%%%%%%%%%%%%%%%%%%%%%%%%%%%%%%%%%%%%%%

clc
clear all;
format long

maxit=200; %Max number of iterations
mincost=-1000; %Minimum cost
popsize=200; %Set population size
Muprob=.2; %Set mutation rate
m=12;            %Number of bits per column
n1=6 ;           %Number of bits per row
n=2*n1;
Nt=m*n1;         %Number of bits in each chromosome
iga=0; %INITIALIZE GENERATION COUNTER
bestfit=200;

%add paths to the required m-files.
addpath('C:\WgGa\WgGA2\WG_12_05\Files\');

%Frequency sweep parameters
fLow = 5e9;          %Simulation start point
fHigh = 6e9;         %Simulation end point
fC = (fHigh+fLow)/2; % Frequency of Interest.
eps_o=8.8541878176e-12; %Free space epsilon
mu_o= 4*pi*1e-7;         %Free space mu
Co=1/sqrt(eps_o*mu_o); %Speed of light
Wv = (Co/fC)*1000; %Wavelength.
nPoints = 1;  %Number of optimized frequencies

%Antenna Parameters.
```

```matlab
Pw=.5;            %Pixel width
Pwb=.5;            %Pixel width
XL=n;             %Nuber of pixels in X direction
ZL=m;             %Nuber of pixels in Y direction
SRR_LX=(Pw*XL); %Unit cells length X-direction
SRR_LZ=(Pwb*ZL);  %Unit cell height Y direction


%Waveguide Dimensions
G_X =60;    %Waveguide length
G_Y =40.3860; %21.86; %Waveguide width
G_Z =20.1930;  %10.16 ;   %Waveguide height
Compx=.5;

%Substrate Dimensions
Sub_X=SRR_LX+ Compx;    %Substrate length
Sub_Y=.78; %Substrate width
Sub_Z=G_Z; %SRR_LZ %54.6100;%Substrate height
Deembed=(G_X-Sub_X)/2; %Deembedding distance


 for ip = 1:popsize
tic
%Generate random population
    for jp = 1:Nt
      if rand() > 0.4
        Pop(ip, jp) = 0;
      else
        Pop(ip, jp) = 1;
       end
    end

%Bit assignment
MetaMM=reshape(Pop(ip,:),m,n1);
Full_SideA=fliplr(MetaMM);
Full_SideB=(MetaMM);
for i=1:m
        for j=1:n/2
            Full_Side(i,j)=Full_SideA(i,j);
        end
end
for i=1:m
        for j=1:n/2
            Full_Side(i,j+n/2)=Full_SideB(i,j);
        end
```

```
end
Meta=Full_Side;
MetaB=flipud(Meta);

%Temporary Files.
tmpPrjFile = 'C:\WgGa\WgGA2\Fband2b.hfss';
tmpDataFile = 'C:\WgGa\WgGA2\FData2b.m';
tmpScriptFile = 'C:\WgGa\WgGA2\FScript2b.vbs';

%HFSS Executable Path.
hfssExePath = 'C:\"Program Files (x86)"\Ansoft\HFSS11\hfss.exe';

% Create a new temporary HFSS script file.
fid = fopen(tmpScriptFile, 'wt');

% Create a new HFSS project and insert a new design.
hfssNewProject(fid);
hfssInsertDesign(fid, 'X_Hor_LHMM2b');


N=0;
 for i=1:n
        NN=0;
        for j=1:m
            if Meta(i,j)==1;
                NN=1+ NN;
            end
        if NN>0
            if Meta(i,j)==0
                N=N+1;
                xp=(i)*Pw;
                yp=(j)*Pwb;
                hfssRectangle(fid, sprintf('RecB%d',N),...
                'Y', [-xp+SRR_LX/2, -Sub_Y/2, yp-...
                (1+NN)*Pwb-SRR_LZ/2], Pwb*NN, Pw,'mm');
                hfssAssignFiniteCond(fid, sprintf('RecBPEC%d',N)...
                , 0, 'um', {sprintf('RecB%d',N)})
                NN=0;
            end
             if j==m
                 if Meta(i,j)==1;
                N=N+1;
                xp=(i)*Pw;
                yp=(j)*Pwb;
                hfssRectangle(fid, sprintf('RecB%d',N),...
```

```
                        'Y', [-xp+SRR_LX/2, -Sub_Y/2, ...
                        yp-NN*Pwb-SRR_LZ/2], Pwb*NN, Pw,'mm');
                        hfssAssignFiniteCond(fid, sprintf('RecBPEC%d',N)...
                        , 0, 'um', {sprintf('RecB%d',N)})
                        NN=0;
                         end
                   end
             end
          end
end
N=0

 for i=1:n
       NN=0;
       for j=1:m
           if MetaB(i,j)==1;
               NN=1+ NN;
           end
       if NN>0
           if MetaB(i,j)==0
               N=N+1;
               xp=(i)*Pw;
               yp=(j)*Pwb;
               hfssRectangle(fid, sprintf('RecA%d',N),...
               'Y', [-xp+SRR_LX/2, Sub_Y/2, yp-...
               (1+NN)*Pwb-SRR_LZ/2], Pwb*NN, Pw,'mm');
               hfssAssignFiniteCond(fid, sprintf('RecAPEC%d',N)...
               , 0, 'um', {sprintf('RecA%d',N)})
               NN=0;
           end
            if j==m
               if MetaB(i,j)==1;
               N=N+1;
               xp=(i)*Pw;
               yp=(j)*Pwb;
               hfssRectangle(fid, sprintf('RecA%d',N),...
               'Y', [-xp+SRR_LX/2, Sub_Y/2,...
               yp-NN*Pwb-SRR_LZ/2], Pwb*NN, Pw,'mm');
               hfssAssignFiniteCond(fid,...
               sprintf('RecAPEC%d',N), 0,...
               'um', {sprintf('RecA%d',N)})
               NN=0;
                end
           end
        end
```

```
        end
  end

%Draw Waveguide
hfssBox(fid, 'Waveguide', [-G_X/2, -G_Y/2, -G_Z/2],...
    [G_X, G_Y, G_Z], 'mm');

%Wavport assignment
hfssRectangle(fid, 'WGY1', 'X', [-G_X/2, -G_Y/2,...
    -G_Z/2], G_Y, G_Z, 'mm');
hfssRectangle(fid, 'WGY2', 'X', [G_X/2, -G_Y/2, -G_Z/2]...
    , G_Y, G_Z, 'mm');
WavePorNoDeembed(fid, 'WGY1', 'WGY1', 2, true, [-G_X/2,...
    0, -G_Z/2], [-G_X/2, 0, G_Z/2], 'mm');
WavePorNoDeembed(fid, 'WGY2', 'WGY2', 2, true, [G_X/2,...
    0, -G_Z/2], [G_X/2, 0, G_Z/2],'mm');

%Assign PE to wave guide face
hfssRectangle(fid, 'WGX1', 'Y', [-G_X/2, -G_Y/2, -G_Z/2]...
    , G_Z, G_X, 'mm');
hfssRectangle(fid, 'WGX2', 'Y', [-G_X/2, G_Y/2, -G_Z/2]...
    , G_Z, G_X, 'mm');
hfssAssignPH(fid, 'WGX1',  {'WGX1'});
hfssAssignPH(fid, 'WGX2',  {'WGX2'});
hfssRectangle(fid, 'WGZ1', 'Z', [-G_X/2, -G_Y/2, -G_Z/2]...
    , G_X, G_Y, 'mm');
hfssAssignPE(fid, 'WGZ1',  {'WGZ1'});
hfssRectangle(fid, 'WGZ2', 'Z', [-G_X/2, -G_Y/2, G_Z/2]...
    , G_X, G_Y, mm');
hfssAssignPE(fid, 'WGZ2',  {'WGZ2'});

%Draw Substrate
hfssBox(fid, 'Substrate', [-Sub_X/2, -Sub_Y/2, -Sub_Z/2],...
    [Sub_X, Sub_Y, Sub_Z], 'mm');
hfssAssignMaterial(fid,...
'Substrate', 'Rogers RT/duroid 5870 (tm)');
hfssSetColor(fid, 'Substrate', [0, 0, 0]);
hfssSetTransparency(fid, {'Substrate'}, 0);

% Add a Solution Setup.
hfssInsertSolution(fid, 'Setup', fC/1e9, 0.00005, 6);

% Save the project to a temporary file and solve it.
hfssSaveProject(fid, tmpPrjFile, true);
hfssSolveSetup(fid, 'Setup');
```

```
% Export the Network data and close script.
hfssExportNetworkData(fid, tmpDataFile, 'Setup',...
    'LastAdaptive');
fclose(fid);

% Execute the Script by starting HFSS.
disp('Solving using HFSS ..');
hfssExecuteScript(hfssExePath, tmpScriptFile);


disp('Solution Completed.');
% Load the data for post processing

run(tmpDataFile);
worst=100;


run(tmpDataFile);
 for np=1:nPoints
    S11(np)=1.*S(np, 1, 1);
    S21(np)=1.*S(np, 1, 3);
 end

% Calculate Mu and Epsilon from S11 and S21
a=G_Y*1e-3;
d=Sub_X*1e-3;
F=f;

%define variable
Fc_o=1/(2*a*sqrt(mu_o*eps_o)); %empty guide cutoff
w=2*pi*F;             %freq in radian
Lamda0=Co./F;

var=sqrt(1-(Fc_o^2)./(F.^2));
Kzo=(w./Co).*var;
Zo=w*mu_o./Kzo;
var1=(S11.^2-S21.^2 + 1)./(2*S11);

P=(var1 - sqrt(var1.^2-1));
U=(1-P.*(S11+S21))./(S11+S21 -P);
Z=(P+1)./(1-P);
nlog=0;
Lu_a= log(abs(U)) +1i*(angle(U) -(nlog)*pi*2);

%Finding Mu
```

```matlab
 ko=w/Co;

Mu_a=(Z.*Lu_a)./(1i*ko.*d.*var);
Ep_a=Lu_a.*var./(Z.*d.*1i.*(ko)) + (Co^2)./(4*Mu_a.*(a.*F).^2);

 fitness(ip)=min(real(Mu_a))
 toc

 end

[fitness,ind]=sort(fitness) ;    %Sort fitness
Pop=Pop(ind,:);    % sorts population
minc(1)=min(fitness);% find min of the population

%reduce population size to hal
 popsize=popsize/2;
 for ii=1:popsize
     Pop(ii,:)=Pop(ii,:);
     fitness(ii)=fitness(ii);
 end


 while iga<maxit
     tic
     NewPop=Pop;  %store the previous
     Muprob=.25; % set mutation rate
selection=0.25; % fraction of population kept

%    %I) Selection of chromozomes to be kept
indx=find(fitness<=mean(fitness));
keep=ceil(selection*popsize); %Number of chrom to keep
fitkeep=fitness(indx);% fitnesses to keep
Popkeep=Pop(indx,:);%Chroms to keep
M1=ceil((popsize-keep)*.5); % Chromosomes to be replaced
M2=ceil((popsize-keep)*.5); % Chromosomes to be replaced

%create complement of 1/2 of the best kept%
comp_chrom=ceil(selection*popsize*0.5);
  for ip2=1:comp_chrom
        Pop(1+comp_chrom,:)=not(Pop(1+comp_chrom,:));
    end

%II) Pairing Chromozomes for Xover/Mutation
%Case I: Tournament selection among 2 individual
Ntourn=2;
```

```
  for ic=1:2:M1
%first Parent
rc=ceil(keep*rand(1,Ntourn)); %Randomly select 2
[c,ci]=min(fitness(rc)); % Select lowest fitness
ma=rc(ci);  % indicies of first parent
%Second parent
rc=ceil(keep*rand(1,Ntourn));%%Randomly select 2
[c,ci]=min(fitness(rc)); % Select lowest fitness
pa=rc(ci);  % indicies of second parent
if ic<=ceil(M1/10)
%2pt Crossover
Xpt=ceil(rand()*(Nt-1));
Pop(keep+ic-1,:)=[Pop(ma,1:Xpt) Pop(pa,Xpt+1:Nt)];%Offspring 1
Pop(keep+ic,:)=[Pop(pa,1:Xpt) Pop(ma,Xpt+1:Nt)];%Offspring 2
end
if ic>=ceil(M1/10) && ic<=ceil(M1/3)
%2pt Crossover
Xpt1=ceil(rand()*Nt/2);
Xpt2=Xpt1 + ceil(rand()*(Nt-1)/2);
Pop(keep+ic-1,:)=[Pop(ma,1:Xpt1) Pop(pa,Xpt1+1:Xpt2)...
    Pop(ma,Xpt2+1:Nt)]; % Offspring 1
Pop(keep+ic,:)=[Pop(pa,1:Xpt1) Pop(ma,Xpt1+1:Xpt2)...
    Pop(pa,Xpt2+1:Nt)];%Offspring 2
end
if ic>=ceil(M1/3)
%3pt Crossover
Xpt1=ceil(rand()*Nt/3);
Xpt2=Xpt1 + ceil(rand()*(Nt)/3);
Xpt3=Xpt2 + ceil(rand()*(Nt-1)/3);
Pop(keep+ic-1,:)=[Pop(ma,1:Xpt1) Pop(pa,Xpt1+1:Xpt2)...
    Pop(ma,Xpt2+1:Xpt3) Pop(pa,Xpt3+1:Nt)]; % Offspring 1
Pop(keep+ic,:)=[Pop(pa,1:Xpt1) Pop(ma,Xpt1+1:Xpt2)...
    Pop(pa,Xpt2+1:Xpt3) Pop(ma,Xpt3+1:Nt)];%Offspring 2
end
  end

  for ic2=1:2:M2
      %Random Selection of Parents
%first Parent
ma=ceil(keep*rand());  % indicies of first parent
%Second parent
pa=ceil(keep*rand());  % indicies of second parent

if ic2<=ceil(M2/3)
%2pt Crossover
```

```matlab
Xpt=ceil(rand()*(Nt-1));
Pop(keep+M1+ic2-1,:)=[Pop(ma,1:Xpt)...
    Pop(pa,Xpt+1:Nt)]; % Offspring 1
Pop(keep+M1+ic2,:)=[Pop(pa,1:Xpt)...
    Pop(ma,Xpt+1:Nt)];%Offspring 2
end
if ic2>=ceil(M2/3) && ic2<=ceil(2*M1/3)
%2pt Crossover
Xpt1=ceil(rand()*Nt/2);
Xpt2=Xpt1 + ceil(rand()*(Nt-1)/2);
Pop(keep+M1+ic2-1,:)=[Pop(ma,1:Xpt1) Pop(pa,Xpt1+1:Xpt2)...
    Pop(ma,Xpt2+1:Nt)]; % Offspring 1
Pop(keep+M1+ic2,:)=[Pop(pa,1:Xpt1) Pop(ma,Xpt1+1:Xpt2)...
    Pop(pa,Xpt2+1:Nt)];%Offspring 2
end
if ic2>=ceil(M2/3)
%3pt Crossover
Xpt1=ceil(rand()*Nt/3);
Xpt2=Xpt1 + ceil(rand()*(Nt)/3);
Xpt3=Xpt2 + ceil(rand()*(Nt-1)/3);
Pop(keep+M1+ic2-1,:)=[Pop(ma,1:Xpt1) Pop(pa,Xpt1+1:Xpt2)...
    Pop(ma,Xpt2+1:Xpt3) Pop(pa,Xpt3+1:Nt)]; % Offspring 1
Pop(keep+M1+ic2,:)=[Pop(pa,1:Xpt1) Pop(ma,Xpt1+1:Xpt2)...
    Pop(pa,Xpt2+1:Xpt3) Pop(ma,Xpt3+1:Nt)];%Offspring 2
end
  end

%III) mutation: k
for iMu=keep:popsize
    if Muprob>=rand()
Mupt=ceil(rand()*Nt);% bit to be mutated
Pop(iMu,Mupt)=not(Pop(iMu,Mupt));
    end
end

CurrentChrom=keep;
for ip = keep:popsize

    %Added so that repeated structures are not analyzed
    for ipp=1:popsize
        if Pop(ip,:)==NewPop(ipp,:)
            for ipp1=1:6
        Mupt1=ceil(rand()*Nt);% bit to be mutated
        Pop(ip,Mupt1)=not(Pop(ip,Mupt1));
            end
```

```
            end
        end


%Bit assignment
MetaMM=reshape(Pop(ip,:),m,n1);
Full_SideA=fliplr(MetaMM);
Full_SideB=(MetaMM);
for i=1:m
        for j=1:n/2
            Full_Side(i,j)=Full_SideA(i,j);
        end
end
for i=1:m
        for j=1:n/2
            Full_Side(i,j+n/2)=Full_SideB(i,j);
        end
end
Meta=Full_Side;
MetaB=flipud(Meta);

%Temporary Files.
tmpPrjFile = 'C:\WgGa\WgGA2\Fband2b.hfss';
tmpDataFile = 'C:\WgGa\WgGA2\FData2b.m';
tmpScriptFile = 'C:\WgGa\WgGA2\FScript2b.vbs';

%HFSS Executable Path.
hfssExePath = 'C:\"Program Files (x86)"\Ansoft\HFSS11\hfss.exe';

% Create a new temporary HFSS script file.
fid = fopen(tmpScriptFile, 'wt');

% Create a new HFSS project and insert a new design.
hfssNewProject(fid);
hfssInsertDesign(fid, 'X_Hor_LHMM2b');


N=0;
 for i=1:n
        NN=0;
        for j=1:m
            if Meta(i,j)==1;
                NN=1+ NN;
            end
        if NN>0
```

```
          if Meta(i,j)==0
              N=N+1;
              xp=(i)*Pw;
              yp=(j)*Pwb;
              hfssRectangle(fid, sprintf('RecB%d',N),...
              'Y', [-xp+SRR_LX/2, -Sub_Y/2, yp-...
              (1+NN)*Pwb-SRR_LZ/2], Pwb*NN, Pw,'mm');
              hfssAssignFiniteCond(fid, sprintf('RecBPEC%d',N)...
              , 0, 'um', {sprintf('RecB%d',N)})
              NN=0;
          end
         if j==m
              if Meta(i,j)==1;
              N=N+1;
              xp=(i)*Pw;
              yp=(j)*Pwb;
              hfssRectangle(fid, sprintf('RecB%d',N),...
              'Y', [-xp+SRR_LX/2, -Sub_Y/2, ...
              yp-NN*Pwb-SRR_LZ/2], Pwb*NN, Pw,'mm');
              hfssAssignFiniteCond(fid, sprintf('RecBPEC%d',N)...
              , 0, 'um', {sprintf('RecB%d',N)})
              NN=0;
              end
          end
      end
    end
end
N=0

 for i=1:n
      NN=0;
      for j=1:m
          if MetaB(i,j)==1;
              NN=1+ NN;
          end
      if NN>0
          if MetaB(i,j)==0
              N=N+1;
              xp=(i)*Pw;
              yp=(j)*Pwb;
              hfssRectangle(fid, sprintf('RecA%d',N),...
              'Y', [-xp+SRR_LX/2, Sub_Y/2, yp-...
              (1+NN)*Pwb-SRR_LZ/2], Pwb*NN, Pw,'mm');
              hfssAssignFiniteCond(fid, sprintf('RecAPEC%d',N)...
              , 0, 'um', {sprintf('RecA%d',N)})
```

```
                      NN=0;
                  end
                   if j==m
                       if MetaB(i,j)==1;
                   N=N+1;
                   xp=(i)*Pw;
                   yp=(j)*Pwb;
                   hfssRectangle(fid, sprintf('RecA%d',N),...
                   'Y', [-xp+SRR_LX/2, Sub_Y/2,...
                   yp-NN*Pwb-SRR_LZ/2], Pwb*NN, Pw,'mm');
                   hfssAssignFiniteCond(fid,...
                   sprintf('RecAPEC%d',N), 0,...
                   'um', {sprintf('RecA%d',N)})
                   NN=0;
                    end
               end
          end
        end
 end

%Draw Waveguide
hfssBox(fid, 'Waveguide', [-G_X/2, -G_Y/2, -G_Z/2],...
    [G_X, G_Y, G_Z], 'mm');

%Wavport assignment
hfssRectangle(fid, 'WGY1', 'X', [-G_X/2, -G_Y/2,...
    -G_Z/2], G_Y, G_Z, 'mm');
hfssRectangle(fid, 'WGY2', 'X', [G_X/2, -G_Y/2, -G_Z/2]...
    , G_Y, G_Z, 'mm');
WavePorNoDeembed(fid, 'WGY1', 'WGY1', 2, true, [-G_X/2,...
    0, -G_Z/2], [-G_X/2, 0, G_Z/2], 'mm');
WavePorNoDeembed(fid, 'WGY2', 'WGY2', 2, true, [G_X/2,...
    0, -G_Z/2], [G_X/2, 0, G_Z/2],'mm');

%Assign PE to wave guide face
hfssRectangle(fid, 'WGX1', 'Y', [-G_X/2, -G_Y/2, -G_Z/2]...
    , G_Z, G_X, 'mm');
hfssRectangle(fid, 'WGX2', 'Y', [-G_X/2, G_Y/2, -G_Z/2]...
    , G_Z, G_X, 'mm');
hfssAssignPH(fid, 'WGX1',  {'WGX1'});
hfssAssignPH(fid, 'WGX2',  {'WGX2'});
hfssRectangle(fid, 'WGZ1', 'Z', [-G_X/2, -G_Y/2, -G_Z/2]...
    , G_X, G_Y, 'mm');
hfssAssignPE(fid, 'WGZ1',  {'WGZ1'});
hfssRectangle(fid, 'WGZ2', 'Z', [-G_X/2, -G_Y/2, G_Z/2]...
```

```
     , G_X, G_Y, mm');
hfssAssignPE(fid, 'WGZ2',  {'WGZ2'});

%Draw Substrate
hfssBox(fid, 'Substrate', [-Sub_X/2, -Sub_Y/2, -Sub_Z/2],...
     [Sub_X, Sub_Y, Sub_Z], 'mm');
hfssAssignMaterial(fid,...
'Substrate', 'Rogers RT/duroid 5870 (tm)');
hfssSetColor(fid, 'Substrate', [0, 0, 0]);
hfssSetTransparency(fid, {'Substrate'}, 0);

% Add a Solution Setup.
hfssInsertSolution(fid, 'Setup', fC/1e9, 0.00005, 6);

% Save the project to a temporary file and solve it.
hfssSaveProject(fid, tmpPrjFile, true);
hfssSolveSetup(fid, 'Setup');
% Export the Network data and close script.
hfssExportNetworkData(fid, tmpDataFile, 'Setup',...
     'LastAdaptive');
fclose(fid);

% Execute the Script by starting HFSS.
disp('Solving using HFSS ..');
hfssExecuteScript(hfssExePath, tmpScriptFile);


disp('Solution Completed.');
% Load the data for post processing

run(tmpDataFile);
worst=100;


run(tmpDataFile);
 for np=1:nPoints
    S11(np)=1.*S(np, 1, 1);
    S21(np)=1.*S(np, 1, 3);
 end

% Calculate Mu and Epsilon from S11 and S21
a=G_Y*1e-3;
d=Sub_X*1e-3;
F=f;
```

```matlab
%define variable
Fc_o=1/(2*a*sqrt(mu_o*eps_o)); %empty guide cutoff
w=2*pi*F;            %freq in radian
Lamda0=Co./F;

var=sqrt(1-(Fc_o^2)./(F.^2));
Kzo=(w./Co).*var;
Zo=w*mu_o./Kzo;
var1=(S11.^2-S21.^2 + 1)./(2*S11);

P=(var1 - sqrt(var1.^2-1));
U=(1-P.*(S11+S21))./(S11+S21 -P);
Z=(P+1)./(1-P);
nlog=0;
Lu_a= log(abs(U)) +1i*(angle(U) -(nlog)*pi*2);

%Finding Mu
 ko=w/Co;

Mu_a=(Z.*Lu_a)./(1i*ko.*d.*var);
Ep_a=Lu_a.*var./(Z.*d.*1i.*(ko)) + (Co^2)./(4*Mu_a.*(a.*F).^2);

 fitness(ip)=min(real(Mu_a))

 CurrentChrom=CurrentChrom+1
 BiLoop_CurPop1=Pop;
 savefile = 'BiLoop_CurPop1.mat';
 save(savefile, 'BiLoop_CurPop1');
 BiLoop_Curfit1=fitness;
 savefile = 'BiLoop_Curfit1.mat';
 save(savefile, 'BiLoop_Curfit1');
 toc
 end %of the evaluation of the current population

% % % %_____
%Do statistics for new generation
[fitness,ind]=sort(fitness) ;   %Sort fitness
Pop=Pop(ind,:);   % sorts population
minc(1)=min(fitness);% find min of the population


 BianiLoop_Pop1=Pop;
      savefile = 'BianiLoop_Pop1.mat';
 save(savefile, 'BianiLoop_Pop1');
 BianiLoop_fit1=fitness;
```

```matlab
        savefile = 'BianiLoop_fit1.mat';
 save(savefile, 'BianiLoop_fit1');

% % %_____
% % %                        Stopping criteria
  if iga>maxit || fitness(1)<mincost
    break
  end
% %
 GenTopFit= [iga fitness(1) fitness(2)]
 iga=iga+1

 Store_Fit(iga)=min(fitness);
 savefile = 'Store_Fit.mat';
 save(savefile, 'Store_Fit');

 PopBest(iga,:)=Pop(1,:);
 savefile = 'PopBest.mat';
 save(savefile, 'PopBest');
  end %iga
```

APPENDIX D

COPYRIGHT LETTER GRANTING PERMISSION TO REUSE THE CONTENT OF THE PAPER "IN SITU OPTIMIZATION OF METAMATERIAL-INSPIRED LOOP ANTENNAS" [47]

Figure D.1. Copyright letter II.

APPENDIX E

MATLAB CODE USED TO CREATE CSRR LOADED

MINIATURIZED PATCH ANTENNAS

```
%%%%%%%%%%%%%%%%%%%%%%%%%%%%%%%%%%%%%%%%%%%%%%%%%%%%%%%%%%
%Created by Raoul Ouedraogo to design miniaturized patch
%antennas loaded with complementary split ring resonators.
%%%%%%%%%%%%%%%%%%%%%%%%%%%%%%%%%%%%%%%%%%%%%%%%%%%%%%%%%%

clc
clear all;
format long

%%%%%%%%%%%%%%%%%%%%%%%%%%%%%%%%%%%%%%%%%%%%%%%%%%%%%%%%%%%%%%%%%%
%                     III. GA parameters
maxit=100;      % max number of iterations
mincost=-10000; % minimum cost
popsize=500;    % set population size
Muprob=.2;    % set mutation rate
iga=0; %INITIALIZE GENERATION COUNTER
bestfit=0
minfit=0;
%-------------------------------------------------------------
%             Create the initial population for each individua

% add paths to the required m-files.
addpath('C:\MatlabHFSS\Finalpatch\6mm\Files');

eps_o=8.8541878176e-12;  %Free space epsilon
mu_o= 4*pi*1e-7;           %Free space Mu
Co=1/sqrt(eps_o*mu_o); %Speed of light in free space
fLow =2.4e9;      %Simulation start frequency
fHigh =2.5e9;    %Simulation end frequency
nPoints = 1;  %Number of analyze frequency points
fC =(fHigh+ fLow)/2; % Frequency of Interest.
Wv = (Co/fC)*1000; % Wavelength.

%Ground Plane
```

```
Gnd_Ra=12.5; %ground radius
Sub1_Ra=Gnd_Ra; % radius of the substrate
% Crab_Z=0;
Sub_Z1=.78*1; %spacing between the radiating patch and the CSRR
Sub_Z2=.78*2; %Spacing between the CSRR and the ground plane
Patch_Ra=6; %Radius of the patch antenna
Comp=Gnd_Ra-1; %radius of the CSRR disk
% Airbox Dimensions (WR-430  1.70 to 2.60)
G_R =Wv/2+Gnd_Ra ;   %Waveguide length
G_H =Wv/2+Gnd_Ra ;   %Waveguide length


%Dimensions of the feed
R_oc=2.6; % Radius of the outer conductor
Th_oc=R_oc-.2; % Radius of the teflon
R_feed=.635; %radius of the inner feed
Hi_feed=25; %Length of the feed
CapZ=3; % Length of the feed cap
Deembed=Hi_feed; %Deembeding distance
Feed_X=-Gnd_Ra+1; % X coordinate of the feed
Feed_Y=0;  % Y coordinate of the feed
Feed_Z=Sub_Z1; % Z coordinate of the feed
StrX=1; %Width of the feed line
StrY=Gnd_Ra; % Length of the feed line


ChromLength=21;
for ip=1:popsize
    tic

%Create random initial population

        for jp = 1:ChromLength
            if rand() > 0.5
                Pop(ip,jp) = 0;
            else
                Pop(ip,jp) = 1;
            end
        end

%Determine the dimensions of the CSRR parameters

gap=.3; Cthick=.3;Split_W=0.1;C1_R=5; nn=0;
```

```
for nn=1:6
    C1_R=C1_R+0.1*((2^(nn-1))*Pop(ip,nn));
end

for nn=1:5
    gap=gap+.075*((2^(nn-1))*Pop(ip,nn+6));
    Cthick=Cthick+.075*((2^(nn-1))*Pop(ip,nn+11));
    Split_W=Split_W+.075*((2^(nn-1))*Pop(ip,nn+16));
end

Split_L=C1_R;
RingNum=(C1_R/(Cthick+gap)); %Find the number of rings

%HFSS Executable Path.
hfssExePath = 'C:\"Program Files (x86)"\Ansoft\HFSS11\hfss.exe';

%Temp files location.
tmpPrjFile = 'C:\MatlabHFSS\Finalpatch\DualComp.hfss';
tmpDataFile = 'C:\MatlabHFSS\Finalpatch\DualCompData.m';
tmpScriptFile = 'C:\MatlabHFSS\Finalpatch\DualCompScript.vbs';
FarFieldpath='C:/MatlabHFSS/Finalpatch/farField.m' ;

% Create a new temporary HFSS script file.
fid = fopen(tmpScriptFile, 'wt');

% Create a new HFSS Project and insert a new design.
hfssNewProject(fid);
hfssInsertDesign(fid, 'GA_Loop');

%Draw airBox
hfssCylinder(fid, 'AirBox', 'Z', [0, 0, -G_H/2], G_R, G_H, 'mm');
hfssAssignRadiation(fid, 'Box_Rad', 'AirBox');
hfssSetTransparency(fid, {'AirBox'}, 0.9);

%Drawfeed
hfssHollowCylinder(fid, 'Outer_C', 'X', [Feed_X, Feed_Y, Feed_Z],...
 Th_oc, R_oc, -Hi_feed, 'mm');
hfssAssignPE(fid, 'PEC_oc',  {'Outer_C'});
%
hfssHollowCylinder(fid, 'Tef', 'X', [Feed_X, Feed_Y, Feed_Z],...
 R_feed, Th_oc, -Hi_feed, 'mm');
hfssAssignMaterial(fid, 'Tef', 'Neltec NX9294 (tm)');
%
hfssCylinder(fid, 'Inner_C', 'X', [Feed_X, Feed_Y, Feed_Z],...
```

229

```
 R_feed, -Hi_feed, 'mm');
hfssAssignPE(fid, 'PEC_Ic',  {'Inner_C'});
%Draw waveport
hfssCircularPort(fid, 'LPort', 'port1', 'X', [Feed_X-(Hi_feed),...
 Feed_Y, Feed_Z], Th_oc,Deembed, 'mm');


%Draw feed cap
hfssCylinder(fid, 'PortCup', 'X', [Feed_X-(Hi_feed),...
 Feed_Y, Feed_Z], R_oc, -CapZ, 'mm');
hfssAssignMaterial(fid, 'PortCup', 'pec');


%Create the vertical flange of the feed
hfssRectangle(fid, 'FeedRec', 'X', [-Gnd_Ra+1, -4, -Sub_Z2-1],...
 8, 8, 'mm');
hfssCircle(fid, 'FeedRec2', 'X', [-Gnd_Ra+1, 0, Feed_Z],R_oc , 'mm');
hfssSubtract(fid, {'FeedRec'}, {'FeedRec2'});
hfssAssignFiniteCond(fid, 'PEC_FeedRec', 0, 'um',  {'FeedRec'});


%Draw Ground plane
hfssCircle(fid, 'Gnd', 'Z', [0, 0, -Sub_Z2],Gnd_Ra , 'mm');
hfssRectangle(fid, 'Gnd_Sub', 'Z', [-Gnd_Ra, -4, -Sub_Z2],...
 1, 8, 'mm');
hfssSubtract(fid, {'Gnd'}, {'Gnd_Sub'});
hfssAssignFiniteCond(fid, 'PEC_Gnd', 0, 'um',  {'Gnd'});
hfssSetTransparency(fid, {'Gnd'}, 0.9);


%Draw Substrate
hfssCylinder(fid, 'Subs_Patch', 'Z', [0, 0, -Sub_Z2],...
 Sub1_Ra, Sub_Z2+Sub_Z1 , 'mm');
hfssBox(fid, 'Subs_Sub', [-Gnd_Ra,-4, -Sub_Z2],...
 [ 1,8, Sub_Z2+Sub_Z1], 'mm');
hfssSubtract(fid, {'Subs_Patch'}, {'Subs_Sub'});
hfssAssignMaterial(fid, 'Subs_Patch', ...
'Rogers RT/duroid 5870 (tm)');
hfssSetColor(fid, 'Subs_Patch', [0, 128, 0]);
hfssSetTransparency(fid, {'Subs_Patch'}, 0.9);



%Draw Patch
hfssCircle(fid, 'PatchP', 'Z', [0, 0, Sub_Z1],Patch_Ra , 'mm');
hfssAssignFiniteCond(fid, 'PatP', 0, 'um', {'PatchP'});
hfssSetTransparency(fid, {'PatchP'}, 0.9);
hfssRectangle(fid, 'stripF', 'Z', [ -Gnd_Ra+1,-StrX/2, Sub_Z1],...
 StrY, StrX, 'mm');
hfssUnite(fid, 'PatchP' ,'stripF');
```

```
%Draw CSRR disk
hfssCircle(fid, 'comp', 'Z', [0, 0, 0],Comp , 'mm');
hfssAssignFiniteCond(fid, 'PEC_comp', 0, 'um',  {'comp'});
hfssSetTransparency(fid, {'Gnd'}, 0.9);
Move_Y=0;%+YShisft/2;
N=0;
Si=1;

%Draw SRRs and substract from disk
for ix=1:RingNum
hfssCircle(fid,  sprintf('CR%d',N), 'Z', [0, Move_Y, 0],C1_R , 'mm');
hfssCircle(fid,  sprintf('SRs%d',N), 'Z', [0, Move_Y, 0],...
C1_R-Cthick , 'mm');
hfssRectangle(fid, sprintf('Rec%d',N), 'Z', ...
[0,Move_Y-Split_W/2, 0], Si*Split_L, Split_W,  'mm');
hfssSubtract(fid, {sprintf('CR%d',N)}, {sprintf('SRs%d',N)});
hfssSubtract(fid, {sprintf('CR%d',N)}, {sprintf('Rec%d',N)});
hfssSubtract(fid, {'comp'}, {sprintf('CR%d',N)});
C1_R=C1_R-gap-Cthick;
N=N+1;%
Si=-1*Si;
end

%%%%%%%%%%%%%%%%%%%%%%%%%%%%%%%%%%%%%%%%%%%%%%%%
% Add a Solution Setup.
hfssInsertSolution(fid, 'Setup', fC/1e9, 0.001, 7);

%ThetaStart,ThetaStop, ThetaStep, Phistart.......
hfssInsertFarField(fid, 'Infinite Sphere1',0,0,0,0,0,0,'deg');

% Save the project to a temporary file and solve it.
hfssSaveProject(fid, tmpPrjFile, true);
hfssSolveSetup(fid, 'Setup');
FFc=fC*(1e-9);
hfssCreateReportDualComp(fid,FarFieldpath, FFc, 'GHz')

%Export the Network data as an m-file and close the script.
hfssExportNetworkData(fid, tmpDataFile, 'Setup', 'LastAdaptive');
fclose(fid);

% Execute the Script by starting HFSS.
disp('Solving using HFSS ..');
hfssExecuteScript(hfssExePath, tmpScriptFile);
```

```matlab
% Load the data by running the exported matlab file.
%%%%%%%%%%%%%%%%%%%%%%%%%%%%%%%%%
disp('Solution Completed.');
[heffi, FarField] = hdrload('farField.m');

f=FarField(:,1);
Gr=FarField(:,2);

run(tmpDataFile);
S1r=(abs(S(1,:,:)));

if Gr>.3 && 20*log10(S1r)<-8
fitness(ip)=-(1-S1r^2)*sqrt(Gr)
else
fitness(ip)=-(1-S1r^2)*sqrt(Gr)*.1
end

%Save the current population and the fitness
 BianiLoop_Pop=Pop;
      savefile = 'BianiLoop_Pop.mat';
 save(savefile, 'BianiLoop_Pop');
 BianiLoop_fit=fitness;
        savefile = 'BianiLoop_fit.mat';
 save(savefile, 'BianiLoop_fit');

toc
end

%Do statistics for initial population
[fitness,ind]=sort(fitness) ;    %Sort fitness
Pop=Pop(ind,:);    % sorts population
minc(1)=min(fitness);% find min of the population

 popsize=popsize/5;
 for ii=1:popsize
     Pop(ii,:)=Pop(ii,:);
     fitness(ii)=fitness(ii);
 end


Nt=ChromLength;
%Start Iterating through generations
while iga<maxit
      tic
      NewPop=Pop;  %store the previous population
```

232

```
      Muprob=.2;     % set mutation rate
selection=0.2;     % fraction of population kept

%     %I) Selection of chromozomes to be kept
indx=find(fitness<=mean(fitness));
keep=ceil(selection*popsize); %Number of chrom to keep
fitkeep=fitness(indx);% fitnesses to keep
Popkeep=Pop(indx,:);%Chroms to keep
M1=ceil((popsize-keep)*.5);
M2=ceil((popsize-keep)*.5);

%II) Pairing Chromozomes for Xover/Mutation
%Case I: random selection of 2 individual

Ntourn=2;
 for ic2=1:2:M2
       %Random Selection of Parents
%first Parent
ma=ceil(keep*rand());  % indicies of first parent
%Second parent
pa=ceil(keep*rand());  % indicies of second parent

if ic2<=ceil(M2/2)
%1pt Crossover
ma=1;
Xpt=ceil(rand()*(Nt-1));
Pop(keep+M1+ic2-1,:)=[Pop(ma,1:Xpt) Pop(pa,Xpt+1:Nt)]; % Offspring 1
Pop(keep+M1+ic2,:)=[Pop(pa,1:Xpt) Pop(ma,Xpt+1:Nt)];%Offspring 2
end
if ic2>=ceil(M2/3)
%2pt Crossover
Xpt1=ceil(rand()*Nt/2);
Xpt2=Xpt1 + ceil(rand()*(Nt-1)/2);
Pop(keep+M1+ic2-1,:)=[Pop(ma,1:Xpt1) Pop(pa,Xpt1+1:Xpt2)...
 Pop(ma,Xpt2+1:Nt)]; % Offspring 1
Pop(keep+M1+ic2,:)=[Pop(pa,1:Xpt1) Pop(ma,Xpt1+1:Xpt2)...
 Pop(pa,Xpt2+1:Nt)];%Offspring 2
end
 end

  %Case I:  selection the best of 2 individual
  for ic=1:2:M1
%first Parent
rc=ceil(keep*rand(1,Ntourn)); %Randomly select 2
[c,ci]=min(fitness(rc)); % Selectlowest fitness
```

```
ma=rc(ci);  % indicies of first parent
%Second parent
rc=ceil(keep*rand(1,Ntourn));%%Randomly select 2t
[c,ci]=min(fitness(rc)); % Select lowest fitness
pa=rc(ci);  % indicies of second parent
%1pt Crossover
Xpt=ceil(rand()*(Nt-1));
Pop(keep+ic-1,:)=[Pop(ma,1:Xpt) Pop(pa,Xpt+1:Nt)]; % Offspring 1
Pop(keep+ic,:)=[Pop(pa,1:Xpt) Pop(ma,Xpt+1:Nt)];%Offspring 2
  end


%III) mutation: keep best two and mutate a single bit on the other
%chromosomes based on mutating probability

    for iMu=keep:popsize
    if Muprob>=rand()
Mupt=ceil(rand()*Nt);% bit to be mutated
Pop(iMu,Mupt)=not(Pop(iMu,Mupt));
    end
    end



CurrentChrom=keep;
for ip = keep:popsize

    %Added so that repeated structures are not analyzed
    for ipp=1:popsize
        if Pop(ip,:)==NewPop(ipp,:)
            for ipp1=1:Nt
                if Muprob>=rand()
        Pop(ip,ipp1)=not(Pop(ip,ipp1));
                end
            end
        end
    end

%Determine the dimensions of the CSRR parameters

gap=.3; Cthick=.3;Split_W=0.1;C1_R=5; nn=0;

for nn=1:6
    C1_R=C1_R+0.1*((2^(nn-1))*Pop(ip,nn));
end
```

```matlab
for nn=1:5
    gap=gap+.075*((2^(nn-1))*Pop(ip,nn+6));
    Cthick=Cthick+.075*((2^(nn-1))*Pop(ip,nn+11));
    Split_W=Split_W+.075*((2^(nn-1))*Pop(ip,nn+16));
end

Split_L=C1_R;
RingNum=(C1_R/(Cthick+gap)); %Find the number of rings

%HFSS Executable Path.
hfssExePath = 'C:\"Program Files (x86)"\Ansoft\HFSS11\hfss.exe';

%Temp files location.
tmpPrjFile = 'C:\MatlabHFSS\Finalpatch\DualComp.hfss';
tmpDataFile = 'C:\MatlabHFSS\Finalpatch\DualCompData.m';
tmpScriptFile = 'C:\MatlabHFSS\Finalpatch\DualCompScript.vbs';
FarFieldpath='C:/MatlabHFSS/Finalpatch/farField.m' ;

% Create a new temporary HFSS script file.
fid = fopen(tmpScriptFile, 'wt');

% Create a new HFSS Project and insert a new design.
hfssNewProject(fid);
hfssInsertDesign(fid, 'GA_Loop');

%Draw airBox
hfssCylinder(fid, 'AirBox', 'Z', [0, 0, -G_H/2], G_R, G_H, 'mm');
hfssAssignRadiation(fid, 'Box_Rad', 'AirBox');
hfssSetTransparency(fid, {'AirBox'}, 0.9);

%Drawfeed
hfssHollowCylinder(fid, 'Outer_C', 'X', [Feed_X, Feed_Y, Feed_Z],...
 Th_oc, R_oc, -Hi_feed, 'mm');
hfssAssignPE(fid, 'PEC_oc',  {'Outer_C'});
%
hfssHollowCylinder(fid, 'Tef', 'X', [Feed_X, Feed_Y, Feed_Z],...
 R_feed, Th_oc, -Hi_feed, 'mm');
hfssAssignMaterial(fid, 'Tef', 'Neltec NX9294 (tm)');
%
hfssCylinder(fid, 'Inner_C', 'X', [Feed_X, Feed_Y, Feed_Z],...
 R_feed, -Hi_feed, 'mm');
hfssAssignPE(fid, 'PEC_Ic',  {'Inner_C'});
%Draw waveport
hfssCircularPort(fid, 'LPort', 'port1', 'X', [Feed_X-(Hi_feed),...
```

```
 Feed_Y, Feed_Z], Th_oc,Deembed, 'mm');

%Draw feed cap
hfssCylinder(fid, 'PortCup', 'X', [Feed_X-(Hi_feed),...
 Feed_Y, Feed_Z], R_oc, -CapZ, 'mm');
hfssAssignMaterial(fid, 'PortCup', 'pec');

%Create the vertical flange of the feed
hfssRectangle(fid, 'FeedRec', 'X', [-Gnd_Ra+1, -4, -Sub_Z2-1],...
 8, 8, 'mm');
hfssCircle(fid, 'FeedRec2', 'X', [-Gnd_Ra+1, 0, Feed_Z],R_oc , 'mm');
hfssSubtract(fid, {'FeedRec'}, {'FeedRec2'});
hfssAssignFiniteCond(fid, 'PEC_FeedRec', 0, 'um',  {'FeedRec'});

%Draw Ground plane
hfssCircle(fid, 'Gnd', 'Z', [0, 0, -Sub_Z2],Gnd_Ra , 'mm');
hfssRectangle(fid, 'Gnd_Sub', 'Z', [-Gnd_Ra, -4, -Sub_Z2],...
 1, 8, 'mm');
hfssSubtract(fid, {'Gnd'}, {'Gnd_Sub'});
hfssAssignFiniteCond(fid, 'PEC_Gnd', 0, 'um',  {'Gnd'});
hfssSetTransparency(fid, {'Gnd'}, 0.9);

%Draw Substrate
hfssCylinder(fid, 'Subs_Patch', 'Z', [0, 0, -Sub_Z2],...
 Sub1_Ra, Sub_Z2+Sub_Z1 , 'mm');
hfssBox(fid, 'Subs_Sub', [-Gnd_Ra,-4, -Sub_Z2],...
 [ 1,8, Sub_Z2+Sub_Z1], 'mm');
hfssSubtract(fid, {'Subs_Patch'}, {'Subs_Sub'});
hfssAssignMaterial(fid, 'Subs_Patch',...
 'Rogers RT/duroid 5870 (tm)');
hfssSetColor(fid, 'Subs_Patch', [0, 128, 0]);
hfssSetTransparency(fid, {'Subs_Patch'}, 0.9);


%Draw Patch
hfssCircle(fid, 'PatchP', 'Z', [0, 0, Sub_Z1],Patch_Ra , 'mm');
hfssAssignFiniteCond(fid, 'PatP', 0, 'um', {'PatchP'});
hfssSetTransparency(fid, {'PatchP'}, 0.9);
hfssRectangle(fid, 'stripF', 'Z', [ -Gnd_Ra+1,-StrX/2, Sub_Z1],...
 StrY, StrX, 'mm');
hfssUnite(fid, 'PatchP' ,'stripF');

%Draw CSRR disk
hfssCircle(fid, 'comp', 'Z', [0, 0, 0],Comp , 'mm');
hfssAssignFiniteCond(fid, 'PEC_comp', 0, 'um',  {'comp'});
```

```
hfssSetTransparency(fid, {'Gnd'}, 0.9);
Move_Y=0;%+YShisft/2;
N=0;
Si=1;


%Draw SRRs and substract from disk
for ix=1:RingNum
hfssCircle(fid,  sprintf('CR%d',N), 'Z', [0, Move_Y, 0],C1_R , 'mm');
hfssCircle(fid,  sprintf('SRs%d',N), 'Z', [0, Move_Y, 0],...
C1_R-Cthick , 'mm');
hfssRectangle(fid, sprintf('Rec%d',N), 'Z', ...
[0,Move_Y-Split_W/2, 0], Si*Split_L, Split_W,  'mm');
hfssSubtract(fid, {sprintf('CR%d',N)}, {sprintf('SRs%d',N)});
hfssSubtract(fid, {sprintf('CR%d',N)}, {sprintf('Rec%d',N)});
hfssSubtract(fid, {'comp'}, {sprintf('CR%d',N)});
C1_R=C1_R-gap-Cthick;
N=N+1;%
Si=-1*Si;
end
%%%%%%%%%%%%%%%%%%%%%%%%%%%%%%%%%%%%%%%%%%%%%%%%%%%%%%%%%%%%%%%%%%%%

% Add a Solution Setup.
hfssInsertSolution(fid, 'Setup', fC/1e9, 0.001, 7);

%ThetaStart,ThetaStop, ThetaStep, Phistart.......
hfssInsertFarField(fid, 'Infinite Sphere1',0,0,0,0,0,0,'deg');

% Save the project to a temporary file and solve it.
hfssSaveProject(fid, tmpPrjFile, true);
hfssSolveSetup(fid, 'Setup');
FFc=fC*(1e-9);
hfssCreateReportDualComp(fid,FarFieldpath, FFc, 'GHz')

%Export the Network data as an m-file and close the script.
hfssExportNetworkData(fid, tmpDataFile, 'Setup', 'LastAdaptive');
fclose(fid);

% Execute the Script by starting HFSS.
disp('Solving using HFSS ..');
hfssExecuteScript(hfssExePath, tmpScriptFile);

% Load the data by running the exported matlab file.
%%%%%%%%%%%%%%%%%%%%%%%%%%%%%%%%%%%%%%%%%%%%%%%%%%%%%%%%%%%
disp('Solution Completed.');
```

```matlab
[heffi, FarField] = hdrload('farField.m');

f=FarField(:,1);
Gr=FarField(:,2);

run(tmpDataFile);
S1r=(abs(S(1,:,:)));

if Gr>.3 && 20*log10(S1r)<-8
fitness(ip)=-(1-S1r^2)*sqrt(Gr)
else
fitness(ip)=-(1-S1r^2)*sqrt(Gr)*.1
end


%Save the current population and the fitness
 BiLoop_CurPop=Pop;
        savefile = 'BiLoop_CurPop.mat';
 save(savefile, 'BiLoop_CurPop');
 BiLoop_Curfit=fitness;
        savefile = 'BiLoop_Curfit.mat';
 save(savefile, 'BiLoop_Curfit');
 toc
 CurrentChrom=CurrentChrom+1
 end %of  current population

% % % %_____
%Do statistics for new generation
[fitness,ind]=sort(fitness), % min cost in  1
Pop=Pop(ind,:) ;  % sorts population
minc(iga+1)=min(fitness);% min of population



%Stopping criteria
if iga>maxit || fitness(1)<mincost
    break
end

 GenTopFit=[iga fitness(1) fitness(2)]
 iga=iga+1

end
```

BIBLIOGRAPHY

BIBLIOGRAPHY

[1] J. B.Pendry, A. J. Holden, D. J. Robbins, and W. J. Stewart, "Low frequency plasmons in thin wire structures," J. Phys. Condens. Matter, Vol. 10, 4785 – 4809, 1998.

[2] J. B.Pendry, A. J. Holden, D. J. Robbins, and W. J. Stewart, "Magnetism from conductors and enhanced nonlinear phenomena," IEEE Trans. on Microwave Theory and Techniques, Vol. 47, 2075 - 2084, 1999.

[3] J. B. Pendry, "Negative refraction makes a perfect lens," Phys. Rev. Lett., vol. 85, no. 18, pp. 3966 - 3969, 2000.

[4] R. A. Shelby, D. R. Smith, S. Schultz, "Experimental verification of a negative index of refraction," Science, vol. 292, pp. 77 - 79, 2001.

[5] L. Rayleigh. 1892. "On the instability of cylindrical fluid surfaces," Phil. Mag., vol. 34, no. 5, pp. 177 – 180, 1892.

[6] J. C. Bose, "On the rotation of plane of polarization of electric waves by a twisted structure," Proc. Roy. Soc., vol. 63, pp. 146 – 152, 1898.

[7] W. E. Kock, " Metal-lens antennas," Proc. of I.R.E., vol 34 pp. 828 – 836, 1946.

[8] W. E. Kock, " Metallic delay lenses," Bell Sys. Tech. J., vol. 27, pp. 58 – 82, 1948.

[9] S. B. Cohn, "Analysis of the metal-strip delay structure for microwave lenses," Journal Appl. Phys., vol. 20, pp. 257 - 262, 1949.

[10] J. Brown, "Artificial dielectrics," Proc in dielectrics, vol. 2, pp. 195 - 225, 1960.

[11] W. Rotman, "Plasma simulation by artificial dielectrics and parallel plate media," IRE Trans. Antennas Propag., vol. 10, pp. 82 - 95, 1962.

[12] S. A. Schelkunoff and H. T. Friis, Antennas: theory and practice, New York: John Wiley & Sons, 1952.

[13] M. V. Kostin and V. V. Shevchenko, Artificial magnetics based on double circular elements, Proc. Bian- isotropic, Perigueux, France, pp. 4956, 1994.

[14] I. V. Lindell, A. H. Sihvola, S. A. Tretyakov, and A. J. Viitanen, "Electromagnetic waves in chiral and bi-isotropic media," Artech House, Norwood, MA, 1994.

[15] V. Veselago, "The electrodynamics of substances with simultaneously negative values of epsilon and mu," Sov Phys Usp 10(4), pp. 509 – 514, 1968.

[16] D. M. Pozar, "Microstrip Antennas," Proc, IEEE, vol. 80, no. 1, pp. 79-81, 1992.

[17] C. M. Krowne, "Cylindrical- rectangular microstrip antenna," IEEE Trans. Antennas Propag., vol. 31, no. 1, pp. 194-199, 1983.

[18] S. B. De Assis Fonseca, and A. J. Giarola, "Microstrip disk antennas, part I: efficiency of space wave launching," IEEE Trans. Antennas Propag., vol. 32, no. 6, pp 561-567, 1984.

[19] S. B. De Assis Fonseca, and A. J. Giarola, "Microstrip disk antennas, part II: The problem of surface wave radiation by dielectric truncation," IEEE Trans. Antennas Propag., vol. 32, no. 6, pp 568-573, 1984.

[20] J. Huang, "The finite ground plane effect on the microstrip antenna radiation patterns," IEEE Trans. Antennas Propag., vol. 31, no. 7, pp. 649-653, 1983.

[21] I. Lier and K. R. Jakobsen, "Rectangular microstrip patch antenna with infinite and finite ground plane dimensions," IEEE Trans. Antennas Propag., vol. 31, no. 6, pp. 978-984, 1983.

[22] C. A. Balanis, *Antenna Theory, 3rd edition*, John Wiley & Sons, Hoboken, NJ, 2005.

[23] C. A. Balanis, *Modern Antenna handbook*, John Wiley & Sons, Hoboken, NJ, 2008.

[24] D. M. Pozar,, *Microstrip Antennas*, John Wiley & Sons, Hoboken, NJ, 1995.

[25] G. Subodh, V. Deepu, P. Mohanan, and M. T. Sebastian, "A dielectric response of high permittivity polymer ceramic composite with low loss tangent," Applied Physics Lett., vol. 95, 062903 pp. 1-3, 2009.

[26] Z. M. Dang, T. Zhou, S. H. Yao, J. K. Yuan, J. W. Zha, H. T. Song, J. Y. Li, Q. Chen, W. T. Yang, and J. Bai, "Advanced calcium copper titanate/polyimide

functional hybrid films with high dielectric permittivity," Adv. Mater., vol. 21, pp. 20772082, 2009.

[27] K. D. Chandrasekhar, A. Venimadhav, and A. K. Das, "High dielectric permittivity in semiconducting Pr0.6Ca0.4MnO3 filled polyvinylidene fluoride nanocomposites with low percolation threshold," Applied Physics Lett., vol 95, 062904 pp. 1-3, 2009.

[28] R. Waterhouse, "Small microstrip patch antenna," Electron. Lett., vol. 31, no. 8, pp. 604-605, 1995.

[29] S. Dey, and R. Mittra, "Compact microstrip patch antenna," Microwave Opt. Technol. Lett., vol. 13, pp. 12-14, 1996.

[30] C. L. Tang, and K. L. Wong, "Small circular microstrip antenna with dual frequency operation," Electron. Lett. vol. 33, pp. 1112-1113, 1997.

[31] K. L. Wong, and W. S. Chen, "Compact microstrip antenna with dual frequency operation," Electron. Lett., vol. 33, pp. 646-647, 1997.

[32] K. L. Wong, *Compact and broadband microstrip antennas*, John Wiley & Sons, Hoboken, NJ, 2002.

[33] K. L. Wong, and W. S. Chen, "Compact triangular microstrip antenna," Electron. Lett., vol. 33, pp. 433-434, 1997.

[34] S. C. pan, and K. L. Wong, "Dual frequency triangular microstrip antenna with a shorting pin," IEEE Trans. Antennas Propag. vol. 45, pp 1889-1891, 1997.

[35] S. A. Bokhari, J. F. Zuercher, J. R. Mosig, and F. E. Gardiol, "A small microstrip patch antenna with a convenient tuning option," IEEE Trans. Antennas Propag., vol. 44, no. 11, pp. 1521-1528, 1996.

[36] K. L. Wong, C. L. Tang, and H. T. Chen, " A compact meandered circular microstrip antenna with a shorting pin," Microwave Opt. Technol. Lett, vol. 15, pp. 147-149, 1997.

[37] J. Anguera, C. Puente, C. Borja, R. Montero, and J. Soler, "Small and high directivity bowtie patch antenna based on the sierpinski fractal," Microwave Opt. Technol. Lett., Nov. 2001.

[38] J. P. Gianvittorio, Y. Rahmat-Samii, "Fractal antennas: a novel antenna miniaturization technique, and applications" IEEE Trans. Antennas Propag. Mag, vol. 44, no. 1, pp. 20-36, 2002.

[39] R. Chair, K. M. Luke, and K. F. Lee "Miniature multi-layer shorted patch antenna," Electron. Lett., vol. 36, no. 1, pp. 3-4, 2000.

[40] R. W. Ziolkowski and A. Erentok,"Metamaterial-based efficient electrically small antennas," IEEE Trans. Antennas Propag., vol. 54, no. 7, pp. 2113-2130, July 2006.

[41] R. W. Ziolkowski, A. Erentok and E. Okay, "Densely packed arrays of metamaterial-inspired antennas," European Conference on Antennas and Propagation, Edinburgh, Scotland, pp. 1-4, Nov. 2006.

[42] A. Erentok and R. W. Ziolkowski , "An efficient metamaterial-inspired electrically-small antenna," Microw. Opt. Tech. Lett., vol. 49, no. 6, pp. 1287-1290, 2007.

[43] A. Erentok and R. W. Ziolkowski , "Two dimensional-efficient metamaterial-inspired electrically-small antenna," Microw. Opt. Tech. Lett., vol. 49, no. 7, pp. 1669-1673, 2007.

[44] F. Bilotti and L. Vegni, "From metamaterial-based to metamaterial-inspired miniaturized antennas: a possible procedure and some examples," URSI XXIX General Assembly, Chicago, Il, pp. 1-4, Aug. 2008.

[45] N. Engheta and R. W. Ziolkowski, *Metamaterials: Physics and Engineering Explorations*, Wiley-IEEE Press, Hoboken, NJ, 2006.

[46] O. S. Kim, and O. Breinbjerg, "Miniaturised self-resonant split-ring resonator antenna," IEEE Electron. Lett., vol. 45, no. 4, pp. 196-197, February 2009.

[47] S. Y. Chen, R. Ouedraogo, E. J. Rothwell, A. Temme and Alejandro R. Diaz, "MNG-metamaterial-based efficient small loop antenna," International Symposium on Antennas and Propagation and URSI Radio Science Meeting, Charleston, SC, Digest, pp. 1-4, June 1-5, 2009.

[48] P. M. T. Ikonen, K. N. Rozanov, A. V. Osipov, P. Alitalo and S. A. Tretyakov, "Magneto-dielectric substrates in antenna miniaturization: potential and limitations," IEEE Trans. Antennas Propag., vol. 54, no. 11, pp. 3391-3399, 2006.

[49] K. Buell, H. Mosallaei and K. Sarabandi, "A substrate for small patch antennas providing tunable miniaturization factors," IEEE Trans. Microw. Theory Tech., vol. 54, no. 1, pp. 135-146, 2006.

[50] J. McVay, N. Engheta, and A. Hoorfar, "High-impedance metamaterial surfaces using Hilbert-curve inclusions," IEEE Microw. Wireless Compon. Lett., vol. 14, no. 3, pp. 130-132, 2004.

[51] A Erentok, P Luljak, and R. W. Ziolkwoski, "Antenna performance near a volumetric metamaterial realization of an artificial magnetic conductor," IEEE Trans. Antennas Propag., vol 53, pp. 160-172, 2005.

[52] A. Alu, F. Bilotti, N. Engheta, and L. Vegni, "Sub-wavelength, compact, resonant patch antennas loaded with metamaterials," IEEE Trans. Antennas Propag., vol. 55, no. 1, pp. 13-25, 2007.

[53] F. Bilotti, A. Alu and L. Vegni, "Design of miniaturized metamaterial patch antennas with μ-negative loading," IEEE Trans. Antennas Propag., vol. 56, no. 6, pp. 1640-1647, 2008.

[54] H. Mosallaei and K. Sarabandi, "Design and modeling of patch antenna printed on magneto-dielectric embedded-circuit metasubstrate," IEEE Trans. Antennas Propag., vol. 55, no. 1, pp. 45-52, 2007.

[55] D. Sievenpiper, L. Zhang, R. F. J. Broas, N. G. Alexpoulos, and E. Yablonovitch, "High-impedance electromagnetic surfaces with a forbidden frequency band," IEEE Trans. Microwave Theory Tech., vol. 47, pp. 20592074, 1999.

[56] D. Sievenpiper, H. P. Hsu, J. Schaffner, G. Tangonan, R. Garcia, and S. Ontiveros, "Low profile, four sector diversity antenna on high-impedance ground plane," Elect. Lett., vol. 36, pp. 1343-1345, 2000. IEEE Trans. Microwave Theory Tech., vol. 47, pp. 20592074, 1999.

[57] K. Sarabandi, M. D. Casciato, and I. S. Koh, "Efficient calculation of the fields of a dipole radiating above an impedance surface, IEEE Trans. Antennas Propag., vol. 50, pp. 12221235, 2002.

[58] H. Mosallaei and K. Sarabandi, "Antenna miniaturization and bandwidth enhancement using a reactive impedance substrate," IEEE Trans. Antennas Propag., vol. 52, no. 9, pp. 2403-2414, 2007.

[59] F. Falcone, T. Lopetegi, J. D. Baena, R. Marqus, F. Martin, and M. Sorolla, "Effective negative-stop-band microstrip lines based on complementary split ring resonators," IEEE Microw. Wireless Compon. Lett., vol. 14, no. 6, pp. 280-282, 2004.

[60] Y. Lee, S. Tse, Y. Hao, and C. G. Parini, "A compact microstrip antenna with improved bandwidth using complementary split-ring resonator (CSRR) loading," IEEE International Symposium on Antennas and Propagation and URSI Radio Science Meeting Digest, pp. 5431-5434, 2007.

[61] A. U. Limaye, J. Venkataraman, "Size reduction in microstrip antennas using left-handed materials realized by complementary split-ring resonators in ground plane," IEEE International Symposium on Antennas and Propagation and URSI Radio Science Meeting Digest, pp. 1869-1872, 2007.

[62] A. Ali, M. A. Khan, and Z. Hu, "Microstrip Patch Antenna with Harmonic Suppression using complementary split ring resonators," IWAT International Workshop on, pp. 361-363, 2007.

[63] M. Li; M. Lu, T. J. Cui, "Novel miniaturized dual band antenna design using complementary metamaterial," Metamaterials, 2008 International Workshop on , vol., no., pp. 374-376, 2008.

[64] F. Bilotti, A. Toscano, and L. Vegni, "Design of spiral and multiple split-ring resonators for the realization of miniaturized metamaterial samples," IEEE Trans. Antennas Propag., vol 55, no. 8, pp. 2258-2267, 2007.

[65] R. O. Ouedraogo and E. J. Rothwell, "Metamaterial-inspired patch antenna miniaturization technique," IEEE International Symposium on Antennas and Propagation and URSI Radio Science Meeting Digest, pp. 1-4, 2010.

[66] R. O. Ouedraogo, E. J. Rothwell, A. R. Diaz, K. Fuchi, and A. Temme, "Miniaturization of patch antennas using a metamaterial-inspired technique," IEEE Antennas Wireless Propag. Lett., vol. 9, pp. 75-78, 2010.

[67] U. L. Rohde, J. Whitaker and A. Bateman, *Communications Receivers: DPS, Software Radios, and Design*, McGraw-Hill Professional, Dec. 2000.

[68] R. S. Kshetrimayum, L. Zhu and K. J. Vinoy, "Equivalent material parameter extraction of double strip loaded waveguide," IEICE Electron. Express., vol. 2, no. 5, pp. 165-169, March 2005.

[69] X. Chen, T. M. Grzegorczyk, B. I. Wu, J. Pacheco, and J. A. Kong,"Robust method to retrieve the constitutive effective parameters of metamaterials," Phys. Rev. E 70, 016608 , pp. 1-7, July 2004.

[70] D. R. Smith, D. C. Vier, T. Koschny, and C. M. Soukoulis, "Electromagnetic parameter retrieval from inhomogeneous metamaterials," Phys. Rev. E 71, 036617, pp. 1-11, March 2005.

[71] A. R. Diaz and O. Sigmund, "A topology optimization method for design of negative permeability metamaterials," Struct. Mult. Optim., vol. 41, no. 2, pp. 163 – 177, 2010.

[72] R. O. Ouedraogo, E. J. Rothwell, A. R. Diaz, S. Y. Chen, A. Temme, and K. Fuchi, "In situ optimization of metamaterial-inspired loop antennas," IEEE Antennas and Wireless Propag. Lett., vol. 9, pp. 75-78, 2010.

[73] R. Levy and S. B. Cohn, "A history of microwave filter research, design, and development," IEEE Trans. Microw. Theory Tech., vol. 32, no. 9, pp. 1055-1067, 1984.

[74] M. Guglielmi, R. Molina, and A. Melcon, "Dual-mode circular waveguide filters without tuning screw," IEEE Microw. Guided Wave Lett., vol. 2, no. 11, pp. 457-458, 1992.

[75] Y. Konishi and K. Uenakada, "The design of a bandpass filter with inductive strip-planar circuit mounted inwaveguide," IEEE Trans. Microw. Theory Tech., vol. 22, no. 9, pp. 869-873, 1974.

[76] F. Arndt, J. Bornemann, D. Grauerholz ,R.Vahldieck,, " Theory and Design of Low-Insertion Loss Fin-Line Filters ", IEEE Trans. Microw. Theory Tech., vol. 30, no. 2, pp. 155-163, 1982.

[77] R. Vahldieck, J. Bomemann, F. Arndt, and D. Grauerholz, " Optimized waveguide E-plane metal insert filters for millimeter-wave applications," IEEE Trans Microwave Theory Tech., vol. MTT-31, pp. 65-69, Jan. 1983.

[78] R. Vahldieck and W. J. R. Hoefer, "Finline and metal insert filters with improved passband separation and increased stopband attenuation," IEEE Trans. Microw. Theory Tech., vol. 33, no. 12, pp. 1333-1339, 1985.

[79] P. Savi, D. Trinchero, R. Tascone, and R. Orta, "A new approach to the design of dual-mode rectangular waveguide filters with distributed coupling," IEEE Trans. Microw. Theory Tech., vol. 45, no. 2, pp. 221-228, 1997.

[80] Y. C. Shih, "Design of waveguide E-plane filters with all-metal inserts," IEEE Trans. Microw. Theory Tech., vol. 32, no. 7, pp. 695-704, 1984.

[81] G. Goussetis, D Budimir, "Novel periodically loaded E-plane filters," IEEE Microw. Wireless Compon. Lett., vol. 13, no. 6, pp. 193-195, 2003.

[82] D. W. Kim, and J. H. Lee, "Partial H-plane filters with partially inserted H-plane metal vane," IEEE Microw. Wireless Compon. Lett., vol. 15, no. 5, pp. 351-353, 2005.

[83] A. J. Robinson, R. D. Seager, and J. C. Vardaxoglou, "Waveguide with resonant array inserts," Electron. Lett., vol. 28, no. 23, Nov. 1992. Complicated to build because array of resonant structures have to be place against each wall

[84] R. J. Langley, "A dual-frequency band waveguide using FSS," IEEE Microw. Guided Wave Lett., vol. 3, no. 1, pp. 9-10, Jan. 1993.

[85] R. D. Seager, J. C.Vardaxoglou, and D. S. Lockyer, "Close coupled resonant aperture inserts for waveguide filtering applications," IEEE Microw. Wireless Compon. Lett., vol. 11, no. 3, pp. 112-114, Mar. 2001.

[86] A. Monorchio, G. Manara, U. Serra, G. Marola, E. Pagana, "Design of waveguide filters by using genetically optimized frequency selective surfaces," IEEE Microw. Wireless Compon. Lett., vol. 15, no. 6, pp. 407-409, 2005.

[87] N. Engheta and R. W. Ziolkowski, *Metamaterials: Physics and Engineering Explorations*, Wiley-IEEE Press, Hoboken, NJ, 2006.

[88] S. Hrabar, J. Bartolic, and Z. Sipus, "Waveguide miniaturization using uniaxial negative permeability metamaterial," IEEE Trans. Antennas Propag., vol. 53, no. 1, pp. 110-119, 2005.

[89] A. Shelkovnikov, and D. Budimir, "Left-handed rectangular waveguide bandstop filters," Microw. Opt. Tech. Lett. ,vol. 48, no. 5, 2006.

[90] B. Jitha, C. S. Nimisha, C. K. Aanandan, P. Mohanan, and K. Vasudevan, "SRR loaded waveguide band rejection filter with adjustable bandwidth," Microw. Opt. Tech. Lett. ,vol. 48, no. 7, pp. 1427-1429, 2006.

[91] R. O. Ouedraogo, E. J. Rothwell, A. R. Diaz, and K. Fuchi, "Waveguide bandstop filter design using optimized pixelated inserts," IEEE Trans. Antennas Propag., (Under Revision).

[92] I. Gil, J. Garcia-Garcia, J. Bonache, F. Martin, M. Sorolla, and R. Marques, "Varactor-loaded split ring resonators for tunable notch filters at microwave frequencies," Electron. Lett. vol. 40, no. 21, pp. 1347-1348, 2004.

[93] I. Gil, J. Bonache, J. Garcia-Garcia, F. Martin, "Tunable metamaterial transmission lines based on varactor-loaded split-ring resonators", IEEE Transactions Microwave Theory and Techniques, vol. 54, no. 6, pp 2665-2674, 2006.

[94] K. Aydina and E. Ozbay, "Capacitor loaded split ring resonators as tunable metamaterial componentss," Journal Appl. Phys., vol. 101, no. 2, pp. 024911-1 - 024911-5, 2007.

[95] H. Li, Y. Zhang, and L. He, "Tunable filters based on the varactor-loaded spilt-ring resonant structure coupled to the micropstrip line," Microwave and Millimeter Wave Technology International Conference, vol. 3, pp. 1580-1582, 2008.

[96] T. H. Hand, and S. A. Cummer, "Frequency tunable electromagnetic metamaterial using ferroelectric loaded split rings, J. App. Phys., vol.103, 2008.

[97] T. H. Hand, and S. Cummer, "controllable magnetic metamaterial using digitally addressable split-ring resonators ," IEEE Antennas Wireless Propag. Lett., vol. 8, pp.262-265, 2009.

[98] H. Lim, W. S. Jeong, S. H. Lim, D. H. Shin, and N. H. Myung, "A Tunable notch resonator based on varactor-loaded complementary split-ring resonators", Small Antennas and Novel Metamaterials International Workshop, pp. 426-429, 2008.

[99] A. Velez, J. Bonache, F. Martin, "Varactor-loaded complementary split ring resonators (VLCSRR) and their application to tunable metamaterial transmission lines", Microwave and Wireless Components Letters, vol. 18, no. 1, pp. 28-30, 2008.

[100] T. Hand, and S. Cummer, "Characterization of tunable metamaterial elements using MEMS switches," IEEE Antennas Wireless Propag. Lett., vol. 6, pp.401-404, 2008.

[101] W. M. Zhu, H. Cai, T. Mei, T. Bourouina, J. F. Tao, G. Q. Lo, D. L. Kwong and A. Q. Liu, "A MEMS tunablemetamaterial filter," Micro Electro Mechanical Systems (MEMS) International Conference, pp. 196-199, 2010.

[102] T. Driscoll, S. Palit, M. M. Qazilbash, M. Brehm, F. Keilmann, B. G. Chae, S. J. Yun, H. T. Kim, S. Y. Cho, N. M. Jokerst, D. R. Smith, and D. N. Basov, "Dynamic tuning of an infrared hybrid-metamaterial resonance using vanadium dioxide," App. Phys. Lett., vol. 93, pp. 024101-1 - 024101-3, 2008.

[103] T. Driscoll, H. T. Kim, B. G. Chae, B. J. Kim, Y. W. Lee, N. M. Jokerst, S. Palit, D. R. Smith, and D. N. Basov, "Memory metamaterials," Science App. Phys. Lett., vol. 325, pp. 1518 - 1521, 2009.

[104] I. C. Khoo, D. H. Werner, X. Liang, A. Diaz, and B. Weiner, Nanosphere dispersed liquid crystals for tunable negative-zero-positive index of refraction in the optical and terahertz regimes, Opt. Lett., vol. 31, pp. 25922594, 2006.

[105] D. H. Werner, D.H. Kwon, I. C. Khoo, A. V. Kildeshev, and V. M. Shalaev, "Liquid crystal-clad near-infrared metamaterials with tunable negative zero-positive refractive indices," Opt. Exp., vol. 15, pp. 33423347, 2007.

[106] Q. Zhao, L. Kang, B. Du, B. Li, and J. Zhou, "Electrically tunable negative permeability metamaterials based on nematic liquid crystals," App. Phys. Lett., vol.90, pp. 011112-1 - 011112-3, 2007.

[107] I. C. Khoo, A. Diaz, IEEE, J. Liou, M. V. Stinger, J. Huang, and Y. Ma, "Liquid crystals tunable optical metamaterials" IEEE Journal of Selected Topics in Quantum Electronics, vol. 16, no. 2, pp. 410 - 417, 2010.

[108] D. R. Smith, J. B. Pendry, " Homogenization of metamaterials by field averaging," J. Opt. Soc., vol. 23. no. 3, pp. 391 – 403, 2006.

[109] D. R. Smith, W. J. Padilla, D. C. Vier, S. C. Nemat-Nasser, S. Schultz S, "A composite medium with simultaneously negative permeability and permittivity," Phys. Rev. Lett., vol. 84, pp. 4184 – 4187, 2000.

[110] S. Hrabar and J. Bartolic, "Experimental Investigation of backward metamaterials in waveguide environment," IEEE Trans. Antennas Propag., vol. 53, no. 1, pp. 110 – 119, 2005.

[111] R. Marques, J. Martel, F. Mesa and F. Medina, "Left-handed-media simulation and transmission of EM waves in subwavelength split-ring-resonator-loaded metallic waveguides," Phys. rev. Lett., pp. 183901 – 183904, 2002.

[112] J. J. Meeusen,"Error analysis of material characterization using a wave guide applicator," Thesis of the degree of M. S., MSU 2004.

[113] D. M. Pozar, *Microwave Engineering*, John Wiley & Sons Inc, Hoboken, NJ, 2005.

[114] HFSS: "http://www.ansoft.com/products/hf/hfss/" (last visited: 08/03/2011).

[115] Matlab: "http://www.mathworks.com/" (last visited: 08/03/2011).

[116] "http://www.rogerscorp.com/" (last visited: 08/03/2011).

[117] "http://www.skyworksinc.com/" (last visited: 08/03/2011).

[118] "http://www.psemi.com/content/careers/careers.html/" (last visited: 08/03/2011).